DARK MATTER AND ANGULAR MOMENTUM

IN NEARBY DISC GALAXIES

PAVEL E. MANCERA PIÑA

DARK MATTER AND ANGULAR MOMENTUM IN NEARBY DISC GALAXIES PAVEL E. MANCERA PIÑA

rijksuniversiteit
groningen

Dark matter and angular momentum in nearby disc galaxies

Proefschrift

ter verkrijging van de graad van doctor aan de
Rijksuniversiteit Groningen
op gezag van de
rector magnificus prof. dr. C. Wijmenga
en volgens besluit van het College voor Promoties.

De openbare verdediging zal plaatsvinden op

dinsdag 5 juli 2022 om 14.30 uur

by

Pavel Enrique Mancera Piña

geboren op 10 juli 1993
te Mexico Stad, Mexico

Promotores
Prof. dr. F. Fraternali
Prof. dr. T. A. Oosterloo

Copromotor
Dr. E. A. K. Adams

Beoordelingscommissie:
Prof. dr. J. J. Binney
Prof. dr. K. Spekkens
Prof. dr. J. M. van der Hulst

A mi familia

'Si viéramos realmente el universo, tal vez lo entenderíamos.'
'If we truly saw the universe, perhaps we would understand it'

Jorge Luis Borges

The research leading to this thesis has received funding from the Netherlands Research School for Astronomy (Nederlandse Onderzoekschool Voor Astronomie, NOVA) through Project 10.1.5.6, and from the Netherlands Institute for Radio Astronomy (ASTRON).

Cover designed by Minke Koopman

Thesis printed by Ipskamp in FSC-certified paper

Contents

Chapter 1

Introduction

The discernible history of our Universe started with the Big Bang. Today, about 14 billion years later, we are witnesses to an evolutionary pathway that led to the observed bewildering diversity of present-day galaxies, including our own Milky Way. The steps of this complex pathway are far from fully understood, and tracing the processes that shaped galaxies through cosmic time is one of the major goals of modern astrophysics. Looking at nearby galaxies is particularly useful for this task given the high degree of detail in which we can study them using multi-wavelength observations. Because of this, nearby galaxies provide some of the cleanest and most robust constraints for galaxy evolution models.

In this thesis, we have studied the dark matter and angular momentum contents of nearby disc galaxies, both of which largely regulate most stages of galaxy evolution. Disc galaxies are supported by rotation, allowing us to perform accurate measurements of their kinematics on a robust observational basis, and from that to trace their distribution of dark matter and their angular momentum. In this chapter, from Sec. 1.1 to Sec. 1.3, we introduce relevant background in the context of this thesis. In Sec. 1.4 we highlight some of the most urgent open questions addressed in this dissertation. Finally, in Sec. 1.5 we detail the structure and content of the rest of this thesis.

1

1.1 Dark matter haloes and their angular momentum

In the currently favored cosmological model, ΛCDM, the Universe originates from the Big Bang about 13.8 Gyr ago, has a flat geometry, and expands at an accelerated rate. According to the latest results of the Planck collaboration, the mass-energy budget of the Universe consists of about 68.5% of dark energy, 25.6% of dark matter, and 5.9% of ordinary matter (Planck Collaboration et al. 2020). In the name ΛCDM, Λ – the cosmological constant– represents the 'dark energy' responsible for the acceleration of the Universe, and CDM stands for 'cold dark matter', a non-relativistic particle accounting for about 80% of all the matter.

While CDM is a central piece in essentially all our understanding of galaxies, we still know very little about its nature. One of the reasons for this is that dark matter does not seem to interact with baryonic[1] matter other than through gravity. To date, there is no direct or indirect detection of the particles that could constitute dark matter, nor have particles with the expected properties been produced in lab experiments (e.g. Bertone et al. 2005; Bertone & Tait 2018). Despite of this lack of detection of a dark matter particle and the proposal of alternative gravitational theories (e.g. Milgrom 1983; Sanders & McGaugh 2002; Famaey & McGaugh 2012; Verlinde 2017), significant astrophysical evidence suggests dark matter must exist (see Bertone & Hooper 2018 for a historical review). Different constraints (mostly based on the observed large-scale structure of the Universe and on lab experiments, e.g. Davis et al. 1992; Viel et al. 2005; Bullock & Boylan-Kolchin 2017; Agnes et al. 2018; Nadler et al. 2021) have been set regarding the properties of dark matter, and the favored CDM particle is thought to be collisionless and to have a mass around $m_{\rm DM}\ c^2 \approx 100$ GeV. Setting constraints on the nature of dark matter is one of the most urgent tasks in astrophysics.

In our standard picture of galaxy formation, the baryonic components of galaxies (stars, multi-phase gas, and dust) settle within more massive, nearly-spherical dark matter haloes (e.g. Frenk et al. 1988; Franx & de Zeeuw 1992; Schoenmakers et al. 1997; Mo et al. 2010). According to the hierarchical structure formation scenario, small dark matter haloes form first, thanks to the gravitational collapse of overdensities in the early-universe, and then grow by merging with surrounding haloes. The baryonic component of galaxies grows both via mergers but also as gas is accreted from their surroundings into their haloes (e.g. Press & Schechter 1974; Binney 1977; White & Rees 1978; Fall & Efstathiou 1980; Mo et al. 1998; Bullock et al. 2001a; Cimatti et al. 2019 and references therein).

N-body cosmological simulations find that the density profiles of dark matter haloes of galaxies are reasonably well described (but see also Navarro et al. 2010)

[1] In astronomy, it is customary to use the generic term 'baryons' to refer to the matter made of both leptons and baryons. This is justified on the basis that the contribution from leptons to the mass budget of the universe is comparatively extremely small.

by the functional form (Navarro et al. 1997)

$$\rho_{\rm NFW}(r) = \frac{4\rho_{\rm s}}{(r/r_{\rm s})(1+r/r_{\rm s})^2} \ , \tag{1.1}$$

where r is the spherical radius, $r_{\rm s}$ a scale radius, and $\rho_{\rm s}$ the volume density at $r_{\rm s}$. NFW haloes are often also described in terms of their virial mass $M_{\rm h}$ and the so-called concentration parameter related to the innermost shape of the dark matter density profile, $c \equiv r_{\rm h}/r_{\rm s}$, with $r_{\rm h}$ the virial radius of the halo.

Cosmological N-body simulations report an anti-correlation between halo mass and concentration, as illustrated in Fig. 1.1 (e.g. Macciò et al. 2007; Dutton & Macciò 2014; Ludlow et al. 2014). While there is some scatter that depends on each specific halo merger history, on average low-mass galaxies have higher concentrations than high-mass galaxies. Observational work (see Sec. 1.2.3), however, suggests that the anti-correlation is not well recovered from the data under the assumption of NFW profiles (e.g. Katz et al. 2017; Li et al. 2020), perhaps due to the imprint of baryonic physics and the gravitational effects of the baryons on dark matter haloes (e.g. Blumenthal et al. 1986; Sellwood 2008; Duffy et al. 2010).

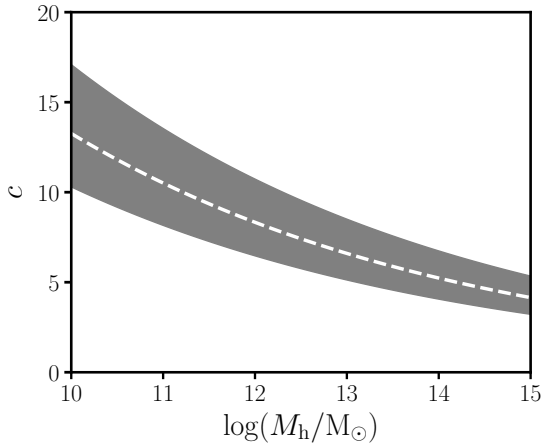

Figure 1.1: Relation between the virial mass of dark matter haloes and their concentration parameters. The white dashed line shows the relation from the N-body cosmological simulations of Dutton & Macciò (2014), and the grey band its 1σ scatter.

While observational determinations of the dark matter parameters of massive galaxies typically agree well with NFW haloes, discrepancies have been observed in the low-mass regime. A particularly persistent issue is the so-called 'cusp-core problem': NFW density profiles are cuspy while the density profiles of the dark matter haloes in some galaxies are cored (e.g. Binney & Evans 2001; McGaugh et al. 2001; de Blok et al. 2008; Read et al. 2017). In order to address this cusp-core tension and other problems (see Bullock & Boylan-Kolchin 2017 for a recent review), solutions invoking baryonic physics have been proposed (e.g. Navarro et al. 1996; Navarro & Steinmetz 2000; Binney et al. 2001). The leading idea is that episodic stellar feedback (but see also e.g. Nipoti & Binney 2015 for mechanisms that do not require feedback) produced by bursty star formation

histories can create cores in the dark matter distribution of galaxies (e.g. Read & Gilmore 2005; Pontzen & Governato 2012; Di Cintio et al. 2014). According to hydrodynamical simulations, this core creation would depend on the mass of the dark matter halo ($M_{\rm h}$) and of the stars (M_*): core creation would be inefficient for the lowest-mass systems – too heavily dark matter dominated to be affected by a weak stellar feedback–, and at relatively high masses – where the strong stellar potential overpowers outflows caused by feedback (e.g. Di Cintio et al. 2014; Lazar et al. 2020).

Following this logic, alternative profiles with cored distributions have been proposed, both within (e.g. Read et al. 2017; Lazar et al. 2020) and outside (e.g. Bullock & Boylan-Kolchin 2017; Tulin & Yu 2018; Ren et al. 2019) the CDM framework. The fact that the dark matter haloes of galaxies can be described by generic profiles arising from cosmological simulations can be very insightful. Not only we can study the properties of dark matter itself using N-body simulations, but with a careful comparison between observations and hydrodynamical simulations it is also possible to assess the impact of baryonic physics and processes such as stellar feedback at imprinting changes on the dark matter haloes (e.g. Navarro et al. 1996; Binney et al. 2001; Read & Gilmore 2005; Duffy et al. 2010; Brook et al. 2012b; Pontzen & Governato 2012; Di Cintio et al. 2014).

A crucial property of dark matter haloes is that they are not perfectly spherical. Because of this, they exert tidal forces into neighboring haloes, with the global effect of the acquisition of angular momentum. This gain of angular momentum is thought to occur mostly before virialisation, as detailed in the seminal papers by Peebles (1969), Doroshkevich (1970), and White (1984), which shaped what we call today the 'tidal torque theory'.

Because most of the angular momentum of the haloes ($J_{\rm h}$) is gained when the dark matter and the primordial gas are well mixed, it is expected that the baryons acquire the same tidal torques and thus roughly the same specific angular momentum (i.e. $j = J/M$), and thus $j_{\rm bar} \approx j_{\rm h}$. This, coupled with the fact that angular momentum is subject to conservation laws, largely dictates the size and dynamical state of primordial galaxies. As the baryonic component of galaxies shrink and collapse towards the centres of the dark matter haloes, their rotational support must increase (e.g. Binney 1977; White & Rees 1978; Fall & Efstathiou 1980; Blumenthal et al. 1984; Dalcanton et al. 1997; Mo et al. 1998). In general, angular momentum is one of the most prominent parameters regulating galaxy evolution, arguably at all cosmic times. As we discuss in Sec. 1.3.2, the link between angular momentum and galaxy properties is particularly evident in present-day galaxies.

The angular momentum content of dark matter haloes is usually characterised by the so-called spin parameter (Peebles 1971; Bullock et al. 2001b), defined as

$$\lambda \equiv \frac{J_{\rm h}|E_{\rm h}|^{1/2}}{G\ M_{\rm h}^{5/2}}\ , \tag{1.2}$$

with G the gravitational constant, and $E_{\rm h}$ and $M_{\rm h}$ the energy and mass of

the dark matter haloes. The spin parameter measures the degree of rotational support in a system. For instance, a non-rotating spheroid has $\lambda = 0$, and a rotation-supported self-gravitating disc $\lambda \approx 0.4$ (Cimatti et al. 2019). According to N-body cosmological simulations simulations, dark matter haloes follow a nearly log-normal distribution with a peak at $\lambda \approx 0.035$, regardless of the assumed cosmology, halo mass, redshift or environment (e.g. Bullock et al. 2001a; Macciò et al. 2007). It can be shown that a prediction from the tidal torque theory for the specific angular momentum of the dark matter halo is $j_{\rm h} \propto \lambda M_{\rm h}^{2/3}$ (see Fall 1983; Shaya & Tully 1984; Heavens & Peacock 1988).

While deriving general properties of dark matter haloes can be done analytically and with N-body cosmological simulations, considering the baryonic content of galaxies changes the picture, as baryons are subject to complex physics that directly affects their properties and the overall dynamical structure. In order to understand such processes observational constraints are needed. In the next sections we delve into the stellar and gas content of disc galaxies, discussing how can we use them to measure their angular momentum and infer the properties of their host dark matter haloes.

1.2 Star-forming galaxies

The rich variety of the morphology and structure of galaxies makes it imperative to try to classify them according to some common features. Different ways to classify galaxies have been proposed, most of them according to observed features at optical wavelengths, inspired by the early work of Hubble (1926). Broadly speaking, galaxies can be divided into two main groups, as often depicted in the Hubble classification diagram. The first group are the so-called early-type galaxies, which have elliptical morphology, are dynamically supported by random motions, have small gas reservoirs, and show very low star formation activity, with most of their stars being old. The second group, called late-type galaxies, have discy morphology, are supported by rotation, have significant gas fractions, relatively young stellar populations, and show active star formation[2] (see e.g. Cimatti et al. 2019 and references therein).

Both early-and late-type galaxies show a wide span in mass, including dwarf ($M_* \lesssim 10^9$ M$_\odot$) and more massive systems. In the case of early-types, the range appears to go from ultra-faint dwarfs with $M_* \sim 10^{2-5}$ M$_\odot$ to bright cluster galaxies with M_* values of a few times 10^{12} M$_\odot$ (e.g. Tolstoy et al. 2009; Bellstedt et al. 2016; Bullock & Boylan-Kolchin 2017). In late-types, the detected population extends from dwarf irregular galaxies with stellar and gas masses of $\sim 10^{5-6}$ M$_\odot$ (e.g. Bernstein-Cooper et al. 2014; Adams & Oosterloo 2018) to massive spirals with $M_* \approx 10^{12}$ M$_\odot$ (e.g. Ogle et al. 2019a; Di Teodoro et al. 2021).

[2] Across this thesis, we will consider as synonyms the terms disc galaxies, late-type galaxies, and star-forming galaxies, unless specified.

Late- and early-type galaxies tend to reside in different environments, with a well-established morphology-density relation (e.g. Dressler 1980; Thomas et al. 2010; van der Wel et al. 2010): star-forming galaxies, on average, reside within environments with lower galaxy densities than early-types. In addition to this, at fixed M_*, the gas content of galaxies in high-density environments tends to be lower with respect to their more isolated counterparts (e.g. Dressler 1986; Solanes et al. 2001; Cortese et al. 2011; Calvi et al. 2012; Serra et al. 2012). These trends are particularly relevant when studying galaxies in massive groups or clusters, as they are thought to be a consequence of processes such as tidal stripping, harassment, ram pressure striping, and dynamical friction (e.g. Moore et al. 1998; Abadi et al. 1999; van den Bosch et al. 1999; Mo et al. 2010).

1.2.1 Stellar content

The stellar body of star-forming galaxies consist of a relatively thin (e.g. Bershady et al. 2010) stellar disc and often, especially for galaxies with $M_* \gtrsim 10^{10}$ $M_\odot$, of a bulge component, more centrally concentrated and of spheroidal shape. About 60% percent of disc galaxies also show prolate bar-like structures (Cimatti et al. 2019). Stellar discs are supported by rotation, and have light profile is typically well described by a Sérsic law (Sersic 1968) with index $n = 1$, i.e. an exponential profile. Bulges can be broadly classified into 'classical' and 'pseudobulges'. The kinematics of the former are distinguished by random motions, and their light profiles usually has $n \gtrsim 2$ (e.g. Cappellari et al. 2013b; Krajnović et al. 2013). The latter, instead, show a larger amount of rotation and $n \lesssim 2$. Bars have complex kinematics with strong non-circular motions and Sérsic index $n \lesssim 1$ (e.g. Kormendy & Kennicutt 2004).

Disc galaxies are often characterised by their stellar mass and their size. While the size of a galaxy is somewhat ambiguous (e.g. Trujillo et al. 2020), a commonly-used metric is the effective radius R_e enclosing 50% of their flux in a given wavelength band. Fig. 1.2 shows the $M_* - R_e$ plane for a set of nearby galaxies, including samples of late- and early-type massive and dwarf galaxies. The general trend of this mass-size relation is such that massive galaxies have more extended light distributions than low-mass galaxies, although there is a large scatter (see also e.g. Tolstoy et al. 2009; Cebrián & Trujillo 2014). At fixed M_*, late-type systems have larger R_e than their early-type counterparts, which is not surprising as their light distributions are less concentrated.

Ultra-diffuse galaxies

Among all the galaxies shown in Fig. 1.2, a subset that stands out and has recently attracted significant attention in the literature is that of ultra-diffuse galaxies (UDGs, van Dokkum et al. 2015). UDGs are defined as galaxies with an effective radius larger than 1.5 kpc and surface brightness[3] (usually in the

[3]Different works use different types of surface brightness measures, but the most common ones are the central value or the average within R_e.

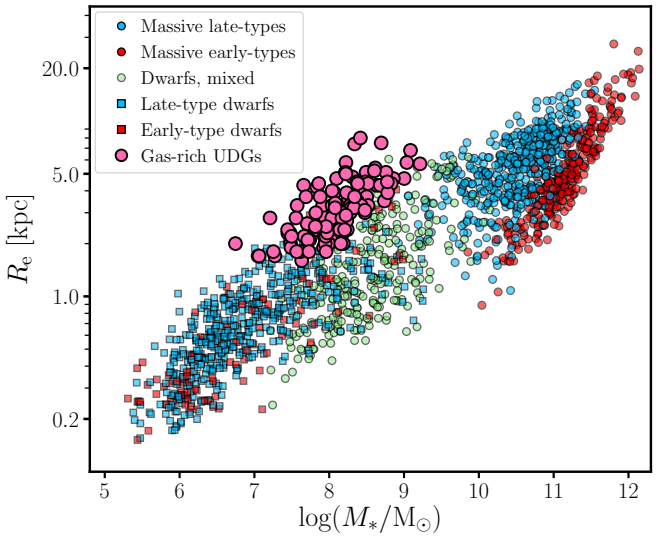

Figure 1.2: Different galaxy populations distributed in the stellar mass-size ($M_* - R_e$) plane. More massive galaxies tend to have more extended light distributions, although the scatter is large at any M_*. At fixed mass, late-type systems have typically larger R_e than early-types. Ultra-diffuse galaxies (UDGs) are an extreme subset of dwarfs with R_e as extended as for galaxies $\sim 2-3$ orders of magnitude more massive. The data for the late- and early-type massive galaxies comes from Trujillo et al. (2020). The green points showing dwarf galaxies are also from Trujillo et al. (2020), but have no morphological classification. The late- and early-type dwarfs come from Venhola et al. (2018) and correspond to objects in the Fornax cluster. Finally, the sample of gas-rich UDGs is from Leisman et al. (2017); gas-poor UDGs found in galaxy clusters (not shown) follow a similar distribution in the $M_* - R_e$ plane (e.g. van Dokkum et al. 2015; Mancera Piña et al. 2019a).

$r-$ or $g-$band) fainter than about 24 mag arcsec^{-2}, which typically means $M_* \lesssim 10^9$ M$_\odot$.

Given this definition, which is rather naming a parameter space than a distinct galaxy population, UDGs are peculiar as they have surface brightnesses, and stellar masses of dwarf galaxies (see also Sandage & Binggeli 1984; Impey et al. 1988; Conselice 2018), but effective radii as large as massive galaxies like the Milky Way. The light distribution of UDGs is typically exponential, but in general they have Sérsic indices $0.5 \lesssim n \lesssim 1$. UDGs have been found mostly in galaxy clusters, where they show mostly red colours (e.g. van Dokkum et al. 2015; van der Burg et al. 2016; Mancera Piña et al. 2018), but they have also been reported in low density environments, where they usually appear bluer (e.g. Román & Trujillo 2017b; Greco et al. 2018; Román et al. 2019; Barbosa et al. 2020). Moreover, some field UDGs host gas reservoirs (e.g. Leisman et al. 2017; Spekkens & Karunakaran 2018), which, as we discuss below, allow us to accurately trace their dynamical properties.

While widely investigated in the last few years, the formation mechanisms of UDGs are still unknown and debated to date, with different models and simulations proposed trying to explain such extended light distributions in faint low-mass galaxies (e.g. van Dokkum et al. 2015; Amorisco & Loeb 2016; Di Cintio et al. 2017; Rong et al. 2017; Chan et al. 2018; Tremmel et al. 2020; Wright et al. 2021; Liao et al. 2019). Most of these models and simulations can be divided into two broad groups. The first idea suggests that the extended R_e are due to episodic stellar feedback processes that create dark matter cores, weakening the potential well and allowing stars to move to more external orbits. Instead, the second idea proposes that UDGs inhabit dark matter haloes with higher-than-average angular momentum, which then translates into larger sizes for the stellar component. UDGs are therefore a promising galaxy population to test our theories of galaxy formation at extreme scales, and it is important to add observational constraints on their fundamental properties.

1.2.2 Interstellar medium

Together with the stars, atomic and molecular gas dominate the baryonic mass budget of nearby disc galaxies. The two gas phases, in addition to the dust, are usually referred to as the interstellar medium (ISM)[4]. The ISM encodes treasured information about galaxy evolution and the baryon cycle. It is directly linked to gas accretion from the circumgalactic medium (in turn coming from the intergalactic medium), star formation, outflows, and stellar and AGN feedback activity (cf. Lilly et al. 2013; Cimatti et al. 2019; Saintonge & Catinella 2022).

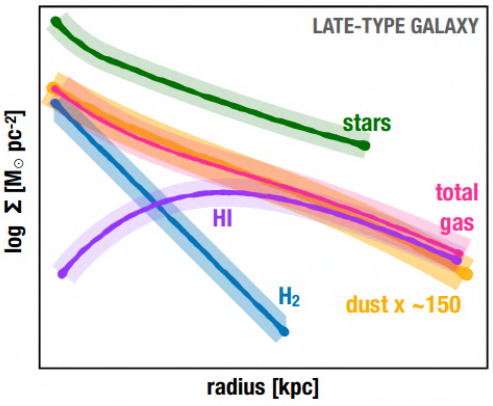

Figure 1.3: Sketch of the typical stellar and cold ISM distribution in nearby massive late-type galaxies. Note that 'total gas' here refers only to H I and H_2, neglecting the presence of ionised gas. Taken from Saintonge & Catinella (2022).

The atomic gas (H I, observed with the 21-cm emission line) can be divided into the warm (WNM, $T \sim 6000 - 8000$ K) and cold neutral medium (CNM, $T \sim 50 - 100$ K), in pressure equilibrium with each other (Field 1965; Heiles & Troland 2003; Wolfire et al. 2003). In the Milky Way, both media contribute

[4]Galaxies are also surrounded by the so-called circumgalactic medium (CGM), with a similar extension as the dark matter haloes. The CGM is also multi-phase, with a hot ($T \sim 10^{6-7}$ K) corona and cool/warm ($T \sim 10^{4-5}$ K) gas (see e.g. Tumlinson et al. 2017).

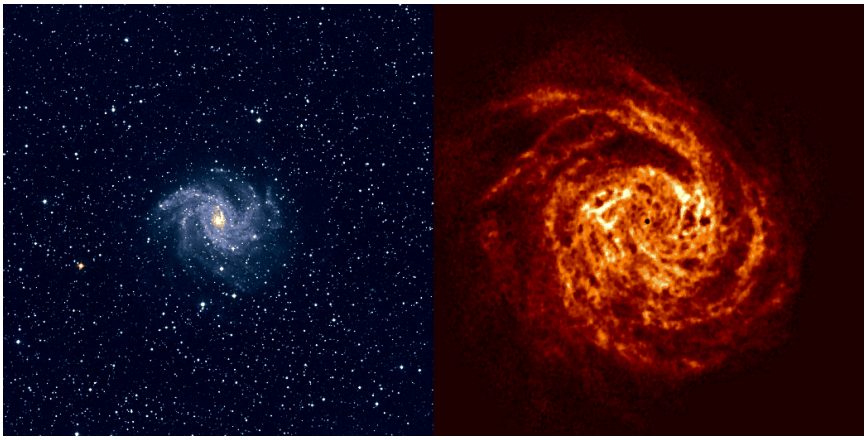

Figure 1.4: *Left:* Optical image of the stellar disc of the galaxy NGC 6946. *Right:* H I disc of NGC 6946. Both panels are at the same scale. Taken from Boomsma (2007).

nearly equally to the atomic mass budget. Molecular gas (H_2, often studied through CO emission lines), the coldest gas-phase, has a temperature of about 10 K and densities that can be larger than 100 cm^{-3}. Molecular gas is considered the main fuel for star formation (see Kennicutt 1989; Bacchini et al. 2019a, and references therein). Ionised gas (either photo- or collisionally-ionised) at higher temperatures ($T \sim 10^{4-5}$ K) also exists. Its total within galaxy discs is considered typically negligible compared to the stars and colder gas phases (Tielens 2005), although the mass budget of this warm phase is extremely difficult to measure accurately, in larger part because of the highly unconstrained electron densities (e.g. Osterbrock 1989; Sanders et al. 2016).

A sketch of the typical spatial distribution of the stars and ISM in a nearby, massive star-forming galaxy can be seen in Fig. 1.3. H_2 surface densities in galaxy centres can be high (e.g. Leroy et al. 2008), although H_2 discs are often less extended than the stellar distribution. On the other hand, H I is often suppressed in the centre but it is significantly more extended than the stellar disc (e.g. Begeman 1987; van der Hulst et al. 1993; Broeils & Rhee 1997; Verheijen 1997; Swaters 1999); the depression in the H I profiles usually overlaps with the peak of the CO emission, although this is not a hard and fast rule (Bigiel & Blitz 2012). Fig. 1.4 shows the comparison between the stellar and H I discs in a nearly face-on galaxy. In nearby galaxies, the typical ratio between the H I radius (defined as the radius at which the H I surface density reaches a value of 1 $M_\odot/pc^2$) and the optical radius (defined as the 25^{th} mag $arcsec^2$ isophotal level) is about 2 (Broeils & Rhee 1997). As discussed in Sec. 1.2.3 and Sec. 1.2.4, the large extent of H I discs is key to study the dynamics of late-type galaxies. Moreover, their low outer column densities are also a great tool to trace interactions between galaxies that would otherwise remain hidden (e.g. van der Hulst 1979; Yun et al. 1994; Sancisi et al. 2008).

While Fig. 1.3 provides a representative picture of the cold ISM distribution in nearby, massive star-forming galaxies, the relative amount of the gas phases varies significantly from galaxy to galaxy. Quantifying the mass budget of stars, H I, and H_2 is very important, as their relative fractions encode information about the efficiency of star formation and the consumption time scales of molecular gas to form stars and of the atomic gas to condensate and form molecular gas (e.g. Leroy et al. 2008; Bigiel et al. 2010; Catinella et al. 2018; Saintonge & Catinella 2022).

Large surveys measuring the stellar, atomic, and molecular gas content of galaxies show that there are correlations between different mass components. Fig. 1.5 shows the average trends (and standard deviation) of the H I- and H_2-to-M_* ratios as a function of M_* for a large sample of about 2000 nearby late-type galaxies compiled by Calette et al. (2018). In general, galaxies with larger M_* have lower $M_{\rm HI}/M_*$ and $M_{\rm H_2}/M_*$ ratios, albeit the scatter is large and there are also trends (not shown in Fig. 1.5) with the star formation rate (Saintonge et al. 2017; Calette et al. 2018). The H I reservoir of nearby star-forming galaxies is on average larger than that of H_2. In addition to this, while low-mass galaxies have nearly monotonically increasing H I fractions with decreasing M_*, the $M_{\rm H_2}/M_*$ ratios seems to reach a plateau. Note that despite the figure showing the standard deviation of the sample at fixed M_*, individual H_2 masses are fairly uncertain given the difficulty of estimating accurately the CO-to-H_2 conversion factor (Bolatto et al. 2013; Sandstrom et al. 2013). In addition to this, CO measurements often yield non-detections for dwarf galaxies (e.g. Leroy et al. 2008; Hunter et al. 2012, 2021). In general, stars are the main baryonic component of star-forming galaxies at $M_* \gtrsim 5 \times 10^8$ $M_\odot$, while the gas fractions become progressively more important at lower M_*, and for many dwarf galaxies gas (H I to be specific) dominates the baryonic mass budget (see also e.g. Geha et al. 2006; Papastergis et al. 2016).

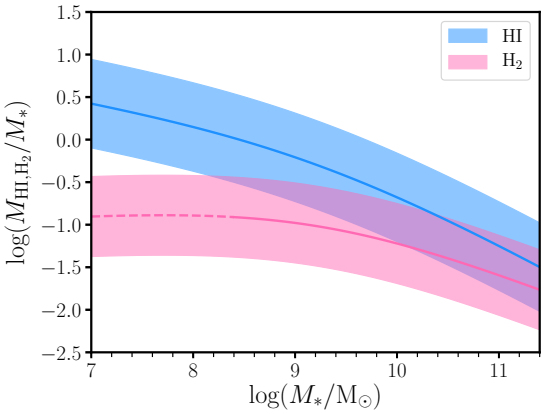

Figure 1.5: Average trends of the $M_{\rm HI}/M_*$ and $M_{\rm H_2}/M_*$ ratios as a function of M_* for about 2000 nearby star-forming galaxies. The original data comes from Calette et al. (2018). The dashed segment in the relation for H_2 corresponds to masses where the relations have been extrapolated.

Finally, a note on the vertical structure of the gas discs. For simplicity, H I and H_2 discs are often assumed to be razor-thin. While this assumption is justified given the much larger radial than vertical extent, observation and

theoretical arguments indicate that gas discs are flared, with a scale heights increasing as a function of radius and reaching kpc scales (e.g. Olling 1995; Sicking 1997; Bacchini et al. 2019b; Patra 2020b). The flaring is a consequence of the interplay between the gravitational pull near the midplane and the gas pressure, and it has important repercussions for star formation laws and our interpretation of gas turbulence (Bacchini et al. 2019a, 2020a). Regardless, the flaring has not been taken into account when deriving dynamical properties of nearby galaxies in a systematic way, and its effects are yet to be quantified.

1.2.3 ISM kinematics

The Doppler effect on absorption and emission lines has been used for more than 100 years (e.g. Slipher 1914) to study the kinematics of galaxy discs. As galaxies are observed to move at a systemic velocity $V_{\rm sys}$ with respect to us, their approaching (receding) side will be shifted towards lower (higher) velocities than $V_{\rm sys}$. As discussed in the previous section, gas discs typically enable the possibility to study the rotation of galaxies at larger radii than the stars, and we will now focus on the gas kinematics of nearby systems.

The first kinematic measurements of the gas discs were obtained using single-dish observations of the H I (van de Hulst et al. 1954, 1957) and CO lines (Rickard et al. 1975). Even though single-dish imaging results in unresolved measurements for any but the nearest galaxies, it is still possible to use them to study global kinematic properties (e.g. Dickey & Kazes 1992; Giovanelli et al. 2005). However, the interpretation of unresolved kinematics can be complex, and resolved H I and CO observations are essential to understand and characterise the ISM kinematics (e.g. Broeils 1992; Verheijen 1997).

Resolved observations of the cold ISM can be obtained with radio interferometers, which allow us to trace the total intensity and line-of-sight velocities of gas in galaxies at a high spatial resolution. From radio interferometric observations one can obtain a collection of spectral slices showing the resolved spatial distribution of the gas at different frequencies or line-of-sight velocities. From these data cubes, it is possible to extract a total intensity map of the gas in the galaxy, as well as kinematic maps showing the line-of-sight gas rotation velocity and velocity dispersion, which is tightly linked to the ISM turbulence (e.g. Tamburro et al. 2009; Bacchini et al. 2020a). As an example, the top row of Fig. 1.6 shows the total H I intensity map, velocity field, and velocity dispersion field of the nearby star-forming galaxy NGC 6503. From the kinematic maps one can then extract the rotation velocity ($V_{\rm rot}$) and velocity dispersion of the gas ($\sigma_{\rm gas}$) as a function of the galactocentric radius. The resulting rotation curves have different shapes depending on galaxy properties, in particular their stellar or total mass (e.g. Verheijen 1997; Swaters 1999). Broadly speaking, massive galaxies have rapidly rising rotation curves in the inner regions, while in dwarf galaxies the increase is slower, resembling more a solid-body. Provided that the rotation curves are traced far enough, they become flat (e.g. Bosma 1978; Begeman 1987; Spekkens & Giovanelli 2006; de Blok et al. 2008; Kuzio de

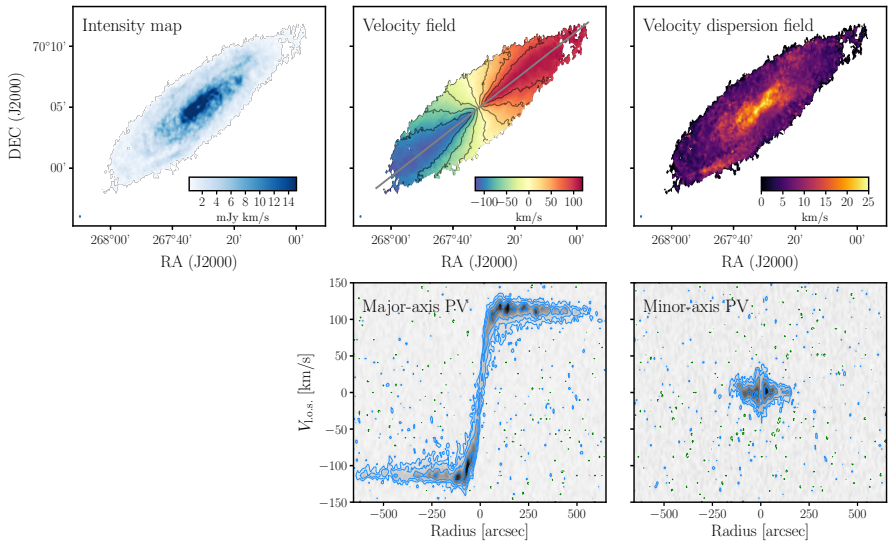

Figure 1.6: H I interferometric data for the galaxy NGC 6503. *Top left:* Total intensity map. *Top middle:* Line-of-sight velocity field. *Top right:* Velocity dispersion map. The small blue ellipse near the bottom left corner of all the top panels shows the beam of the observations. The grey line in the velocity field shows the kinematic major axis of the galaxy. *Bottom:* Major- and minor-axis PV diagrams. The emission is show in gray levels and blue contours (green for negative values). The contours are at $-2, 2, 4, 8, 16$ times the r.m.s. noise of the PV diagrams. The original data cube comes from Walter et al. (2008).

Naray et al. 2008).

The traditional method to obtain the rotation curves of late-type galaxies is by using the so-called tilted-ring model (e.g. Rogstad et al. 1974; Begeman 1987; Swaters 1999; Fraternali et al. 2002). The basic idea is that galaxy discs are treated as axisymmetric systems than can be described as a set of razor-thin concentric rings defined by a number of geometric and kinematic parameters. In this type of model, the line-of-sight velocity ($V_{\rm los}$) at a (x, y) location on the sky is given by (e.g. Begeman 1987)

$$V_{\rm los}(x, y) = V_{\rm sys} + [V_{\rm rot}(R)\cos\theta + V_{\rm rad}(R)\sin\theta]\sin i \ , \tag{1.3}$$

with $V_{\rm rad}$ the radial velocity, i the inclination angle between the plane of the disc and the line-of-sight, and θ the kinematic position angle, measured in the plane of the galaxy between its receding side and the North axis, in the North-East direction.

While galaxies may have some non-zero $V_{\rm rad}$ component, most of the time this term is neglected in Eq. 1.3 as it is usually very small compared to $V_{\rm rot}$ (Di Teodoro & Peek 2021). Still, signs of radial motions can be seen as systematic positive and negative residuals on each side of the velocity field when compared

to a model in pure rotation, or as distortions in position-velocity slices along the minor axes of galaxies (e.g. Fraternali et al. 2002; Spekkens & Sellwood 2007). In general, position-velocity (PV) diagrams along the major and minor axes showing the line-of-sight velocity as a function of radius (see bottom row in Fig. 1.6) are extremely useful to investigate the kinematics of the ISM, as the presence of non-circular motions caused by bars, inflow and outflow motions, and extraplanar gas can be observed directly (e.g. Oosterloo et al. 2007; Spekkens & Sellwood 2007; Sancisi et al. 2008; Gallimore et al. 2016; Iorio et al. 2017).

Gas kinematics in 3D

The approach of fitting Eq. 1.3 to the velocity fields works well for galaxies that can be observed at high spatial resolution (with $\sim 5-10$ resolution elements). However, the approach becomes unreliable for observations at low spatial resolution when the resolution element (called 'beam' in radio astronomy and analogous to the point spread function in optical astronomy) is of comparable size to the angular extent of the galaxies. This is because low-resolution data suffer from the so-called beam smearing effect (see Bosma 1978; Swaters 1999; Di Teodoro & Fraternali 2015). In practice, what happens is that the line profile of any pixel receives flux from different regions with different kinematics. As a consequence, the line profiles become skewed towards regions with high fluxes, and any velocity gradient is smoothed. At the same time, the profiles become artificially broader, which could be misinterpreted as intrinsic gas velocity dispersion. Because of this, fitting beam-smeared velocity and velocity dispersion fields typically results in the underestimation of $V_{\rm rot}$ and overestimation of $\sigma_{\rm gas}$.

Fig. 1.7 shows a specific example of how beam smearing can lead to a wrong interpretation of gas kinematics in the nearby galaxy NGC 2403. Tilted-ring fits to the high-resolution (beam of 15 arcsec) velocity maps obtained from the Very Large Array (VLA) lead to the 'true' gas rotation velocity and velocity dispersion profiles. Instead, using the low-resolution (beam of 525 arcsec) velocity fields from the single-dish Green Bank Telescope (GBT) results in a severe misinterpretation of the kinematics.

Fortunately, meaningful kinematic parameters can still be recovered from low-resolution observations. To do so, in this thesis we use the software ^{3D}Barolo (Di Teodoro & Fraternali 2015)[5]. Instead of fitting the beam-smeared velocity fields, ^{3D}Barolo creates mock emission-line data cubes out of tilted-ring models and fits them to the whole observed data cube minimising the residuals channel by channel (and thus using more information than the collapsed 2D maps). Crucially, before the comparison between model and data is performed, ^{3D}Barolo takes into account the spatial resolution by convolving the models with the same beam as the observations (rightmost panels in Fig. 1.7). At high resolution, ^{3D}Barolo yields the same results as traditional 2D methods, but for low-resolution data it largely overcomes the effects of beam smearing, as shown by the red points in Fig. 1.7. In addition to this, ^{3D}Barolo has the advantage of fitting

[5]See also e.g. Bouché et al. 2015; Józsa et al. 2007 for alternative codes.

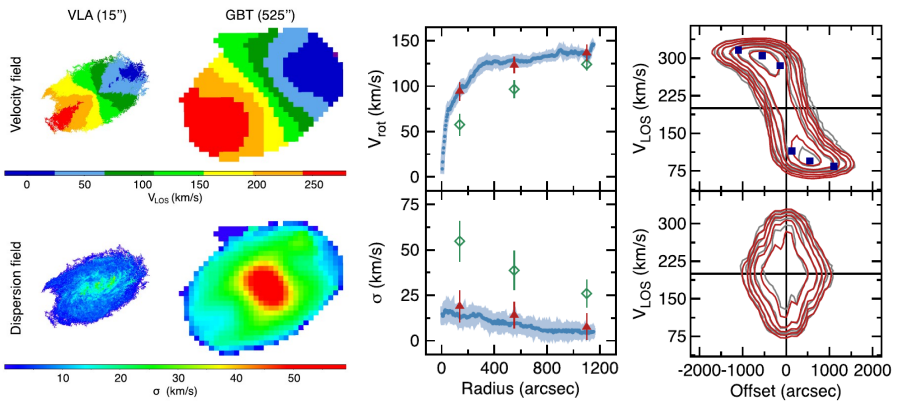

Figure 1.7: Example of how beam smearing affects the galaxy NGC 2403. The *leftmost* columns show the line-of-sight velocity (*top*) and velocity dispersion (*bottom*) maps of the galaxy obtained from high- (VLA) and low-resolution (GBT) H I observations. Next to the maps, the rotation curve and velocity dispersion profile recovered using the high- (low-) resolution velocity fields fitting Eq. 1.3 are shown in blue (green). Shown in red are the parameters recovered by ^{3D}Barolo using a 3D kinematic modelling fitting technique on the low-resolution GBT data cube. Finally, the *rightmost* panels show the major (*top*) and minor (*bottom*) position-velocity slices for the low-resolution data (grey contours) and the best-fitting ^{3D}Barolo model (red contours), including the obtained line-of-sight rotation velocities (blue squares). The 3D approach of ^{3D}Barolo largely mitigates the effects of beam smearing, allowing for a robust recovery of the gas kinematics also in low-resolution data. Adapted from Di Teodoro & Fraternali (2015).

simultaneously $V_{\rm rot}$ and $\sigma_{\rm gas}$, rather than treating them independently as in 2D methods.

1.2.4 Dark matter from dynamical measurements

The rotation of galaxy discs reflects the underlying gravitational potential, enabling us to accurately trace the dark matter distribution within late-type galaxies. Extended H I rotation curves have played a major role when studying galaxy dynamics and dark matter, historically providing some of the strongest observational evidence for the existence of dark matter (e.g. Bosma 1978; van Albada & Sancisi 1986; Begeman 1987; Verheijen 1997; Swaters 1999).

For a given galaxy considered axisymmetric, the total gravitational potential $\Phi(r, z)$ is directly related to the observed rotation velocity $V_{\rm rot}$ as (e.g. Binney & Tremaine 2008; Cimatti et al. 2019)

$$V_{\rm rot}^2 = V_{\rm c}^2 - \frac{R}{\rho}\,\frac{\partial(\rho\sigma_{\rm gas}^2)}{\partial R}\ , \tag{1.4}$$

where ρ is the density of the gas, $\sigma_{\rm gas}$ the gas velocity dispersion (expected to

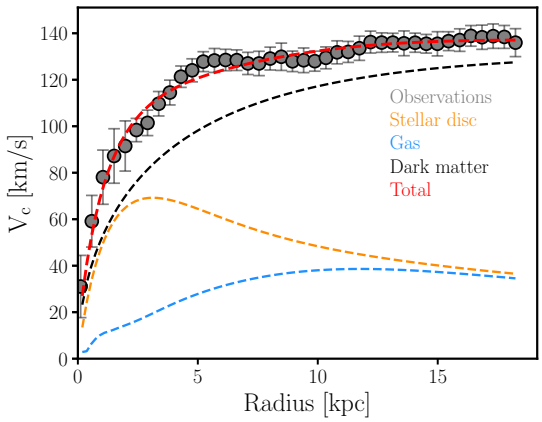

Figure 1.8: Mass model of the galaxy NGC 2403 from its rotation curve decomposition. The observed circular speed profile (taken from Di Teodoro & Peek 2021 and Chapter 6) of the galaxy is shown with grey circles. The circular speeds of the stellar and gas discs, as inferred from their mass surface densities, are shown in orange and blue, respectively. A best-fitting NFW halo is shown in black, while the red line indicates the total mass model after taking into account all the individual components.

be isotropic), and $V_c \equiv \sqrt{R \left.\frac{\partial \Phi}{\partial R}\right|_{z=0}}$ the circular speed.

As seen from Eq. 1.4, the circular speed of a disc galaxy is obtained by measuring the rotation velocity and correcting it for pressure-supported motions (second term on the right hand side). Pressure-supported motions are negligible (and thus $V_c \approx V_{rot}$) when V_{rot}/σ_{gas} is high as in massive galaxies, but become relevant for dwarf galaxies with low V_{rot}/σ_{gas}. In those cases we can have $V_c > V_{rot}$ (e.g. Iorio et al. 2017). Given its definition, V_c encodes information about the total gravitational potential, and thus about both the baryonic and dark matter distribution. For instance, for a system consisting of a stellar disc, a gas disc, and a dark matter halo, $V_c^2 = V_*^2 + V_{gas}^2 + V_{DM}^2$, with V_*, V_{gas}, and V_{DM} the individual contributions to the circular speed from the stellar disc, gas disc, and dark halo, respectively. These individual circular speeds depend only on their respective mass distributions and geometry, and therefore V_* and V_{gas} can be, in principle, constrained from observations of their mass surface density profiles (e.g. Casertano 1983; Cuddeford 1993; Binney & Tremaine 2008). From this, one can fit the observed circular speed profile to infer the dark matter mass distribution. This technique, exemplified in Fig. 1.8 and called mass modelling from rotation curve decomposition, is a powerful took to study the underlying dark matter density profile in disc galaxies. In Sec. 1.3.3, we delve into the dark matter content of late-type galaxies.

Despite being a tool used for longer than 40 years, mass models from rotation curve decomposition are still useful and widely exploited nowadays, especially with the advent of relatively large samples with high-quality H I data and the more common use of robust statistical fitting techniques. Using these new developments, obtaining and modelling the rotation curve of dwarf and massive galaxies is essential to test our cosmological and feedback models.

Dynamics of UDGs

In Sec. 1.2.1 we discussed the puzzling nature of UDGs, having modest stellar masses ($M_* \lesssim 10^9$ $M_\odot$) but large effective radii ($R_e \gtrsim 1.5$ kpc). Recent observations suggest that they may also have unexpected dynamical properties judging from different kinematic measurements.

First, two gas-poor UDGs near (at least in projection) the massive early-type galaxy NGC 1052 have been reported to have very low dark matter content based on their stellar and globular cluster kinematics (e.g. van Dokkum et al. 2018, 2019; Danieli et al. 2019). Second, the general population of isolated, gas-rich UDGs has been found to have rotation velocities lower than expected for their baryonic mass (Leisman et al. 2017; Janowiecki et al. 2019), which could be due to a lower-than-average dark matter content, although the results are somewhat uncertain as they rely on unresolved kinematics. While the interpretation of the data of these faint systems is challenging, different observations from two different classes of UDGs point to the possibility of them having unusual dynamical properties. It is therefore desirable to obtain more robust kinematic measurements not only to investigate the origin of UDGs, but also to test dark matter theories using the type of tools and analyses described in this section.

1.3 Scaling relations

Understanding the relation between the expected and observed properties of galaxies and their host dark matter haloes is one of the most ambitious, challenging, and important goals in modern-day astrophysics. We know that this connection is rather complex given all the processes involved and the apparent stochasticity of some of them. And yet, there should be a high degree of universality and regularity during galaxy evolution, as we are witnessing strong self-similarity among present-day galaxies imprinted in the existence of tight scaling relations between their fundamental parameters.

Observationally, a number of scaling relations have been inferred in the last decades (e.g. Faber & Jackson 1976; Tully & Fisher 1977; Larson 1981; Fall 1983; Burstein et al. 1997; Marconi & Hunt 2003; Courteau et al. 2007; Cappellari et al. 2013a; Lelli et al. 2014b; Catinella et al. 2018; Stone et al. 2021), and are used on a daily basis to test (and sometimes calibrate) the outcome of hydrodynamical simulations and (semi)analytical models (e.g. Wang et al. 2015; Schaye et al. 2015; Sawala et al. 2015; Tremmel et al. 2017; Hopkins et al. 2018). These scaling relations include dependencies between kinematic parameters (e.g. rotation velocity, velocity dispersion), but also dynamical (e.g. mass, angular momentum), structural (e.g. size, compactness) or more specific (e.g. star formation rate, metallicity) properties. The visible features in scaling laws are footprints of the physical processes shaping galaxies, and therefore it is of top priority to obtain observational constraints on them. For disc galaxies (although also relevant for early-type systems), three of the most fundamental scaling laws are those between baryonic mass and circular speed (the baryonic

Tully-Fisher relation), between stellar specific angular momentum and mass (the Fall relation), and between stellar mass and dark matter halo mass (the stellar-to-halo mass relation).

1.3.1 The Baryonic Tully-Fisher relation

The baryonic Tully-Fisher relation (BTFR, McGaugh et al. 2000) is a tight sequence followed by both late- and early-type galaxies in the baryonic mass–circular speed plane (e.g. den Heijer et al. 2015; Lelli et al. 2016b; Ponomareva et al. 2018). Its existence, while not fully understood, is of significant relevance as it connects the baryonic mass components of galaxies with their dark matter haloes, as the circular speed captures the contribution from dark matter to the total gravitational potential (Eq. 1.4).

As the name suggests, the BTFR is a modified version of the original Tully-Fisher relation (Tully & Fisher 1977, see also Rhee 1996 for a detailed study) between stellar masses and circular speeds (originally absolute magnitudes and the width of H I global profiles). As pointed out by McGaugh et al. (2000), the Tully-Fisher relation breaks at $M_* \lesssim 10^9$ $M_\odot$, with dwarf galaxies having larger velocities than expected from the extrapolation of the trend defined by massive spirals. The break disappears when using the baryonic mass $M_{\rm bar}$ instead of M_*, given that dwarf galaxies are H I dominated (cf. Fig. 1.5). The BTFR has been widely used to test galaxy evolution models, obtain distance estimations, and even to measure cosmological parameters (e.g. McGaugh 2005; Dutton 2012; McGaugh 2012; Oman et al. 2016; Papastergis et al. 2016; Sales et al. 2017; Schombert et al. 2020; Kourkchi et al. 2022).

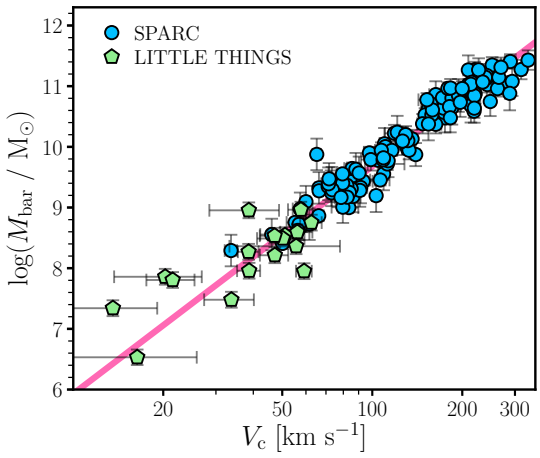

Figure 1.9: Baryonic Tully-Fisher relation for a sample of nearby massive (Lelli et al. 2016b) and dwarf late-type galaxies (Iorio et al. 2017). The pink line shows the best-fit linear relation of Lelli et al. (2016b) extrapolated towards lower velocities.

Fig. 1.9 shows the BTFR for a sample of local late-type galaxies based on their H I kinematics. At the high-velocity regime ($V_{\rm c} \gtrsim 70$ km s^{-1}), the relation is very tight. In fact, the observed scatter can be almost entirely explained by observational uncertainties, meaning that the relation has an extremely low

intrinsic scatter (Ponomareva et al. 2018; Lelli et al. 2019). The figure shows the best-fit relation for the massive galaxies of Lelli et al. (2016b), which has a dependency of the form $M \propto V^{\alpha}$, with $\alpha \approx 3.75$. In general, depending on the exact way in which $M_{\rm bar}$ and $V_{\rm c}$ are measured, α takes values around $3.5 - 4$ (Lelli et al. 2016b; Ponomareva et al. 2018; Lelli et al. 2019). It has also been suggested that the small residuals from the BTFR do not correlate with other galaxy properties like size, colour, morphology, or star formation (e.g. Lelli et al. 2016b; Ponomareva et al. 2018).

The behavior of the BTFR is less clear in the low-velocity regime given the low number statistics, which is also related to the difficulties in measuring robust kinematics for dwarfs. While the extrapolation from the high-mass BTFR seems to work well at intermediate velocities, the scatter in the data increases at circular speeds below ~ 40 km s^{-1}. Given that the BTFR encodes information on both dynamical and baryonic physics processes, it is important to improve its statistics in the dwarf regime. This would allow us to asses whether the intrinsic scatter of the BTFR is as low as at high masses, if there are outliers (and what would that mean) or if the relation bends downwards at $V_{\rm c} \lesssim 40$ km s^{-1}, as predicted by some simulations (e.g. Sales et al. 2017, see also Brook et al. 2016). Besides linking the baryons with the dark matter, the above information can also be used to constrain the efficiency of feedback and star formation at the lowest-mass regime (e.g. Geha et al. 2006; Sales et al. 2017).

1.3.2 The Fall relation

Another key scaling law is that between the stellar specific angular momentum ($j_* \equiv J_*/M_*$) and M_*. First studied by Fall (1983), the relation is now well constrained observationally across about four orders of magnitude in M_* and for galaxies of different morphological type (e.g. Fall & Romanowsky 2013; Romanowsky & Fall 2012; Cortese et al. 2016; Posti et al. 2018b; Rizzo et al. 2018).

Fig. 1.10 shows the $j_* - M_*$ relation (often also called the Fall relation) for a sample of galaxies spanning a wide range in their bulge-to-total stellar mass ratio (B/T). As noticed already by Fall (1983), for both early- and late-type galaxies the relation has a shape $j_* \propto M_*^{\alpha}$ with $\alpha \approx 0.6$, but the normalisations are rather different: at fixed M_* late-type galaxies have a higher j_*. Moreover, there is a systematic trend of galaxies with progressively lower B/T to shift towards higher j_* values. In general terms, $j_* \propto R_* V_{\rm rot}$, where R_* is some characteristic scale of the stellar distribution (e.g. Romanowsky & Fall 2012). The light distribution of disc galaxies is less concentrated than for ellipticals, and thus R_* is larger. In addition to this, stellar discs have a larger rotational support the bulges. These arguments explain qualitatively the relative location of late- and early-type galaxies in the Fall relation.

Interestingly, the mass dependency $j_* \propto M_*^{0.6}$ is very close to the scaling expected for the dark matter haloes $j_{\rm h} \propto M_{\rm h}^{2/3}$. As discussed in Sec. 1.1, baryons and dark matter are expected to acquire the same specific angular momentum

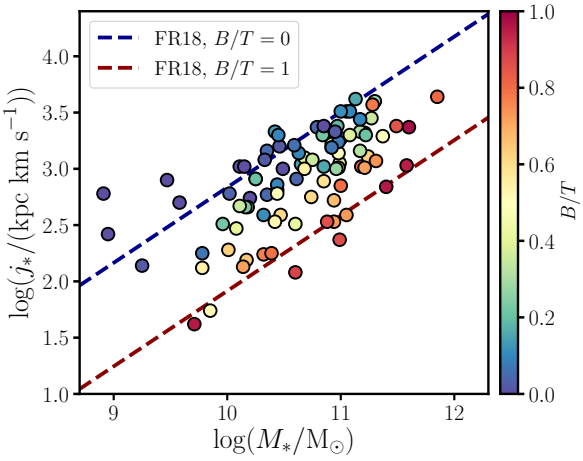

Figure 1.10: Fall ($j_* - M_*$) relation for a sample of nearby galaxies. The colours indicate B/T, the bulge-to-total stellar mass ratio. At fixed M_*, late-type galaxies have a higher j_* than early types. The dashed lines show the expected relations for pure discs ($B/T = 0$) and pure ellipticals ($B/T = 1$) from a semi-empirical parametrisation by Fall & Romanowsky (2018). Data from Fall & Romanowsky (2018).

and to roughly conserve it, and therefore one may argue that slopes close to each other are expected. However, through galaxy evolution there is a strong internal redistribution of angular momentum (e.g. Stevens et al. 2018; Cimatti et al. 2019; Sweet et al. 2020). Given this, the similar mass dependency of the stellar and dark matter $j - M$ relations is remarkable and not yet fully understood, considering as well that gas accretion, selective star formation, feedback, mergers, and dynamical friction can all affect the angular momentum distribution within galaxies. Models and simulations often try to use the constraining power of the Fall relation on these different processes, highlighting the relevance of such scaling law (e.g. Dutton & van den Bosch 2012; Brook et al. 2012a; Lagos et al. 2017; Teklu et al. 2015; Posti et al. 2018a; Stevens et al. 2018; Zoldan et al. 2018).

A discrepancy found between observational work (e.g. Posti et al. 2018b) and some models and simulations (e.g. Obreja et al. 2016; Stevens et al. 2016) is that the former find the $j_* - M_*$ relation to be, empirically, an unbroken power law, while the latter report a break or flattening at low masses ($M_* \lesssim 10^9$ $\mathrm{M}_\odot$). As discussed by Posti et al. (2018b), this can be related to stellar feedback implementations in models and simulations being too efficient at redistributing angular momentum, and to the fraction of angular momentum in the stellar discs relative to the angular momentum in the haloes; increasing the statistics of the Fall relation at $M_* \lesssim 10^9$ $\mathrm{M}_\odot$ would provide stronger constraints on such processes than currently available.

Finally, it is relevant to highlight that a crucial step towards obtaining an integral view of angular momentum in galaxies is to extend the Fall relation to its gas ($j_{\mathrm{gas}} - M_{\mathrm{gas}}$) and baryonic ($j_{\mathrm{bar}} - M_{\mathrm{bar}}$) counterparts. One would expect the $j_{\mathrm{bar}} - M_{\mathrm{bar}}$ relation to provide the most relevant telltale clues since it incorporates the stellar and gas content of both gas- and stellar-dominated galaxies. This has started to be addressed in the literature (e.g. Obreschkow & Glazebrook 2014; Elson 2017; Kurapati et al. 2018, 2021), but analyses using

large and homogeneous samples are needed.

1.3.3 The stellar-to-halo mass relation

As the BTFR is an empirical relation relating the visible mass and dynamical properties of galaxies, the most direct link between visible and dark matter masses is given by the stellar-to-halo mass relation (SHMR). The left panel of Fig. 1.11 shows the SHMR for a sample of late- and early-type galaxies with accurate dynamical measurements of $M_{\rm h}$ based on H I rotation curves and globular cluster kinematics (Posti et al. 2019; Posti & Fall 2021). The general trend is that galaxies with high M_* reside in more massive dark matter haloes than those with low M_*. There is also a segregation between late- and early-types, with the latter having larger $M_{\rm h}$ values at fixed M_* (or lower M_* values at fixed $M_{\rm h}$). Detailed dynamical measurements of individual galaxies show that early-types follow better the global theoretical expectations based on number counts of galaxies and dark matter haloes (abundance matching, e.g. Moster et al. 2013; Wechsler & Tinker 2018), while late-type galaxies seem to show a monotonically increasing behavior (e.g. Posti et al. 2019; Posti & Fall 2021), although the scatter is large. This effect, also seen in some models and simulations (e.g. Rodríguez-Puebla et al. 2015 and references therein), may imply that galaxies of different morphologies followed significantly different evolutionary paths.

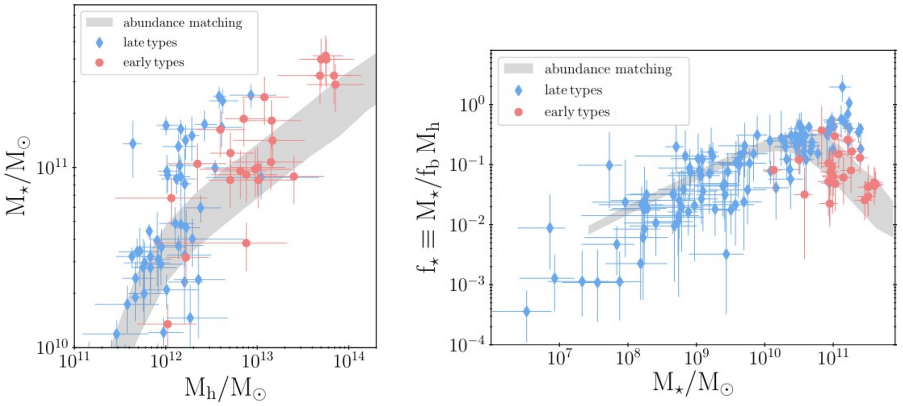

Figure 1.11: Stellar-to-halo mass (*left*) and stellar fraction-stellar mass (*right*) relations for a sample of late- (Posti et al. 2019) and early-type (Posti & Fall 2021) galaxies, compared to abundance matching predictions (Moster et al. 2013). Figure adapted from Posti & Fall (2021).

The SHMR is also connected with the quantity $M_*/M_{\rm h}$, often normalised to the average cosmological baryon fraction $f_{\rm bar,cosmic} = \Omega_{\rm bar}/\Omega_{\rm m} \approx 0.18$ (cf. Komatsu et al. 2011; Planck Collaboration et al. 2020). The ratio $f_* \equiv M_*/(M_{\rm h}\ f_{\rm bar,cosmic})$ is of high interest as it encloses information on how efficient are galaxies at converting their available baryons into stars; from this, f_* is

sometimes called stellar mass fraction or star formation efficiency. As shown in the right panel of Fig. 1.11, the emerging picture is that f_* for late-type galaxies increases monotonically with M_* and also deviates from abundance-matching expectations. The most massive late-type galaxies have values of f_* comparable to unity, implying they have converted nearly all of their available baryons into stars (Posti et al. 2019). Instead, early-type galaxies follow better the trend from abundance matching, having much lower f_* than late-types of similar M_*.

The above relations can also be explored using models and simulations to constrain the efficiency of galaxies at converting gas into stars. For instance, it has recently been shown that some of the most advanced cosmological hydrodynamical simulations produce disc galaxies which are too inefficient at converting their baryons into stars, and have thus a much lower f_* than observed, probably due to overly-efficient feedback mechanisms (Marasco et al. 2020). This exemplifies how relevant is to study and accurately constrain the SHMR and the $f_* - M_*$ relation from observations. It is also pertinent to look at correlations similar to those in Fig. 1.11 but after incorporating the cold gas content, which will dominate the baryonic mass budget for $M_* \lesssim 10^9$ $M_\odot$ and thus provide a more global picture of how galaxies use their cosmological baryons.

1.4 Open questions

As discussed in this introductory chapter, current theories of galaxy formation and evolution give a general understanding of the general processes governing the growth and rise of present-day late-type galaxies. Still, many questions remain unsolved. In this section, we summarise some of these main questions, in particular those that we try to address in this thesis.

- ⋆ **What can we learn about the BTFR at low circular speeds from UDGs?**
  The BTFR is one of the most fundamental scaling laws of galaxies. While its extremely low intrinsic scatter at high circular speeds is well established, the low-velocity regime is somewhat less explored, and it is not clear whether low-mass galaxies, and UDGs in particular, obey the relation as tightly as massive systems.

- ⋆ **What are the dark matter properties of UDGs?**
  A number of UDGs appear to have puzzling dynamical properties, likely related with atypical dark matter fractions compared to other dwarf galaxies. Reliable kinematic measurements can help at pinpointing the dark matter content of UDGs, and potentially to provide insights on the nature of dark matter.

- ⋆ **What is origin of UDGs?**
  UDGs have larger-than-expected effective radii given their stellar masses. Simulations and models suggest that this could be either a consequence of episodic feedback-driven outflows, or of a higher-than-average angular

momentum. Observational constraints do not manage to discriminate among these (or other) options yet. Characterising the kinematic properties of UDGs is a crucial piece of information needed to attempt to understand their formation mechanisms.

- ⋆ **What is the behavior of the stellar, gas, and baryonic specific angular momentum-mass relations?**
  Disc galaxies appear to follow an unbroken power law in the $(j_* - M_*)$ plane. However, it is not clear whether the relation breaks at dwarf galaxy scales, as suggested by some models and simulations. Moreover, the equivalent relations for the gas and baryonic content have not been explored homogeneously for large galaxy samples. Characterising the three $j - M$ laws down to dwarf galaxy scales would allow us to obtain a complete picture of the angular momentum content in disc galaxies and its relation with the angular momentum of the dark matter haloes.

- ⋆ **How important is the dynamical effect of the flaring of the gas discs for rotation curve decomposition?**
  The gaseous discs of star-forming galaxies show a strong flaring, which has significant impact in the context of star formation processes and turbulence. However, the dynamical effects of the flaring (e.g. in mass models from rotation curve decomposition) have not been quantified and it is not known if the flaring could bias the recovered dark matter halo parameters, especially for gas-rich galaxies. Characterising these dynamical effects is very relevant for the upcoming large H I surveys and the interpretation of mass models. By using detailed mass models it is also possible to explore important correlations such as the stellar-to-halo mass relation and the dark matter concentration-mass relations, and to investigate how do the recovered trends compare to the expectations of models and simulations.

1.5 This thesis

In this Ph.D. thesis, we aim to provide new insights into how the dark matter and angular momentum content of disc galaxies regulate their evolution. To do so, we exploit resolved cold gas kinematic measurements to address the questions highlighted in Sec. 1.4. The structure of the rest of this thesis is as follows.

After this introductory chapter, the next three chapters focus on the gas kinematics of ultra-diffuse galaxies. Specifically, in Chapter 2 we use low-resolution H I interferometric observations of six gas-rich ultra-diffuse galaxies. We discuss the position of our sample in the baryonic Tully-Fisher relation, and investigate their baryon-to-dynamical mass ratios. In Chapter 3, we provide a detail description of our kinematic models, present a qualitative scenario to explain the position of gas-rich ultra-diffuse galaxies in the baryonic Tully-Fisher relation, and contrast our results with some of the most discussed formation mechanisms of such galaxies proposed in the literature. In Chapter 4, we present high-resolution data for AGC 114905, the most extreme of our galaxies, which

allow us to derive a mass model from its rotation curve decomposition. Our mass models allow us to compare the inferred dark matter properties of the halo of AGC 114905 with the expectations of the cold dark matter model.

Chapters 5 and 6 focus on the accurate derivation and analysis of the stellar, gas, and baryonic specific angular momentum-mass relations, which we have built using a high-quality sample of about 160 galaxies. More specifically, in Chapter 5 we build our galaxy sample, measure the specific angular momenta, and estimate the fraction of the baryonic (stars plus gas) component relative to that of the halo. Then, in Chapter 6, we present the discovery of extremely tight scaling relations -among the tightest known in the literature- connecting the mass, specific angular momentum, and cold gas fraction of galaxies.

In Chapter 7 we present the first systematic study quantifying the effects of the flaring of the gas discs in the recovery of mass models from rotation curve decomposition. We present detailed mass models that self-consistently take into account the flaring of the discs when recovering the parameters of the best-fitting dark matter haloes. Our detailed mass models allow us to study the correlations between halo mass and concentration, stellar mass, and baryonic mass; this allow us to asses whether or not the data are in agreement with expectations from models and cosmological N-body simulations.

Finally, in Chapter 8 we summarise our main findings and we discuss future prospects following from this Ph.D. research. At the end of the thesis, a summary for a non-academic audience can be found in Dutch, English, and Spanish.

Chapter 2

Off the baryonic Tully-Fisher relation: a population of baryon-dominated ultra-diffuse galaxies

based on

– P. E. Mancera Piña, F. Fraternali, E. A. K. Adams et al. 2019 –

Published in The Astrophysical Journal Letters, ApJ, 883, L33

Abstract

We study the gas kinematics traced by the 21-cm emission of a sample of six H I–rich low surface brightness galaxies classified as ultra-diffuse galaxies (UDGs). Using the 3D kinematic modelling code ^{3D}Barolo we derive robust circular velocities, revealing a startling feature: H I–rich UDGs are clear outliers from the baryonic Tully-Fisher relation, with circular velocities much lower than galaxies with similar baryonic mass. Notably, the baryon fraction of our UDG sample is consistent with the cosmological value: these UDGs are compatible with having no 'missing baryons' within their virial radii. Moreover, the gravitational potential provided by the baryons is sufficient to account for the amplitude of the rotation curve out to the outermost measured point, contrary to other galaxies with similar circular velocities. We speculate that any formation scenario for these objects will require very inefficient feedback and a broad diversity in their inner dark matter content.

2.1 Introduction

The baryonic Tully-Fisher relation (BTFR; McGaugh et al. 2000; McGaugh 2005) is a tight sequence in the baryonic mass–circular velocity plane followed by galaxies of different types (e.g. den Heijer et al. 2015; Lelli et al. 2016b; Ponomareva et al. 2017). It has been of paramount importance and widely used for calibrating distances to extragalactic objects and to constrain, for example, semi-analytical and numerical models of galaxy formation and evolution (e.g. Governato et al. 2007; Dutton 2012; McGaugh 2012; Sales et al. 2017, and references therein).

Among the galaxies populating the BTFR, low surface brightness (LSB) galaxies are of particular interest, and have been used to investigate the mass distribution and stellar feedback processes at dwarf galaxy scales (e.g. Zwaan et al. 1995; de Blok 1997; Dalcanton et al. 1997; Di Cintio et al. 2019). Ultra-diffuse galaxies (UDGs; van Dokkum et al. 2015) are an especially notable subset of the LSB galaxy population due to their extremely low surface brightness values while having effective radii comparable to L* galaxies. While these galaxies have been known for decades (e.g. Sandage & Binggeli 1984; Impey et al. 1988), their recent detection in large numbers in different galaxy clusters, groups, and even in isolated environments (e.g. Román & Trujillo 2017b; Leisman et al. 2017; Mancera Piña et al. 2019a), has sparked a renewed interest in them.

Many UDGs in isolation are H I–rich, opening the possibility of investigating their gas kinematics. The most systematic study of H I in UDGs has been carried out by Leisman et al. (2017), who studied 115 sources[1] from the Arecibo Legacy Fast Arecibo L-band Feed Array (`ALFALFA`) catalogue (Giovanelli et al. 2005), as well as a small subsample of three sources with interferometric H I data, that meet the optical criteria of having $R_e \geq 1.5$ kpc and $\langle \mu(r, R_e) \rangle \geq 24$ mag arcsec^{-2}, according to Sloan Digital Sky Survey photometry. The authors reported that such galaxies are H I–rich for their stellar masses and have low star formation efficiencies, similar to other gas-dominated dwarfs (e.g. Geha et al. 2006). Perhaps most intriguing, Leisman et al. (2017) reported that the velocity widths (W_{50}) of the global H I profiles of their UDGs were significantly narrower than in other `ALFALFA` galaxies with similar H I masses. However, without resolved H I imaging of a significant sample, this result could be attributed to a very strong inclination selection effect for their sample, or systematics when deriving W_{50}. Taking all of the above as a starting point, in this study we undertake 3D–kinematic modeling of resolved H I synthesis data to study the gas kinematics of six H I–rich UDGs. The rest of this Letter is organised as follows: in Section 2.2 we introduce our sample of galaxies with their main properties and we describe our strategy for deriving their kinematics. We present our results and discussion in Section 2.3, to then conclude in Section 2.4. Throughout this work we adopt a ΛCDM cosmology with $\Omega_m = 0.3$, $\Omega_\Lambda =$

[1] H I–rich UDGs represent $\sim 6\%$ of all galaxies with $M_{HI} \sim 10^{8.8}$ M$_\odot$, with a cosmic abundance similar to cluster UDGs (Jones et al. 2018; Mancera Piña et al. 2018).

0.7 and $H_0 = 70$ km s^{-1} Mpc^{-1}.

2.2 Sample and kinematics

Our sample consists of six galaxies identified as H I–bearing UDGs by Leisman et al. (2017). They have $M_{\rm HI} \sim 10^9$ M$_\odot$ and are relatively isolated, by requiring that any neighbor with measured redshift within ± 500 km s^{-1} should be at least at 350 kpc away in projection. Moreover, they have $R_{\rm e} > 2$ kpc, to ease optical follow-up. Our observations were obtained with two interferometers: the data for AGC 122966 and AGC 334315 come from the Westerbork Synthesis Radio Telescope (program R13B/001; PI Adams) and the rest from the Karl G. Jansky Very Large Array (programs 14B-243 and 17A-210; PI Leisman). The observations and data reduction procedure are described in Leisman et al. (2017) and more details will be given in Gault et al. (2021). Three more galaxies for which we have data are excluded from this analysis. AGC 238764 seems to have ordered rotation of about 20 km s^{-1}, but our data-cube misses significant flux with respect to the `ALFALFA` detection. AGC 749251 shows hints of a velocity gradient but it is barely resolved and we are not able to constrain its inclination better than $i \lesssim 30°$. AGC 748738 shows signs of a gradient in velocity but the data are very noisy. We decide not to consider these three galaxies to keep a reliable sample for the kinematic fitting, but more details on these sources will be given in Gault et al. (2021). We estimate the baryonic mass of our UDGs as $M_{\rm bar} = 1.33\ M_{\rm HI} + M_\star$, with $M_{\rm HI}$ given by (Kennicutt & Evans 2012):

$$\frac{M_{\rm HI}}{\rm M_\odot} = 2.343 \times 10^5 \left(\frac{d}{\rm Mpc}\right)^2 \left(\frac{F_{\rm HI}}{\rm Jy\ km\ s^{-1}}\right) \tag{2.1}$$

where we assume (Hubble flow) distances as listed in Leisman et al. (2017), and fluxes derived from the total H I–maps using the task FLUX from GIPSY (van der Hulst et al. 1992).

Stellar masses are obtained from the mass-to-light ratio–colour relation of Herrmann et al. (2016) for an absolute magnitude in the g band and a $(g - r)$ colour. In order to derive such measurements we perform aperture photometry following the procedure described in Marasco et al. (2019) on deep optical data, obtained with the One Degree Imager of the WIYN 3.5-m telescope at the Kitt Peak National Observatory (Leisman et al. 2017; Gault et al. 2021).

We find a mean $M_{\rm HI}/M_\star \approx 15$, confirming that the baryonic budget is mainly set by the H I content, which we can robustly measure. Table 2.1 gives the name, distance, inclination, baryonic mass, gas-to-stellar mass ratio, circular velocity, central surface brightness and colour of our galaxies. Fig. 2.1 shows the stellar image, $0^{\rm th}$-moment map, major-axis position-velocity (PV) diagram, and observed velocity field for a representative case, AGC 248945. Fig. 2.2 shows the PV diagrams for the rest of our sample.

Rotation velocities are derived with the software $^{\rm 3D}$Barolo[2] (Di Teodoro & Fraternali 2015), which fits tilted-ring disc models to the H I data-cubes (e.g.

[2]Version 1.4, `http://editeodoro.github.io/Bbarolo/`

Table 2.1: Name, distance, inclination, baryonic mass, gas-to-stellar mass ratio, circular velocity, central surface brightness and colour of our sample. Distances, taken from Leisman et al. (2017), have an uncertainty of ±5 Mpc, while the uncertainty for the inclination is ±5°. The central surface brightness is obtained from an exponential fit to the $g-$band surface brightness profile.

Name AGC	Distance (Mpc)	Inclination (deg)	$\log(M_{\rm bar/M_\odot})$	$M_{\rm gas}/M_\star$	$V_{\rm circ}$ (km s^{-1})	μ(g, 0) (mag arcsec^{-2})	$g-r$ (mag)
114905	76	33	9.21 ± 0.20	$7.1^{+4.9}_{-2.3}$	19^{+6}_{-4}	23.62 ± 0.13	0.30 ± 0.12
122966	90	34	9.21 ± 0.14	$29.1^{+11.9}_{-7.0}$	37^{+6}_{-5}	25.38 ± 0.23	-0.10 ± 0.22
219533	96	42	9.36 ± 0.27	$19.7^{+12.2}_{-8.8}$	37^{+5}_{-6}	24.07 ± 0.33	0.12 ± 0.12
248945	84	66	9.05 ± 0.20	$2.4^{+1.6}_{-0.8}$	27^{+3}_{-3}	23.32 ± 0.35	0.32 ± 0.11
334315	73	52	9.32 ± 0.14	$23.7^{+9.8}_{-5.9}$	26^{+4}_{-3}	24.52 ± 0.13	-0.08 ± 0.18
749290	97	39	9.17 ± 0.17	$6.1^{+2.9}_{-1.7}$	26^{+6}_{-6}	24.66 ± 0.30	0.17 ± 0.12

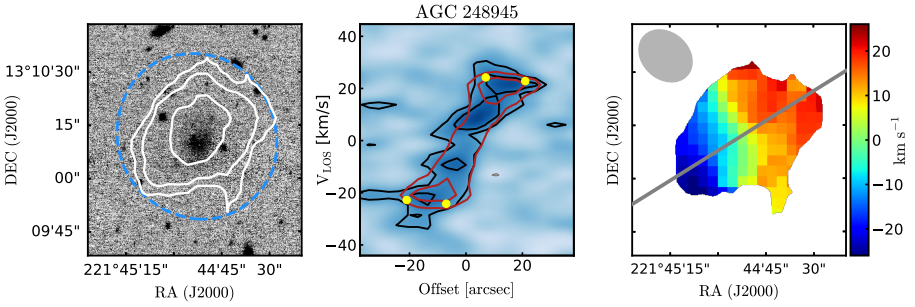

Figure 2.1: A representative galaxy from our sample, AGC 248945. *Left*: H I contours on top of the $r-$band image; the contours are at 0.88, 1.76 and 3.52 × 10^{20} H I atoms per cm^2, the outermost contour corresponds to S/N ≈ 3. The blue ellipse shows the inclination the galaxy would need to be in the BTFR (see the text for details). *Middle*: PV-diagram along the kinematic major axis; black and red contours correspond to data and ^{3D}Barolo best-fit model, respectively; the yellow points show the recovered rotation velocities. *Right*: Observed velocity field, at the same scale as the left panel. The grey line shows the kinematic major axis and the grey ellipse the beam.

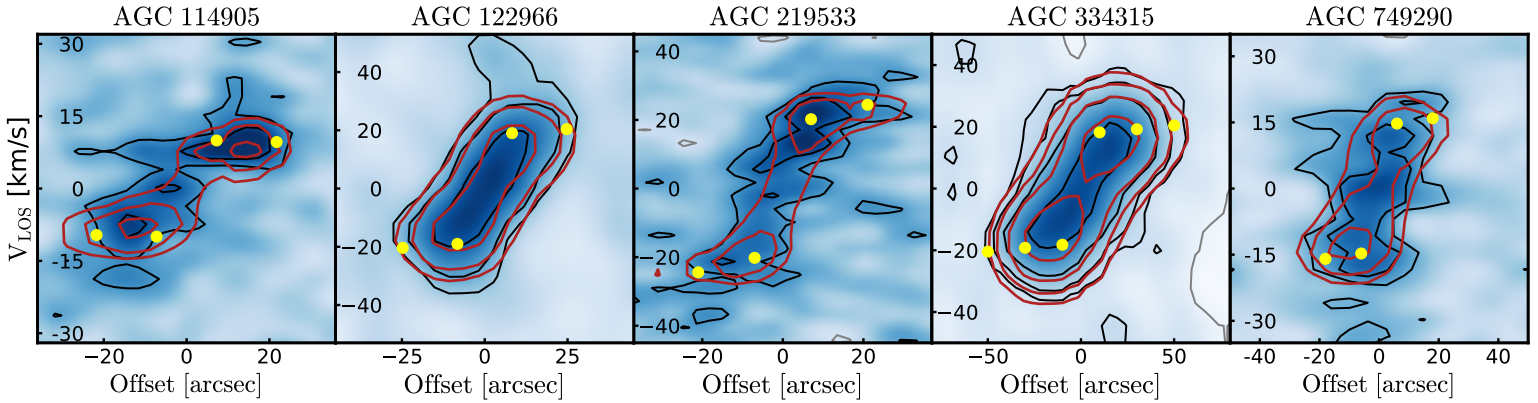

Figure 2.2: PV slices along the major axes of our galaxies. Contours and points as in Fig. 2.1, where AGC 248945 is shown. The narrowness of the PV diagrams suggests low gas velocity dispersions, as confirmed by ^{3D}Barolo.

Iorio et al. 2017; Bacchini et al. 2019a). This approach is particularly suited to deal with our low spatial resolution data ($2-3$ resolution elements per galaxy side) as it is virtually unaffected by beam-smearing (e.g. Di Teodoro et al. 2016). While further details about the properties of our sample and the configuration used in ^{3D}Barolo are provided in Chapter 3 (Mancera Piña et al. 2020), here we briefly summarise our methodology.

We give the position angle and inclination to ^{3D}Barolo. For the former we choose the angle that maximises the amplitude of the PV slice along the major axis. The inclination of each galaxy is derived by minimising the residuals between its observed 0^{th}-moment map and the 0^{th}-moment map of models of the same galaxy projected at different inclinations between $10°-80°$. We have tested this method blindly, without a priori knowledge of the position angle, inclination nor rotation velocity, on a sample of 32 H I–rich dwarfs drawn from the APOSTLE cosmological hydrodynamical simulations (Sawala et al. 2015; Fattahi et al. 2016), from which mock data-cubes have been produced at resolution and S/N matching our observations, using the MARTINI software[3] (Oman et al. 2019). We find that we can consistently recover the position angle within $\pm8°$ and the inclination within $\pm5°$ as long as $i \gtrsim 30°$, with no systematic trends. These small uncertainties in position angle and inclination have no significant impact on the recovered rotation velocities.

We run ^{3D}Barolo with fixed inclination and position angle, and the rotation velocity and velocity dispersion as free parameters, for our fiducial inclination i, as well as for $i+5°$ and $i-5°$. We find rotation velocities ($V_{\rm rot}$) suggesting flat rotation curves for all our sample. For calculating $V_{\rm rot}$, we use the mean velocity of the rings, as found with our fiducial inclination. The associated uncertainties come from the 16^{th} and 84^{th} percentiles of the velocity distribution obtained when considering the uncertainty in our inclination.

To convert from $V_{\rm rot}$ to circular velocity ($V_{\rm circ}$), we correct for pressure supported motions using ^{3D}Barolo as well (cf. Iorio et al. 2017). As suggested by the narrowness of the PV diagrams (Fig. 2.1 and 2.2), we find low gas velocity dispersions, giving rise to very small asymmetric drift corrections ($\lesssim 2$ km s^{-1}).

2.3 Results and discussion

In Figure 2.3 we present the circular velocity–baryonic mass plane for our H I–rich UDGs, compared with galaxies from the SPARC (Lelli et al. 2016a), SHIELD (McNichols et al. 2016) and LITTLE THINGS (Iorio et al. 2017) samples. Clearly, all the UDGs studied here lie significantly above the BTFR.

Our galaxies rotate about 3 times lower than galaxies with comparable $M_{\rm bar}$ and effective radius (but higher surface brightness). Alternatively, they have about 10–100 times the $M_{\rm bar}$ of galaxies with similar $V_{\rm circ}$ (but smaller effective radius and higher surface brightness, on average). These low velocities are consistent with the observations by Leisman et al. (2017) and Janowiecki et al. (2019) of H I–rich UDGs having narrower W_{50} than galaxies of similar H I mass.

[3]Version 1.0.2, `http://github.com/kyleaoman/martini`

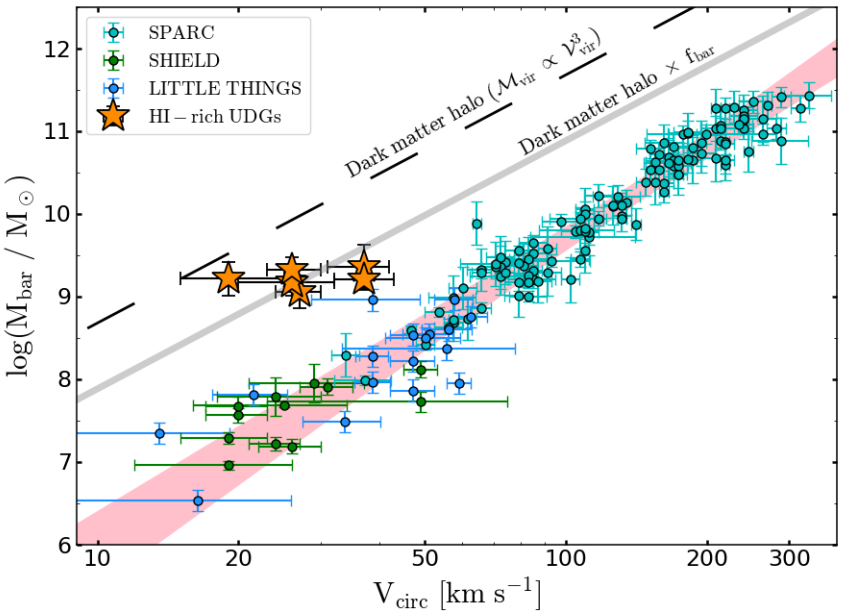

Figure 2.3: Circular velocity versus baryonic mass plane. Galaxies from the SPARC, SHIELD and LITTLE THINGS samples lie on top of the BTFR. The pink area is the 99% confidence interval of an orthogonal distance regression to the SPARC sample. The dashed black line is the theoretical relation between the mass of dark matter haloes and their circular speed at the virial radius. The solid grey line shows the same relation but multiplied by the cosmological baryon fraction. H I–rich UDGs are clear outliers of the BTFR, and in a position consistent with having no 'missing baryons'.

Before discussing the implications of this result we address its robustness. The baryonic masses here derived cannot be substantially overestimated: H I line fluxes can be measured with good accuracy (and we find fluxes in agreement with those derived from `ALFALFA` data by Leisman et al. 2017), and the distances to the galaxies in our sample ($\langle d \rangle \sim 90$ Mpc) are large enough to be well represented by Hubble flow models, so the estimation of their H I mass is reliable. The H I–rich nature of our galaxies also implies that the stellar mass and its systematics play a rather minor role: even $M_\star = 0$ would not move the galaxies significantly in Fig. 2.3.

A severe underestimation of the rotation velocities is also unlikely. First, the H I emission of the galaxies extends out to radii $\approx$ 8–18 kpc, and velocities obtained at such large radii are expected to be tracing the maximum of the rotation curve for any plausible dwarf galaxy dark matter halo (e.g. Oman et al. 2015, their Fig. 2). Second, regarding the inclination correction, bringing the galaxies back to the BTFR would require a nearly face-on inclination ($i \approx 10° - 20°$) for *all* of them, which is both unlikely and incompatible with the

observed intensity maps, as illustrated in Fig. 2.1, with an ellipse showing the inclination that the galaxy would need to be on the BTFR. Third, non-circular motions are not strong enough to solve the observed discrepancy: regardless of the mode(s), their order, phase or amplitude, harmonic non-circular motions do not bias $V_{\rm rot}$ towards lower values systematically, as long as the viewing angle of the galaxy is random (Oman et al. 2019, their Fig. 7), and the symmetry of the approaching and receding sides of our PV-diagrams suggests the absence of anharmonic components. We also investigated with ^{3D}Barolo the presence of radial motions, but no clear evidence for this was found, although higher-resolution observations are needed to further confirm this.

Finally, it is worth to mention that the observed velocity gradients cannot be attributed to H I winds: in that case the gas velocity dispersion would be much higher than observed, and the galaxies would need very high star formation rate densities, opposite to what is measured (Leisman et al. 2017).
Previous studies already suggested the existence of outliers in the BTFR, or at least an increase in its scatter at low $V_{\rm circ}$ (e.g. Geha et al. 2006). Sometimes, however, the robustness of the measurements of the rotation velocities (usually estimated from the global H I profile) and inclinations of such outliers were unclear (cf. Oman et al. 2016 and references therein).

Based on the discussion above, we conclude that the positions of H I–rich UDGs in the $M_{\rm bar} - V_{\rm circ}$ plane derived here are robust, and our UDGs do not follow the BTFR[4]. This suggests that the distribution of late-type systems in such plane is broader than previously observed, and may have important implications for the scatter in the BTFR, which is a strong constraint for cosmological models. Despite the small scatter previously reported (e.g. Lelli et al. 2016b; Ponomareva et al. 2017), our findings open the possibility for a scenario where the parameter space in the $M_{\rm bar} - V_{\rm circ}$ plane between the UDGs presented here and the BTFR is populated by LSB galaxies whose resolved H I kinematics have not been studied yet, and which are not in our sample due to sharp selection effects. This may increase the error budget of the intrinsic scatter of the relation, but to properly understand the magnitude of this effect a more complete census of the relative abundances of these galaxies is required.

A second result emerges when comparing the position of our galaxies with the curves in Fig. 2.3. The black dashed curve is the relation between the circular velocity at the virial radius and the virial mass of dark matter haloes ($M_{\rm vir}/{\rm M}_\odot \approx 4.75 \times 10^5\ (V_{\rm vir}/{\rm km\ s^{-1}})^3$, for $\Delta_{\rm c} = 100$, cf. McGaugh 2012). If $M_{\rm vir}$ is multiplied by the cosmological baryon fraction ($f_{\rm bar} \approx 0.16$), this gives rise to the solid grey curve, indicating the expected position for galaxies with a baryon fraction equal to $f_{\rm bar}$[5]. Unexpectedly, our UDGs lie on top this curve, meaning that they are consistent with having no 'missing baryons'.

Posti et al. (2019) recently discovered that some massive spirals have virtually

[4]It is worth to notice that the two outliers close to our UDGs, DDO 50 and UGC 7125, also have relatively large effective radii and/or low surface brightness.
[5]Note that this assumes $V_{\rm circ} \approx V_{\rm vir}$, but in general $V_{\rm circ}$ tends to be slightly larger for massive galaxies ($V_{\rm circ} \approx 1.5\ V_{\rm vir}$). This would flatten the grey curve at high $V_{\rm circ}$ values.

no 'missing baryons'. There is, however, a substantial difference between our UDGs and these massive spirals, as the former are H I–dominated and have very shallow potential wells compared to the latter. How, then, is it possible that they retained all of their gas? One intriguing possibility is that they have not experienced strong episodes of gas ejection: feedback processes must have been relatively weak and the shallow gravitational potentials managed to retain (or promptly re-accrete) all of their baryons. We surmise that this could be related to the low gas velocity dispersions we find for our sample, which suggest a currently weak heating of the gas. This may be analogous to the 'failed feedback problem' of Posti et al. (2019), although in their case feedback has failed at limiting the star formation efficiency of massive spiral galaxies.

Extremely efficient feedback has been invoked to solve different discrepancies between observations and ΛCDM predictions (see Tulin & Yu 2018 and Bullock & Boylan-Kolchin 2017 for a review, including limitations of such solutions), as well as to explain the formation of UDGs via feedback-driven outflows resulting from bursty star formation histories (e.g. Di Cintio et al. 2017). These new observations seem to present a challenge to these models.

An alternative scenario could be that our galaxies reside in haloes with $V_{\rm circ} \approx 80$ km s^{-1} but very low concentration, such that their rotation curves are still rising at our outermost measured radii. However, this does not seem feasible since the concentration parameter needed for this is $c \approx 1$, instead of the expected $c \approx 10$ (Dutton & Macciò 2014), making the existence of such galaxies within the volume of the Universe basically impossible.

Figure 2.4 shows the ratio between baryonic and dynamical mass of our UDGs, with a dynamical mass estimated as $M_{\rm dyn}(< R_{\rm out}) = V_{\rm circ}^2\ R_{\rm out}/G$, with $R_{\rm out}$ the radius of the outermost point of the rotation curve. Both our sample and LITTLE THINGS galaxies have a mean $R_{\rm out}/R_{\rm d} \approx 4$, with $R_{\rm d}$ the optical disc-scale length.

Even if our H I–rich UDGs have a baryon fraction equal to the cosmological average, their dynamics could be dark matter-dominated at all radii, as other galaxies of similar $V_{\rm circ}$, but this is does not seem to be the case, since $M_{\rm bar}(R < R_{\rm out}) \approx M_{\rm dyn}(R < R_{\rm out})$. Although more precise values of $M_{\rm bar}$ and $M_{\rm dyn}$ should be determined with better data, Fig. 2.4 indicates that these galaxies have much less dark matter within the extent of their discs than other dwarfs and LSB galaxies, and that, inside their discs, the baryonic component dominates.

The dynamical properties here shown resemble those of tidal dwarf galaxies (Hunter et al. 2000; Lelli et al. 2015). However, given the isolation (mean distance to nearest neighbor ~ 1 Mpc) of our UDGs, a tidal dwarf origin does not seem likely, but this is hard to test with the current data.

Based on their globular clusters kinematics the UDGs NGC1052-DF2 (van Dokkum et al. 2018; Danieli et al. 2019) and NGC1052-DF4 (van Dokkum et al. 2019) have recently been claimed to lack dark matter, although some concerns exist regarding their distances and environments (Trujillo et al. 2019; Monelli & Trujillo 2019). Our UDGs have robust distances determined from their recession

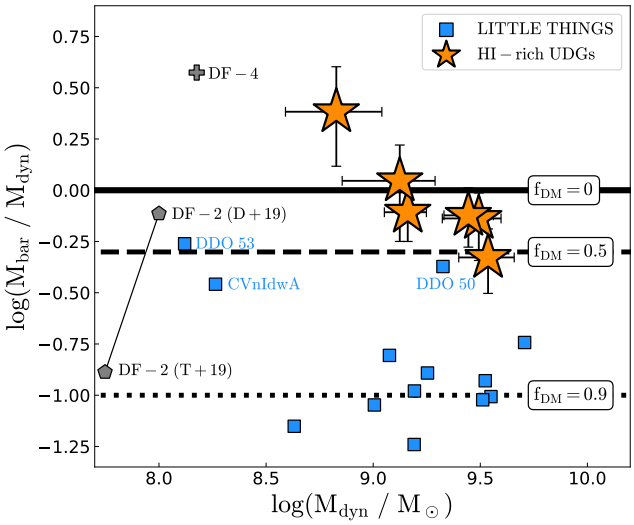

Figure 2.4: Baryonic to dynamical mass ratio as a function of the dynamical mass, measured inside $\approx$ 4 $R_{\rm d}$. The solid, dashed and dotted lines show the position where galaxies with 0%, 50% and 90% dark matter lie, respectively. LITTLE THINGS galaxies (Iorio et al. 2017) are shown for comparison, as well as two estimates for DF–2 (Danieli et al. 2019, D+19 and Trujillo et al. 2019, T+19) and DF–4 van Dokkum et al. (2019), for which we assume $M_{\rm bar} = M_{\star}$.

velocities and avoid dense environments, mitigating these concerns. They may be subject to different systematics, but demonstrate that there may indeed exist a previously under-appreciated population of unusually dark matter-deficient galaxies.

2.4 Conclusions

We have analysed a set of interferometric H I line observations of gas–dominated UDGs. Using a 3D fitting technique we obtain robust measurements of their circular velocities, allowing us to place them in the circular velocity–baryonic mass plane.

We find that our six galaxies lie well above the BTFR, with rotation velocities too low given their baryonic masses. Their position in the circular velocity–baryonic mass plane implies that they have a baryon fraction within their virial radius equal or close to the cosmological value, and we speculate that this could be due to extremely inefficient feedback, challenging our current understanding of feedback processes in dwarfs. Additionally, the dynamics of these galaxies are dominated by the baryonic component out to the outermost measured radii, and they have very low dark matter fractions inside such radii, suggesting a broader distribution in the dark matter content of galaxies than previously thought.

The fact that galaxies with these properties had not been reported before is perhaps because interferometric H I observations are usually targeted based on previous optical studies. Since UDGs are an extremely optically faint population, it is not particularly surprising that this galaxy population has not been identified before. With the advent of large H I interferometric surveys we expect this hidden population to come to light.

Chapter 3

Robust H I kinematics of gas-rich ultra-diffuse galaxies: hints of a weak-feedback formation scenario

based on

– P. E. Mancera Piña, F. Fraternali, K. A. Oman et al., 2020 –

Published in Monthly Notices of the Royal Astronomical Society, MNRAS 495, 3636

Abstract

We study the gas kinematics of a sample of six isolated gas-rich low surface brightness galaxies, of the class called ultra-diffuse galaxies (UDGs). These galaxies have recently been shown to be outliers from the baryonic Tully-Fisher relation (BTFR), as they rotate much slower than expected given their baryonic mass, and to have baryon fractions similar to the cosmological mean. By means of a 3D kinematic modelling fitting technique, we show that the H I in our UDGs is distributed in 'thin' regularly rotating discs and we determine their rotation velocity and gas velocity dispersion. We revisit the BTFR adding galaxies from other studies. We find a previously unknown trend between the deviation from the BTFR and the disc scale length valid for dwarf galaxies with circular speeds $\lesssim 45$ km s^{-1}, with our UDGs being at the extreme end. Based on our findings, we suggest that the high baryon fractions of our UDGs may originate due to the fact that they have experienced weak stellar feedback, likely due to their low star formation rate surface densities, and as a result they did not eject significant amounts of gas out of their discs. At the same time, we find indications that our UDGs may have higher-than-average stellar specific angular momentum, which can explain their large optical scale lengths.

3.1 Introduction

In the last five years there have been a significant number of studies aiming to detect and systematically characterise a population of low surface brightness (LSB) galaxies with Milky Way-like effective radius, similar to those earlier reported by Sandage & Binggeli (1984) or Impey et al. (1988). Following the work by van Dokkum et al. (2015), who discovered 47 of these so-called ultra-diffuse galaxies (UDGs), different studies have found them in both high- and low-density environments (e.g. van der Burg et al. 2016; Román & Trujillo 2017b,a; Greco et al. 2018; Mancera Piña et al. 2019a; Román et al. 2019, and references therein). Among them, Leisman et al. (2017), hereafter L17, found a population of field galaxies, detected in the ALFALFA catalogue (Giovanelli et al. 2005), that meet the usual optical definition for UDGs ($\langle\mu(r, R_e)\rangle \gtrsim 24$ mag arcsec^{-2}, $R_e \gtrsim 1.5$ kpc[1]), but have also large atomic gas reservoirs ($\geq 10^8$ M$_\odot$), in contrast to the cluster population. This gas-rich field population is likely to be small in terms of total number. Prole et al. (2019b) estimated that gas-rich UDGs represent about one-fifth of the overall UDG population (cf. Mancera Piña et al. 2018; Lee et al. 2020), and Jones et al. (2018) found that they represent a small correction to the galaxy stellar and H I mass functions at all masses, with a maximum contribution to the H I mass function of 6% at $\sim 10^9$ M$_\odot$. Despite this, their extreme properties make them puzzling and interesting objects to study.

It is well known that resolved 21-cm observations not only reveal interactions between the extended H I galaxy discs and their environments (e.g. Yun et al. 1994; de Blok & Walter 2000; Fraternali et al. 2002; Oosterloo et al. 2007; Di Teodoro & Fraternali 2014), but also allow us to estimate their rotation velocity, angular momentum and matter distribution, key ingredients to understand their formation and evolution (e.g. de Blok 1997; Verheijen 1997; Swaters 1999; Noordermeer 2006; Posti et al. 2018b). Because of these key properties, that may reveal telltale clues about their origins, pursuing studies of UDGs from an H I perspective is potentially very interesting.

From a theoretical perspective, different ideas have been proposed to explain the puzzling nature of UDGs. Di Cintio et al. (2017) presented hydrodynamical simulations where UDGs originate in isolation due to powerful feedback-driven outflows that modify the dark matter density profile allowing the baryons to move to external orbits, increasing the scale length of the galaxies (see also Chan et al. 2018; Cardona-Barrero et al. 2020). On the other hand, Amorisco & Loeb (2016) suggested that the extended sizes of UDGs can be explained if they live in dark matter haloes with high spin parameter (see also Rong et al. 2017; Posti et al. 2018a). While currently those seem to be the most popular ideas, more mechanisms have been proposed in the literature, as we discuss in detail later.

[1] With $\langle\mu(r, R_e)\rangle$ the mean effective surface brightness within the effective radius, measured in the $r-$band, and R_e the optical effective (half-light) radius.

To test these theories, *isolated* UDGs are very useful. Some of their properties like morphology, circular speed, baryon fraction or angular momentum, can be contrasted with expectations from the above mentioned theories in a relatively straightforward way, since they are not affected by their environments and cannot be explained by interactions with other galaxies (e.g. Venhola et al. 2017; Bennet et al. 2018). Using a combination of H I interferometric data and deep optical images for a sample of six gas-rich UDGs, in Chapter 2 (i.e. Mancera Piña et al. 2019b) studied the baryonic mass–circular speed plane, finding that these galaxies show a set of intriguing properties: they lie well above the canonical baryonic Tully-Fisher relation (BTFR, McGaugh et al. 2000), in a position compatible with having 'no missing baryons' within their virial radii, and with little room for dark matter inside the extent of their gaseous discs. In this chapter we delve into the kinematic properties of the galaxies presented in Chapter 2, explaining in detail the methodology used to derive 3D kinematic models. Further, we expand our investigation to other properties of these LSB galaxies, and discuss possible interpretations for our results.

The rest of this chapter is organised as follows. In Sec. 3.2 we describe our sample and give the structural parameters obtained from the optical and H I observations, and in Sec. 3.3 we provide details on our methodology and kinematic modelling. In Sec. 3.4 we estimate the scale height of the sample and we look briefly into the properties of their interstellar medium (ISM), while in Sec. 3.5 we revisit the BTFR, examine the existence of outliers and show that the deviation from the relation at low rotation velocities correlates with the galaxy scale length. A discussion on the implications of our results for proposed UDG formation mechanisms, including the addition of UDGs to the stellar specific angular momentum–mass relation, is given in Sec. 3.6. In Sec. 3.7 we present our conclusions. Throughout this Chapter magnitudes are in the AB system, and a ΛCDM cosmology with $\Omega_{\rm m} = 0.3$, $\Omega_{\Lambda} = 0.7$ and $\rm H_0 = 70$ km s^{-1} Mpc^{-1} is adopted.

3.2 The sample

The sample studied in this chapter and in Chapter 2 consists of six gas-rich UDGs, originally identified by L17, for which dedicated optical and interferometric observations were obtained. The observations and data reduction strategies are explained in detail in L17 and Gault et al. (2021). We note here that the sample from Gault et al. (2021) consists of eleven galaxies while ours consists of six. As briefly discussed in Chapter 2, we selected the galaxies that were more suitable in terms of data-quality for our kinematic modelling (see below). Fig. 3.1–3.6 present our data and 3D kinematic modelling, while Table 3.1 gives the main properties of our galaxy sample.

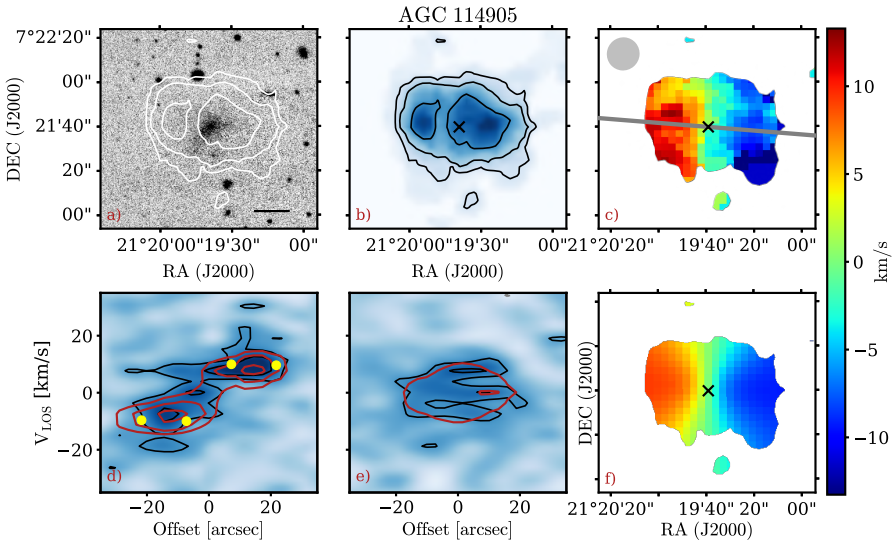

Figure 3.1: Data and kinematic models for the gas-rich UDG AGC 114905 (01:25:18.60, +07:21:41.11, J2000). *a)*: $r-$ band image with H I contours on top at 1, 2, 4×10^{20} atoms cm^{-2}, with the lowest one at S/N $\approx$ 3. The black solid line indicates a physical scale of 5 kpc. *b)*: total H I map in blue, and contours as in panel *a)*. *c)*: Observed velocity field (first-moment map). The grey line shows the major axis, while the grey ellipse shows the beam. *d)*: PV diagram along the major axis. Black and red contours correspond to data and best-fit model, respectively, and are at the 2σ and 4σ levels. If present, grey dashed contours indicate negative values in the data. The recovered rotation velocities are indicated with the yellow points. *e)*: PV diagram along the minor axis (perpendicular to the major axis), colours as in *d)*. *f)*: Modelled velocity field. The black cross in panel *b*, *c* and *f* shows the kinematic centre. The rightmost panel shows the velocity colour-bar for panels *c)* and *f)*.

3.2.1 Optical data

Given the LSB nature of our galaxies, the imaging of wide-field public surveys like the Sloan Digital Sky Survey (SDSS, e.g. York et al. 2000) is not deep enough to provide accurate photometric parameters on an individual basis. Because of this, the six galaxies were observed using the One Degree Imager (Harbeck et al. 2014) of the 3.5-m WIYN telescope at the Kitt Peak National Observatory. The g and r bands were used, with a total exposure time of 45 min per filter. The optical image production is described in detail in Gault et al. (2021). Panel *a)* in Fig. 3.1–3.6 shows the $r-$band optical images of our sample.

As introduced in Chapter 2 and shown thoroughly in Gault et al. (2021), aperture photometry is performed on these images to obtain total magnitudes (and colours) and surface brightness profiles. The central surface brightness and disc scale length ($R_{\rm d}$) are obtained from a fit to the observed surface brightness profiles assuming that the light distribution follows an exponential profile, which

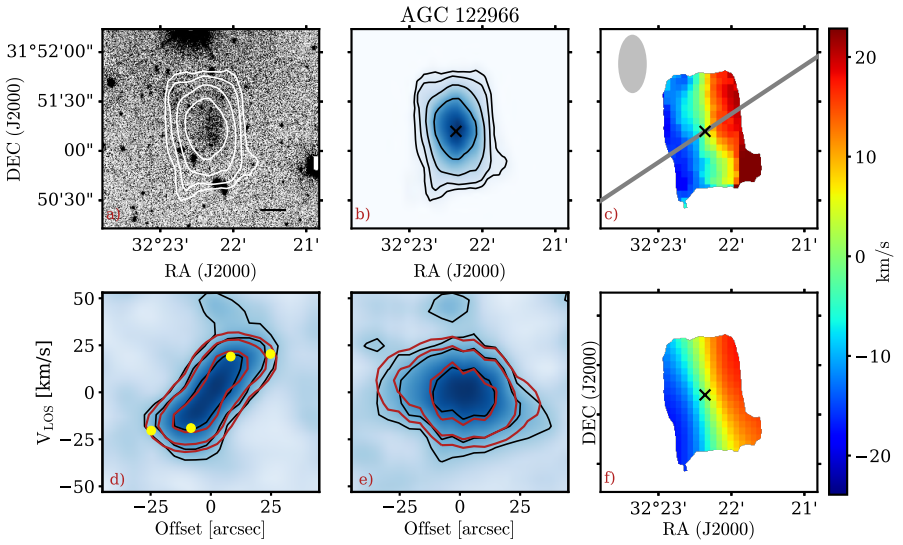

Figure 3.2: Data and kinematic models for the gas-rich UDG AGC 122966 (02:09:29.49, +31:51:12.77, J2000). Panels and symbols as in Fig. 3.1. The H I contours are at 0.35, 0.7, 1.4 and 2.8×10^{20} atoms cm^{-2}. Note that the kinematic and morphological position angles seem to be different, but this apparent effect is due to the peculiar elongated shape of the WSRT beam (see Appendix 3.A).

Table 3.1: Properties of our galaxy sample. (1) Arecibo General Catalogue ID. (2) Systemic velocity. (3) Distance, taken from L17, has an uncertainty of ± 5 Mpc. (4) Optical disc scale length, obtained from an exponential fit to the r–band surface brightness profile. (5) Stellar mass. (6) H I mass. (7) Inclination, derived from the H I data with an uncertainty of ±5°. (8) Kinematic position angle, derived from the H I data, with an uncertainty of ±8°. (9) Circular speed. (10) Mean value of the gas velocity dispersion. (11) Radius of the outermost ring of the rotation curve.

ID AGC (1)	V_{sys} [km s^{-1}] (2)	D [Mpc] (3)	R_d [kpc] (4)	$\log(M_*/M_\odot)$ (5)	$\log(M_{HI}/M_\odot)$ (6)	Inc. [deg] (7)	PA [deg] (8)	V_{circ} [km s^{-1}] (9)	$\langle\sigma\rangle$ [km s^{-1}] (10)	R_{out} [kpc] (11)
114905	5435	76	1.79 ± 0.04	8.30 ± 0.17	9.03 ± 0.08	33	85	19^{+6}_{-4}	$\lesssim 4$	8.02
122966	6509	90	4.15 ± 0.19	7.73 ± 0.12	9.07 ± 0.05	34	300	37^{+6}_{-5}	7	10.80
219533	6384	96	2.35 ± 0.20	8.04 ± 0.12	9.21 ± 0.18	42	115	37^{+5}_{-6}	$\lesssim 4$	9.78
248945	5703	84	2.08 ± 0.07	8.52 ± 0.17	8.78 ± 0.08	66	300	27^{+3}_{-3}	$\lesssim 4$	8.55
334315	5107	73	3.76 ± 0.14	7.93 ± 0.12	9.10 ± 0.10	45	185	25^{+5}_{-5}	7	8.49
749290	6516	97	2.38 ± 0.14	8.32 ± 0.13	8.98 ± 0.08	39	130	26^{+6}_{-6}	$\lesssim 4$	8.47

is a good assumption for these galaxies (see also Román & Trujillo 2017a; Greco et al. 2018; Mancera Piña et al. 2019a).

To derive the stellar masses we employ the mass-to-light–colour relation given by Herrmann et al. (2016):

$$\log(M_*/L_g) = 1.294(\pm0.401) \times (g-r) - 0.601(\pm0.090)\ , \qquad (3.1)$$

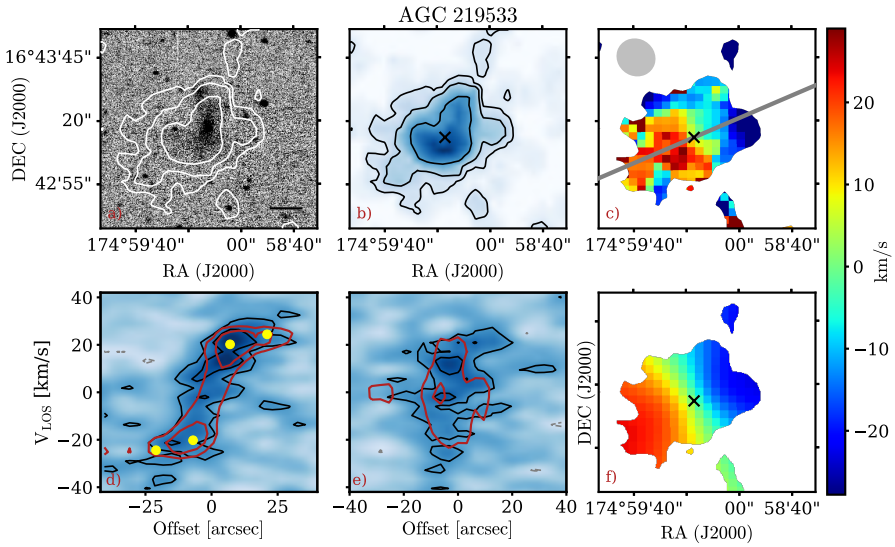

Figure 3.3: Data and kinematic models for the gas-rich UDG AGC 219533 (11:39:57.16, +16:43:14.00, J2000). Panels and symbols as in Fig. 3.1. The H I contours are at 1.1, 2.2 and 4.4×10^{20} atoms cm^{-2}. In this case the data cube is more noisy than in the rest of the sample, and the last contour corresponds to S/N $\approx$ 5.

which was specifically calibrated for dwarf irregular galaxies, whose optical morphology is similar to isolated UDGs. In practice, for each UDG we randomly sample Equation 3.1 using Gaussian distributions on each parameter, to account for the uncertainties in both the relation itself and the photometry. The fiducial value of each parameter is chosen as the mean of its Gaussian distribution while its standard deviation gives the corresponding uncertainty. With this, we obtain a distribution for $\log(M_*/L_g)$ that is then converted to stellar mass using the $g-$band absolute magnitude distribution. The values for the stellar mass, which we report in Table 3.1, are the median values of the final distributions for each galaxy, and the uncertainties the difference between these medians and the corresponding 16^{th} and 84^{th} percentiles.

3.2.2 H I data

We obtained resolved H I-line observations using the Karl G. Jansky Very Large Array (VLA) and the Westerbork Synthesis Radio Telescope (WSRT). All the galaxies have radio data from the VLA, while AGC 122966 and AGC 334315 have also WSRT data. Details of the data reduction are given in L17 and Gault et al. (2021). In the case of the two galaxies with VLA and WSRT observations, we use the data with the best quality in terms of spatial resolution and signal-to-noise (S/N), which were the VLA data for AGC 334315 and the WSRT data for AGC 122966. In the rest of this chapter we use the parameters derived from

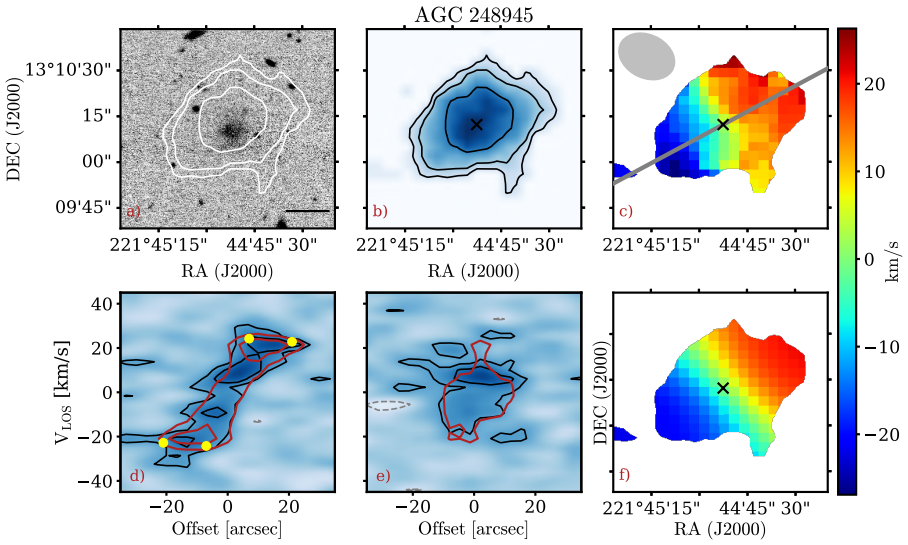

Figure 3.4: Data and kinematic models for the gas-rich UDG AGC 248945 (14:46:59.50, +13:10:12.20, J2000). Panels and symbols as in Fig. 3.1. The H I contours are at 0.8, 1.6 and 3.2×10^{20} atoms cm^{-2}.

these data. For completeness, in Appendix 3.A we present the WSRT data for AGC 334315[2] and the VLA data for AGC 122966, demonstrating the overall good agreement between the different data cubes.

We build total H I maps of our sources using the software ^{3D}Barolo (Di Teodoro & Fraternali 2015, see below for more details). These maps are first obtained using a mask that ^{3D}Barolo generates after smoothing the data cubes by a given factor and then selecting those pixels above a chosen threshold in units of the rms of the smoothed cube. Upon inspection of our data, we find sensible values for the smoothing factor and the cut threshold around 1.2 and 3.5, respectively. The fluxes of our galaxies are measured from the data cubes using the task FLUX from `GIPSY` (van der Hulst et al. 1992). The measurements of the flux from the VLA and WSRT data cubes are fully consistent with the separate analysis by Gault et al. (2021) and L17, and in good agreement (within ≈10%) with the values obtained from the ALFALFA single-dish observations, except for AGC 248945, for which we recover ≈30% less flux. Upon inspection of the data cube, we confirm that the emission missing in the VLA profile with respect to ALFALFA is not biased with respect to the velocity extent of the source. Panel *b)* in Fig. 3.1–3.6 presents the total H I maps of our galaxies.

[2]Note that in Chapter 2 we used the WSRT data for AGC 334315 while we will use its VLA data for the rest of this chapter. Yet, the differences are rather small, as explained in Appendix 3.A.

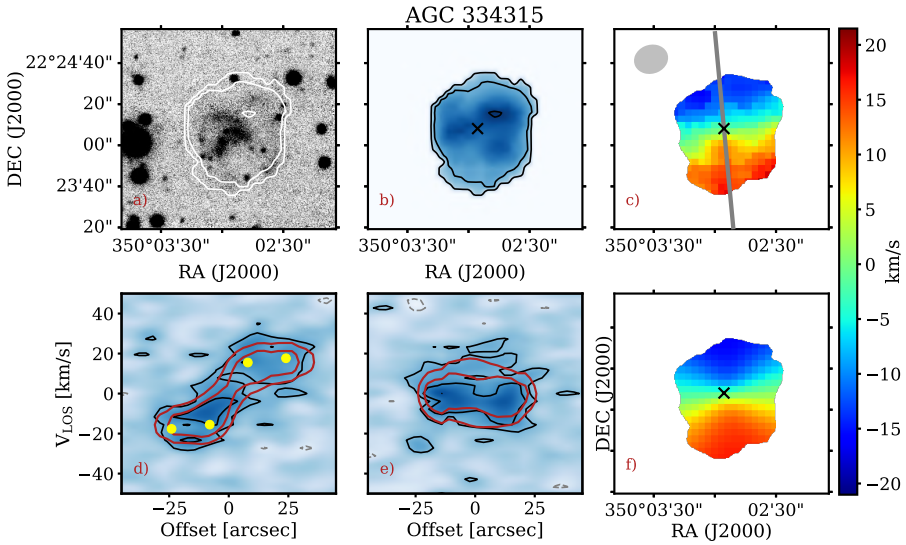

Figure 3.5: Data and kinematic models for the gas-rich UDG AGC 334315 (23:20:11.73, +22:24:08.03, J2000). Panels and symbols as in Fig. 3.1. The H I contours are at 1.8, 3.6 and 7.2×10^{20} atoms cm^{-2}.

We determine the H I mass of our UDGs using the equation

$$\frac{M_{\rm HI}}{\rm M_\odot} = 2.343 \times 10^5 \left(\frac{D}{\rm Mpc}\right)^2 \left(\frac{F_{\rm HI}}{\rm Jy\ km\ s^{-1}}\right), \tag{3.2}$$

with D and $F_{\rm HI}$ the distance and flux of each galaxy, respectively. Distances, taken directly from L17, come from the ALFALFA catalog, which uses a Hubble flow model (Masters 2005). Given the line-of-sight velocities of our sample (see Table 3.1), and considering that these UDGs live in the field, the possible effects of peculiar velocities are not significant and the Hubble flow distances provide a robust measurement of the 'true' distance, with an uncertainty of ± 5 Mpc.

3.2.3 Interpretation of velocity gradients

As can be seen in the panel *c)* of Fig. 3.1–3.6, we observe clear velocity gradients in most of our UDGs; AGC 749290 is the exception and the kinematics of this galaxy is more uncertain, as we discuss below. These gradients are along the morphological H I position angle of the galaxies, and in the following sections we interpret them as produced by the differential rotation of a gaseous disc. Here we briefly discuss other possibilities.

One may wonder if the observed velocity gradients could be generated not by rotation but by gas inflow (see Sancisi et al. 2008 for a review) or blown-out gas due to powerful stellar winds (see for instance McQuinn et al. 2019 and references therein). Such winds have been observed in starburst dwarfs traced

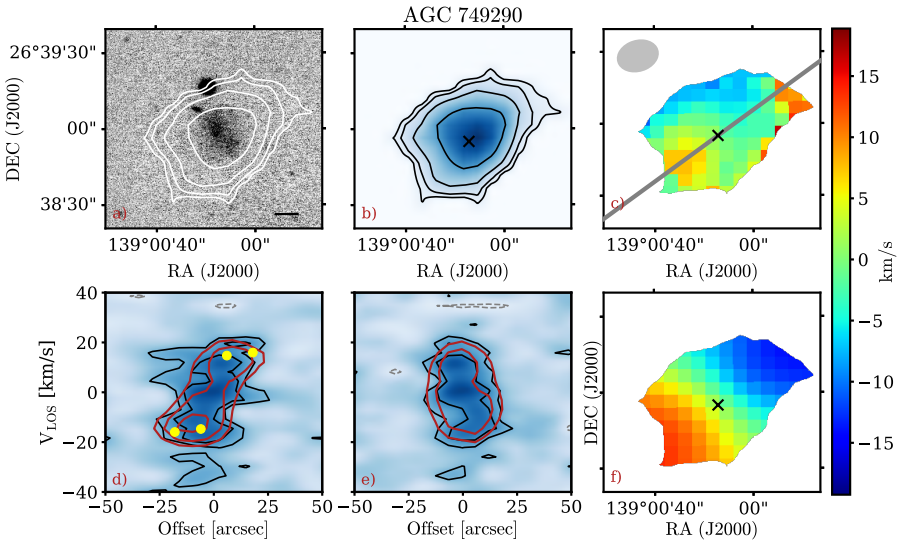

Figure 3.6: Data and kinematic models for the gas-rich UDG AGC 749290 (09:16:00.95, +26:38:56.93, J2000). Panels and symbols as in Fig. 3.1. The H I contours are at 0.35, 0.7, 1.4 and 2.8×10^{20} atoms cm^{-2}. As shown in the major-axis PV diagram (panel *d)*), while ^{3D}Barolo models well the main rotating body, there is signal at around velocities of 10 km s^{-1} and offset 25 arcsec that cannot be reproduced by the best-fit model. The parameters for these galaxy are considered less robust than for the rest of the sample, as we discuss in Sec. 3.3.2.

by Hα emission, where the H I distribution may also be disturbed (e.g. Lelli et al. 2014a; McQuinn et al. 2019). There is, however, clear evidence against these scenarios in the case of our UDGs. First of all, the velocity gradients are aligned with the H I morphological position angle of the galaxies, as happens with normal rotating discs. Further, as we discuss later, our measurements of the gas velocity dispersions point to a rather undisturbed and quiet ISM. Moreover and most importantly, our galaxies have normal-to-low star formation rates (SFR $\approx$ 0.02–0.4 M$_\odot$ yr^{-1}, see L17), which combined with their extended optical scale length leads to SFR surface densities of a factor about $10-20$ lower than in typical dwarfs. The fact that our UDGs are gas dominated and there is only one clear velocity gradient implies that if the gradients are due to winds the whole ISM should be in the wind, requiring very high mass loading factors and SFR densities, in contradiction with the information presented above. Based on this discussion we conclude that the possibility of the observed velocity fields being produced by inflows or outflows is very unlikely. In contrast, we show in Sec. 3.3 how a rotating disc can reproduce the features observed in our data.

3.2.4 Baryonic mass

The baryonic masses of the galaxies are computed with the equation

$$M_{\rm bar} = M_{\rm gas} + M_* = 1.33\ M_{\rm HI} + M_* \ , \tag{3.3}$$

where the factor 1.33 accounts for the presence of helium.

The mass budget of our galaxies is dominated by the gas content, with a mean gas-to-stellar mass ratio $(M_{\rm gas}/M_*) \approx 15$ (see Chapter 2 for more details). This ensures that, despite possible systematics when deriving the stellar mass, the estimation of the baryonic mass is robust.

As seen in Eq. 3.3, we neglect any contribution from molecular gas to the baryonic mass of the galaxies; while the molecular gas mass is indeed often smaller than the stellar and atomic gas ones in dwarfs (e.g. Leroy et al. 2008; Saintonge et al. 2011; Ponomareva et al. 2018, and references therein), it may of course contribute to the total mass budget. This hypothetical baryonic mass gain, however, would place our sources further off the BTFR, only strengthening the results shown in Sec. 3.5.

3.3 Deriving the gas kinematics

3.3.1 Initial parameters for 3D modelling

Our interferometric observations allow us to estimate rotation velocities for the six galaxies. However, the data have low spatial resolution, with only a couple of resolution elements per galaxy side. Low-spatial resolution observations can be severely affected by beam smearing, which tends to blur the observed velocity fields, and traditional 2D approaches that fit tilted-ring models to beam-smeared velocity fields fail at recovering the correct kinematics, by underestimating the rotation and overestimating the gas velocity dispersion (e.g. Bosma 1978; Swaters 1999; Di Teodoro et al. 2016).

^{3D}Barolo (Di Teodoro & Fraternali 2015) is a software tool which produces 3D models of emission-line observations (e.g. Di Teodoro et al. 2016; Iorio et al. 2017; Bacchini et al. 2019a). Instead of fitting the velocity field, it builds 3D tilted-ring realisations of the galaxy that are later compared with the data to find the best-fit model. Thanks to a convolution step before the model is compared with the data, ^{3D}Barolo strongly mitigates the effect of beam smearing, so it is ideal for analysing data like ours. ^{3D}Barolo assumes that the discs are thin; while this is not known a priori, we show in Sec. 3.4.1 that the ratio between the radial and vertical extent of our UDGs is large, confirming the validity of our approach.

Due to the small number of resolution elements we prefer to fit only two parameters with ^{3D}Barolo: the rotation velocity and the velocity dispersion. This means that the rest of the parameters need to be determined and fixed, namely the center of the galaxy, its systemic velocity, position angle and inclination.

^{3D}Barolo can robustly estimate the systemic velocity and the centre of the galaxies from the centre of the global H I profile and the total H I map,

respectively. We use thus these estimations from ^{3D}Barolo and we keep them fixed while fitting the rings. ^{3D}Barolo can also estimate the position angle and inclination, but for low resolution data these estimates may not be accurate. Therefore, we decide to estimate these two parameters independently and to fix them when fitting the kinematic parameters. The position angle is chosen as the orientation that maximises the amplitude of the position-velocity (PV) diagram along the major axis. This is done visually using the task KPVSLICE of the KARMA package (Gooch 1996). Importantly, we find that in every galaxy the kinematic and morphological (H I) position angle are nearly the same. The exception may seem to be AGC 122966, but as we discuss in Sec. 3.3.2 this is an apparent artifact due to the shape of the beam for the WSRT observations of that galaxy.

Estimating the inclination of the galaxies is of crucial importance, as correcting for it can account for a large fraction of the final rotation velocity if the galaxies are seen at low inclinations. Unfortunately, due to the LSB nature of our galaxies, their optical morphologies, often irregular and dominated by patchy regions, provide only an uncertain, if any, constraint on the inclinations (see also Starkenburg et al. 2019 for other limitation of using optical data to determine the inclination of the H I disc.). This, together with the fact that the H I is more extended and massive than the stellar component, motivated us to use the H I maps to estimate the inclinations. We do this by minimising the residuals between the observed H I map of each galaxy and the H I map of models of the same galaxy but projected at different inclinations between 10° and 80°. Such models are produced using the task GALMOD from ^{3D}Barolo, which in turn uses updated routines from the homonym `GIPSY` task, and takes into account the shape of the beam when generating the models. The centre, surface density and position angle for the models are the same as in the galaxy whose inclination we aim to determine. The inclination of the model that produces the lowest residuals when compared with the data (lowest absolute difference between the total H I maps) is chosen as the fiducial inclination.

Testing on simulated galaxies

We test our method to recover the galaxy's initial geometrical parameters using a sample of gas-rich dwarfs from the `APOSTLE` cosmological hydrodynamical simulations (Sawala et al. 2015; Fattahi et al. 2016). Mock H I data cubes of these galaxies, 'observed' at a resolution and S/N matching our data, are obtained with the software MARTINI (Oman et al. 2019). The simulated galaxies have H I masses of $\sim 10^{8-9}$ $M_\odot$ and rotation velocities around $\approx 20-60$ km s^{-1}. We initially work with four simulated galaxies with similar mass and velocity as our sample, but we project them at different random position angles and inclinations, allowing us in practice to test our methods in 40 different mock data cubes. Fig. 3.7 shows two examples of such simulated galaxies: their H I maps, PV diagrams, and rotation curves.

We treat these mock data in exactly the same way as our UDGs data, using the method described above to derive the position angle and inclination. Fig. 3.8

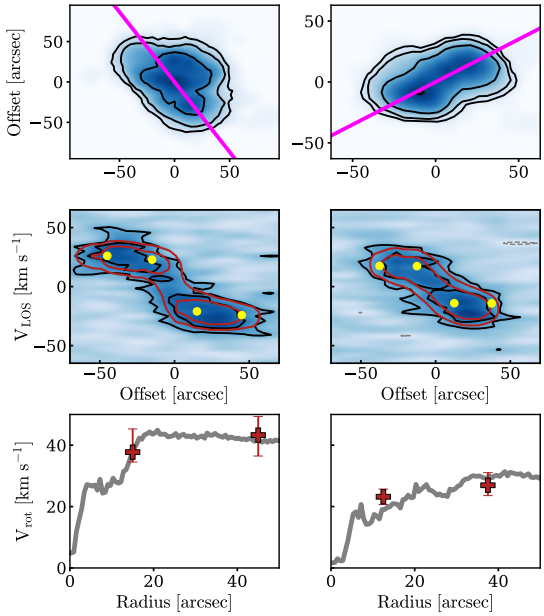

Figure 3.7: Two of the 40 APOSTLE simulated dwarf galaxies used to test our methods. *Top*: Total H I maps with their kinematic major axes in magenta. *Middle*: PV diagrams along the major axis. The black and red contours represent the simulated data and our best-fit model, respectively; grey dashed contours show negative values. The yellow points show the recovered rotation velocities. *Bottom*: True rotation curves (grey lines) derived directly from the simulations and recovered rotation velocities (red crosses).

shows the true and recovered geometrical parameters. We find that we can consistently recover the position angle of the simulated galaxies and, once this is fixed, the inclination. The mean of the absolute difference between truth and recovered position angles and inclination angles is 8° and 5°, respectively. We adopt these values as the uncertainties for these parameters. Note that our method recovers the inclination only for galaxies with inclinations $\gtrsim 25°$; below this all the models look very similar and our method systematically underestimates the inclination by about 10°. For higher inclinations, in two out of 40 cases we underestimate the inclination by about 15°. Given the low incidence of this (5% of the times) we do not expect to underestimate the inclination of our real galaxy sample; in any case this would lower the circular velocities of our sample that we report, which would not affect the nature of our results below. The bottom panels of Fig. 3.7 show that our derived rotation velocities well represent the underlying rotation curves after having estimated the position and inclination angles as described above, and then used ^{3D}Barolo.

3.3.2 Running ^{3D}Barolo on the individual systems

After testing our methods we proceed to run ^{3D}Barolo on all our UDGs. As discussed before, we leave the rotation and dispersion as free parameters, and we fix the position angle and inclination; the values of these parameters are given in Table 3.1. As expected, ^{3D}Barolo is able to estimate the centre and systemic velocity of the sources with good accuracy, as we could verify by visually inspecting the velocity fields and PV diagrams. It is worth mentioning that the

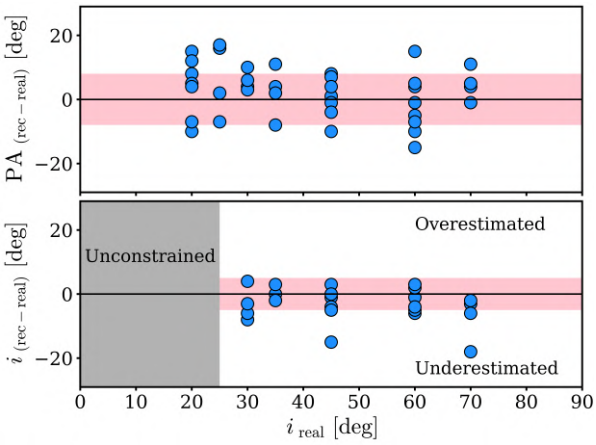

Figure 3.8: Comparison between truth (real) and recovered (rec) position angles (PA) and inclinations (i) in our set of APOSTLE dwarfs. The black lines show the case where the difference is zero, and the pink bands show our adopted uncertainties in both parameters.

systemic velocities in the kinematic fits agree well with the values determined from the ALFALFA global profiles (the mean difference is about 5 km s^{-1}). The kinematic centres and systemic velocities used in the models can be found in Table 3.1. The noise in the data cubes and peak column densities are provided in Gault et al. (2021). ^{3D}Barolo also applies a correction for instrumental broadening, controlled by the parameter `LINEAR`, which depends on the spectral smoothing of the data. In our case, we use `LINEAR` = 0.42 for the VLA data, and `LINEAR` = 0.85 for the (Hanning-smoothed) WSRT data.

The separation between rings is given by the parameter `RADSEP` in ^{3D}Barolo, and the value is chosen taking into account the beam orientation and extension for each galaxy. Below we provide information on the value of `RADSEP` used for each galaxy, as well as some individual comments.

- AGC 114905: The size of the beam is 14.64"×13.31", with a North-West orientation of −5°. The galaxy position angle is 85°. The component of the beam projected along the kinematic major axis has a size of approximately the size of the beam minor axis. Given the extension of the galaxy, we use two rings, with `RADSEP` = 14.5".

- AGC 122966: The size of the beam is 33.16"×18.70", oriented at 15°. Given the orientation of the galaxy, the component of the beam along its kinematic major axis is ≈ 20.5". Considering the extension of the galaxy (≈ 33") we oversample by a factor ≈ 1.2, using `RADSEP` = 16.5" and allowing us to have two points. This galaxy gives the impression of having perpendicular morphological and kinematic major axes, but this is an apparent effect due to the elongated shape of the WSRT beam, as it can be seen in Appendix 3.A with the less elongated beam of the VLA data.

- AGC 219533: Beam size of 14.93"×13.62", with orientation at 25.5°. The

projected beam radius along the kinematic major axis of the galaxy is 13.6". We use two independent resolution elements with RADSEP = 14".

- AGC 248945: Beam size of 18.10"×14.11", with a position angle of 57.3°. The projected beam radius along the kinematic major axis of the galaxy is 14.7". Given the extension of the H I emission we adopt RADSEP = 14.5", ending up with two resolution elements.

- AGC 334315: The galaxy has a beam size of 15.83"×13.94", oriented at −65°. Along the major axis of the galaxy, the projected size of the beam is ≈ 14". We use two independent resolution elements with RADSEP = 16".

- AGC 749290: Beam size of 21.63"×17.88", oriented at −61°. The projected radius of the beam along the major axis of the galaxy is ≈ 21.4". Given the extension of the galaxy we oversample by a factor 1.7 to get two resolution elements per galaxy side, with RADSEP = 12", although the resulting two rings are not independent. Because of this, the kinematic parameters of this galaxy are less certain than for the rest of our sample, and we plot the galaxy as an empty symbol when using its kinematic parameters. Nevertheless, we note that the specific values of its circular speed and velocity dispersion are similar to the values of the rest of the sample.

3.3.3 Kinematic models

For all our galaxies the kinematic fits converge and ^{3D}Barolo finds models which are in good agreement with the data. Fig. 3.1–3.6 show our kinematic models in panels *c)* to *f)*: observed and modelled velocity field, and observed and modelled (1 pixel width) PV diagrams.

The PV diagrams and rotation velocities suggest that we are tracing the flat part of the rotation curve, as the two points of the rotation curves are consistent with each other. This may be a possible source of confusion since some PV diagrams, at first-sight, may look like solid-body rotation. However, this is an effect of the beam smearing, and ^{3D}Barolo is able to recover the intrinsic rotation velocities (see for instance Fig. 7 and 8 in Di Teodoro & Fraternali 2015), although for AGC 749292 this is not possible to establish unambiguously as we oversample the data by a factor 1.7. Moreover, standard rotation curves of simulated dwarf galaxies are expected to reach the flat part well inside our typical values of $R_{\rm out}$ (e.g. Oman et al. 2015). Observed rotation curves do not keep rising after 2-3$R_{\rm d}$ either (e.g. Swaters 1999), which is again inside our values of $R_{\rm out}$. Yet, higher-resolution and higher-sensitivity observations would be desirable to further confirm this, as well as to trace the inner rising part which we cannot observe at the current resolution.

Taking this into account, and the fact that the inclination is the main driver of uncertainties in the rotation velocity, we estimate the circular speeds and their uncertainties reported in Table 3.1 as follows:

1. For each galaxy, we run ^{3D}Barolo two more times, but instead of using our fiducial inclination i, we use $i-5$ and $i+5$. This means that each ring of a galaxy has three associated velocities, obtained with i, $i-5$ and $i+5$. ^{3D}Barolo is able to correct for pressure-supported motions, with the so-called asymmetric drift correction (e.g. Iorio et al. 2017), allowing the conversion from rotation velocities to circular speeds. We apply this correction, although it is found to be small, contributing at most ≈ 1 km s^{-1}.

2. For each of the above velocities (at i, $i-5$ and $i+5$), and for each ring, we generate random Gaussian distributions centred at the value of the velocity, and with standard deviation given by the statistical errors in the fit found by ^{3D}Barolo. A galaxy with two resolution elements has six corresponding Gaussian distributions, three for each ring.

3. Finally, we add all these Gaussian distributions in a broader distribution $\mathcal{G}$. For each galaxy, the circular speed ($V_{\rm circ}$) corresponds to the 50$^{\rm th}$ percentile of $\mathcal{G}$, and its lower and upper uncertainties (Table 3.1) correspond to the difference between that value and the 16$^{\rm th}$ and 84$^{\rm th}$ percentiles of $\mathcal{G}$, respectively.

Circular speeds

Our galaxies have circular speeds between 20 and 40 km s^{-1}. Given their baryonic masses, their velocities are a factor $2-4$ lower than the expectations from the BTFR (see Sec. 3.5 and Chapter 2). Our lower-than-average circular speeds are consistent with earlier observations by different authors that these kinds of galaxies have narrower global H I profiles than other galaxies with similar masses (L17; Spekkens & Karunakaran 2018; Janowiecki et al. 2019).

A question that may arise, given the long dynamical timescales implied by the low rotation velocities of our UDGs, is whether they are in dynamical equilibrium. The average dynamical time for our sample is 2 Gyr. The mean distance from our UDGs to their nearest neighbor, according to the Arecibo General Catalog[3], is 1 Mpc. If we consider the case where *all* our galaxies interacted with their nearest neighbor, and we assume that they come from a 10^{12} M$_\odot$ environment (gas-rich UDGs inhabit low-density large-scale environments, see Janowiecki et al. 2019) with an escape speed of 200 km s^{-1}, the mean interaction back-time (how long ago did the interaction occur) for them is about 5 Gyr, so the galaxies should have had time to reach a stable configuration, having completed on average more than two full rotations.

[3]The Arecibo General Catalog is a catalogue containing all the sources detected in the ALFALFA survey plus all the galaxies with optical spectroscopic detection within the ALFALFA footprint. It is compiled and maintained by Martha Haynes and Riccardo Giovanelli.

Velocity dispersion

The narrowness of the (beam-smeared) PV diagrams of our galaxies, shown in Fig. 3.1–3.6, suggests a rather low gas velocity dispersion for most of them. This is indeed confirmed by the best-fit models of ^{3D}Barolo. The mean velocity dispersion for AGC 114905, AGC 219533, AGC 248945 and AGC 749290, with a channel width of $\Delta_v \approx 4$ km s^{-1}, is $\langle\sigma\rangle = 3 \pm 2$ km s^{-1}, which is below Δ_v. However, based on tests using artificial data cubes, we find that, for data like ours, ^{3D}Barolo cannot recover the exact velocity dispersion if this lies below Δ_v, but it tends to find $\langle\sigma\rangle \approx \Delta_v$. Therefore, for these data cubes we assume an upper limit of $\langle\sigma\rangle \lesssim 4$ km s^{-1}. For AGC 334315, with the same $\Delta_v \approx 4$ km s^{-1}, we find $\langle\sigma\rangle = 7 \pm 2$ km s^{-1}, and we adopt this value. The WSRT data for AGC 122966, which is Hanning smoothed and of lower spatial resolution ($\Delta_v \approx 6$ km s^{-1}), has $\langle\sigma\rangle = 7 \pm 2$ km s^{-1}.

The observed gas velocity dispersions are lower than observed in typical spiral and dwarf galaxies. The upper limit in the velocity dispersion of the VLA cubes is indeed similar to the velocity dispersion of the 'cold' neutral medium of Leo T (Adams & Oosterloo 2018). For comparison, Iorio et al. (2017) in their reanalysis of the kinematics of dwarf galaxies from LITTLE THINGS (Hunter et al. 2012) found $\langle\sigma\rangle \sim 9$ km s^{-1}, similar to the $\langle\sigma\rangle \sim 10$ km s^{-1} of both the more massive spirals of Tamburro et al. (2009) and Bacchini et al. (2019a) and the regularly-rotating starburst dwarfs from Lelli et al. (2014a). In the next section we explore the repercussions of these results.

3.4 Thickness and turbulence in the discs of gas-rich UDGs

3.4.1 Thickness of the gas disc

Given the gravitational potential and gas surface density of a galaxy, the value of its velocity dispersion can be used to estimate its gas disc scale height h (see for instance § 4.6.2 in Cimatti et al. 2019). Since our galaxies are dominated by the gas component rather than the stellar and dark matter components, at least up to the outermost measured point (see Fig. 3 in Chapter 2), we can consider the simple case of a self-gravitating disc with constant circular speed in hydrostatic equilibrium (e.g. van der Kruit 1988; Marasco & Fraternali 2011). This exercise only provides an indicative value for h, but it is still instructive as this measurement has not been yet carried out for UDGs. The scale height of such discs is given by the equation

$$h = \frac{\sigma^2}{\pi G \Sigma_{\rm gas}} \ , \tag{3.4}$$

with σ the gas velocity dispersion, G the gravitational constant and $\Sigma_{\rm gas}$ the gas surface density.

Assuming a mean velocity dispersion constant with radius and the mean surface density of the disc[4], we obtain a mean (median) disc scale height of $\langle h \rangle = 260$ (150) pc. Note that these values may in reality be smaller, as *i)* we are adopting an upper limit in the velocity dispersion for most galaxies, and *ii)* we completely neglect the potential provided by the stars and dark matter, which, even if small, would contribute to flatten the disc. We can conclude that our galaxies do not appear to have H I discs significantly thicker than other disc galaxies. For reference, the H I discs studied in Bacchini et al. (2019a) have mean values for h between $130 - 540$ pc, depending on the galaxy, and the dwarfs from Banerjee et al. (2011) have $\langle h \rangle \approx 500$ pc. Note that the differences in the assumed shape of the vertical profile are not very big: for instance, the correction for using sech^2 instead of a Gaussian function (as in Bacchini et al. 2019a) is less than 10% of the value of h.

It is also worth highlighting that given the H I radius ($R_{\rm HI}$) of our sample (Gault et al. 2021), the values of h indicate that they have relatively 'thin' discs: the extension of their discs (using for reference $R_{\rm HI}$) is on average 50 times larger than the size of the scale height. This result also confirms that our approach of using ^{3D}Barolo (where galaxies are modelled as thin discs) is perfectly adequate.

3.4.2 Turbulence in the ISM

According to the Field criterion for thermal instabilities (cf. Field 1965; Goldsmith et al. 1969), the ISM should only exist in stable conditions in two well-defined phases. These two phases correspond to the cold (CNM) and warm neutral media (WNM), with temperatures of $\sim 70 - 100$ K and $\sim 6000 - 8000$ K, respectively, although in realistic conditions gas in the interfaces of both media exists at intermediate temperatures (e.g. Heiles & Troland 2003). These temperatures imply a thermal speed of $0.75 - 1$ km s^{-1} for the CNM and $7 - 8$ km s^{-1} for the WNM.

In this context, our UDGs are an intriguing case because the observed intrinsic velocity dispersions are lower than the expected thermal speed of the WNM. Assuming that indeed the galaxies lack of a significant amount of WNM, the velocity dispersion can be then attributed entirely to the thermal broadening of the CNM plus turbulence in the disc[5]. By further assuming that turbulence is driven entirely by supernova explosions, we can compute the supernova efficiency in transferring kinetic energy to the ISM (see for instance § 8.7.4 in Cimatti et al. 2019 or § VI in Mac Low & Klessen 2004). We find that efficiencies between 2 and 5% are enough to reproduce the observed low gas velocity dispersions. While these values are limited by all our uncertainties and are valid only within about one order of magnitude, they indicate that the supernova efficiency in our UDGs is likely similar to the expectations for disc galaxies from different theoretical papers like Thornton et al. (1998); Fierlinger et al. (2016) or recent

[4] We do this for simplicity, ending-up with a constant scale height, but our discs may be flared as in other dwarfs and spiral galaxies (e.g. Banerjee et al. 2011; Bacchini et al. 2019a).

[5] Note that neutral gas at $T \sim 2000$ K can produce a dispersion of 4 km s^{-1}, without additional energy input.

observational results (Bacchini et al. 2020a), but different from the results reported in other observational works like Tamburro et al. (2009) or Utomo et al. (2019), where supernova efficiency needs to be very high and even external drivers of turbulence (e.g. magneto-rotational instabilities) are needed. Overall our discussion here and in Sec. 3.3.3 highlights the 'cold' nature of the H I disc of our UDGs.

3.5 Understanding the deviation from the BTFR

As discussed in Chapter 2, our UDG sample lies off the canonical BTFR, with circular speeds 2−4 times lower than galaxies with similar masses or, equivalently, with $10-100$ times more baryonic mass than galaxies with similar circular speeds. This result holds after taking into account all the different possible systematics while deriving the circular speeds and baryonic masses.

Chapter 2 postulates that it may not be surprising that no other galaxies have been found to lie on a similar position off the BTFR as interferometric observations are usually targeted based on optical detection and the UDGs are a faint optical population. Some galaxies in the literature (e.g. Geha et al. 2006; Kirby et al. 2012; Oman et al. 2016) also appear to be outliers from the BTFR, although concerns regarding their kinematic parameters have been raised (see discussion in Oman et al. 2016). In this section we study in more detail the existence of outliers from the BTFR, using more galaxies with resolved 21-cm observations from the literature than in Chapter 2. We plot our UDGs (stars) and the different comparison samples in Fig. 3.9, together with the best-fit line to the SPARC galaxies from Lelli et al. (2016b), extrapolated towards the low-circular speed regime, and the expected relation for galaxies with a baryon fraction equal to the cosmological mean (see Chapter 2). The reader interested in the main results of this comparison, without delving into the details, may wish to go ahead to Fig. 3.9, 3.10 and Sec. 3.5.

We start by considering all the galaxies from the SPARC sample (Lelli et al. 2016a). From the 175 galaxies listed in the data base[6], 135 have an available measurement of their asymptotically flat rotation velocity. Five out of these 135 galaxies are included in the LITTLE THINGS sample of Iorio et al. (2017), and since their analysis is more detailed and similar to ours we do not use the SPARC values for these galaxies. From the remaining 130 galaxies we select those with inclinations $i \geq 30°$ and good quality flag on their rotation curve ($Q = 1, 2$, see Lelli et al. 2016a for details), ending up with 120 galaxies, shown in Fig. 3.9 as cyan circles.

We consider also the LITTLE THINGS galaxies from Iorio et al. (2017), shown in Fig. 3.9 as blue pentagons, and the SHIELD galaxies (McNichols et al. 2016), plotted as green octagons. Additionally, we include UGC 2162 (red hexagon), a UDG with resolved GMRT data presented in Sengupta et al. (2019), and a sample of nearly edge-on 'H I–bearing ultra-diffuse sources' (HUDs, see L17) with ALFALFA data from He et al. (2019), shown as magenta diamonds.

[6] `http://astroweb.cwru.edu/SPARC/SPARC_Lelli2016c.mrt`

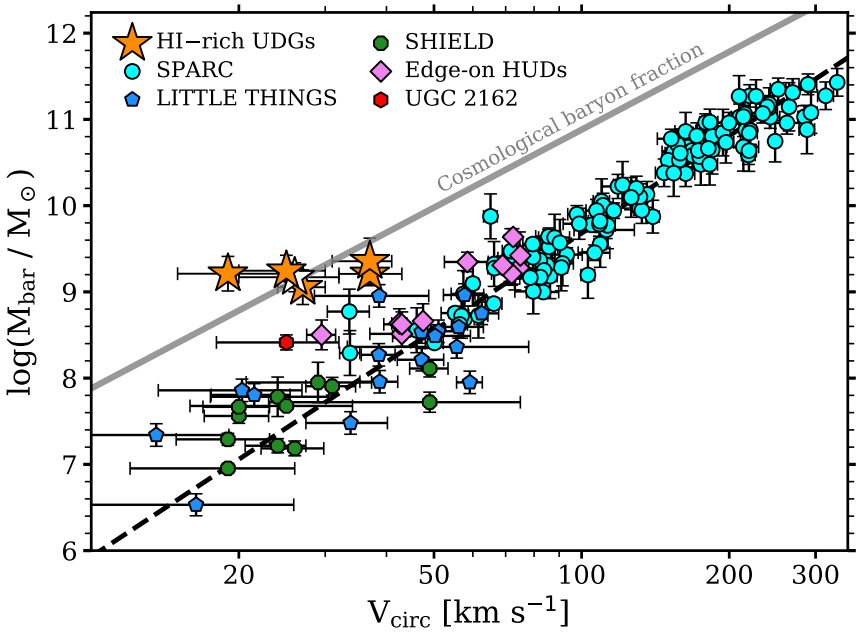

Figure 3.9: Circular speed vs. baryonic mass plane for different galaxy samples. Gas-rich UDGs are shown as orange stars, except for AGC 749290, whose circular speed is less robust than for the rest of the sample, and it is shown as a white star. The black dotted like shows the fit to the SPARC galaxies from Lelli et al. (2016b), extrapolated towards low circular speeds. The grey solid line is the expectation for galaxies that have a baryon fraction equal to the cosmological mean. When including more galaxies from the literature in this plane, the apparent gap between the canonical BTFR and our UDGs is populated. See the text for details.

While we restrict our comparison to samples with resolved H I data and the sample of UDGs from He et al. (2019), some other studies based on unresolved H I data are also worth briefly mentioning in the context of the BTFR. For example, the sample from Geha et al. (2006) shows a number of low-mass dwarf galaxies that increase the scatter of the BTFR at low velocities. In particular, for $V_{\rm rot} \lesssim 40$ km s^{-1}, most of their dwarfs rotate too slowly for their baryonic mass (see their Fig. 7). Also, Guo et al. (2020) have recently used unresolved data from ALFALFA and faint SDSS imaging to suggest that 19 dwarfs they observe show similar properties as those discussed in Chapter 2: the galaxies seem to rotate too slowly for their masses and to have less dark matter than expected. The result from Guo et al. (2020) by itself, however, may be subject of concern as they used unresolved data to estimate the rotation velocities, and lack information on the inclination of the H I disc as they derive an inclination from shallow SDSS data that may not inform us on the actual orientation of the disc (see for instance Starkenburg et al. 2019; Sánchez Almeida & Filho 2019;

Gault et al. 2021).

The outcome of including all the different samples can be seen in Fig. 3.9. Appendix 3.B provides comments on the most interesting individual galaxies from each of the samples discussed above. In general, Fig. 3.9 suggests that it is likely that our UDGs are not the only outliers from the canonical BTFR at low circular speeds, although they may be the most extreme cases. In this context, we examine the deviation from the SPARC fit as a function of central surface brightness and disc scale length; in Appendix 3.B we provide the references from which the structural parameters of the galaxies in Fig. 3.9 are obtained.

We realise that those galaxies above the SPARC fit usually have lower surface brightness than galaxies in the relation, as expected for a constant M/L (see discussion in Zwaan et al. 1995 and McGaugh & de Blok 1998). However, this is not true for all the galaxies, and the analysis may be significantly influenced by the different strategies employed to derive the surface brightness in the literature (e.g. if values are corrected or not for inclination, dust reddening and Galactic extinction, and if different filters were used). Instead, measuring the disc scale length or effective radius of galaxies is more straightforward, as it has been shown to be less dependent on the different optical and infrared bands used to derive it (see for instance Fig. B2 in Román & Trujillo 2017a and Fig. 1 in Falcón-Barroso et al. 2011).

Different authors have found no correlation of the residuals of the best-fit BTFR and observations with other galaxy parameters. For instance, Lelli et al. (2016b) reported no trend as a function of effective radius, scale length or central surface brightness, and Ponomareva et al. (2018) extended these results for Hubble type, colour, SFR and gas fraction (see also Ponomareva et al. 2017 and references therein). Notwithstanding, Avila-Reese et al. (2008), with a larger fraction of LSB galaxies, reported that the scale lengths of their sample do correlate with the residuals of the BTFR, with smaller galaxies deviating towards higher velocities at fixed baryonic mass (note however that they looked at the BTFR using $V_{\rm max}$, instead of $V_{\rm flat}$ like in the other two mentioned studies). Apart from the existence of these discrepancies, those works include only a few galaxies with circular speeds similar to those of our UDGs ($V_{\rm circ} \approx 20 - 40$ km s^{-1}), so it is interesting to re-consider the possible existence of correlations within the same range in velocity as our sample, using the compilation of galaxies that we have shown in this section.

Given the values of $V_{\rm circ}$ for our sample, we consider galaxies with $15\,{\rm km\,s^{-1}} < V_{\rm circ} < 45$ km s^{-1}, and we use them in Fig. 3.9 to build the $R_{\rm d} - \Delta_{\rm M_{bar}}$ plane. Here $R_{\rm d}$ is the stellar scale length and $\Delta_{\rm M_{bar}}$ the vertical distance of the galaxies from the BTFR, defined as the logarithmic difference between the observed baryonic mass and the value expected from the extrapolated SPARC BTFR, $\Delta_{\rm M_{bar}} \equiv \log(M_{\rm bar,obs}/M_{\rm bar,BTFR})$. A clear trend is found: at these low circular speeds, larger (more diffuse) galaxies lie systematically above the SPARC BTFR while the more compact ones lie below; the correlation has a slope around 1.5.

Spearman tests tell us that the correlation is significant at a 99.9% confidence

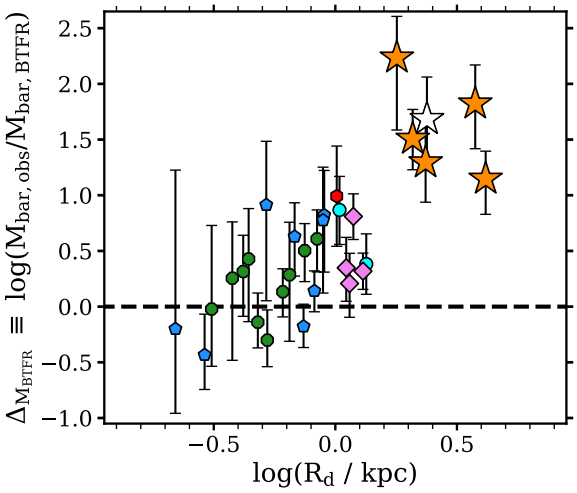

Figure 3.10: Disc scale length vs. vertical distance from the BTFR, for galaxies of different samples with 15 km s^{-1} < V_{circ} < 45 km s^{-1}. Symbols are as in Fig. 3.9 and the dashed line represents no offset from the SPARC BTFR. A correlation between both parameters is observed, with larger galaxies falling systematically above the BTFR. Some samples have no reported uncertainty in R_d, so we do not plot any horizontal error-bar for consistency.

level ($p-$value $\approx 10^{-8}$) when all the samples are considered. This holds even if we exclude our UDGs ($p-$value ≈ 0.0003). The correlation is less robust but still significant at the 95% level when considering exclusively the SPARC and LITTLE THINGS galaxies ($p-$value ≈ 0.02).

This trend is potentially of great importance because it provides evidence supporting the idea that the deviation from the BTFR at low circular speeds is driven by physical processes related to the optical size of the galaxies (which is independent of the kinematics), and that it is not only an effect produced by observational biases.

One may wonder whether it is possible to interpret the trend as a spurious relation due to a severe underestimation of the circular speed of the galaxies: if the galaxies that deviate from the SPARC BTFR have wrong measurements but actually have $V_{circ} \approx 80 - 100$ km s^{-1}, then they would be expected to have larger scale lengths, giving rise to the trend observed in Fig. 3.9.

We find this unlikely for several reasons. First, as discussed in Chapter 2, a significant underestimation of the circular speeds of our sample is extremely unlikely. Further, since galaxies from several independent samples analysed with independent techniques all seem to follow the trend in Fig. 3.9, so the circular speeds of all the other galaxies would need to be underestimated in precisely the same way, which seems very unlikely. Finally, let us consider, ad absurdum, the following scenario. If we assume that all galaxies that deviate from the SPARC BTFR have wrong measurements, but they actually lie on it with $V_{circ} \sim 80$ km s^{-1}, then those galaxies should have higher surface brightness than dwarfs with $V_{circ} \sim 20 - 40$ km s^{-1}. So, if the trend in Fig. 3.9 is spurious, we should also find that galaxies which (apparently, due to wrong measurements) deviate from the BTFR have higher surface brightness than the dwarfs ($V_{circ} \sim 20 - 40$ km s^{-1}) in the BTFR, which is not observed. Based on

this we are led to believe that the correlation in Fig. 3.9 is real, and it provides an extra parameter to explain the deviation from the canonical BTFR and its larger scatter at the low-velocity regime.

The vertical offset from the BTFR can also be seen as a progression in the baryon fraction of the galaxies: at fixed $V_{\rm circ}$, the more baryonic mass a galaxy has, the higher its baryon fraction is. This, coupled with our results above, implies that at low circular speeds $R_{\rm d}$ plays a role affecting the baryon fraction of galaxies (see Sec. 3.6.5 for more details).

Based on our discussion, we outline a possible interpretation of our results regarding the phenomenology of the BTFR. Perhaps, the SPARC BTFR holds at low circular speeds ($V_{\rm circ} \lesssim 50$ km s^{-1}), but the distribution of galaxies in the $V_{\rm circ} - M_{\rm bar}$ plane may be more complex than a well-defined and tight relation as the one established at larger circular velocities, with dwarf galaxies showing baryon fractions above the one implied by the canonical BTFR but still below the cosmological limit. From our analysis, it looks very possible that the disc scale length is an important parameter regulating the deviation from the canonical BTFR. A more extreme scenario would be one where the canonical BTFR breaks down at low circular speeds, being replaced by a 2D distribution. Given the selection biases and small statistics of the samples being analysed, we cannot discern among these options, and this should be addressed with more complete and representative samples.

3.6 Discussion: the origin of gas-rich UDGs

Using the kinematic information derived in the previous sections, here we discuss how our results compare with predictions from some of the main theories that have been proposed to explain the origin and properties of UDGs.

3.6.1 Brief comparison with NIHAO simulations: formation via feedback-driven outflows?

Di Cintio et al. (2017) studied simulated dwarf galaxies from the Numerical Investigation of a Hundred Astrophysical Objects (NIHAO) simulations (Wang et al. 2015), and found a subset of them with properties similar to observed UDGs in isolation. They found that intermittent feedback episodes associated with bursty star formation histories modify the dark and luminous matter distribution, allowing dwarf galaxies to expand, as their baryons move to more external orbits (see also e.g. Navarro et al. 1996; Read & Gilmore 2005; Pontzen & Governato 2012 or Read et al. 2016b for further considerations). Because of this, some of their simulated dwarf galaxies become larger, entering in the classification of UDGs. Chan et al. (2018) reported similar results with the FIRE simulations (e.g. Hopkins et al. 2018). We have observational evidence suggesting that our galaxies have low velocity dispersions and thus a low turbulence in the ISM. In principle, this seems at odds with models that require stellar feedback strong enough to modify the matter distribution. A detailed comparison between

our observations and this kind of simulations it is beyond the scope of this study. Yet, it is interesting to make some brief comments on some apparent similarities and discrepancies between the simulated NIHAO UDGs and our sample.

By inspecting the optical scale lengths, we see that our largest galaxies have no counterparts among the NIHAO UDGs (their largest simulated UDG has $R_{\rm d} \approx 2$ kpc). In general, the mean values differ by a factor 2.5 (ours being larger), but strong selection effects are at play so this should be studied with a complete sample. The gas mass of our galaxies and NIHAO UDGs largely overlap, but our distribution has a sharp selection cut around $M_{\rm HI} < 10^{8.5}$ M$_\odot$.

The UDGs formation mechanism proposed by Di Cintio et al. (2017) can also be contrasted with the observational results of Chapter 2, in particular the baryon fraction of the galaxies with respect to the cosmological mean and the inner amount of dark matter. Di Cintio et al. (2017) mention that their simulated UDGs show a correlation between their optical size and baryon fraction, with their largest UDG having a baryon fraction up to 50% of the cosmological value, with a mean of 20% for the whole sample. Our UDGs have $\approx 100\%$ of the cosmological value. Nevertheless, as mentioned before, our galaxies have also larger scale lengths than the NIHAO UDGs, so one may wonder whether their higher baryon fraction is just a consequence of this. Extending our sample to include UDGs with smaller $R_{\rm e}$ may shed light on the connection between them and the simulated NIHAO UDGs. The inner dark matter content is a major discrepancy between our observations and the UDGs that the NIHAO simulation produces: our galaxies show very low dark matter fractions within their discs (measured within ~ 2 $R_{\rm e}$ on average), while Jiang et al. (2019) found that the NIHAO UDGs are centrally dark-matter dominated (measuring the dark-matter content within 1 $R_{\rm e}$). Related to this, Di Cintio et al. (2017) reported that their UDGs have dark matter concentration parameters typical of galaxies with similar halo masses. This does not seem to be the case in our sample: preliminary attempts of rotation curve decomposition of our UDGs show that if they inhabit 'normal' NFW (Navarro et al. 1997) dark matter haloes (i.e. with a halo mass typical of galaxies with their stellar mass), their concentration parameters need to be extremely low (see also Sengupta et al. 2019), far off expectations of canonical concentration-halo mass relations (e.g. Dutton & Macciò 2014). This should be investigated further with data at higher spatial resolution, but it opens the exciting possibility of providing clues on the nature of dark matter itself (e.g. Yang et al. 2020). Producing artificial data cubes of the NIHAO UDGs to explore their H I kinematic parameters (like their position with respect to the BTFR), as well as obtaining SFR histories for our sample would also allow an interesting and conclusive comparison, although the latter has been proved to be challenging even for closer UDGs (e.g. Ruiz-Lara et al. 2018; Martín-Navarro et al. 2019). Stellar kinematics seems to be a promising tool as well (Cardona-Barrero et al. 2020).

3.6.2 High angular momentum

Angular momentum is a fundamental quantity to understand the origin of high surface brightness and LSB galaxies (e.g. Dalcanton et al. 1997; Di Cintio et al. 2019), and it is usually studied via the so-called spin or λ–parameter for dark matter haloes (e.g. Mo et al. 1998; Dutton & van den Bosch 2012; Rodríguez-Puebla et al. 2016; Posti et al. 2018a) or with the specific angular momentum–mass relation for the stellar component (e.g. Fall 1983; Romanowsky & Fall 2012; Fall & Romanowsky 2018; Posti et al. 2018b).

One of the main ideas to explain the large scale lengths and faint luminosities of UDGs is that they are dwarfs living in high spin (high-λ) dark matter haloes. This is supported by some semi-analytical models and hydrodynamical simulations, where the size of a galaxy is set by its λ, that seem to reproduce different observational properties of the (*cluster*) UDG population like abundance, colours and sizes (e.g. Amorisco & Loeb 2016; Rong et al. 2017; Liao et al. 2019). Some other simulations, however, do not find anything atypical in the angular momentum content of UDGs (e.g. Di Cintio et al. 2017; Tremmel et al. 2020). In this Section we investigate the angular momentum content of our sample, looking separately at the specific angular momentum of gas and stars.

H I specific angular momentum

Based on H I observations, L17 and Spekkens & Karunakaran (2018) suggested that gas-rich UDGs could indeed have higher λ–parameter than other galaxies of similar mass. However, these results are derived from the relation given by Hernandez et al. (2007) to estimate λ from observations, which is highly assumption-dependent, as discussed in detail in Dutton & van den Bosch (2012). In particular, our galaxies do not follow the same BTFR nor seem to have the same disc mass fraction as the galaxies used by Hernandez et al. (2007) to calibrate their relation. Therefore, we decided not to estimate the λ–parameter in that way, and we emphasise that the calibration of Hernandez et al. (2007) should be used with caution, as also mentioned in L17, Spekkens & Karunakaran (2018) and Sengupta et al. (2019).

Unfortunately, we cannot robustly estimate the angular momentum of the gas component of our galaxies as we lack the resolution needed to determine the shape of the surface density profile (e.g. Obreschkow & Glazebrook 2014; Kurapati et al. 2018), so we can only make qualitative statements (see also Sengupta et al. 2019). In this context, the fact that our gas-rich UDGs lie on the H I mass–size relation (Gault et al. 2021) is useful, as it tells us that their H I discs have normal sizes for their H I mass. Additionally, we have shown that the gas rotates at velocities much lower than other galaxies with the same H I mass. Together, these results suggest that our UDGs have low-to-normal gas specific angular momenta compared with galaxies of similar H I mass.

Stellar specific angular momentum

As mentioned before, the stellar specific angular momentum–mass relation (sometimes called 'Fall' relation, see Fall 1983; Romanowsky & Fall 2012) is often used as a more direct way to study the angular momentum of galaxies. To compute this relation, high-resolution (stellar) rotation curves and stellar surface density profiles are needed. However, it is common (see discussion in Romanowsky & Fall 2012; Rizzo et al. 2018) to adopt the approximation

$$j_* = 2\ R_{\rm d}\ V_{\rm rot,*}\ , \tag{3.5}$$

where j_* is the stellar specific angular momentum, $R_{\rm d}$ the optical disc scale length and $V_{\rm rot,*}$ the stellar rotation velocity. This approximation has been proved to work very well, and it is valid for galaxies with exponential light profiles and flat rotation curves. Thus, to use this simplified version to compute j_* for our sample, we have to assume flat rotation curves, which seems at least tentatively supported by our data, and exponential profiles, that describe reasonably well the stellar profile of our galaxies (see Gault et al. 2021).

As the rotation velocity of the stars is needed, the next step is assuming that their rotation can be inferred from the circular velocity of the galaxies, by means of the stellar asymmetric drift correction ($V_{\rm AD,*}$), via the equation

$$V^2_{\rm rot,*} = V^2_{\rm circ} - V^2_{\rm AD,*}\ . \tag{3.6}$$

To compute $V_{\rm AD,*}$, we follow the approach described in Posti et al. (2018b), using the equation:

$$V^2_{\rm AD,*} = \sigma^2_{0,z} \frac{3R}{2R_{\rm d}} e^{-R/R_{\rm d}}\ , \tag{3.7}$$

with $\sigma_{0,z}$ the vertical stellar velocity dispersion[7]. For simplicity we use only the outermost point of the rotation curve, so effectively $R = R_{\rm out}$. As discussed by Posti et al. (2018b), the value of $\sigma_{0,z}$ depends on the central surface brightness (Martinsson et al. 2013), and for our sample it is about 5 km s^{-1}.

The results of this exercise are shown in Fig. 3.11, where we plot our galaxies in the M_* vs. j_* plane. We compare our UDGs with the galaxies studied in Posti et al. (2018b), showing also the best-fit relation (dashed line) and scatter (pink band) that they obtain. We stress here that the assumptions that we have made in our analysis are the same as in Posti et al. (2018b), making the comparison in Fig. 3.11 as fair as our data allow.

Three of our galaxies (AGC 114905, AGC 248945 and AGC 749290) lie within the 1σ scatter of the relation. AGC 219533 and AGC 334315 have a j_* about $3-4$ times larger than the best-fit line, although the observational scatter is relatively large at those values of M_*. The outlier with the highest j_* is AGC 122966, which has both the largest optical disc scale length and

[7] Eq. 3.7 assumes isotropy, i.e. $\sigma_R = \sigma_z$. However, as explored by Posti et al. (2018b), the difference between this or assuming extreme anistropic profiles is rather small, of less than 10%.

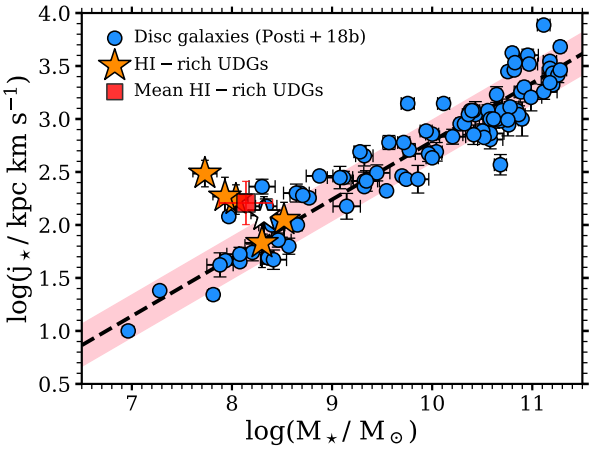

Figure 3.11: Stellar specific angular momentum–mass relation. Orange stars show our UDGs (AGC 749290 is in white as in Fig. 3.9) and the red square their mean position. Blue circles show the sample analysed by Posti et al. (2018b), while the black dashed line and the pink band are their best-fit relation and its 1σ scatter, respectively.

highest rotation velocity of our sample, resulting in a j_* about 9 times larger than expected. Note, however, that the Fall relation is not well-constrained at $M_* < 10^8$ $M_\odot$. A caveat to bear in mind regarding AGC 122966 is that it has the lowest surface brightness of our sample (see Table 1 in Chapter 2), so its scale length is relatively more uncertain than for the other UDGs. The mean (median) ratio between the measured and expected j_* of our galaxies is 3.3 (2.5). These numbers are of course dependent on the several assumptions we have made, and need to be confirmed with better data and more accurate calculations (for instance by obtaining high-resolution stellar rotation curves to formally compute j_* instead of using the approximation of Eq. 3.5 with Eq. 3.7). Yet, our simple analysis indicates that, as a population, our gas-rich UDGs may have a j_* a factor ≈ 3 higher than the expectations for dwarf irregular galaxies with similar M_*, as shown graphically with in Fig. 3.11, where the mean value for our sample is indicated in red. This larger j_* may help explaining why UDGs have more extended optical disc scale length/effective radius than other dwarf irregulars.

The H I component of our galaxies is both more massive and more extended, so one may speculate that its specific angular momentum is likely to be more representative of the spin of the dark matter halo. If this is the case, our UDGs would be galaxies that inhabit dark haloes with normal-to-low λ but with higher-than-average j_*, meaning that they would be galaxies with a higher-than-average 'retained' fraction of angular momentum ($j_*/j_{\rm halo}$), as suggested by Posti et al. (2018a).

3.6.3 'Failed' Milky Way galaxies

Another mechanism proposed to explain the nature of UDGs is that they could be 'failed' Milky Way-like galaxies, with massive dark matter haloes that for different reasons (e.g. strong supernova feedback or gas stripping) failed at converting their gas into stars (van Dokkum et al. 2016). This idea is mainly

motivated by the high velocity dispersions of globular cluster observed around a few UDGs (e.g. van Dokkum et al. 2016; Toloba et al. 2018) and by the large effective radius of UDGs (but see Chamba et al. 2020). However, several other studies, both observational and theoretical, show that most UDGs should reside in dwarf galaxy-sized dark matter haloes (e.g. Beasley & Trujillo 2016; Rong et al. 2017; Amorisco 2018; Ruiz-Lara et al. 2018; Kovács et al. 2019; Prole et al. 2019a; Tremmel et al. 2020).

A dark matter NFW halo of virial mass 10^{12} $M_\odot$, following a standard concentration-mass relation, is expected to have a maximum circular speed around 170 km s^{-1}, with a value of about 120 km s^{-1} at our typical $R_{\rm out}$, much larger than the velocities observed in our sample. Thus, our data can safely exclude the 'failed' Milky Way scenario as an origin for our gas-rich UDGs.

Actually, the fact that our galaxies have a baryon fraction close to the cosmological mean (see Fig. 3.9) suggests that they may reside in $\sim 10^{10}$ $M_\odot$ dark mater haloes[8], although this should be confirmed with a detailed mass decomposition and will be the subject of future work.

3.6.4 Ancient tidal dwarfs

Tidal dwarf galaxies (TDGs) are self-gravitating systems formed from the collapsed tidal debris of interacting galaxies. Because of this, one expects to find them inhabiting the chaotic environments near their progenitors, even after some Gyr (e.g. Duc et al. 2014; Lelli et al. 2015). In fact, TDGs in the nearby universe are usually found within 15 $R_{\rm e,p}$ of their progenitors ($R_{\rm e,p}$ being the effective radius of the progenitor, Kaviraj et al. 2012). As they form from pre-enriched material they are expected to show high metallicities (e.g. Duc & Mirabel 1998, but see also Hunter et al. 2000), and due to their weak gravitational potential they should be free of dark matter (see Hunter et al. 2000; Braine et al. 2001; Lelli et al. 2015 and references therein).

From an observational point of view, TDGs present some properties similar to those in our sample of UDGs. For instance, it has been argued that they are comparable in terms of effective radius and surface brightness (Duc et al. 2014). Perhaps more intriguingly, they also share dynamical properties: they lie off the BTFR and show dark matter fractions close to zero within their H I discs (Lelli et al. 2015). Given all this, it is pertinent to ask whether or not our gas-rich UDGs may be TDGs. In this Section we explain why we consider this scenario unlikely.

The strongest evidence against a tidal origin is the environment of our UDGs. They cannot be *young* tidal dwarfs given their totally different environments: they are isolated with the mean distances to their nearest, second-nearest and third-nearest neighbors being 1 Mpc, 1.4 Mpc and 1.7 Mpc, respectively. This is completely different from the expected progenitor-TDG separation of 15 $R_{\rm e,p}$,

[8]This comes from the fact that the cosmological baryon fraction $f_{\rm bar} = M_{\rm bar}/M_{\rm DM} \approx 0.16$, so a galaxy with a baryon fraction equal to $f_{\rm bar}$ should reside in a dark matter halo with $M_{\rm DM} = M_{\rm bar}/f_{\rm bar} \approx 6 M_{\rm bar}$.

which would typically be around 100 kpc. It would be required that *all* our galaxies formed as TDGs some Gyr ago, and the separation between all of them and the other interacting galaxy increased up to at least 1 Mpc, which seems unlikely (see also the text in Sec. 3.3.3).

One may also argue that we do not find remaining signs of tidal interactions around our galaxies, but this could be just because detecting such interactions is hard (e.g. Holwerda et al. 2011; Müller et al. 2019). Perhaps more importantly, from cosmological simulations one would expect TDGs to have smaller sizes than typical dwarfs (see the discussion in Haslbauer et al. 2019a), while UDGs are exactly the opposite, a population of galaxies with much larger optical radii than other dwarfs; Duc et al. (2014), however, argue that some old TDGs are larger than normal dwarfs.

Currently, our interpretation is that our galaxies live in $\sim 10^{10}$ $M_\odot$ dark mater haloes and the dark-matter deficiency is restricted to the extent of the H I disc. However, our current data cannot unambiguously distinguish between this scenario and one where our UDGs have very little, if any, dark matter in their whole extension, as expected in TDGs. The mass decomposition in our galaxies would then conclusively tell us if in fact there is room to accommodate (low-concentration) 10^{10} $M_\odot$ dark mater haloes or if their lack of dark matter is analogous to that in TDGs.

3.6.5 Weak feedback producing little mass losses

Different cosmological hydrodynamical simulations predict large mass loading factors in dwarf galaxies (e.g. Vogelsberger et al. 2013; Ford et al. 2014), although other theoretical studies show that big mass losses do not necessarily take place (see for instance Strickland & Stevens 2000; Dalcanton 2007; Emerick et al. 2018; Romano et al. 2019). Supporting this latter scenario, there is recent observational evidence (McQuinn et al. 2019, see also Lelli et al. 2014b) that the mass loading factors in dwarf galaxies are indeed relatively small, as often the outflows do not reach the virial radii of the galaxies and are kept inside their haloes, available for the regular baryon cycle. These results suggest that some dwarfs may have baryon fractions larger than expected, qualitatively in agreement with our gas-rich UDGs with 'no missing baryons'.

In this chapter, along with Chapter 2, we suggest that a scenario where feedback processes in our UDGs have been relatively weak and inefficient in ejecting gas out of their virial radii could explain their quiescent ISM (inferred from the velocity dispersion) and high baryon fractions (as derived from the BTFR). In Fig. 3.9, we found a significant trend for low-mass galaxies ($15 \text{ km s}^{-1} < V_{\rm circ} < 45 \text{ km s}^{-1}$) where they deviate more from the canonical BTFR, towards higher masses (and thus have a larger baryon fraction), if they have large disc scale lengths. As most of these galaxies have normal or low SFRs with respect to their stellar masses (e.g. Teich et al. 2016; L17, but more robust measurements would be desirable), their large disc scale lengths then imply that they have lower-than-average (about an order of magnitude) SFR

surface densities, and we speculate that this affects their capability to drive outflows powerful enough to eject baryons out of their virial radius, and thus allowing the galaxies to retain a higher-than-average baryon fraction. Recently, using high-resolution hydrodynamical simulations, Romano et al. (2019) have shown, for a ultra faint dwarf galaxy, that this indeed may be the case: the gas removal of a galaxy depends on the distribution of supernovae explosions and thus on the distribution of star formation. Those authors find that the more evenly spread or 'diluted' the distribution of OB associations is, the higher is the gas fraction that the galaxy keeps, in agreement with our interpretation.

3.7 Conclusions

In this chapter we present the 3D kinematic models of six dwarf gas-rich ultra-diffuse galaxies (UDGs). By analysing VLA and WSRT 21-cm observations with the software ^{3D}Barolo, we derive reliable measurements of the circular speed and gas velocity dispersion of our sample galaxies. Our models have been used by Chapter 2 to show that the galaxies lie significantly above the baryonic Tully-Fisher relation.

Our main findings can be summarised as follows:

- We have shown that the kinematic models are robust (Fig. 3.1-3.8) and our galaxies have circular speeds of $20 - 40$ km s^{-1}.
- Our UDGs exhibit low gas velocity dispersions, lower than observed in most dwarf irregular galaxies before. Their H I layers have the typical thicknesses observed in other dwarfs and disc galaxies, and gas turbulence appears to be fed by supernovae with efficiencies of just a few percent.
- We have reviewed the canonical baryonic Tully-Fisher relation, showing that these gas-rich UDGs are likely not the only outliers, although they may represent the most extreme cases (Fig. 3.9).
- At circular speeds below ≈ 45 km s^{-1} the vertical deviation from the canonical baryonic Tully-Fisher relation correlates with the disc scale length of the galaxies (Fig. 3.9).
- The low velocity dispersions observed in our sample seem at odds with models where UDGs originate from feedback-driven outflows. Our galaxies tend to have larger scale lengths than the simulated NIHAO UDGs and to have higher baryon fractions, but they share some other structural properties. The most important discrepancy is that, unlike NIHAO simulated UDGs, our galaxies have little dark matter in the inner regions (within $\sim 2R_{\rm e}$).
- We find indications that the gas specific angular momentum of our sample is similar or slightly lower than that in other galaxies of similar H I mass.

However, the specific angular momentum of the stellar component may be (a factor ≈ 3) higher-than-average at given M_* (Fig. 3.11). This can help to explain the large optical scale length of UDGs.

- The measured low circular speeds rule out the possible origin as 'failed' Milky Way galaxies for our UDGs.
- Fully testing the idea that all our six galaxies are old tidal dwarf galaxies is not possible with our observations, but their isolation seems to go against this possibility.
- To explain the high baryon fractions and low turbulence in the discs, in Chapter 2 we have suggested that these galaxies experienced 'weak' feedback, allowing them to retain all of their baryons. Here we have shown that this idea is consistent with our findings: the larger the optical disc scale length of dwarf galaxies is, the more they depart from the canonical baryonic Tully-Fisher relation towards higher baryonic masses. Their extended optical sizes coupled with normal star formation rates result in very low star formation rate surface densities, impacting their capability to lose mass via outflows.

3.A WSRT vs. VLA data

As mentioned in the main text, two galaxies in our sample, AGC 122966 and AGC 334315, have both VLA and WSRT data. Given the spatial resolution and S/N of the data, we adopt as our 'fiducial' data the WSRT observations for AGC 122966 and the VLA observations for AGC 334315. Here we delve into the reasons in which we based these choices, and we show the complementary data: the VLA data for AGC 122966 as well as the WSRT data for AGC 334315. We also make the comparison between the kinematic and geometrical parameters of the different data.

The VLA data cube of AGC 122966 has a lower S/N than the WSRT one. Moreover, the emission is less extended, and we have to oversample by a factor 2 in order to fit the galaxy with ^{3D}Barolo. Fig. 3.12 shows the stellar image, H I map, and observed and modelled velocity fields and PV diagrams. From inspecting the major-axis PV, we can see that the emission connecting approaching and receding sides is not detected. More importantly, it looks likely that there is emission missing at the end of the approaching and residing sides too, which would significantly affect the recovered value of the rotation velocity. In fact, while for the WSRT cube ^{3D}Barolo finds a projected velocity of 26 km s^{-1}, it finds 16 km s^{-1} for the VLA cube. Given all this, we decided to use the WSRT data for this galaxy (Fig. 3.2).

Despite the problems deriving the kinematics, we can still use the VLA data to independently estimate the inclination of the galaxy as described in the main text. Our method finds an inclination of $44° \pm 5°$ using the WSRT H I map and of $40° \pm 5°$ with the VLA data, meaning that the inclination estimates from the different data cubes are consistent with each other. The VLA data of AGC 122966 is not only useful to confirm our inclination measurements, but also because the morphology of the galaxy can be better appreciated without the elongated beam of the WSRT observations (Fig. 3.12). Finally, the models for the different cubes have the same systemic velocity and physical center.

On the other hand, for AGC 334315 the VLA data (Fig. 3.5) have better quality (although a factor 2 less extended) than the WSRT data, shown in Fig. 3.13: the spatial and spectral resolution are better, and the beam is more circular. With this, one can more clearly appreciate the H I structure as well as the intrinsic shape and velocity field of the galaxy. Apart from this, the parameters found for the two different data cubes are perfectly compatible with each other: we find an inclination of $45° \pm 5°$ for the VLA map and of $52° \pm 5°$ with the WSRT one, in agreement within the reported uncertainties. The final circular speed is also the same within the uncertainties: 25 km s^{-1} at 8.5 kpc for the VLA data, and 26 km s^{-1} at 18 kpc for the WSRT observations. The models for the different cubes share also the same systemic velocity and physical center.

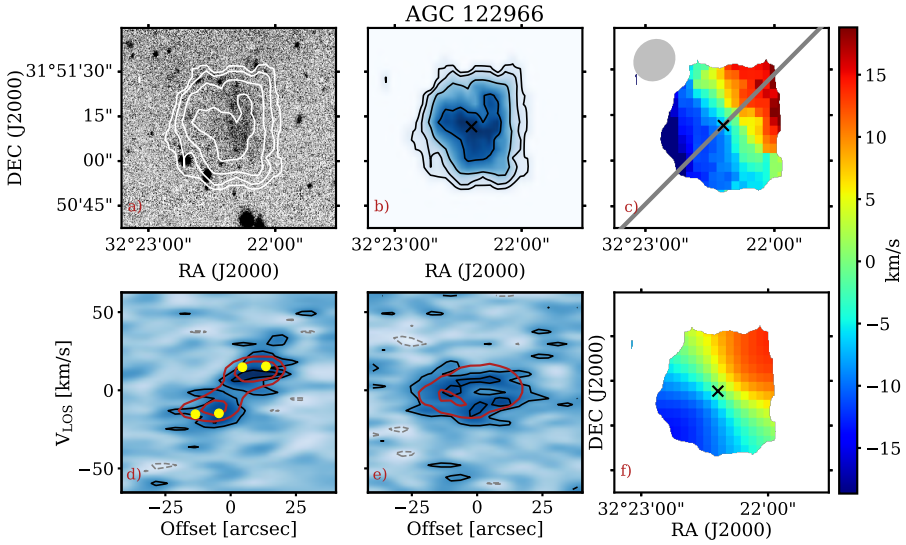

Figure 3.12: VLA data and kinematic models for AGC 122966. Panels and symbols as in Fig. 3.1. The H I contours are at 0.5, 1, 2 and 4×10^{20} atoms cm^{-2}.

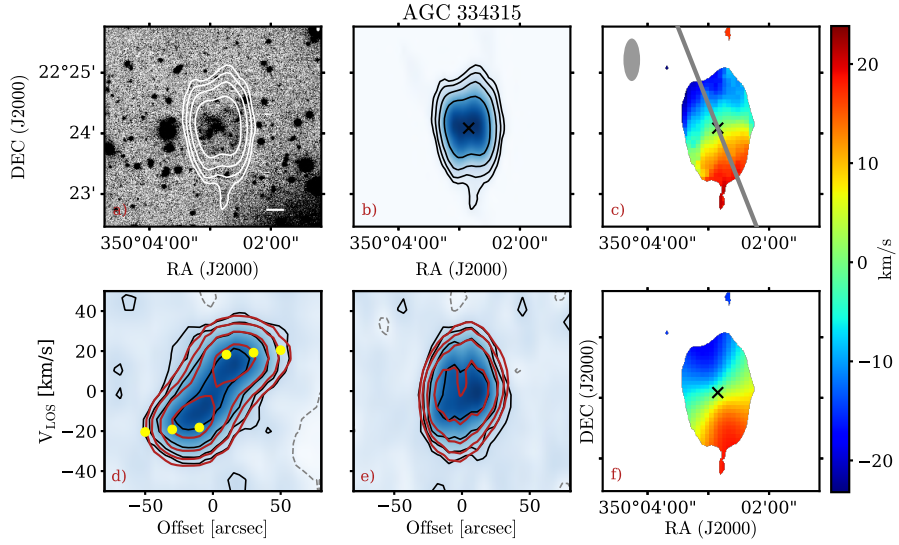

Figure 3.13: WSRT data and kinematic models for AGC 334315. Panels and symbols as in Fig. 3.1. The H I contours are at 0.35, 0.7, 1.4 and 2.8×10^{20} atoms cm^{-2}.

3.B Comparison samples

3.B.1 The BTFR

Fig. 3.9 shows the circular speed–baryonic mass plane, with galaxies scattering around the BTFR. The main result from the figure is that the region between our extreme UDGs and galaxies following the extrapolation of the SPARC BTFR at low masses, is populated by other dwarf galaxies. When discussing specific galaxies which are particularly interesting given their position with respect to the SPARC BTFR, we provide their coordinates on the $V_{\rm circ} - M_{\rm bar}$ plane.

SPARC

Within this sample (cyan circles in Fig. 3.9), two galaxies deviate significantly from the SPARC BTFR: UGC 7125 (65 km s^{-1}, $10^{9.86}$ M$_\odot$) and UGC 9992 (34 km s^{-1}, $10^{8.77}$ M$_\odot$).

UGC 7125 has an inclination of 90° and $Q = 1$, so its position seems robust, even though, as Lelli et al. (2016b) mention, the galaxy has a relatively large uncertainty on its mass due to a high distance-correction for Virgocentric infall.

UGC 9992 has an inclination of $30° \pm 10°$ and $Q = 2$. Its PV diagram (Swaters 1999) is regular and traces the flat part of the rotation curve. To bring this galaxy back to the BTFR an inclination of $\sim 17°$ would be needed. For this hypothetical inclination to be correct, an error of 13° in the measured inclination is needed, a bit larger than the quoted uncertainty of 10° but within 1.5σ. It is worth mentioning that two other galaxies with $i = 30° \pm 10°$ (F571-V1 and UGC 7261) lie much closer to the BTFR, as well as, for instance, the galaxies UGC 11914, UGC 6930 and UGC 10310, with $i = 31° \pm 5°, 32° \pm 5°$ and $34° \pm 6°$, respectively.

LITTLE THINGS

Most LITTLE THINGS galaxies lie around the extrapolation of the SPARC BTFR, even when some of their rotation curves have *not* clearly reached their flat part (see Iorio et al. 2017). DDO 50 (also known as UGC 4305 or Ho II) is an outlier, in a position very close to our UDGs (39 km s^{-1}, $10^{8.95}$ M$_\odot$). Its rotation curve has clearly reached the flat part but the inclination of the galaxy is relatively low, 30°. Different values have been proposed, ranging from 30° to 50° (see Oman et al. 2016; Iorio et al. 2017 and references therein), so the exact value of its circular speed remains somewhat uncertain. However, an inclination of $\sim 18°$ is needed for the galaxy to lie directly on the canonical BTFR, which is outside the wide range proposed in the literature.

IC 1613 (also known as DDO 8, not shown in Fig. 3.9), is another well known candidate to be an outlier from the BTFR with a baryonic mass of $10^{7.9}$ M$_\odot$ and rotation velocity of about 20 km s^{-1} (Oh et al. 2015; Oman et al. 2016). It is part of the LITTLE THINGS galaxies studied in Oh et al. (2015), but was excluded in the work of Iorio et al. (2017). While the galaxy is potentially interesting, there may be issues with its inclination and equilibrium state, as

mentioned in Read et al. (2017), Because of this, as in Iorio et al. (2017), we do not consider this galaxy in Fig. 3.9.

In the sample from Iorio et al. (2017), DDO 101 (59 km s^{-1}, $10^{7.94}$ $M_{\odot}$) stands out but for being an outlier that rotates too fast for its baryonic mass. However, Read et al. (2017) have demonstrated that this discrepancy is largely mitigated if the galaxy is farther away than the distance used in Iorio et al. (2017), so it is possible that the uncertainties in distance (and thus in baryonic mass) have been underestimated for this galaxy.

SHIELD

Due to the very low spatial resolution data the analysis of this sample was very challenging, as discussed in McNichols et al. (2016). Five out of twelve galaxies in the sample have rotation velocities estimated from fitting tilted-ring models to the observed low-spatial resolution velocity fields, and at least three of the resulting rotation curves have no indication of a flattening. The remaining velocities were derived from the visual inspection of different PV slices (see McNichols et al. 2016 for details). In addition to this, the asymmetric drift correction was not applied to the galaxies, and the inclination comes from optical data rather than from the H I itself. Despite these differences with other analyses, the twelve galaxies lie around the extrapolation of the canonical BTFR.

Edge-on HUDs

He et al. (2019) selected a sample of nearly edge-on HUDs that were not originally selected in the catalogue of L17 due to selection effects (given their high inclination the galaxies have apparent higher surface brightness). As the optical morphology indicates that the galaxies are edge-on, corrections for inclination are negligible. Their optical images, shown in He et al. (2019), suggest that their stellar structure is not exactly the same as in our sample, as theirs look more regular and thinner, but it is hard to unequivocally judge this as our sample is not edge-on. However, the stellar component of our sample is both more extended and of lower surface brightness.

Most of these galaxies (magenta diamonds in Fig. 3.9) show velocities nearly compatible with the SPARC BTFR. The clear outlier is AGC 202262, that shows the narrowest velocity width, with a rotation of about 30 km s^{-1}. An inclination of $\sim 40°$, totally incompatible with the optical image (but see the caveats on the optical-gas misalignment reported in Starkenburg et al. 2019 or Gault et al. 2021), would be required to put the galaxy on the canonical BTFR.

UGC 2162

UGC 2162 is a UDG which has been studied using ^{3D}Barolo in resolved GMRT observations (Sengupta et al. 2019). Two caveats exist regarding this galaxy. First, Sengupta et al. (2019) mention that it has large uncertainties in its baryonic mass (probably because of the uncertainty associated with its distance; the galaxy is much closer than those in our sample), and second, its rotation

curve is oversampled and does not show signs of flattening (the emission is less extended than in our data), although it is presumably close to reaching the flat part (see Fig. 2 in Oman et al. 2015).

While these caveats should be taken into account, the position of UGC 2162[9] in Fig. 3.9 (red hexagon) seems in line with our results. Note also that UGC 2162 is less 'extreme' than our UDGs: it is less massive, smaller and slightly brighter. Assuming that the amplitude of the rotation curve does not increase significantly beyond the outermost measured radius, the galaxy would need an inclination of $\approx 39°$ to be on the SPARC BTFR, far from the measured inclination of 55° in Sengupta et al. (2019).

3.B.2 Disc scale length and central surface brightness values

In Fig. 3.9 we study the deviation from the BTFR as a function of the disc scale length; the central surface brightness of the galaxies was also inspected. We have obtained these structural parameters from the following sources in the literature. For the SPARC galaxies, scale lengths are taken directly from Lelli et al. (2016a) and surface brightnesses from Verheijen (1997); de Blok (1997) and Swaters (1999). For LITTLE THINGS, scale lengths come from Read et al. (2016b) and surface brightnesses from Hunter et al. (2012). Regarding SHIELD, size and surface brightness come from Teich et al. (2016) and Haurberg et al. (2015), respectively. He et al. (2019) provides both size and surface brightness for their sample, and the values used for UGC 2162 come from Trujillo et al. (2017).

[9] UGC 2162 has no reported uncertainties in rotation velocity nor H I mass by Sengupta et al. (2019), so we assume an uncertainty of 7 km s^{-1} for the velocity (the spectral resolution of the data, which is also larger than the difference in the velocity obtained from the best-fit model of ^{3D}Barolo and the global H I profile) and a typical value of 20% in the H I mass.

Chapter 4

No need for dark matter: resolved kinematics of the ultra-diffuse galaxy AGC 114905

based on

– P. E. Mancera Piña, F. Fraternali, T. Oosterloo et al., 2022 –

Published in Monthly Notices of the Royal Astronomical Society, MNRAS 512, 3230

Abstract

We present new H I interferometric observations of the gas-rich ultra-diffuse galaxy AGC 114905, which previous work, based on low-resolution data, identified as an outlier of the baryonic Tully-Fisher relation. The new observations, at a spatial resolution ~ 2.5 times higher than before, reveal a regular H I disc rotating at about 23 km s^{-1}. Our kinematic parameters, recovered with a robust 3D kinematic modelling fitting technique, show that the flat part of the rotation curve is reached. Intriguingly, the rotation curve can be explained almost entirely by the baryonic mass distribution alone. We show that a standard cold dark matter halo that follows the concentration-halo mass relation fails to reproduce the amplitude of the rotation curve by a large margin. Only a halo with an extremely (and arguably unfeasible) low concentration reaches agreement with the data. We also find that the rotation curve of AGC 114905 deviates strongly from the predictions of Modified Newtonian dynamics. The inclination of the galaxy, which is measured independently from our modelling, remains the largest uncertainty in our analysis, but the associated errors are not large enough to reconcile the galaxy with the expectations of cold dark matter or Modified Newtonian dynamics.

4.1 Introduction

The properties, origin, and formation mechanisms of ultra-diffuse galaxies (UDGs) have been widely discussed in the last years. UDGs (van Dokkum et al. 2015) are low surface brightness galaxies (e.g. Impey et al. 1988, see also discussion in Conselice 2018) with an extended light distribution. At fixed stellar mass or luminosity, UDGs have significantly larger effective radii than the 'classical' dwarf galaxy population (e.g. van Dokkum et al. 2015; Mihos et al. 2015; Mancera Piña et al. 2019a; Chamba et al. 2020).

UDGs are mostly found by number in massive galaxy clusters, but they are also present in galaxy groups, in the field, and even in voids (e.g. van der Burg et al. 2016; Leisman et al. 2017; Román & Trujillo 2017b; Mancera Piña et al. 2019a; Román et al. 2019; Barbosa et al. 2020; Karunakaran et al. 2020). The ubiquity of UDGs across different environments indicates that even if some of them form due to environmental processes, this is not the case for all UDGs, and they can also form due to their own internal processes. The population of UDGs is likely a mixed bag of galaxies with similar sizes and surface brightness, but perhaps multiple formation mechanisms.

The above idea seems confirmed by a number of results from semi-analytic models and hydrodynamics simulations that produce UDG-like simulated galaxies based on different physical processes. On the one hand, different authors report that classical dwarf galaxies can become UDGs (i.e. increase their size and likely decrease their surface brightness) due to cluster pre-processing phenomena such as tidal striping and tidal heating (Carleton et al. 2019; Tremmel et al. 2020; Sales et al. 2020). On the other hand, it has also been suggested that internal processes can explain the optical properties of UDGs. Amorisco & Loeb (2016) proposed a model where UDGs form due to a higher than average dark-matter angular momentum, which then gives rise to an extended stellar effective radius (see also Rong et al. 2017). Here it is worth mentioning that even if UDGs inhabit normal dark matter haloes, they could still have a higher than average retained fraction of stellar specific angular momentum (Posti et al. 2018a). Another idea is that UDGs are dwarfs that became larger due to feedback-driven outflows, which change the dark matter and baryonic potential and allow the stars to migrate to more external orbits, increasing their effective radius (Di Cintio et al. 2017; Chan et al. 2018). It has also been argued that the expansion of the stellar orbits can be the result of massive mergers at early ($z > 1$) epochs (Wright et al. 2021) or the by-product of very efficient globular cluster feedback (Trujillo-Gomez et al. 2022).

While the above models and simulations seem to produce simulated galaxies that match a number of properties of real UDGs, surprising observations of two different populations of UDGs have been more challenging to reproduce. First, it has been found that two gas-poor UDGs (DF−2 and DF−4) near (at least in projection) the galaxy NGC 1052, contain significantly less dark matter than expected based on stellar and globular cluster kinematics (e.g. van Dokkum et al.

2018, 2019; Danieli et al. 2019; Emsellem et al. 2019). While caveats regarding the distance and accuracy of the kinematic tracers used to study these UDGs have been raised (e.g. Laporte et al. 2019; Trujillo et al. 2019), DF−2 and DF−4 have motivated multiple studies aiming to explain the existence of dark-matter free galaxies. The main ideas to explain their existence involve dark matter removing mechanisms such as high-velocity collisions and tidal stripping, or a tidal dwarf origin (Haslbauer et al. 2019b; Silk 2019; Montes et al. 2020; Shin et al. 2020; Doppel et al. 2021; Jackson et al. 2021).

The second set of puzzling observations, still very much lacking a quantitative explanation, is related to the H I kinematics of some gas-rich UDGs (sometimes also called H I-bearing UDGs). Using unresolved ALFALFA data (see Haynes et al. 2018), Leisman et al. (2017, see also Jones et al. 2018; Karunakaran et al. 2020) first found that gas-rich UDGs have narrow global H I profiles for their gas mass. Then, in Chapters 2 and 3 (i.e. Mancera Piña et al. 2019b, 2020) we studied a set of six of those gas-rich UDGs with low-resolution (two independent resolution elements per galaxy side) interferometric H I observations. Using a state-of-the-art kinematic modelling fitting technique (^{3D}Barolo, Di Teodoro & Fraternali 2015) to overcome beam smearing effects, they recovered the circular speeds of their galaxies, unveiling two intriguing features. First, that having a baryonic mass a factor $10 - 100$ larger than galaxies with similar circular speed, H I-rich UDGs shift off the baryonic Tully-Fisher relation (BTFR, McGaugh et al. 2000), with the offset from the BTFR correlating with the UDGs optical disc scale lengths. And second, that their dynamical mass within the extent of the H I disc is about the same as their baryonic mass, meaning that the galaxies have very low dark matter fractions within scales as large as 10 kpc. These features suggest that gas-rich UDGs have atypical non-luminous mass distributions, making them a promising population to test dark matter theories. It is also important to stress that these gas-rich UDGs are selected to be fairly isolated (Leisman et al. 2017), and they lie at distances of several tens of Mpc where Hubble flow distances are robust, negating some of the main concerns raised for DF−2 and DF−4.

Given all this, it is important to further characterise the properties of these UDGs, which are apparently gas-rich but also dark-matter poor (at least within the observed radii). One way to do this is by studying their H I rotation curves, as H I provides arguably the best kinematic tracer for disc galaxies, both massive and dwarfs (e.g. Begeman 1987; de Blok et al. 2008; Iorio et al. 2017).

In this chapter, we present and analyse new, high-resolution interferometric observations of one of these peculiar gas-rich UDGs, AGC 114905. As we will show, the galaxy seems to pose a challenge to the currently favoured galaxy formation framework. This chapter is organised in the following way. In Sec. 4.2, we describe the main properties of AGC 114905 and we present the data used in this work. In Sec. 4.3 we show the kinematic modelling of the galaxy, and in Sec. 4.4 the resulting mass models. We discuss our results in Sec. 4.5, to then present our conclusions and summary in Sec. 4.6.

4.2 Data and properties of AGC 114905

AGC 114905 (01:25:18.60, +07:21:41.11, J2000) lies at a (Hubble-flow) distance $D = 76 \pm 5$ Mpc (Leisman et al. 2017). The stellar distribution of AGC 114905, consists of an exponential disc with a disc scale length $R_{\rm d} = 1.79 \pm 0.04$ kpc. The left panel of Fig. 4.1 shows its $r-$band stellar image. The galaxy has a relatively blue colour, $(g - r) = 0.3 \pm 0.1$ (Chapter 3; Gault et al. 2021). We estimate the stellar mass (M_*) of the galaxy using the mass-to-light-colour relation from Du et al. (2020), which has been recently calibrated using a large sample of low surface brightness galaxies. We obtain $M_* = (1.3 \pm 0.3) \times 10^8$ M$_\odot$; this is slightly smaller than the value used in Chapters 2 and 3, owing to the different mass-to-light-colour calibrations.

We gathered H I data of AGC 114905 at different resolutions, obtained with the Karl G. Jansky Very Large Array. Specifically, we collected data from the D-, C- and B-array configurations. Details on the D and C configuration observations (PI: Leisman, ID 17A-210) can be found in Leisman et al. (2017) and Gault et al. (2021). The new B-array observations (PI: Mancera Piña, ID 20A-095) were obtained between July and October 2020. 40 hours were observed (about 34 hours on-source) and combined with the existing C- and D-array observations. The data reduction was done with the software `Miriad` (Sault et al. 1995) following standard procedures, using a robust weighting of 0.75 to make the final data cube, which results in a cleaned beam of size 7.88 arcsec × 6.36 arcsec. After Hanning-smoothing, our final cube has a rms noise per channel of about 0.26 mJy/beam and a spectral resolution of 3.4 km s^{-1}.

The peak H I column density is $8.4{\times}10^{20}$ atoms cm^{-2}, and the noise level is $4.1{\times}10^{19}$ cm^{-2}. The integral flux of the total H I map is 0.73±0.07 Jy km s^{-1}, close to the value of 0.78 Jy km s^{-1} used in Chapter 2, although lower than the 0.96 ± 0.04 Jy km s^{-1} reported by Leisman et al. (2017) from unresolved ALFALFA observations. At the distance of AGC 114905, our integral flux yields $M_{\rm HI} = (9.7 \pm 1.4) \times 10^8$ M$_\odot$.[1]

We combine $M_{\rm HI}$ and M_* to obtain the baryonic mass $M_{\rm bar} = 1.33 M_{\rm HI} + M_* = (1.4 \pm 0.2) \times 10^9$ M$_\odot$. The factor 1.33 accounts for the presence of helium, and we neglect any contribution of molecular gas, whose mass is expected to be negligible compared to $M_{\rm HI}$ (e.g. Hunter et al. 2019; Wang et al. 2020). The galaxy gas fraction $f_{\rm gas} = M_{\rm gas}/M_{\rm bar} \approx 0.9$, ensures that $M_{\rm bar}$ is robust against possible systematics related to M_*, since the main uncertainty in $M_{\rm gas}$ comes from the distance, which is well constrained.

The total H I map of the galaxy is shown in the middle panel of Fig. 4.1, and also on the left panel with the H I contours overlaid on top of the stellar emission. It is clear that the gas extends well beyond the optical emission, despite UDGs being optically extended. There is also some degree of misalignment between the optical and H I position angles (see also Gault et al. 2021), although the optical morphology is likely affected by bright, patchy star formation regions.

[1]The ALFALFA flux would instead imply $M_{\rm HI} \approx 1.3 \times 10^9$ M$_\odot$, only strengthening the results shown below.

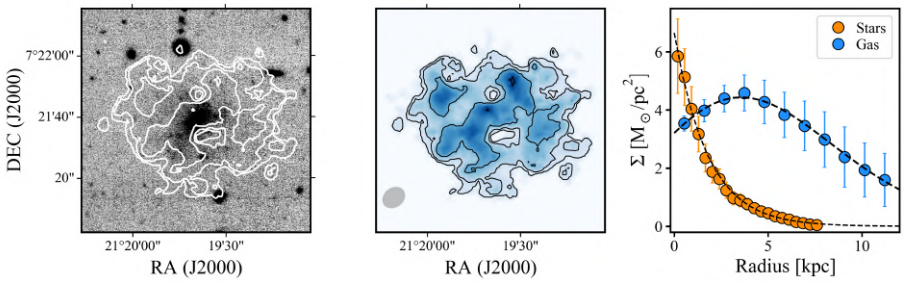

Figure 4.1: *Left:* Stellar image of AGC 114905 with the total H I contours overlaid. The contours are at 1, 2, 4×10^{20} atoms cm^{-2}, the noise level is 4.1×10^{19} atoms cm^{-2}. *Middle:* Total H I intensity map; contours as in the previous panel. The grey ellipse shows the beam of our data. *Right:* Stellar (orange) and gas (blue, includes helium correction) surface mass density profiles of AGC 114905. The dashed black lines on top show the fits to the distributions used to obtain the stellar and gas circular speeds (see Sec. 4.4).

The right panel of Fig. 4.1 shows the surface mass density profiles of the stellar and gaseous discs of AGC 114905. The stellar profile comes from converting our optical surface brightness profiles into mass density using a mass-to-light ratio in the $r-$band of 0.47 $M_\odot/L_\odot$ (Du et al. 2020). The gas profile is obtained using the `gipsy` (van der Hulst et al. 1992) task ELLPROF, and converted to mass density using the conversion factor 1 $M_\odot$ pc^{-2} = 1.25×10^{20} atoms cm^{-2}. Once this conversion is applied, we multiply by the factor 1.33 to account for the presence of helium.

4.3 Kinematics

In order to obtain reliable kinematic information (rotation velocity and velocity dispersion) for our galaxy, we use the software ^{3D}Barolo (Di Teodoro & Fraternali 2015). As extensively explained in Di Teodoro & Fraternali (2015), Di Teodoro et al. (2016), and Iorio et al. (2017), ^{3D}Barolo builds 3D realisations of tilted-ring models of a galaxy data cube, which are then convolved with the beam of the observations and compared channel by channel with the real data. This allows for a robust recovery of the rotation curve and gas velocity dispersion, since the method largely mitigates the effects of beam smearing (Bosma 1978; Begeman 1987; Swaters 1999; Di Teodoro & Fraternali 2015).

Before delving into the details and results of our modelling, we will briefly discuss the observed kinematics as well as the derivation of two important geometrical parameters: the position angle of the galaxy and its inclination.

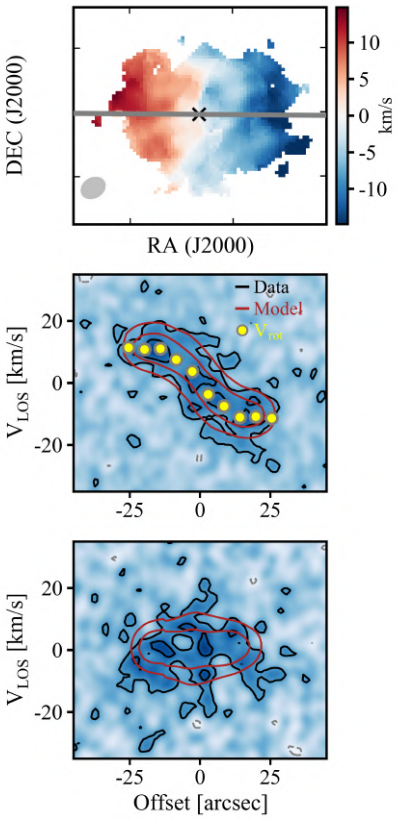

Figure 4.2: *Top:* Observed velocity field (same physical scale as the total H I map in Fig. 4.1); the grey ellipse shows the beam of the observations, the grey line the kinematic major axis, and the black cross the kinematic centre. *Middle (Bottom):* Major (minor)-axis PV diagram; data are shown in blue background and black contours (grey for negative values), and the best-fitting ^{3D}Barolo azimuthal model in red contours. The yellow points show the recovered rotation velocities.

4.3.1 Velocity field and geometrical parameters

The velocity field (1st moment map) of AGC 114905, shown in the top panel of Fig. 4.2, has the clear kinematic pattern of a regularly rotating disc. The position angle of the velocity field is estimated by trial and error as the angle that maximises the amplitude of the major-axis position-velocity (PV) diagram (e.g. Chapter 3). We find a position angle of 89°, as shown in Fig. 4.2 with a line on top of the velocity field. Our value is similar to the 84° reported in Chapters 2 and 3 derived from the less resolved data. If we fit the position angle during our kinematic modelling (see below) we find values between $85 - 92°$ depending on our initial estimates. The middle (bottom) panel of Fig. 4.2 shows, in blue background and black contours, the PV diagram along the major (minor) axis of AGC 114905. The major-axis PV shows the typical pattern of a rotating disc and seems to reach a flat velocity in the outer regions.

While differences of a few degrees in the position angle do not significantly affect the final rotation curve, the inclination of the galaxy is more critical, as small changes at low inclinations can severely affect the value of the deprojected rotation curve. Undoubtedly, the inclination is the main uncertainty in our

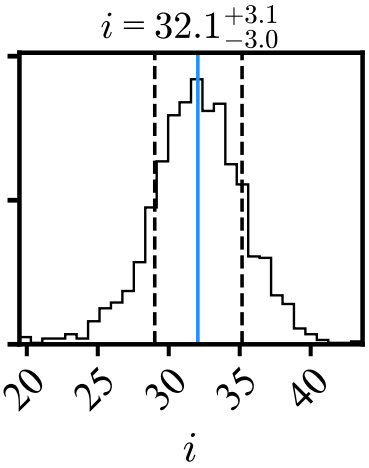

Figure 4.3: MCMC posterior distribution of the inclination of AGC 114905. The central value, shown in blue, is the median of the distribution, while the uncertainties represent the difference between the median and the 16^{th} and 84^{th} percentiles (dashed black lines). See Sec. 4.3.1 for details.

kinematic modelling and results, and we pay special attention to it. Traditionally, the inclination of high-resolution data can be obtained during the kinematic fitting using the velocity field (e.g. de Blok et al. 2008). However, this method is not particularly robust as it depends on the shape of the rotation curve: for solid-body rotation the iso-contours on the velocity field are parallel, nullifying the power to measure the inclination. Given the above, and following Chapter 3, we decide to estimate the inclination with an approach that is independent of the kinematics, relying only on the H I map of the galaxy.

Our method works as follows. We use ^{3D}Barolo to build azimuthal models of the galaxy at different inclinations, with these inclinations being drawn from a flat prior distribution between $10° - 80°$ and sampled using a Markov chain Monte Carlo (MCMC) routine (based on the Python package `emcee`, see Foreman-Mackey et al. 2013). Each model is convolved with the beam of the observations, and its total intensity map is built. We then compare these model intensity maps with the real data, with our MCMC routine minimising the absolute residuals between model and observed intensity maps. We have tested this method extensively using artificial data cubes matching our resolution and signal-to-noise (S/N), finding it robust and reliable (see also Fraternali et al. 2021). In the end, we find an inclination of $32 \pm 3°$ for AGC 114905, which we adopt as our fiducial value; the posterior distribution is shown in Fig 4.3.

As an extra check, we also estimated the inclination in two other ways[2]. First, using the method described in Chapter 3, which is equivalent to our method described above but independent of the MCMC sampling. We find an inclination of $34 \pm 5°$, although the quoted uncertainty is just an expected mean value rather than a well defined statistical uncertainty. Similarly, in Chapters 2 and

[2]The optical inclination, derived from the optical axis ratio, is around 45°. We do not use this inclination in our analysis as it is not clear if the optical data follows the H I emission (see also e.g. Gault et al. 2021; Kado-Fong et al. 2021), but we provide the value for completeness. Clearly, this inclination would lower the value of the circular speed, strengthening our results.

3 we found an inclination of $33 \pm 5°$ from their lower-resolution data. Second, we derive kinematic-dependent inclinations. We use both ^{3D}Barolo (fitting the whole data cube) and the `gipsy` task ROTCUR (fitting the velocity field). Depending on the exact initial value, mask, and ring separation, both methods find inclinations between $30° - 37°$. It is reassuring that despite not being our favoured approaches to measure the inclination, we find these different values consistent with the results of our preferred method. Overall, it is important to highlight that we do not find any evidence favouring inclinations lower than 30°.

Finally, it is worth mentioning that while deriving the inclination we assume that the H I resides on a razor-thin disc, a significant thickness of the disc would imply a higher inclination than what we have derived due to projection effects (Iorio 2018). From this point of view $32 \pm 3°$ gives a lower limit on the inclination of AGC 114905 (see also Sec 4.5.4). On the other hand, if the gas disc is non-axisymmetric, but instead has some intrinsic elongation, we could be overestimating its inclination. While some simulations suggest this is possible[3], in what follows we assume that the observed H I total intensity map and velocity gradient correspond to an inclined axisymmetric disc galaxy with gas moving in circular orbits.

4.3.2 Kinematic modelling

With the position angle and inclination determined, we proceeded to perform our kinematic modelling with ^{3D}Barolo, leaving as free parameters the systemic velocity ($V_{\rm sys}$), the rotation velocity ($V_{\rm rot}$), and the velocity dispersion ($\sigma_{\rm HI}$). We fit an azimuthal model and we use a ring separation of 6 arcsec. This represents a minor oversampling of less than 10 percent with respect to the size of the beam along the major axis of the galaxy (6.5 arcsec), allowing us to trace the rotation curve of the galaxy with five, basically uncorrelated, resolution elements per galaxy side. We also check that the rotation velocities obtained using four or five rings (see below) are well consistent with each other.

We first perform an iteration where $V_{\rm sys}$ is a free parameter. The best $V_{\rm sys}$ turns out to be 5435 km s^{-1}, which matches the centre of a Gaussian fit to the global H I profile. For our final model we keep this $V_{\rm sys}$ fixed and we only fit $V_{\rm rot}$ and $\sigma_{\rm HI}$. The final model faithfully reproduces the observations. This can be seen in the middle and bottom panels of Fig. 4.2, where we compare the PV diagrams of the best-fitting model (red) and data (black). There are some low−S/N features at low velocities ($\lesssim 5$ km s^{-1}) not reproduced, but ^{3D}Barolo closely mimics the overall kinematics of the galaxy. This can also be seen in Appendix 4.A, where we show representative channel maps of AGC 114905 and of our best-fitting model. The resulting rotation curve, uncorrected for inclination, is shown as yellow points overlaid on top of the major-axis PV

[3]Marasco et al. (2018) have reported that about half of the massive dwarf galaxies ($60 < V_{\rm max} < 120$ km s^{-1}, with $V_{\rm max}$ the maximum rotation velocity) in the APOSTLE simulations (Sawala et al. 2015; Fattahi et al. 2016) inhabit dark matter haloes with intrinsic axis ratios $b/a < 0.8$; if the disc of AGC 114905 has a similar intrinsic b/a (i.e. it is an elongated disc instead of an inclined circular disc) its inclination could be as low as 10°.

diagram of Fig. 4.2, and it is clear that it reaches its flat part well before our outermost radius. To take into account pressure-supported motions, we apply the asymmetric drift correction to our rotation curve (see Iorio et al. 2017), ending up with the circular speed V_c. The correction is found to be very small, contributing less than 2 km s^{-1} at all radii.

In Fig. 4.4, we explicitly show the circular speed profile of AGC 114905, as well as its velocity dispersion profile. The uncertainties in V_c include the uncertainties in the inclination, by means of a Monte Carlo sampling approach as detailed in Chapter 3. The flat part of the circular speed profile has a velocity of $\simeq 23$ km s^{-1}. This, together with the M_{bar} of the galaxy, confirms its position as an outlier of the BTFR. In Fig. 4.4 we also include for comparison the values for V_c and σ_{HI} obtained in Chapters 2 and 3 at lower resolution, showing the good agreement between them and our new determinations. This is important not only for AGC 114905, but for all the UDGs in Chapters 2 and 3, as it is a direct validation of the lower-resolution results presented previously.

4.3.3 Local and global disc stability

With a median value of ~ 5 km s^{-1}, the velocity dispersion σ_{HI} of AGC 114905 is slightly below the average value in rotation-supported dwarfs (~ 8 km s^{-1}, e.g. Iorio et al. 2017) although consistent within the uncertainties. The low values of V_c and σ_{HI} of our UDG imply a relatively low value of the Toomre parameter $Q_{gas} = \kappa\sigma_{HI}/(\pi G\Sigma_{gas})$, with κ the epicycle frequency (Toomre 1964). The Q_{gas} profile shows a slight decrease with radius, with a median (mean) value of 0.95 (1.6), after applying a small correction to account for thickness, see Romeo 1994; Romeo & Falstad 2013). The uncertainties are relatively large (typically a factor $2-3$), but these values of Q_{gas} suggest that the galaxy could be susceptible to *local* instabilities (see Romeo & Falstad 2013 and references therein for a detailed discussion on the interpretation of Q_{gas}). While these local instabilities may lead to fragmentation and subsequent star formation, observations suggest this is not always the case (Hunter et al. 1998; Leroy et al. 2008; Elmegreen & Hunter 2015). The value of Q_{gas} for AGC 114905 is lower on average but consistent within 2σ with the median values of LITTLE THINGS dwarf galaxies (Iorio et al. 2017). Finally, it should be noted that a more detailed calculation that takes into account the gas disc flaring (e.g. Elmegreen & Hunter 2015; Bacchini et al. 2020b) would increase the value of Q_{gas}, especially in the outer parts.

While Q_{gas} is in principle only related to local instabilities, we can also investigate the *global* disc stability of our UDG. The ordered kinematics seen in Fig. 4.2 and the isolation of the galaxy (see Chapter 3) strongly suggest an equilibrium state. We further tested this by allowing ^{3D}Barolo to fit radial motions overlaid on the rotation, but we did not find evidence of such radial motions as their amplitude is always consistent with zero within the uncertainties. We also computed the global stability parameter $X_2 = \kappa^2 R/(4\pi G\Sigma_{gas})$ (Toomre 1981), finding a median of 1.2 and with X_2 being smaller than 1 (0.9) only at

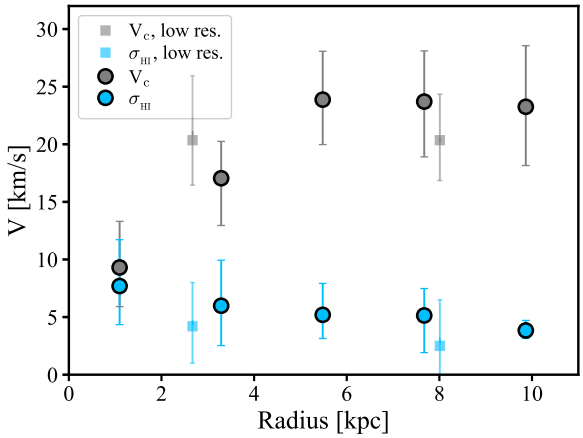

Figure 4.4: Circular speed (grey circles) and velocity dispersion (blue circles) profiles of AGC 114905, as obtained with our kinematic modelling. Squares show previous results obtained at a lower spatial resolution.

the outermost radius, suggesting the system is stable against bar instabilities ($X_2 \lesssim 1$ is the instability condition often used for dwarf galaxies, see e.g. Mihos et al. 1997; Hidalgo-Gámez 2004).

Overall, these investigations show that it is reasonable to assume that the cold gas in AGC 114905 is in closed orbits tracing its gravitational potential and allowing us to build mass models based on the derived rotation curve.

4.4 Mass modelling

4.4.1 A baryon-dominated rotation curve

AGC 114905 has a baryonic mass much higher than other dwarf galaxies with similar circular speeds (Iorio et al. 2017; Chapter 3). It is therefore interesting to see if AGC 114905, like most dwarfs, is dominated by dark matter at all radii.

Prior to obtaining any mass model, we can compare the circular speed profile of the galaxy with the circular speed profile of the baryonic distribution ($V_{\rm bar}$), which is simply the sum in quadrature of the contributions of the stellar and gas discs, this is $V^2_{\rm bar} = V^2_* + V^2_{\rm gas}$. We derive $V_{\rm c,*}$ and $V_{\rm c,gas}$ using the software GALPYNAMICS (Iorio 2018). GALPYNAMICS[4] takes as input the mass density profile of a given component, fitted with an appropriate function (see below), computes its gravitational potential via numerical integration, and returns the associated circular speed.

In the case of the stellar disc, we use an exponential profile with $M_* = 1.3 \times 10^8$ M$_\odot$ and an exponential disc scale length $R_{\rm d} = 1.79$ kpc; this profile can be compared with the data in Fig. 4.1. We assume a sech^2 profile along the vertical direction, and a constant thickness $z_{\rm d} = 0.196 R_{\rm d}^{0.633} \approx 280$ pc, as found in low-inclination star forming galaxies (Bershady et al. 2010).

[4] https://github.com/giulianoiorio/galpynamics

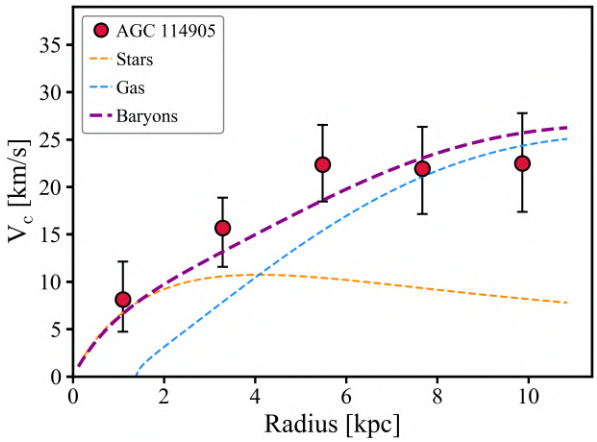

Figure 4.5: Circular speed profile of AGC 114905 (red points) compared to the contribution expected from stars (orange line), gas (blue line), and baryons (stars plus gas, magenta line).

For the gas component (H I plus helium), we fit the density profile with a profile of the form

$$\Sigma_{\rm gas} = \Sigma_{0,\rm gas} e^{-R/R_1} (1 + r/R_2)^{\alpha} \ , \tag{4.1}$$

where $\Sigma_{0,\rm gas}$ is the gas central surface density, R is the cylindrical radius, and R_1, R_2, and α are the fitting parameters (equal to 3.2 $\rm M_\odot/pc^2$, 1.1 kpc, 16.5 kpc, and 18, respectively). This profile provides a good fit to the observations, as seen in Fig. 4.1. For the vertical structure of the gaseous disc we assume a Gaussian profile and a constant vertical scale-height $z_{\rm d} = 250$ pc. It is worth mentioning that the results we show below do not depend significantly on the assumed thickness of the stellar or gaseous discs.

Fig. 4.5 shows the contribution of V_*, $V_{\rm gas}$, and $V_{\rm bar}$ to the total $V_{\rm c}$ of AGC 114905. Remarkably, $V_{\rm bar}$ provides a reasonable description of $V_{\rm c}$ at all radii. This implies that as opposed to classical dwarf galaxies (e.g. Iorio et al. 2017; Read et al. 2017), the dynamics of AGC 114905, at least within the observed radii extending to about 10 kpc, are baryon-dominated rather than dark-matter dominated. This was already postulated in Chapter 2, but it is now confirmed with a well traced rotation curve.

4.4.2 Fitting cold dark matter haloes

In our current framework of galaxy formation, we expect every galaxy to be embedded in a cold dark matter (CDM) halo. Because of this, it is relevant to investigate whether or not physically motivated CDM haloes can be consistent with our rotation curve, even if Fig. 4.5 suggests the absence of a dynamically significant halo in AGC 114905. We aim to find a dark matter halo whose

circular speed $V_{\rm DM}$ meets

$$V_{\rm c}^2 = V_*^2 + V_{\rm gas}^2 + V_{\rm DM}^2 \ . \tag{4.2}$$

Dark matter haloes are often described with the so-called NFW profile (Navarro et al. 1997), whose density as a function of the spherical radius in cylindrical coordinates r ($r = \sqrt{R^2+z^2}$) is given by

$$\rho_{\rm NFW}(r) = \frac{4\rho_{\rm s}}{(r/r_{\rm s})(1+r/r_{\rm s})^2} \ , \tag{4.3}$$

where $r_{\rm s}$ is a 'scale radius' and $\rho_{\rm s}$ is the density at $r_{\rm s}$. We will denote the corresponding mass profile as $M_{\rm NFW}(r)$:

$$M_{\rm NFW}(<r) = \frac{M_{200}}{\ln(1+c_{200}) - \frac{c_{200}}{1+c_{200}}} \left[\ln\left(1+\frac{r}{r_{\rm s}}\right) - \frac{r}{r_{\rm s}}\left(1+\frac{r}{r_{\rm s}}\right)^{-1} \right] \ . \tag{4.4}$$

The parameter M_{200} is defined as the mass within a sphere with radius r_{200} within which the average density is 200 times the critical density of the universe, while the concentration c_{200} is defined as $c_{200} = r_{200}/r_{\rm s}$.

While NFW haloes provide good descriptions for massive galaxies, this is not the case for dwarf galaxies (see Bullock & Boylan-Kolchin 2017). Therefore, for our UDG, we assume that the dark matter halo is described by a 'coreNFW' profile (Read et al. 2016a), which is an extension of the classical NFW profile that has the flexibility to develop -or not- a core. In Sec. 4.5.2 we discuss other halo profiles. The coreNFW profile has been found to fit very well rotation curves of dwarf galaxies, both real and simulated (Read et al. 2016a,b).

The density profile of the coreNFW halo can be written as

$$\rho_{\rm coreNFW}(r) = f^n \rho_{\rm NFW}(r) + \frac{n f^{n-1}(1-f^2)}{4\pi r^2 r_{\rm c}} M_{\rm NFW}(r) \ . \tag{4.5}$$

Here, $\rho_{\rm NFW}$ and $M_{\rm NFW}$ are the above NFW parameters, while f is a function (defined as $f = \tanh(r/r_{\rm c})$) that generates a core of size $r_{\rm c}$. In principle, $r_{\rm c}$ can be a fitting parameter, but as discussed in detail by Read et al. (2016a,b, 2017), fixing it to $r_{\rm c} = 2.94\ R_{\rm d}$[5] is in good agreement with simulations and observations where $r_{\rm c}$ is fitted as free parameter. Importantly, the factor 2.94 cannot be significantly larger as there is not enough energy from supernovae to create cores of size much larger than 2.94 $R_{\rm d}$ (see also e.g. Benítez-Llambay et al. 2019; Lazar et al. 2020; Trujillo-Gomez et al. 2022). The degree of transformation from cusp to core is described by the parameter n, with $n = 0$ defining a cuspy NFW profile and $n = 1$ a completely cored profile. The parameter n is defined as $n = \tanh(\kappa t_{\rm SF}/t_{\rm dyn})$, with $\kappa = 0.04$ a fixed parameter, $t_{\rm SF}$ the time whilst the galaxy has been forming stars (set to 14 Gyr), and $t_{\rm dyn}$ the NFW dynamical

[5]In principle, $r_{\rm c} = 1.75\ R_{\rm e}$, with $R_{\rm e}$ the half-light radius. For an exponential profile ($R_{\rm e} = 1.678 R_{\rm d}$) this becomes $r_{\rm c} = 2.94\ R_{\rm d}$.

time at the scale radius $r_{\rm s}$, which can be expressed in terms of $M_{\rm NFW}$, $r_{\rm s}$, and G (the Newtonian gravitational constant) as

$$t_{\rm dyn} = 2\pi\sqrt{\frac{r_{\rm s}^3}{GM_{\rm NFW}(< r_{\rm s})}} \quad . \tag{4.6}$$

The dark matter profile has then the same two free parameters as a NFW halo: the mass of the halo (M_{200}) and its concentration (c_{200}). N-body cosmological simulations find a strong correlation between c_{200} and M_{200} (e.g. Dutton & Macciò 2014; Ludlow et al. 2014), so in practice one can even fit NFW-like profiles with one single parameter. While the other parameters of the halo (n, $r_{\rm s}$, $r_{\rm c}$), are not considered free parameters, they also change on each step of the MCMC, as they depend on M_{200} and c_{200} as described above.

To find the best-fitting CDM halo we use a MCMC routine (also based on `emcee`) that minimises the residuals of Eq. 4.2 using a standard $\exp(-0.5\chi^2)$ function as likelihood, with χ^2 given by

$$\chi^2 = \sum \frac{(V_{\rm c} - V_{\rm c,mod})^2}{\delta_{V_{\rm c}}^2} \ , \tag{4.7}$$

where $V_{\rm c}$ and $V_{\rm c,mod}$ are the observed and model circular speed profiles, respectively, and $\delta_{V_{\rm c}}$ is the $^{\rm 3D}$Barolo uncertainty in the kinematic modelling, which we assume to be Gaussian (see Di Teodoro 2015). As we discuss next, the inclination is a free parameter in our MCMC, and thus $\delta_{V_{\rm c}}$ itself does not include the contribution from the inclination uncertainty; these error bars are, therefore, smaller than those shown in Figs. 4.4 and 4.5.

The MCMC explores the (M_{200}, c_{200}) parameter space and retrieves the best-fitting combination. In addition to M_{200} and c_{200}, we include the distance D and the inclination i as nuisance parameters. In practice, we impose a Gaussian prior on D centered at 76 Mpc and with a standard deviation of 5 Mpc, exploring the 2σ range $66 \leq D/{\rm Mpc} \leq 86$. Similarly, for i, we impose a Gaussian prior centered at 32° with a standard deviation of 3°, within $26° \leq i \leq 38°$; in Sec. 4.5 we also discuss the case where the priors for D and i are wider. It is worth pointing out that a change in D introduces a change in the conversion factor between arcsecond and kpc, thus modifying our sampling of the rotation curve. Additionally, it affects the value of $R_{\rm d}$, which in turn changes $r_{\rm c}$ and the thickness of the stellar disc. On the other hand, i affects the overall normalisation of the rotation curve and of the circular speed profile of the gas. Having established this, we explore different scenarios, which differ by our chosen priors on M_{200} and c_{200}.

In a very first attempt, we use the flat priors $6 \leq \log(M_{200}/{\rm M}_\odot) \leq 12$ and $0.1 \leq c_{200} \leq 30$. However, c_{200} remains completely unconstrained as its posterior distribution is flat over all the explored range. Upon imposing the $c_{200} - M_{200}$ relation of Dutton & Macciò (2014) as a Gaussian prior on c_{200}, we find $\log(M_{200}/{\rm M}_\odot) = 7.6^{+0.7}_{-1.0}$, $c_{200} = 21^{+5}_{-3}$, $D = (76 \pm 5)$ Mpc, and $i = 33 \pm 3°$.

While the resulting fit is close to the data (given that $V_{\rm bar} \approx V_{\rm c}$ and $V_{\rm DM}$ is subdominant), the value of $M_{200} \sim 10^8$ M$_\odot$ is too low to be plausible in a

CDM cosmology. Given $M_{\rm bar} = 1.4 \times 10^9$ M$_\odot$, the very minimum expected M_{200} (assuming the galaxy has a baryon fraction as high as the cosmological average: $f_{\rm c,bar} \simeq 0.16$, see Cimatti et al. 2019) is about 0.9×10^{10} M$_\odot$. It is clear that the MCMC routine finds a low mass since $V_{\rm c} \simeq V_{\rm bar}$, but the resulting halo does not seem to have a physical justification.

Taking the above into consideration, we decided to impose a lower boundary to the prior of M_{200} such that the minimum halo would produce $M_{\rm bar}/M_{200} \simeq 0.16$ (i.e. the cosmological baryon fraction). With this, the prior for M_{200} becomes $10 \leq \log(M_{200}/{\rm M}_\odot) \leq 12$. We stress that the lower limit on the prior corresponds to the minimum expected value of M_{200}. In theory one expects the galaxy to have a significantly larger M_{200}. For example, the ΛCDM stellar-to-halo mass relation from Posti et al. (2020) would predict $\log(M_{200}/{\rm M}_\odot) \approx 10.6$. For c_{200} we explore two scenarios: one where we impose again the $c_{200} - M_{200}$ relation of Dutton & Macciò (2014) as a Gaussian prior in the MCMC routine, and one where c_{200} has a flat wide prior $0.1 \leq c_{200} \leq 30$. In what follows, we refer to these two scenarios as Case 1 and Case 2, respectively.

The posterior distributions of both Case 1 and Case 2 are shown in Appendix 4.6. Somewhat unsurprisingly, for both cases we find $\log(M_{200}/{\rm M}_\odot) \simeq 10$, with posterior distributions that simply try to go to the lower bound. In Case 1, (imposing the Gaussian prior on the $c_{200} - M_{200}$ relation), we find $D = (67 \pm 1)$ Mpc and $i = 26.1^{\circ +0.2}_{-0.1}$, with posterior distributions also trying to go towards their lower bounds (see Fig. 4.10). The concentration, on the other hand, is well constrained, and we find $c_{200} = 11.7 \pm 0.3$. The other parameters of the coreNFW profile are $n = 0.7$, $r_{\rm c} = 4.6$ kpc, and $r_{\rm s} = 3.8$ kpc.

For Case 2, while D and i are well constrained following their priors ($D = 73 \pm 4$ Mpc, $i = 29^\circ \pm 2^\circ$), the posterior distribution of c_{200} goes to its lower bound, $c_{200} = 0.3^{+0.3}_{-0.2}$ (see Fig. 4.11). The other parameters of the coreNFW profile are $\log(M_{200}/{\rm M}_\odot) = 10.2$, $n = 0.03$ (i.e. coreNFW ≈ NFW) driven by a high $t_{\rm dyn}$ (Eq. 4.6), $r_{\rm c} = 5.1$ kpc, and $r_{\rm s} = 166$ kpc, driven by the extremely low c_{200} ($r_{\rm s} = r_{200}/c_{200}$).

Fig. 4.6 shows the two resulting mass models. Case 1, on the left panel, is in clear disagreement with the data as it significantly overestimates $V_{\rm c}$, even when the distance and inclination go to their lowest allowed values. Case 2, on the right panel, lies closer to the data but presents other problems, as we discuss in the next Section.

4.5 Discussion

Having presented our main results, we now discuss their implications. Provided our rotation curve for AGC 114905 faithfully traces its circular speed, the fact that it is baryon-dominated out to the outermost observed radius (Fig. 4.5) implies two possible scenarios in a ΛCDM context: that our UDG lacks a significant amount of dark matter across all radii (even beyond the range probed by our data), or that it has a peculiar dark matter halo with little mass within 10 kpc (e.g. right panel in Fig. 4.6).

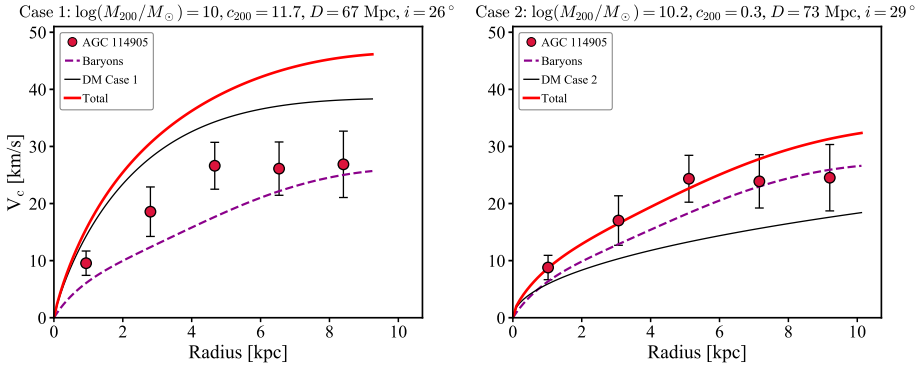

Figure 4.6: Mass models of AGC 114905. Case 1 and Case 2 are shown on the left and right panels, respectively. In both panels the red points show the V_c profile of AGC 114905, while the dashed magenta lines represent the V_c expected from the baryons (stars plus gas). The dark matter haloes are shown with black lines, and the red lines give the total contribution of baryons and dark matter together. Case 1, which follows the CDM $c_{200} - M_{200}$ relation, is inconsistent with the observations. Case 2 fits the data better, but it has a c_{200} too low for CDM. Note also that the assumed distance and inclination are different between both panels. Because the assumed distance is different on each panel, the sampling of the rotation curve along the horizontal axes is also different. In a similar way, the normalisation of the rotation curves differ from each other due to the different inclinations. See the text for details.

4.5.1 AGC 114905 compared to 'dark-matter free' galaxies

Since van Dokkum et al. (2018) and van Dokkum et al. (2019) postulated that DF−2 and DF−4 have very low or no dark matter content, different mechanisms to create such peculiar galaxies have been proposed. One of the leading ideas is that high-velocity ($\sim$ 300 km s^{-1}) collisions between gas-rich dwarf galaxies can create dark-matter free (or almost dark-matter free, $M_{\rm DM} \sim 10^5$ M$_\odot$) galaxies (Silk 2019; Shin et al. 2020). Importantly, those types of galaxies are expected to form in dense environments and to have a baryonic mass dominated by stars rather than cold gas. Another mechanism proposed to explain the existence of DF−2 and DF−4 are tidal interactions with massive neighbouring galaxies that strip the dark matter away (Jackson et al. 2021; Doppel et al. 2021); Montes et al. (2020) claim that in fact DF−4 currently shows signs of such interactions.

While the above scenarios can manage to produce dark-matter poor, UDG-like galaxies that show some degree of similarity with DF−2 and DF−4, it is important to bear in mind that gas-rich UDGs are rather different objects. Not only are they gas-dominated ($f_{\rm gas} \simeq 0.9$ for AGC 114905), but they are also isolated (by selection, see Leisman et al. 2017). In the specific case of AGC 114905, the nearest galaxy within a recession velocity of 500 km s^{-1} with confirmed (optical or HI) redshift, is the faint dwarf AGC 114806 at a projected distance of 2.1 Mpc and with a systemic velocity within a few km s^{-1}. Using

data from the Sloan Digital Sky Survey (Alam et al. 2015), we also looked for possible unconfirmed massive companions of AGC 114905. We explored the area within 45 arcmin of AGC 114905, corresponding to a circle of radius 1 Mpc at the distance of AGC 114905, querying for galaxies with $R_e \geq 1$ kpc and with color $(g-r) \leq 1$ mag. In this region, there are only seven galaxies with $M_* \gtrsim 10^9$ $M_\odot$ (assuming a distance of 76 Mpc and the mass-to-light-colour relation from Du et al. 2020) with unknown distance. All of them resemble confirmed background red galaxies, and the closest in projection lies at 700 kpc. All this evidence, together with the lack of tidal features in the optical and H I morphology of our UDG, suggests that it is truly isolated.

An idea that could reconcile a tidal origin with the current isolation of AGC 114905 is that it is an old tidal dwarf galaxy (TDG, e.g. Duc et al. 2014), since TDGs are expected to have a low dark matter content and low rotation velocities (e.g. Hunter et al. 2000; Lelli et al. 2015). If the interaction that originated the TDG happened at high redshift ($z \sim 4-6$) and the galaxy had an escape velocity of ~ 400 km s^{-1}, the parent galaxy would lie today at distances about ~ 5 Mpc from AGC 114905. While this scenario is impossible to test in practice, the population of known old TDGs in the nearby universe both in observations and simulations are found at much closer distances and recessional velocities from their parent galaxies than what AGC 114905 (and the similar gas-rich UDGs from Chapters 2 and 3) is from any massive galaxy (Hunter et al. 2000; Kaviraj et al. 2012; Duc et al. 2014; Haslbauer et al. 2019b). Overall, while is difficult to give a final answer, it seems unlikely that the small (if any) amount of dark matter in AGC 114905 can be attributed to the above mentioned mechanisms perhaps valid for DF−2 and DF−4.

Recently, Trujillo-Gomez et al. (2022) proposed a semi-empirical model where strong feedback from globular clusters can produce UDGs with dark matter cores as large as $10-30$ kpc. However, the model does not include a detailed treatment of the gas component which is the dominant mass budget of gas-rich UDGs, and a thorough comparison with our data is not yet possible to carry out.

It would be instructive to obtain information about the kinematics of AGC 114905 beyond 10 kpc, where the contribution of stars and gas becomes smaller and would produce a declining rotation curve. Instead, if a flat rotation curve were to be found, it would suggest the presence of dark matter. In the next Section, motivated by our results in Fig. 4.6, we discuss which type of CDM haloes are in agreement or disagreement with our observations.

4.5.2 The c_{200} of a CDM halo for AGC 114905 is too low

It follows from Fig. 4.6 that it does not seem possible to fit the circular speed profile of AGC 114905 with a CDM-motivated c_{200}. As mentioned above, if the $c_{200}-M_{200}$ relation is imposed (Case 1, left panel of Fig. 4.6), it fails by a large margin at reproducing the amplitude of the circular speed profile. Case 2 (right panel of Fig. 4.6), fitting a free c_{200}, does a better job and it is consistent with

the circular speed profile within the uncertainties. However, c_{200} is too low and completely off the expected $c_{200} - M_{200}$ relation that emerges from cosmological simulations[6] (e.g. Dutton & Macciò 2014; Ludlow et al. 2014) and it might even be non-physical: McGaugh et al. (2003) argue that CDM haloes with $c_{200} < 2$ are not produced in any sensible cosmology. Sengupta et al. (2019) and Shi et al. (2021) also suggested that the gas-rich UDGs AGC 242019 and UGC 2165, respectively, have a c_{200} around 2. Drawing conclusions from those galaxies might be less straightforward: the rotation curve of AGC 242019 does not seem to reach its flat part, while the data of UGC 2165 have low resolution and its rotation curve (apparently rising as solid-body) is significantly oversampled. Still, it is interesting that similarly low values of c_{200} are reported.

It is important to highlight that while low surface brightness galaxies have been historically found to inhabit low-concentration haloes (e.g. McGaugh et al. 2003), the concentrations of those haloes are still usually in broad to good agreement with ΛCDM cosmology (Macciò et al. 2007), while the concentration of AGC 114905 is rejected at a high significance level. Given the volume explored by Leisman et al. (2017) when building the parent sample of AGC 114905 ($\sim 10^6$ Mpc^3, see Haynes et al. 2018; Jones et al. 2018), finding a single galaxy with the properties of AGC 114905 should be practically impossible in a CDM Universe. This result becomes even stronger considering the rest of the sample studied in Chapters 2 and 3 possibly shows similar properties, even if slightly less extreme as AGC 114905 presents the largest offset from the BTFR. In this context, it is important to bear in mind that gas-rich UDGs as a whole population have significantly narrower velocity widths (a proxy for their rotation velocities) than galaxies of similar mass (Leisman et al. 2017; Jones et al. 2018).

We also note that the implausibility of the CDM halo needed in AGC 114905 is not just related with the cusp-core problem (Bullock & Boylan-Kolchin 2017), since by fitting a coreNFW profile we do not force the halo to be cored or cuspy per se. It is also clear that the scales at which dark matter is deficient in AGC 114905 (10 kpc) are larger than any realistic core size for dwarf galaxies in both observations and simulations (e.g. Read et al. 2016a, 2017; Lazar et al. 2020). To further explore this, we performed a run of our MCMC routine where r_c is kept as a free parameter. In practice, we use a flat prior exploring the range $0 \leq r_c/\mathrm{kpc} \leq 44$. The maximum value of 44 kpc is chosen because it is the value of r_{200} given $M_{200} = 10^{10}$ M$_\odot$. Additionally, we impose a minimum value on the prior of M_{200}, $\log(M_{200}/\mathrm{M}_\odot) = 10$, as well as the Gaussian prior on the $c_{200} - M_{200}$ relation. The MCMC routine finds the parameters $\log(M_{200}/\mathrm{M}_\odot) \approx 10^{10}$, $c_{200} \approx 12$, $D \approx 71$ Mpc, $i \approx 27°$, and $r_c \approx 41$ kpc, with the i and r_c posterior distributions simply going to their minimum and maximum allowed values, respectively. While the fit is just slightly worse than Case 2 (right panel of Fig. 4.6) it seems non-physical. Expressing the core radius

[6] Assuming that the scatter of the $c_{200} - M_{200}$ relation measured at high masses ($\sigma_{\log(c_{200})} = 0.11$ dex, see Dutton & Macciò 2014) is applicable also at $M_{200} \lesssim 10^{10}$ M$_\odot$, then c_{200} of AGC 114905 is about 15σ below the expected value, although this number could be reduced if the $c_{200} - M_{200}$ or its scatter depart from Gaussian (Kong et al. 2022).

as $r_c = \eta R_e$ implies $\eta \sim 15$. As discussed by Read et al. (2017), there is not enough supernovae energy in galaxies to drive $\eta > 2.75$, and $\eta = 1.75$ fits real and simulated galaxies well. Even if other energy sources (e.g. Cimatti et al. 2019) can affect the distribution of dark matter in galaxies, it seems unlikely that they would contribute much more than supernovae, as required to achieve $r_c \approx r_{200}$.

Finally, it is worth clarifying that the problem of fitting a CDM halo to AGC 114905 is not restricted to specific functional forms such as the coreNFW profile. In addition to coreNFW, we also try with the coreEinasto halo, which allows the Einasto profile to develop a core, and which has been found by Lazar et al. (2020) to successfully reproduce the cored dark matter profile of a variety of galaxies in the FIRE-2 simulations (Hopkins et al. 2018). For this profile we also impose a minimum $\log(M_{200}/\mathrm{M}_\odot) = 10$, but the only way to find agreement with our data is again if the size of the core is as large as r_{200}.

Overall, the existence of galaxies like AGC 114905 seems to pose a major challenge for CDM haloes. An interesting line of research is to explore whether or not the current issues can be mitigated by invoking a different type of dark matter (e.g. Kaplinghat et al. 2020; Yang et al. 2020).

4.5.3 AGC 114905 challenging MOND

Modified Newtonian dynamics (MOND, Milgrom 1983; Sanders & McGaugh 2002) is an alternative approach to dark matter theories which aims to explain dark matter physics by invoking a modification to Newtonian dynamics. One of the major achievements of MOND is how well it predicts rotation curves of galaxies (e.g. Sanders & McGaugh 2002; Famaey & McGaugh 2012 and references therein). Rather than a fit, MOND makes a direct prediction of the shape of the rotation curve given the stellar and gas mass distributions. The only other parameter is $a_0 \simeq 1.2 \times 10^{-8}$ cm s^{-2}, postulated to be a universal constant.

The fact that some isolated UDGs are off the BTFR already posed a challenge to MOND, which predicts a tight (zero intrinsic scatter) BTFR with slope of 4 for isolated galaxies. Yet, some doubts about this may exist, as it could be argued that the circular speeds reported in Chapters 2 and 3 were not tracing the flat part of the rotation curve or were too affected by the resolution; here we have shown that this is not the case for AGC 114905.

Following Gentile (2008), in the absence of an 'external' gravitational field of a neighbouring massive galaxy, the MOND rotation curve can be written as

$$V^2_{\mathrm{MOND}}(r) = V^2_{\mathrm{bar}} + \frac{V^2_{\mathrm{bar}}}{2}\left(\sqrt{1 + \frac{4a_0 r}{V^2_{\mathrm{bar}}}} - 1\right) . \tag{4.8}$$

We stress that the above formula is applicable to our UDG given the lack of massive galaxies in its vicinity. In order to test this prediction, we performed another MCMC fit with D and i as free parameters (which affect both V_c and V_{MOND}), following the same Gaussian priors as for our Case 1 and Case 2 above.

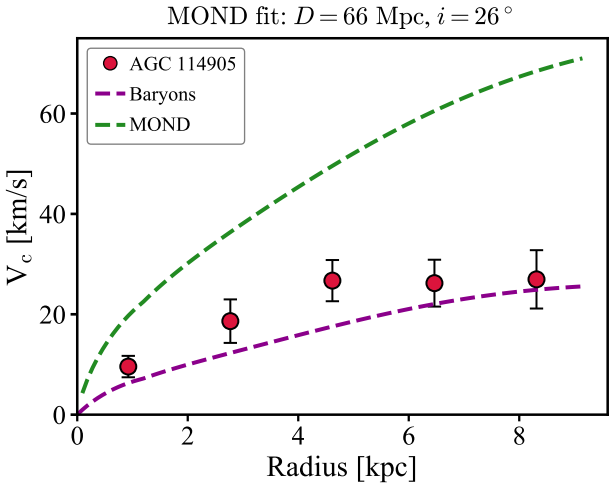

Figure 4.7: MOND prediction (green line) of the circular speed profile of AGC 114905 (red points). The baryonic circular speed profile is shown with a magenta line.

Even with the posterior distributions for D and i going to their lower bounds ($D \approx 66$ Mpc and $i \approx 26°$, see Fig. 4.12 in Appendix 4.6), the MOND prediction markedly overestimates the circular speed of our UDG (consistent with the offset from the BTFR), as we show in Fig. 4.7. There may be also some tension with the shape of the rotation curve, which is not predicted to be flat as in the observations. Therefore, our UDG seemingly presents a challenge to MOND, which can only be reconciled by invoking a much lower inclination, as we discuss in Sec. 4.5.4.

4.5.4 The effects of a lower inclination

As described in Sec. 4.3, we measure the inclination of AGC 114905 to be $32° \pm 3°$, using a well tested method that relies exclusively on the total H I map and is independent of the kinematics of the galaxy and our posterior kinematic modelling. While we argue that our inclination is robust, our results are certainly dependent on it. In particular, if AGC 114905 had a much lower inclination, the amplitude of its rotation curve would be significantly larger, having more room for dark matter within the observed radii and potentially alleviating some of the tensions presented in this chapter (see for instance the case of IC 1613 in Oman et al. 2016).

Given this, it is interesting to quantify by how much the inclination of our UDG would need to decrease to make it consistent with the CDM (and MOND) expectation. For this exploration we assume a coreNFW profile with $r_c = 2.94\ R_d$. The 'minimum' expectation is such that the galaxy has $\log(M_{200}/M_\odot) = 10$ and a c_{200} in agreement (within some scatter) with the $c_{200} - M_{200}$ relation. We run again our MCMC routine, but this time we use

wider Gaussian priors for D and i: $50 \leq D/\mathrm{Mpc} \leq 100$ and $5^\circ \leq i < 85^\circ$, with centre and standard deviations as in Case 1. The resulting parameters are $\log(M_{200}/\mathrm{M}_\odot) = 10.03^{+0.06}_{-0.03}$ $\mathrm{M}_\odot$, $c_{200} = 12.1 \pm 0.3$, $D = (72.7 \pm 5)$ Mpc, and $i = (15 \pm 1)^\circ$. The low inclination brings up the circular speed of AGC 114905 to velocities around 45 km s^{-1},which are consistent with a coreNFW halo similar to the halo in Case 1 (the other parameters are $n = 0.73$, $r_\mathrm{c} = 5$ kpc, and $r_\mathrm{s} = 3.8$ kpc).

With an inclination of 15° the galaxy would be still quite puzzling, as it would have a baryon fraction about 70% the value of the cosmological average (90% if $D = 76$ Mpc), as opposed to most dwarf galaxies that have low baryon fractions of a few per cent (McGaugh et al. 2010; Read et al. 2017). Additionally, AGC 114905 would still lie off the BTFR. If one instead imposes $\log(M_{200}/\mathrm{M}_\odot) = 10.6$ (which gives a baryon fraction of about 20%) assuming the ΛCDM stellar-to-halo mass relation from Posti et al. (2020), a corresponding $c_{200} = 11.5$ (following the $c_{200} - M_{200}$ relation), and $D = 76$ Mpc, the needed inclination is $10.4 \pm 0.3^\circ$. Similarly, an inclination of $i = 10.8 \pm 0.3^\circ$ would be needed in order to find agreement between the MOND prediction and the V_c profile of AGC 114905, at least on average, since the shape predicted by MOND seems to also differ from our rotation curve. Note, however, that a radially varying inclination could potentially alleviate this tension between the rotation curves shapes.

The above values for the inclination are about 20° degrees off the inclination we determined in Sec. 4.3. This is a discrepancy a factor 6−7 larger than the nominal uncertainty estimate of our measurement (see Fig. 4.3), although inclinations below $\sim 25^\circ$ become increasingly difficult to constrain as ellipses with lower inclinations all have very similar shapes. We can also inspect visually if inclinations as low as $11^\circ - 15^\circ$ can be consistent with the data. In Fig. 4.8 we show the outer contour of the H I map of AGC 114905 superposed on the $r-$band optical image, and we compare it with the equivalent contours of two $^{3\mathrm{D}}$Barolo azimuthal models (convolved with the observed beam) of AGC 114905 at different inclinations. The models are razor-thin axisymmetric discs (but see Sec. 4.3.1). The model at 32° does an overall good job at following the H I contour, while the contour for the model at 11° appears inconsistent with it, being significantly more elongated along the minor axis. This is also shown in Fig. 4.9 where we compare the channel maps of AGC 114905 with the channel maps of our best-fitting model and those of a model with an inclination of 11°.

Given all of the above, we find it unlikely that we are severely overestimating the inclination of our UDG, although this remains the largest source of uncertainty in our analysis. Something else to consider is that there are other gas-rich UDGs showing a similar set of properties, all at different inclinations (Chapters 2 and 3, see also Sengupta et al. 2019; Shi et al. 2021, and the spatially unresolved data from e.g. Leisman et al. 2017; Karunakaran et al. 2020). This means that the inclinations of all of them would need to be overestimated by a large margin. Still, it is desirable to repeat our analysis with a gas-rich UDG at a similar resolution as we have now for AGC 114905, but at higher inclination,

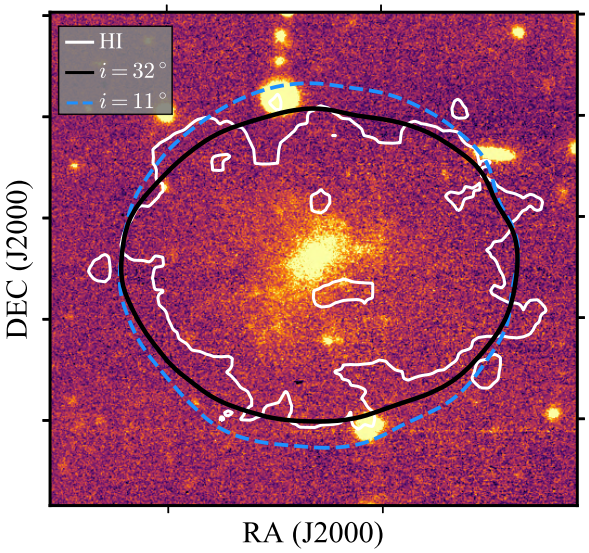

Figure 4.8: Comparison between the outer contours (S/N = 3) of the H I map of AGC 114905 (white) and two azimuthal models at different inclinations. While the model at 32° (solid black line) provides a good fit to the data, the model at 10° (dashed blue) is significantly more elongated than the data along the minor axis. The background shows the optical image of AGC 114905.

and we aim to do this in the near future.

4.6 Conclusions

We obtained new H I interferometric observations of the gas-rich ultra-diffuse galaxy (UDG) AGC 114905 using the Karl G. Jansky Very Large Array in its B-, C- and D-configurations. The new data, tracing the H I emission up to 10 kpc from the galaxy centre, have a spatial resolution a factor about 2.5 higher than previous data, and confirm that AGC 114905 has a regularly rotating gas disc.

We performed 3D kinematic modelling of the data cube using ^{3D}Barolo, which allowed us to recover the intrinsic rotation curve and velocity dispersion profile of the galaxy. AGC 114905 has a regular rotation curve that reaches a flat part with a circular speed (after a minor correction for asymmetric drift) of about 23 km s^{-1}. This result confirms that this UDG lies off the baryonic Tully-Fisher relation, as suggested in Chapters 2 and 3 with low-resolution data.

The observed circular speed profile of our UDG can be explained almost entirely by the contribution of the baryons alone, with little room for dark matter within our observed outermost radius ($R_{\rm out} \approx 10$ kpc). Moreover, we found that the circular speed profile cannot be reproduced by standard cold dark matter (CDM) haloes: the only possibility to find a good fit to the data is if the concentration of the halo is as low as ~ 0.3, completely off CDM expectations. We tested whether the rotation of our UDG is instead reproduced within the MOND framework, but we find that there is a significant mismatch on the normalisation and shape of the MOND rotation curve with respect to our observations.

The geometry of the system (assumed to be an inclined axisymmetric disc)

is the main source of uncertainty in our results. The inclination of AGC 114905 ($32\pm3°$), which we measure from its total H I map independently of its kinematics, is a significant caveat, but a number of independent pieces of evidence suggest that it cannot be overestimated to the extent of significantly changing the above results. Efforts to observe another gas-rich UDG at a similar spatial resolution but at higher inclination are under way. Finally, it is important to consider that we have confirmed for one UDG the robustness of the results obtained in Chapters 2 and 3 at low resolution. The fact that the six UDGs (and see also e.g. Leisman et al. 2017; Shi et al. 2021) at different inclinations show the same behavior argues in favor of them being really exotic and suggests that our results are not the byproduct of systematic uncertainties.

We have strengthened and clarified previous results on the nature and startling dynamics of gas-rich UDGs. Yet, their origin and precise evolutionary pathways remain largely a mystery. The present work has also shown that gas-rich UDGs are a promising population to study dark matter, as they can potentially provide telltale clues to understand its nature.

4.A Channel maps

Fig. 4.9 shows representative channel maps of the data cube of AGC 114905. The observed emission is shown in grey background and dark blue contours (open contours for negative values). The green cross shows the centre of the galaxy and the velocity of each channel map is given on the bottom right corner of each panel. In red, we show the contours for the best-fitting ^{3D}Barolo azimuthal tilted-ring model; while low S/N features are not fully reproduced, the model captures well the overall kinematics of the galaxy, as also shown in Fig. 4.2 with the PV diagrams. We also overlay in light blue the contours for a model with a fixed inclination of 11° (as needed to match CDM and MOND expectations, see Sec. 4.5.4). A close inspection shows that the model at 11° has an excess of flux along the minor axis in the channels close to the systemic velocity; the model at 32° does a better job in this regard (however, this comparison is better appreciated in Fig. 4.8). Moreover, the model at 32° matches in a better way the spectral extent of the observations.

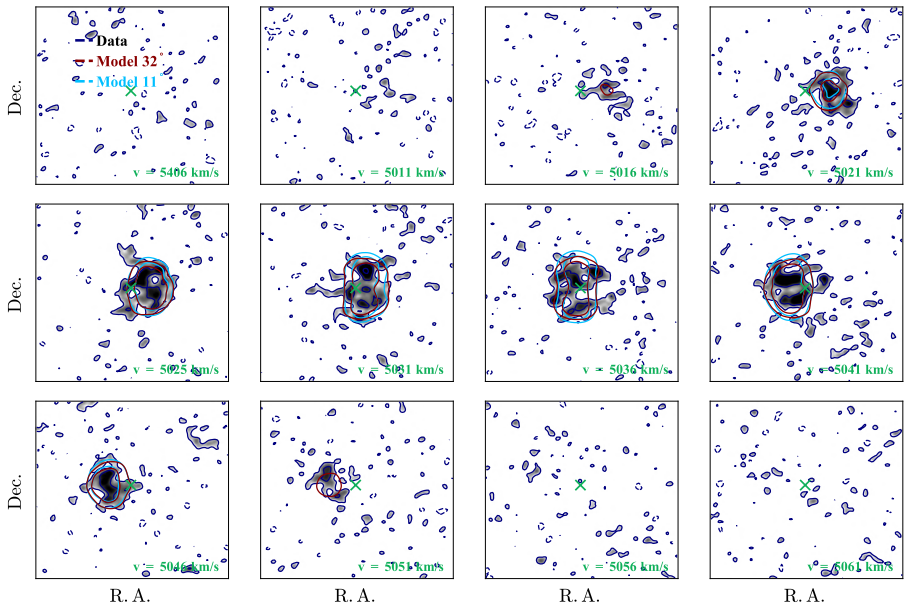

Figure 4.9: Representative channel maps of AGC 114905. The emission of the galaxy is shown in grey background and dark blue contours (open contours for negative values). The green crosses show the centre of the galaxy, and we indicate the velocity corresponding to each channel map on the bottom right corner. The contours for the best-fitting ^{3D}Barolo azimuthal tilted-ring model are shown in red, while the contours for a model at 11° are shown in light blue. Contours are at -2, 2, 4 times the rms noise per channel.

4.B MCMC posterior distributions

In this appendix we provide the main posterior distributions of our mass models obtained with our MCMC analyses as described in the main text.

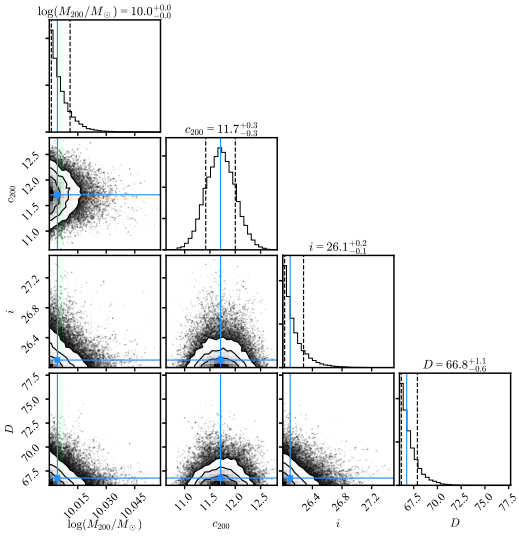

Figure 4.10: MCMC posterior distribution for our Case 1 mass model. Lines are as in Fig. 4.3. See Sec. 4.4 for details.

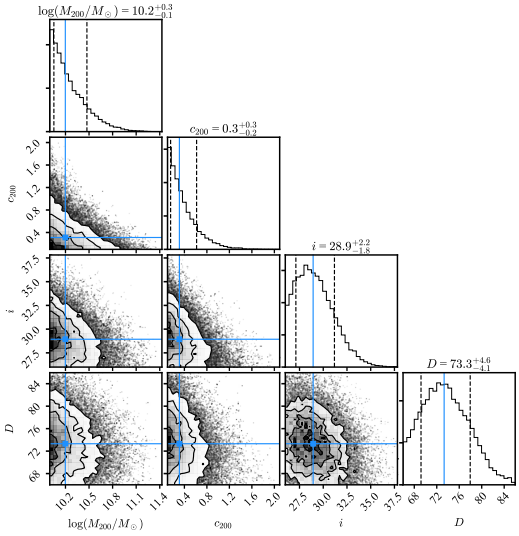

Figure 4.11: MCMC posterior distribution for our Case 2 mass model. Lines are as in Fig. 4.3. See Sec. 4.4 for details.

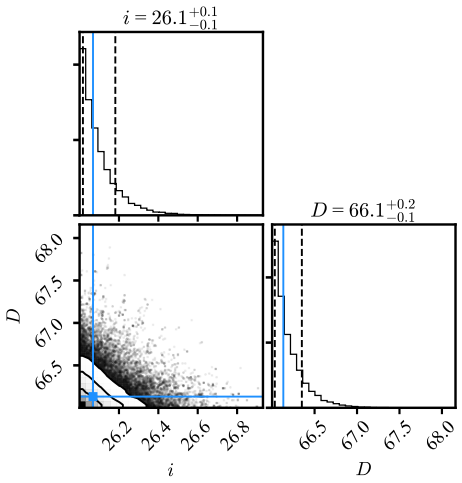

Figure 4.12: MCMC posterior distribution for the MOND model. Lines are as in Fig. 4.3. See Sec. 4.5.3 for details.

Chapter 5

The baryonic specific angular momentum of disc galaxies

based on

– P. E. Mancera Piña, L. Posti, F. Fraternali, et al., 2021 –

Published in Astronomy & Astrophysics, A&A 647, A76

Abstract

Specific angular momentum (the angular momentum per unit mass, $j = J/M$) is one of the key parameters that control the evolution of galaxies, and it is closely related with the coupling between dark and visible matter. In this work, we aim to derive the baryonic (stars plus atomic gas) specific angular momentum of disc galaxies and study its relation with the dark matter specific angular momentum. Using a combination of high-quality H I rotation curves, H I surface densities, and near-infrared surface brightness profiles, we homogeneously measure the stellar (j_*) and gas ($j_{\rm gas}$) specific angular momenta for a large sample of nearby disc galaxies. This allows us to determine the baryonic specific angular momentum ($j_{\rm bar}$) with high accuracy and across a very wide range of masses. We confirm that the $j_* - M_*$ relation is an unbroken power-law from $7 \lesssim \log(M_*/{\rm M}_\odot) \lesssim 11.5$, with a slope 0.54 ± 0.02, setting a stronger constraint at dwarf galaxy scales than previous determinations. Concerning the gas component, we find that the $j_{\rm gas} - M_{\rm gas}$ relation is also an unbroken power-law from $6 \lesssim \log(M_{\rm gas}/{\rm M}_\odot) \lesssim 11$, with a steeper slope of 1.02 ± 0.04. Regarding the baryonic relation, our data support a correlation characterised by a single power-law with a slope 0.60 ± 0.02. Our analysis shows that our most massive spirals and smallest dwarfs lie along the same $j_{\rm bar} - M_{\rm bar}$ sequence. While the relations are tight and unbroken, we find internal correlations inside them: At fixed M_*, galaxies with larger j_* have larger disc scale lengths, and at fixed $M_{\rm bar}$, gas-poor galaxies have lower $j_{\rm bar}$ than expected. We estimate the retained fraction of baryonic specific angular momentum, $f_{\rm j,bar}$, finding it constant across our entire mass range with a value of $\sim$0.6, indicating that the baryonic specific angular momentum of present-day disc galaxies is comparable to the initial specific angular momentum of their dark matter haloes. In general, these results set important constraints for hydrodynamical simulations and semi-analytical models that aim to reproduce galaxies with realistic specific angular momenta.

5.1 Introduction

Understanding the relation between the observed properties of galaxies and those expected from their parent dark matter haloes, as well as the physical processes that regulate such properties, is one of the major goals of present-day astrophysics.

Angular momentum, in addition to the total mass, arguably governs most stages of galaxy formation and evolution (e.g, Fall & Efstathiou 1980; Dalcanton et al. 1997; Mo et al. 1998). From its origin in a cold dark matter (CDM) universe via primordial tidal torques (Peebles 1969) to its repercussions on the morphology of present-day galaxies (e.g. Romanowsky & Fall 2012; Cortese et al. 2016; Lagos et al. 2018; Sweet et al. 2020; Kulier et al. 2020), angular momentum, or specific angular momentum if weighted by the total mass, plays a crucial role in shaping galaxies at all redshifts (e.g. Stevens et al. 2016; Posti et al. 2018b; Marasco et al. 2019; Sweet et al. 2019; Marshall et al. 2019). Yet, the exact interplay between the angular momentum of dark mater haloes and that of the baryons is not completely understood.

The 'retained fraction of angular momentum'– the ratio between the specific angular momentum of the baryons ($j_{\rm bar}$) and that of the parent dark matter halo ($j_{\rm h}$)– is one of the parameters of paramount importance in this context. Still, its behaviour as a function of galaxy mass or redshift (e.g. Romanowsky & Fall 2012; Posti et al. 2018b) has not yet been fully established on an observational basis.

Galaxy scaling relations can be reasonably well reproduced if this global fraction ($f_{j,\rm bar} = j_{\rm bar}/j_{\rm h}$) is close to unity (e.g. Dalcanton et al. 1997; Mo et al. 1998; Navarro & Steinmetz 2000); otherwise, scaling laws like the Tully-Fisher relation would be in strong disagreement with observations. In general, if $f_{j,\rm bar}$ is too low, then the baryons do not have enough angular momentum to reproduce the size distribution observed in present-day galaxies, giving rise to the so-called angular momentum catastrophe (see for instance Steinmetz & Navarro 1999; D'Onghia et al. 2006; Dutton & van den Bosch 2012; Somerville et al. 2018; Cimatti et al. 2019). These problems are mitigated by including the effects of stellar and active galactic nucleus feedback, which prevent the ratio $f_{j,\rm bar}$ from being too small (e.g. Governato et al. 2007; Dutton & van den Bosch 2012). These and other phenomena, such as galactic fountains or angular momentum transfer between baryons and dark matter, also participate in shaping the detailed local baryonic angular momentum distribution within galaxies (e.g. van den Bosch et al. 2001; Cimatti et al. 2019; Sweet et al. 2020).

In a pioneering work, Fall (1983) first determined the shape of the stellar specific angular momentum–mass relation (the $j_* - M_*$ relation); because of this, the $j - M$ laws are sometimes called Fall relations. The results from Fall (1983) were later confirmed in the literature with more and better data (e.g. Romanowsky & Fall 2012; Fall & Romanowsky 2018). Particularly, Posti et al. (2018b, hereafter P18) recently studied the $j_* - M_*$ relation relation with a

large sample of disc galaxies with extended and high-quality rotation curves, also taking subtle effects, such as the difference in the rotation of gas and stars, into account.

The general picture of these studies is that disc galaxies define a tight sequence in the $j_* - M_*$ plane, following an unbroken power-law with a slope around 0.5−0.6. Early-type galaxies follow a similar trend, but with a lower intercept such that, at a given M_*, they have about five times less j_* than late-type galaxies (Fall 1983; Romanowsky & Fall 2012). The fact that the slope of the relation is $0.5 - 0.6$ is remarkable as this value is very close to the slope of the relation of dark matter haloes, $j_{\rm h} \propto M_{\rm h}^{2/3}$ (e.g. Fall 1983; Romanowsky & Fall 2012; Obreschkow & Glazebrook 2014; P18 and references therein)

While these studies have built a relatively coherent picture of the stellar component, the gas ($j_{\rm gas} - M_{\rm gas}$) and baryonic ($j_{\rm bar} - M_{\rm bar}$) relations remain somewhat less well explored, although studies performed in recent years have started to delve into this (Obreschkow & Glazebrook 2014; Butler et al. 2017; Chowdhury & Chengalur 2017; Elson 2017; Kurapati et al. 2018; Lutz et al. 2018; Murugeshan et al. 2020). In fact, different authors have reported different results regarding the nature of the $j_{\rm bar} - M_{\rm bar}$ relation, such as whether or not the slope of the correlations in the $j_{\rm bar} - M_{\rm bar}$ and $j_* - M_*$ planes are the same, if dwarf galaxies follow a different sequence than higher-mass spirals, or whether or not the relations have a break at a characteristic mass.

This work focuses on homogeneously deriving the stellar, gas, and baryonic specific angular momenta of a large sample of disc galaxies with the best rotation curves and photometry data available. This chapter is organised as follows. In Sec. 5.2, we describe the sample of galaxies used in this study. Sec. 5.3 contains our methods for deriving the specific angular momentum−mass relation for each component (stars, gas, baryons), and Sec. 5.4 presents our main results. In Sec. 5.5 we discuss these results, including an empirical estimation of the retained fraction of specific angular momentum, and we summarise our findings and conclude in Sec. 5.6.

5.2 Building the sample

To compute the baryonic specific angular momentum, we needed to determine the contribution of the stellar (j_*) and gas ($j_{\rm gas}$) components, as described in detail in Sec. 5.3. To obtain the stellar and gas specific angular momenta, stellar and gas surface density profiles are necessary, together with extended rotation curves.

In their study of j_*, P18 used the galaxies in the Spitzer Photometry and Accurate Rotation Curves database (SPARC, Lelli et al. 2016a). Unfortunately, radial H I surface density profiles are not available in SPARC. Because of this, we built a compilation of galaxies with high-quality H I and stellar surface density profiles and extended rotation curves from different samples in the literature. In the rest of this section we describe these samples.

We started by considering the SPARC galaxies (rotation curves and stellar

surface density profiles) for which H I surface density profiles are available from the original sources or authors (Begeman 1987; Sanders 1996; Sanders & Verheijen 1998; Fraternali et al. 2002; Swaters et al. 2002; Begum & Chengalur 2004; Battaglia et al. 2006; Boomsma 2007; de Blok et al. 2008; Verheijen & Sancisi 2001; Noordermeer 2006; Swaters et al. 2009; Fraternali et al. 2011). If needed, distance-dependent quantities were re-scaled to the distance given in SPARC.

We complemented these galaxies with the sample of disc galaxies compiled and analysed by Ponomareva et al. (2016). We only slightly modified the data provided by those authors: For a few galaxies we exclude the outermost $\lesssim 10\%$ of the rotation curve, where it is not clear how well traced the emission of the galaxy is (see for instance NGC 224, NGC 2541, or NGC 3351 in their appendix). The radial coverage in these few galaxies is, however, still sufficiently extended, and the removal of those few points has no significant effect in the computation of j. Similarly to SPARC, the sample from Ponomareva et al. (2016) has 3.6 μm photometry (Ponomareva et al. 2017), which is needed to compute j_*, as we show in Sec. 5.3.

To populate the low-mass regime, which is not well sampled in SPARC, we took advantage of the recent and detailed analysis of dwarf galaxies from the Local Irregulars That Trace Luminosity Extremes, The H I Nearby Galaxy Survey (LITTLE THINGS, Hunter et al. 2012) by Iorio et al. (2017). These galaxies have 3.6 μm photometry from Zhang et al. (2012), except for DDO 47, which was therefore excluded from our sample.

Furthermore, we considered a set of dwarf galaxies from the Local Volume H I Survey (LVHIS, Koribalski et al. 2018), for which we derived accurate kinematic models using the software ^{3D}BAROLO (Di Teodoro & Fraternali 2015) in the same way as done in Iorio et al. (2017). We provide further details on this modelling in Appendix 5.A. These galaxies have near-infrared photometry ($H-$band at 1.65 μm) available in the literature (Kirby et al. 2008; Young et al. 2014).

Finally, we considered a few dwarf galaxies from the Very Large Array-ACS Nearby Galaxy Survey Treasury (VLA-ANGST, Ott et al. 2012) and the Westerbork observations of neutral Hydrogen in Irregular and SPiral galaxies (WHISP, van der Hulst et al. 2001) projects, for which we also obtained kinematic models using ^{3D}BAROLO (see Appendix 5.A). These dwarfs have publicly available 3.6 μm surface brightness profiles from Bouquin et al. (2018), except for UGC 10564 and UGC 12060, for which we built the 3.6 μm surface brightness profiles (see Marasco et al. 2019) from the data in the Spitzer Heritage Archive.

Stellar and gas masses were computed in the same way as in P18, by integrating the infrared and gas surface density profiles out to the last measured radius: $M_k = 2\pi \int_0^{R_{\rm max}} R' \Sigma_k(R') dR'$. The near-infrared mass-to-light ratio Υ used to calculate M_* varies slightly depending on the available data. For galaxies in the SPARC database, that have available surface brightness profile decomposition, we assumed the same mass-to-light ratio as P18: $\Upsilon_{\rm d}^{3.6} = 0.5\ {\rm M}_\odot/{\rm L}_\odot$ and $\Upsilon_{\rm b}^{3.6} = 0.7\ {\rm M}_\odot/{\rm L}_\odot$ for the disc and bulge, respectively. For the rest of the galaxies with 3.6 μm data, which are disc-dominated, we adopted $\Upsilon_{\rm d}^{3.6} = 0.5\ {\rm M}_\odot/{\rm L}_\odot$. For

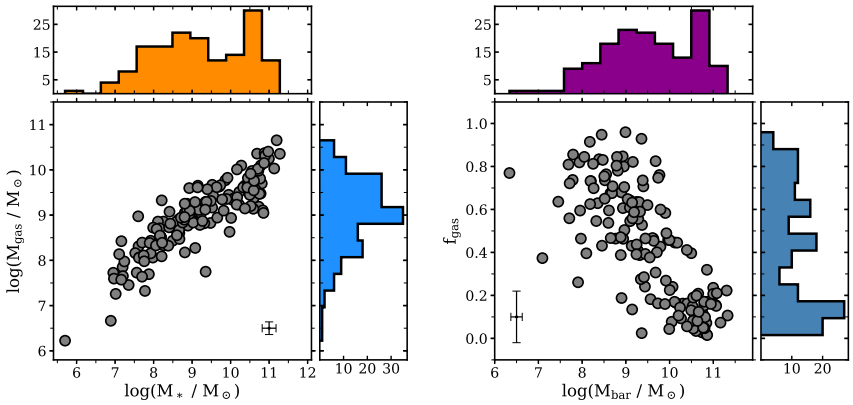

Figure 5.1: $M_* - M_{\rm gas}$ (*left*) and $M_{\rm bar} - f_{\rm gas}$ (*right*) relation for our sample of galaxies. Typical errorbars are shown in black. The panels at the top and right of each relation show the histograms of the M_*, $M_{\rm gas}$, $M_{\rm bar}$, and $f_{\rm gas}$ distributions.

the LVHIS dwarfs, which have H-band photometry, we adopted $\Upsilon_{\rm d}^{H} = 1\ {\rm M}_\odot/{\rm L}_\odot$ (see more details in Kirby et al. 2008; Young et al. 2014). For the mass gas, all the H I surface densities ($\Sigma_{\rm HI}$) in the different samples were homogenised to include a helium correction such that $\Sigma_{\rm gas} = 1.33\ \Sigma_{\rm HI}$.

After taking out the galaxies that overlap between the different subsamples, we ended up with 90 from SPARC and the above references, 30 from the Ponomareva et al. (2016) sample, 16 from LITTLE THINGS, 14 from LVHIS, four from VLA-ANGST, and three from WHISP. This gave us a total of 157 galaxies, making this the largest sample for which detailed derivations of the three $j - M$ laws have been performed to date. This sample, like the SPARC database, is not volume-limited, but it is representative of nearby regularly rotating galaxies. It is also worth mentioning that the high-quality rotation curves for all the galaxies were derived from the same type of data (HI interferometric observations) using consistent techniques (tilted ring models, e.g. Di Teodoro & Fraternali 2015), so we do not expect any systematic bias between the different subsamples. Our final sample of galaxies spans a mass range of $6 \lesssim \log(M_*/{\rm M}_\odot) \lesssim 11.5$ and $6 \lesssim \log(M_{\rm gas}/{\rm M}_\odot) \lesssim 10.5$, with a wide spread of gas fractions ($f_{\rm gas} = M_{\rm gas}/M_{\rm bar}$). Fig. 5.1 shows the $M_* - M_{\rm gas}$ and $M_{\rm bar} - f_{\rm gas}$ relations for our sample, together with their 1D distributions. The rotation curves and surface density profiles are extended, with a median ratio between the maximum extent of the rotation curve $R_{\rm out}$ and the optical disc scale length $R_{\rm d}$ of ~ 6, and with the 84th percentile of the $R_{\rm out}/R_{\rm d}$ distribution of ~ 10.

5.3 Determining the specific angular momentum

5.3.1 Measuring $j_{\rm gas}$ and j_*

In a rotating galaxy disc, the specific angular momentum inside a radius R with rotation velocity V, for a given component k (stars or gas), is given by the expression:

$$j_k(<R) = \frac{2\pi \int_0^R R'^2\ \Sigma_k(R')\ V_k(R')\ dR'}{2\pi \int_0^R R'\ \Sigma_k(R')\ dR'}\ . \tag{5.1}$$

For the gas, the velocity profile that goes into Eq. 5.1 is simply $V_{\rm rot}$, the rotation velocity traced by the H I rotation curve. For the stars, co-rotation with the gas is often assumed ($V_* = V_{\rm rot}$). In such a case, given that $\Sigma_{\rm bar} = \Sigma_{\rm gas} + \Sigma_*$, $j_{\rm bar}$ is computed by taking $\Sigma_k = \Sigma_{\rm bar}$ and $V_k = V_{\rm rot}$ in Eq. 5.1.

Nonetheless, a more careful determination of j_* and $j_{\rm bar}$ should not assume $V_* = V_{\rm rot}$ (e.g. P18). This is because in practice stars usually rotate more slowly than the cold gas as they have a larger velocity dispersion. Even if this effect is not expected to be dramatic for high-mass galaxies (Obreschkow & Glazebrook 2014; P18) or bulgeless galaxies in general (El-Badry et al. 2018), it is more accurate to take it into account, specially when dealing with dwarfs. Considering this, in this chapter we derive V_* using the stellar-asymmetric drift correction as follows.

Stellar-asymmetric drift correction

First, we will consider the circular speed $V_{\rm c}$ of the galaxies. By definition (e.g. Binney & Tremaine 2008), $V_{\rm c}^2 = V_{\rm rot}^2 + V_{\rm AD,gas}^2$, with $V_{\rm AD,gas}^2$ the gas-asymmetric drift correction (e.g. Read et al. 2016b; Iorio et al. 2017), a term to correct for pressure-supported motions. For massive galaxies $V_{\rm c}$ is very close to the rotation traced by the gas, $V_{\rm c} \approx V_{\rm rot}$. For the dwarfs the story is different as pressure-supported motions become more important. Therefore, in all our dwarfs the gas-asymmetric drift correction has been applied to obtain $V_{\rm c}$ from $V_{\rm rot}$. Once $V_{\rm c}$ is obtained for all the galaxies, we aim to derive the stellar rotation velocities via the relation $V_*^2 = V_{\rm c}^2 - V_{\rm AD,*}^2$, where $V_{\rm AD*}$ is the stellar asymmetric drift correction.

It can be shown (e.g. Binney & Tremaine 2008; Noordermeer et al. 2008), that for galaxies with exponential density profile the stellar asymmetric drift correction $V_{\rm AD*}$ is given by the expression

$$V_{\rm AD*}^2 = \sigma_{*,R}^2 \left[\frac{R}{R_{\rm d}} - \frac{1}{2} \right] - R\ \frac{d\sigma_{*,R}^2}{dR}\ , \tag{5.2}$$

where $R_{\rm d}$ is the exponential disc scale length, and $\sigma_{*,R}$ the radial component of the stellar velocity dispersion. This expression assumes the anistropy $\sigma_{*,z} = \sigma_{*,\phi} = \sigma_{*,R}/\sqrt{2}$ (e.g. Binney & Tremaine 2008; Noordermeer et al. 2008; Leaman et al. 2012), but we note that P18 found just small differences (less than 10%) if isotropy is assumed.

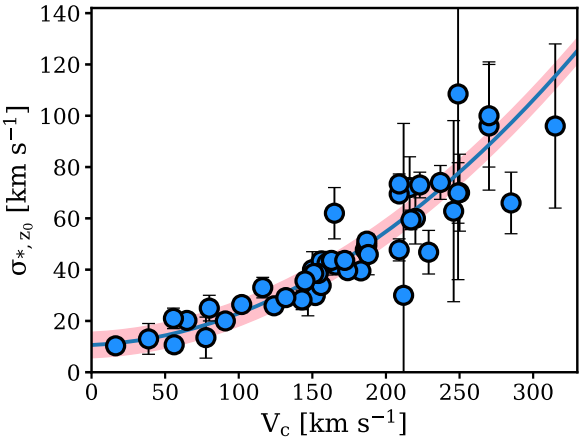

Figure 5.2: Relation between the circular speed and the central stellar velocity dispersion in the vertical direction for spiral and dwarf galaxies. Blue points represent the values from a compilation of studies and the blue line and pink band are a fit to the points and its assumed uncertainty, respectively. Not all the galaxies have a reported uncertainty in V_c, so we do not plot any horizontal errorbar for the sake of consistency.

5

From theoretical arguments (van der Kruit & Searle 1981; van der Kruit 1988), later confirmed by observations (e.g. Bottema 1993; Swaters 1999; Martinsson et al. 2013, and references therein), the stellar velocity dispersion profile follows an exponential vertical profile of the form $\sigma_{*,z} = \sigma_{*,z_0}\ \exp(-R/2R_d)$, although there are not many observational constraints regarding this for the smallest dwarfs (e.g. Hunter et al. 2005; Leaman et al. 2012; Johnson et al. 2015). While we do not know σ_{*,z_0} a priori, different authors have found correlations between σ_{*,z_0} and different galaxy properties, such as surface brightness, absolute magnitude, and circular speed (see for instance Bottema 1993; Martinsson et al. 2013; Johnson et al. 2015).

We exploit the relation between V_c and σ_{*,z_0} to estimate the latter. We compile both parameters for a set of galaxies in the literature, ranging from massive spirals to small dwarf irregulars (Bottema 1993; Swaters 1999; van der Marel et al. 2002; Hunter et al. 2005; Leaman et al. 2012; Martinsson et al. 2013; Johnson et al. 2015; Hermosa Muñoz et al. 2020), as shown in Fig. 5.2. A second-order polynomial provides a good fit to the points through the relation:

$$\frac{\sigma_{*,z_0}}{\text{km s}^{-1}} = 9.7\left(\frac{V_c}{100\text{ km s}^{-1}}\right)^2 + 2.6\left(\frac{V_c}{100\text{ km s}^{-1}}\right) + 10.61\ . \tag{5.3}$$

We adopt an uncertainty of ± 5 km s^{-1} in σ_{*,z_0}, shown as a pink band in Fig. 5.2, motivated by different tests while fitting the observational points.

Finally, it is also observed (see e.g. Barat et al. 2020 and the previous references) that the stellar velocity dispersion profile rarely goes below 5−10 km s^{-1} even at the outermost radii. Therefore, we set a 'floor' value for the $\sigma_{*,z}$ profile equal to 10 km s^{-1}, such that it never goes below this value. With this, we have fully defined $\sigma_{*,z}$, so we can proceed to compute $\sigma_{*,R}$ and thus V_{AD*}. We note here that adopting a floor value has as the consequence that some dwarfs will have a $\sigma_{*,R}$ that stays constant at large radii, similar to what has been reported

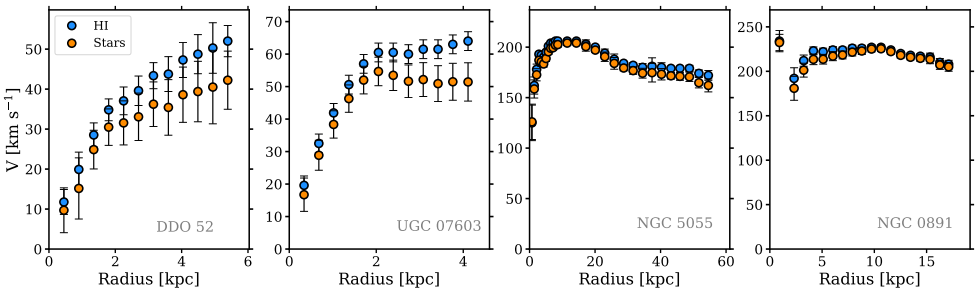

Figure 5.3: Gas (blue) and stellar (orange) rotation curves for two dwarf (*left*) and two massive (*right*) galaxies, showing the relative importance of the asymmetric drift correction.

in some observations of dwarf irregulars (e.g. Hunter et al. 2005; van der Marel et al. 2002).

As expected, we find that for massive discs the correction is very small, but it can be more important for less massive galaxies. Fig. 5.3 illustrates this with four examples that demonstrate that while the correction is negligible for the massive spirals, for the dwarfs it is not. For the dwarfs, while the uncertainty in V_* is often consistent with the values of V_c and V_{rot}, the offset is systematic and important in some cases, highlighting the importance of applying the stellar asymmetric drift correction. For a few dwarf galaxies (DDO 181, DDO 210, DDO 216, NGC 3741, and UGC 07577) the resulting stellar rotation curves are too affected by the correction to be considered reliable: Either they have very large uncertainties such that the stellar rotation curve is compatible with zero at all radii, or it simply goes to zero; the j_* and j_{bar} of these galaxies are therefore discarded. Further tests on our approach to estimate V_* and its robustness can be found in Appendix 5.B.

5

Deriving j_{bar}

Once we estimated j_* after taking into account the stellar asymmetric drift correction, we computed j_{bar} profiles with the expression

$$j_{bar} = f_{gas} j_{gas} + (1 - f_{gas}) j_* \ , \tag{5.4}$$

where f_{gas} is the gas fraction, and with j_{gas} and j_* computed following Eq. 5.1. The uncertainty in j_k (with k being stars or gas) is estimated as (e.g. Lelli et al. 2016b; P18):

$$\delta_{j_k} = 2\ R_{c_k} \sqrt{\frac{1}{N}\sum_i^N \delta_{v_i}^2 + \left(\frac{V_f}{\tan i}\delta_i\right)^2 + \left(V_f \frac{\delta_D}{D}\right)^2} \ , \tag{5.5}$$

with R_c a characteristic radius (defined below in Eq. 5.6), V_f the velocity of the flat part of the rotation curve[1], δ_{v_i} the individual uncertainties in the rotation velocities, i the inclination of the galaxy and δ_i its uncertainty, and D and δ_D the distance to the galaxy and its uncertainty, respectively. In turn, R_c is defined as

$$R_{c_k} = \frac{\int_0^R R'^2 \; \Sigma_k(R') \; (R') \; dR'}{\int_0^R R' \; \Sigma_k(R') \; dR'} \; . \tag{5.6}$$

For an exponential profile, R_c becomes R_d, as used in P18. The uncertainty associated with j_{bar} comes from propagating the uncertainties in Eq. 5.4.

We remind the reader that we have accounted for the presence of helium by assuming $M_{gas} = 1.33 \; M_{HI}$, and neglect any input from molecular gas to j_{bar} or M_{bar}. This does not affect our analysis in a significant way: In comparison with the H I and stellar components, the contribution of molecular gas to the baryonic mass is marginal (e.g. Catinella et al. 2018; Cimatti et al. 2019, and references therein), and since molecular gas is much more concentrated than the H I, it contributes even less to the final j_{bar} (e.g. Obreschkow & Glazebrook 2014). In a similar way, we do not attempt to take the angular momentum of the galactic coronae (e.g. Pezzulli et al. 2017) into consideration.

5.3.2 Convergence criteria

We determined j_{gas} and j_* by means of Eq. 5.1; Fig. 5.4 shows representative examples of j_{gas} and j_* cumulative profiles. Then, we combined them to obtain j_{bar} with Eq. 5.4.

It is important to see whether or not the cumulative profiles converge at the outermost radii because non-converging profiles may lead to a significant underestimation of j. To decide whether or not the cumulative profile of a galaxy (for stars, gas and baryons independently) is converging or not, we proceed as follows. We fit the outer points of the profile with a second-order polynomial $\mathcal{P}$; in practice we fit the outer 20% of the profile or the last four points if the outer 20% of the profile spans only three points, for the sake of robustness in the fit. Then, we extract the value of j at the outermost point of the observed profile, and we compare it with the maximum value that $\mathcal{P}$ would have if extrapolated to infinity. When the ratio $\mathcal{R}$ between these two is 0.8 or larger, we consider the profile as converging. Fig. 5.4 shows representative cases of j_{gas} and j_* cumulative profiles and their corresponding $\mathcal{P}$, exemplifying the cases where the profile has reached the flat part (blue), where it shows signs of convergence (green) and we accept it, and where it is clearly not converging (orchid) and thus is excluded from further analyses.

Our choice of using $\mathcal{R} \geq 0.8$ is empirically driven, and we check its performance as follows. Using about 50 galaxies with clearly convergent j profiles (for instance NGC 7793 in Fig. 5.4), which have $\mathcal{R} = 1$, we do the following exercise. We remove the outermost point of the cumulative profile, and fit the

[1] If the rotation curve does not show clear signs of flattening, according to the criterion of Lelli et al. (2016b), we use the outermost measured circular speed.

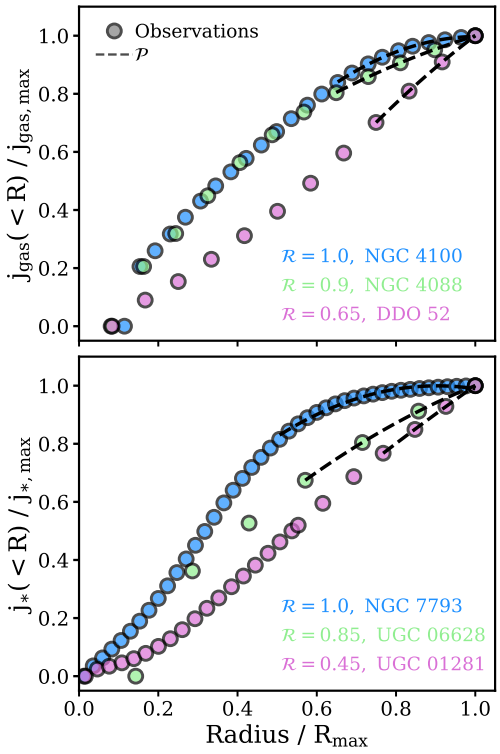

Figure 5.4: Example of representative cumulative j_{gas} and j_* profiles in our sample. The axes are normalised to allow the comparison between the profiles. The points show the observed cumulative profiles for the gas (*top*) and stellar (*bottom*) component, while the dashed lines show the fitted polynomial $\mathcal{P}$ to these profiles (see text). The name of the galaxy and the value of the convergence factor $\mathcal{R}$ for their profiles are provided. Only galaxies with $\mathcal{R} \geq 0.8$ are used in our analysis. We note that, due to the normalisation, the last point of all the profiles overlap with each other.

last 20% of the resulting profile with a new polynomial $\mathcal{P}'$, which then implies a new (lower) $\mathcal{R}'$; this step is repeated until $\mathcal{R}'$ falls to the limit value of 0.8. When this happens, we compare the maximum value of the cumulative profile at the radius where $\mathcal{R}' = 0.8$ with respect to the maximum value of the original ($\mathcal{R} = 1$) profile. Not unexpectedly, these tests reveal that imposing $\mathcal{R} \geq 0.8$ as a convergence criterion allows for a recovery of j with less than 15% of difference with respect to the case where $\mathcal{R} = 1$ in the case of the stars, and less than 20% in the case of the gas. Discrepancies below 20% translate into sub-0.1 dex differences in the final scaling laws. Changing our criterion to a stricter $\mathcal{R} \geq 0.9$ only improves the recovery by $\sim 5\%$. Relaxing the criterion to $\mathcal{R} \geq 0.7$ increases the discrepancies by about $5 - 10\%$, giving total differences of the order of 0.15 dex. Given this, we adopt $\mathcal{R} \geq 0.8$ as a good compromise, but we notice that using $\mathcal{R} \geq 0.7$ or $\mathcal{R} \geq 0.9$ does not change the nature of the results shown below. This criterion is found to be useful not only because it is simple and applicable to stars, gas, and baryons, but also because it uses all the information in the outer part of the cumulative profile, rather than in the last point only (e.g. P18; Marasco et al. 2019). More information on the effects of changing the required $\mathcal{R}$ can be found in Appendix 5.B.

We visually inspect the cumulative profiles to make sure that our convergence criterion is meaningful for all the galaxies. For the rest of this study we will

analyse only those galaxies whose specific angular momentum cumulative profile meets our convergence criteria, defining in this way our final sample. Table 5.1 provides the list of galaxies we compiled, giving their mass and specific angular momentum for stars, gas, and baryons, together with the exponential disc scale length and the value of the convergence factor $\mathcal{R}$. According to our criterion discussed above, out of our 157 galaxies, 132 have a convergent j_* profile, 87 a convergent $j_{\rm gas}$, and 106 a convergent $j_{\rm bar}$.

The fact that the number of galaxies with converging j_* profiles is larger than the number with converging $j_{\rm gas}$ ones is because Σ_* declines much faster than $\Sigma_{\rm gas}$, such that in outer rings of the rotation curves the contribution from stars is often negligible. Instead, $\Sigma_{\rm gas}$ is more extended (in fact enough flux to trace the rotation curve is needed), making it harder for its cumulative profile to converge. This is also clear from Fig. 5.4, where the flattening of the stellar profiles is more evident than for the gas profiles.

Since $j_{\rm bar}$ is not only the sum of j_* and $j_{\rm gas}$ but is weighted by the gas fraction (Eq. 5.4), there can be cases where even if one of the two does not converge, $j_{\rm bar}$ does. For example, in a galaxy with a small gas fraction, the convergence of j_* ensures the convergence of $j_{\rm bar}$, regardless of the behaviour of $j_{\rm gas}$. The same can happen for a heavily gas-dominated dwarf with a converging $j_{\rm gas}$ profile. This explains why there are more converging $j_{\rm bar}$ profiles than $j_{\rm gas}$ ones.

5.4 The stellar, gas & baryonic specific angular momentum−mass relations for disc galaxies

5.4.1 The $j_* - M_*$ relation

In the left panel of Fig. 5.5 we show the $j_* - M_*$ plane for our sample of galaxies. We find a clear power-law relation followed reasonably well by all galaxies. It is particularly tight at the high-mass regime, and the scatter (along with the observational errors) increases when moving towards lower masses; despite this, there is no compelling evidence for a change in the slope of the relation at dwarf galaxy scales.

We fit our points with a power-law of the form

$$\log\left(\frac{j}{\rm kpc\ km\ s^{-1}}\right) = \alpha[\log(M/{\rm M}_\odot) - 10] + \beta\ , \tag{5.7}$$

where in this case $j = j_*$ and $M = M_*$.

We fit Eq. 5.7 using a likelihood as in P18 and Posti et al. (2020), which includes a term for the orthogonal intrinsic scatter ($\sigma_\perp$), and we use a Markov chain Monte Carlo approach (Foreman-Mackey et al. 2013) to constrain the parameters after assuming uninformative priors. We find the best-fitting parameters to be $\alpha = 0.53 \pm 0.02$ and $\beta = 2.71 \pm 0.02$, with a perpendicular intrinsic scatter $\sigma_\perp = 0.15 \pm 0.01$. Table 5.2 provides the coefficients for all the $j - M$ relations found in this chapter.

Table 5.1: Main properties of our galaxy sample. (1) Name. (2 & 3) Stellar mass and uncertainty. (4 & 5) Gas mass and uncertainty. (6 & 7) Baryonic mass and uncertainty. (8 & 9) Stellar specific angular momentum and uncertainty. (10 & 11) Gas specific angular momentum and uncertainty. (12 & 13) Baryonic specific angular momentum and uncertainty. (14) Exponential disc scale length. (15, 16 & 17) Convergence factor for the j_*, $j_{\rm gas}$ and $j_{\rm bar}$ profiles. These convergence criteria should be seen as an indication of the convergence of the j profiles rather than taken at face value to predict the exact value of j. In addition to this, values below 0.7 should be taken with extra caution as we find them to be low not necessarily because they are very far from convergence, but because they rely on an extrapolation of a polynomial that it is usually monotonically increasing for those profiles. Along this chapter we used $\mathcal{R} \geq 0.8$ to define a j profile as convergent. The complete version of this table is available as electronic supplementary material in the published version of this Chapter.

Name	M_*	δM_*	$M_{\rm gas}$	$\delta M_{\rm gas}$	$M_{\rm bar}$	$\delta M_{\rm bar}$	j_*	δj_*	$j_{\rm gas}$	$\delta j_{\rm gas}$	$j_{\rm bar}$	$\delta j_{\rm bar}$	$R_{\rm d}$	$\mathcal{R}^{\dagger}_{*}$	$\mathcal{R}^{\dagger}_{\rm gas}$	$\mathcal{R}^{\dagger}_{\rm bar}$
	[10^8 M$_\odot$]		[10^8 M$_\odot$]		[10^8 M$_\odot$]		[kpc km s^{-1}]		[kpc km s^{-1}]		[kpc km s^{-1}]		[kpc]			
(1)	(2)	(3)	(4)	(5)	(6)	(7)	(8)	(9)	(10)	(11)	(12)	(13)	(14)	(15)	(16)	(17)
DDO 50	1.80	0.48	7.19	1.34	8.99	1.42	58	26	142	28	126	38	0.90	1.00	0.97	0.97
DDO 52	0.88	0.23	2.44	0.43	3.31	0.48	66	13	153	17	130	31	0.94	0.99	0.70	0.75
DDO 87	0.41	0.26	2.04	1.24	2.44	1.27	83	34	141	53	132	118	1.13	0.25	0.79	0.77
DDO 126	0.33	0.10	1.45	0.31	1.78	0.33	40	20	62	8	58	18	0.82	0.98	0.85	0.88
DDO 133	0.43	0.29	1.16	0.77	1.59	0.82	49	24	65	26	60	54	0.80	0.90	0.92	0.92
DDO 168	0.84	0.22	2.71	0.52	3.55	0.57	64	14	109	13	98	26	1.03	0.99	0.87	0.89
NGC 4639	166.10	45.35	17.01	2.78	183.10	45.43	830	48	1394	70	882	63	1.68	0.99	0.90	0.97
NGC 4725	523.10	144.00	35.08	5.86	558.20	144.10	1914	160	3568	270	2018	170	3.39	1.00	0.98	1.00
NGC 5584	114.40	31.21	22.84	3.73	137.20	31.43	757	77	1022	83	802	89	2.63	0.97	0.93	0.96

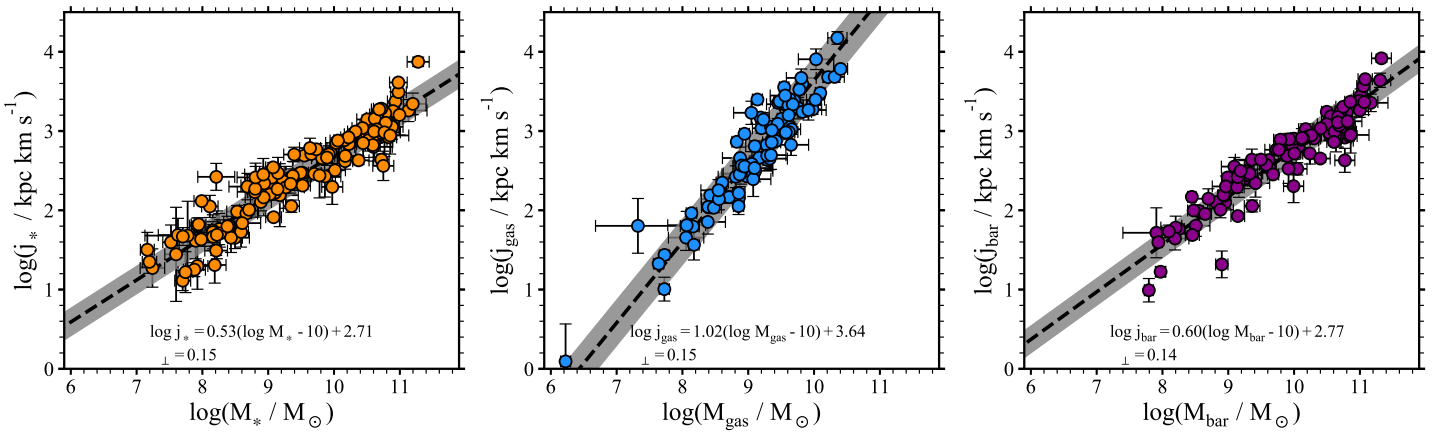

Figure 5.5: From *left* to *right*: stellar, gas, and baryonic $j - M$ relations for our sample of galaxies. In all the panels the circles represent the observed galaxies, while the dashed black line and grey region show, respectively, the best-fitting relations and their perpendicular intrinsic scatter. The three relations are well fitted by unbroken power-laws: The best-fitting relations are shown for each panel (see Table 5.2). We remind the reader that each panel includes only the galaxies with convergent j_*, $j_{\rm gas}$ and $j_{\rm bar}$ profile, respectively, so the galaxies shown in one panel are not necessarily the same as in the other panels.

Table 5.2: Coefficients of the best-fitting $j - M$ laws, as shown in Fig. 5.5, obtained by fitting the observed relations with Eq. 5.7.

	α	β	$\sigma_\perp$
Stars	0.53 ± 0.02	2.71 ± 0.02	0.15 ± 0.01
Gas	1.02 ± 0.04	3.64 ± 0.03	0.15 ± 0.01
Baryons	0.60 ± 0.02	2.77 ± 0.02	0.14 ± 0.01

5.4.2 The $j_{\rm gas} - M_{\rm gas}$ relation

The middle panel of Fig. 5.5 shows the gas specific angular momentum−mass relation. Similarly to the stellar case, the relation of the gas component is also well represented by a simple power-law (Eq. 5.7) with best-fitting parameters $\alpha = 1.02 \pm 0.04$, $\beta = 3.64 \pm 0.03$ and $\sigma_\perp = 0.14 \pm 0.01$.

The slope is significantly steeper than for the stars, but the trend is also followed remarkably well by all galaxies. We mainly cover ∼3 orders of magnitude in gas mass, $8 \leq \log(M_{\rm gas}/{\rm M}_\odot) \leq 11$, although we have one galaxy (DDO 210) at $M_{\rm gas} \approx 10^6$ M$_\odot$ whose position is perfectly consistent with the $j_{\rm gas} - M_{\rm gas}$ sequence of more massive galaxies. Moreover, it is clear that our dwarfs follow the same law as more massive galaxies.

5.4.3 The $j_{\rm bar} - M_{\rm bar}$ relation

In the right panel of Fig. 5.5 we show the $j_{\rm bar} - M_{\rm bar}$ plane for our sample. The relation looks once more like an unbroken power-law, so we fit the observations with Eq. 5.7. The best-fitting coefficients are $\alpha = 0.60 \pm 0.02$, $\beta = 2.77 \pm 0.02$ and $\sigma_\perp = 0.14 \pm 0.01$.

The perpendicular intrinsic scatter of the baryonic relation ($\sigma_\perp = 0.14 \pm 0.01$) is consistent with the individual values of the stellar ($\sigma_\perp = 0.15 \pm 0.01$) and gas ($\sigma_\perp = 0.15 \pm 0.01$) relations. This is likely due to the fact that the stellar and gas components dominate at different $M_{\rm bar}$, such that at high $M_{\rm bar}$ the intrinsic scatter of the baryonic relation is set by the intrinsic scatter of $j_* - M_*$ relation, while at the low $M_{\rm bar}$ it is the scatter of the $j_{\rm gas} - M_{\rm gas}$ relation the one that dominates.

One of the most important results drawn from the baryonic relation in Fig. 5.5 is that the most massive spirals and the smallest dwarfs in our sample lie along the same relation. We discuss this in more detail in Sec. 5.5.3.

In addition to our fiducial best-fitting parameters given above, we performed the exercise of building the $j_{\rm bar} - M_{\rm bar}$ relation using only the 77 galaxies that have both a convergent j_* and $j_{\rm gas}$ profile, instead of the 104 galaxies with converging $j_{\rm bar}$ profile but without necessarily having both convergent j_* and $j_{\rm gas}$ profiles (see Sec. 5.3.2). The best-fitting parameters for Eq. 5.7 using this subsample are $\alpha = 0.56 \pm 0.02$, $\beta = 2.87 \pm 0.02$ and $\sigma_\perp = 0.11 \pm 0.01$. This slope

is consistent with the fiducial slope derived with our convergence criteria within their uncertainties, and the intercept changes by only ~ 0.1 dex. Also, not unexpectedly, the intrinsic scatter is slightly reduced. In this subsample, however, the low-mass regime is significantly reduced, especially below $M_{\rm bar} < 10^{9.5}$ M$_\odot$.

5.5 Discussion

In Sec. 5.4 we showed and described the stellar and gas $j-M$ relations, which are then used to derive the $j_{\rm bar} - M_{\rm bar}$ relation. Empirically, the three laws are well characterised by unbroken linear relations (in log-log space, see Eq. 5.7). While there are no clear features indicating breaks in the relations, we statistically test this possibility by fitting the $j - M$ laws with double power-laws. The resulting best-fitting double power-laws are largely indistinguishable from the unbroken power-laws within our observed mass ranges. Moreover, the linear models are favoured over the double power-law models by the Akaike information criterion (AIC) and the Bayesian information criterion (BIC). Compared to the values obtained for the single power-law, the AIC and BIC of the broken power-law fit are larger by 7 and 12, respectively, in the case of the stellar relation, by 5 and 10 for the gas, and by 6 and 11 for the baryons. Having established that the single power-laws provide an appropriate fit to the observed $j - M$ planes, in the following subsections we discuss some similarities and discrepancies between our results and previous works, as well as other further considerations regarding the phenomenology of these laws.

5.5.1 Comparison with previous works

$j_* - M_*$ relation

The stellar specific angular momentum−mass relation for disc galaxies has been recently reviewed and refined by P18. An important result that they show, is that while some galaxy formation models (e.g. Obreja et al. 2016) predict a break or flattening in the $j_* - M_*$ law at the low-mass end, the observational relation is an unbroken power-law from the most massive spiral galaxies to the dwarfs. While there is evidence for this in Fig. 2 of P18, their sample has very few objects with $M_* < 10^{8.5}$ M$_\odot$, a fact that may pose doubts on the supposedly unbroken behaviour of the relation. Our sample largely overlaps with the sample of P18 who used the SPARC compilation, but importantly, as described in Sec. 5.2, it also includes the dwarf galaxies from LITTLE THINGS, LVHIS, VLA-ANGST, and WHISP, adding several more galaxies with $M_* < 10^{8.5}$ M$_\odot$, and allowing us to set strong constraints on the relation at the low-mass regime. As mentioned before, we find a similar behaviour as the one reported by P18: Dwarf and massive disc galaxies lie in the same scaling law.

P18 report very similar values to ours (see also Fall 1983; Romanowsky & Fall 2012; Fall & Romanowsky 2013; Cortese et al. 2016). Those authors find $\alpha = 0.55 \pm 0.02$ and $\sigma_\perp = 0.17 \pm 0.01$; the parametrisation used to derive their intercept $\beta = 3.34 \pm 0.03$ is different than that used in Eq. 5.7, but close to ours

(0.1 dex higher) once this is taken into account. Therefore, our values are in very good agreement with recent determinations of the $j_* - M_*$ relation, with the advantage of a better sampling at the low-M_* regime. We also notice that despite including more dwarfs ($\sim$ 35, those from LITTLE THINGS, LVHIS, WHISP and VLA-ANGST), which increase the observed scatter at the low-M_* regime, we find a slightly smaller global intrinsic scatter.

$j_{\rm gas} - M_{\rm gas}$ relation

The slope that we find for the $j_{\rm gas} - M_{\rm gas}$ plane ($\alpha = 1.02 \pm 0.04$) is about two times the value of the slope of the stellar relation ($\alpha = 0.53 \pm 0.02$). It is also steeper than the slope of 0.8 ± 0.08 reported in Kurapati et al. (2018) (see also Cortese et al. 2016). Nevertheless, those authors analysed galaxies with $M_{\rm gas} < 10^{9.5}$ M$_\odot$, for which the individual values of their $j_{\rm gas}$ estimates compare well with ours as their points lie within the scatter of ours. Therefore, the differences in the slope reported by Kurapati et al. (2018) and ours are seemingly due to the shorter mass span of their sample: Once galaxies with $6 \leq \log(M_{\rm gas}/{\rm M}_\odot) \leq 11$ are put together, a global and steeper slope close to 1 emerges. Chowdhury & Chengalur (2017) and Butler et al. (2017) do not report the value of their slopes, but as it happens with the sample from Kurapati et al. (2018), the majority of their galaxies lie within the scatter of our larger sample.

$j_{\rm bar} - M_{\rm bar}$ relation

Our best-fitting slope for the $j_{\rm bar} - M_{\rm bar}$ law is 0.60 ± 0.02. This is comparable, within the uncertainties, to the value of 0.62 ± 0.02 reported by Elson (2017), and significantly lower than the value of 0.94 ± 0.05 from Obreschkow & Glazebrook (2014) (this for bulgeless galaxies, see Chowdhury & Chengalur 2017), and than the value of 0.89 ± 0.05 from Kurapati et al. (2018). It is important, however, to bear in mind that the sample from Obreschkow & Glazebrook (2014) consists mainly of massive spirals, and the sample from Kurapati et al. (2018) consists of dwarfs only, so the differences are at least partially explained by the fact that we explore a broader mass range.

Very recently, Murugeshan et al. (2020) reported a slope of 0.55 ± 0.02 for a sample of 114 galaxies. Their slope is slightly shallower but nearly statistically compatible with our value once both $1\sigma_\perp$ uncertainties are taken into account. They do not report the value of their intercept, but based on the inspection of their Fig. 3 we find it also in agreement with ours. Nevertheless, there are some differences in our analysis with respect to theirs. For instance, our mass coverage at $M_{\rm bar} < 10^9$ M$_\odot$ is a bit more complete (11 galaxies in their work vs. 23 in our convergent sample), and, very importantly, we applied a convergence criterion to all our sample in order to select only the most accurate j profiles. In addition to this, while both studies use near infrared luminosities to trace M_* (mostly $3.6\mu m$ in our case, and $2.2\mu m$ for Murugeshan et al. 2020), we use a Υ that has been found to reduce the scatter in scaling relations that depend on M_* such as the baryonic Tully-Fisher relation (see Lelli et al. 2016b), while

the calibration used by Murugeshan et al. (2020) may have a larger scatter, up to one order of magnitude in M_* at given infrared luminosity (Wen et al. 2013). Finally, we determine V_* instead of assuming co-rotation of gas and stars, although this does not play an important role when determining the global $j_{\rm bar} - M_{\rm bar}$ relation (cf. Appendix 5.B).

Despite these differences, which may lead to discrepancies on a galaxy by galaxy basis, the slopes between both works are statistically in agreement. Murugeshan et al. (2020) mention that it is likely that their slope is slightly biased towards flatter values given their lack of galaxies with $M_{\rm bar} < 10^9$ M$_\odot$. For our sample, which extends towards lower masses, the slope is marginally steeper, in agreement with the reasoning of Murugeshan et al. (2020).

5.5.2 Residuals and internal correlations

In this Section we explore whether or not the $j - M$ relations correlate with third parameters. We show in Fig. 5.5 that the three $j - M$ relations are well described by unbroken power-laws. Yet, this does not necessarily imply that there are no systematic residuals as a function of mass or other physical parameters.

To explore this possibility, in Fig. 5.6 we look at the difference between the measured j of each galaxy and the expected $j_{\rm fit}$ according to the best-fitting power-law we found previously, as a function of M. The first conclusion we reach from this figure is that there does not seem to be any systematic trend of the residuals for the stellar and gas relations as a function of M_* or $M_{\rm gas}$, respectively: Within the scatter of our data, a galaxy is equally likely to be above or below the best-fitting relations. The scenario seems to be different for the baryonic relation (bottom panels in Fig. 5.6), where galaxies with higher baryonic masses tend to scatter below the best-fitting relation while less massive galaxies tend to scatter above it. This is the result of a correlation with the gas fraction, as we discuss later in Sec. 5.5.2.

To further study the behaviour of the residuals from the best-fitting relations and identify parameters correlated with such residuals, we look at internal correlations with other quantities. For instance, given the dependence of $j_{\rm bar}$ on $f_{\rm gas}$ (Eq. 5.4), $f_{\rm gas}$ is an interesting parameter to explore within the $j - M$ relations. The same happens with $R_{\rm d}$, given the relation between the spin parameter λ of dark matter haloes and $R_{\rm d}$ (e.g. Mo et al. 1998; Posti et al. 2020; Zanisi et al. 2020), and that for galaxy discs with Sérsic profiles and flat rotation curves $j_* \propto R_{\rm d}$ (Romanowsky & Fall 2012). As shown in Fig. 5.6, there are internal correlations with both parameters, which we briefly describe here.

Disc scale length

In the case of the disc scale length as a third parameter, Fig. 5.6 (left panels) encodes also the well-known $M_* - R_{\rm d}$ relation: More massive galaxies have more extended optical disc scale length, although the scatter is relatively large at

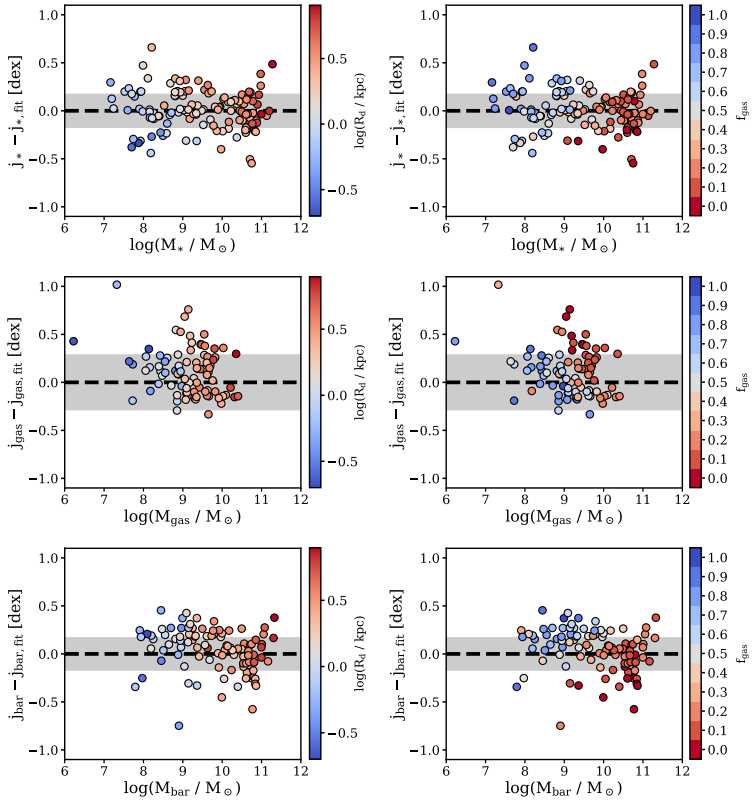

Figure 5.6: Residuals from the best-fitting $j - M$ laws at fixed M. The case of no offset from the best-fitting relation is represented with a dashed black line, while the grey band shows the scatter of the relation. *Left* and *right* panels include, respectively, the disc scale length (see Table 5.1) and the gas fraction as colour-coded third parameters. The main conclusions from this figure are that at fixed M_* galaxies with a higher j_* have larger R_d, and at fixed M_bar galaxies with lower f_gas have a lower j_bar.

given M_* (e.g. Fernández Lorenzo et al. 2013; Cebrián & Trujillo 2014; Lange et al. 2015). Nonetheless, the figure also shows other trends at fixed mass.

At fixed M_* (upper left panel), galaxies with a higher than average j_* have a larger R_d. This is not surprising given Eq. 5.1 (see also Romanowsky & Fall 2012), but it is still interesting to show the precise behaviour of this correlation across nearly five orders of magnitude in mass. The trend is not clearly visible in the gas relation (mid left panel), which is not unexpected given the less clear interplay between R_d and j_gas (as opposed to j_*), and the scattered relation between R_d and the size of the gaseous disc (e.g. Lelli et al. 2016a). The inspection of the $j_\mathrm{bar} - M_\mathrm{bar}$ plane (lowermost left panel) reveals that the trend of high-j galaxies having larger R_d at fixed M_bar is visible at the high-mass regime (where the stellar relation dominates), but becomes less evident at low

masses (where the gas relation is dominant).

Gas fraction

The right hand side panels of Fig. 5.6 show the vertical residuals from the $j - M$ laws adding the gas fraction as a third parameter. Trends also seem to emerge in these cases. In general, the relation between mass and gas fraction (e.g. Huang et al. 2012; Catinella et al. 2018) is clear: More massive galaxies have lower $f_{\rm gas}$ on average (see also Fig. 5.1).

From the $j_* - M_*$ relation, we can see that at fixed M_* galaxies with higher $f_{\rm gas}$ have larger j_* than galaxies with lower $f_{\rm gas}$. Results along the same lines were reported by Huang et al. (2012) using unresolved ALFALFA observations (Haynes et al. 2011), by Lagos et al. (2017) analysing hydrodynamical simulations, and by e.g. Stevens et al. (2018), Zoldan et al. (2018), and Irodotou et al. (2019) using semi-analytic models.

The above trend is inverted in the case of the gas: At fixed $M_{\rm gas}$ disc galaxies with lower gas content have higher $j_{\rm gas}$. This is perhaps due to the fact that the fuel for star formation is the low-j gas, so the remaining gas reservoirs of gas-poor galaxies effectively see an increase in its $j_{\rm gas}$ (see also Lagos et al. 2017 and Zoldan et al. 2018).

That gas-poor galaxies have higher $j_{\rm gas}$ may also be related with the H I surface density profile of galaxies. At fixed $M_{\rm gas}$ galaxies with low $f_{\rm gas}$ have higher M_*, and galaxies with high M_* often present a central depression in their H I distribution (e.g. Swaters 1999; Martinsson et al. 2016, and references therein). At fixed $M_{\rm gas}$ the central depression implies that the mass distribution is more extended, and so $j_{\rm gas}$ should be larger, as we find in our observational result (see also Murugeshan et al. 2019).

Lastly, we inspect the residuals for the baryonic relation (bottom right panel of Fig. 5.6). At fixed $M_{\rm bar}$ galaxies with lower $f_{\rm gas}$ have a lower $j_{\rm bar}$. This is line with both Eq. 5.4 and the fact that across all our observed mass regime $j_{\rm gas} > j_*$: At fixed $M_{\rm bar}$, gas-poor galaxies have a smaller contribution from $j_{\rm gas}$, which is larger than j_*. By adding $f_{\rm gas}$ directly into the $j_{\rm bar} - M_{\rm bar}$ plane in Fig. 5.7 we notice that gas-rich and gas-poor galaxies seem to follow relations with similar slopes but slightly different intercepts, with the intercept of gas-rich galaxies being higher. In fact, the galaxies that fall below the main baryonic relation in Fig. 5.5 and Fig. 5.6 are mostly those with very low $f_{\rm gas}$ for their $M_{\rm bar}$.

Murugeshan et al. (2020) studied the $j_{\rm bar} - M_{\rm bar}$ relation dividing their galaxies in two groups: Those with near neighbours and those relatively more isolated. They find that at the high-mass end, galaxies with close neighbours tend to have lower $j_{\rm bar}$ than expected, and they suggest that this is likely to be the result of past or present interactions that lowered $j_{\rm bar}$ (see also Lagos et al. 2017). However, somewhat surprisingly, those authors find no significant differences in $j_{\rm bar}$ as a function of the second nearest-neighbour density (see their Fig. 5). We do not segregate our galaxies in terms of isolation, but we find that those with lower $j_{\rm bar}$ are those that show a low $f_{\rm gas}$.

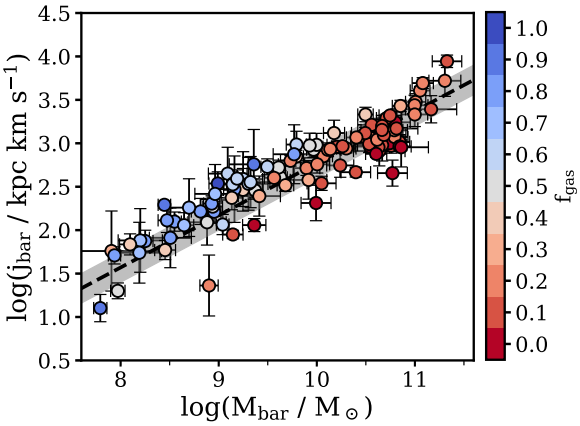

Figure 5.7: Baryonic $j - M$ relation colour-coding the galaxies according to their gas fraction. Gas-rich galaxies seem to have a slightly higher intercept than gas-poor ones.

Some authors have also discussed the relation of $f_{\rm gas}$ with $j_{\rm bar}$ via the stability parameter $q = j_{\rm bar}\sigma/GM_{\rm bar}$, with σ the H I velocity dispersion and G the gravitational constant (see Obreschkow et al. 2016; Lutz et al. 2018; Stevens et al. 2018; Murugeshan et al. 2020). According to them (see also Romeo 2020), at fixed $M_{\rm bar}$ a galaxy with higher $j_{\rm bar}$ has a higher q, meaning that it is more stable against gravitational collapse. On the other hand, galaxies with low-$j_{\rm bar}$ form stars more efficiently as they are less stable. In principle, the bottom right panel of Fig. 5.6 seems in line with their expectations, as $f_{\rm gas}$ increases with positive $j_{\rm bar} - j_{\rm bar,fit}$, although discussion exists in the literature regarding whether or not star formation is primarily regulated by angular momentum and disc stability, or, for instance, by gas cooling or gas volume density (e.g. Leroy et al. 2008; Obreschkow et al. 2016; Bacchini et al. 2019a). A deeper investigation on how j, M and $f_{\rm gas}$ intertwine together will be provided in a forthcoming study (Chapter 6, i.e. Mancera Piña et al. 2021b).

5.5.3 The specific angular momentum of dwarf galaxies

Our results on the $j_* - M_*$ plane provide further support to the conclusions from P18 that dwarfs and massive spirals seemingly follow the same scaling law. There are no features in our measurements suggesting a break, although the scatter seems larger at the low-mass end.

Another result we find is that dwarf galaxies fall in the same baryonic (and gas) sequence that describes more massive galaxies well. Results along the same line were reported by Elson (2017), but for a smaller sample and relying on extrapolations of the rotation curves. These findings seem in tension with the results from Chowdhury & Chengalur (2017), Butler et al. (2017) and Kurapati et al. (2018), who concluded that dwarfs have a higher $j_{\rm bar}$ than expected from an extrapolation of the relation for massive spirals. However, this is due to the fact that those authors were comparing their data with the relation found by Obreschkow & Glazebrook (2014), which has a very steep slope and thus tends to progressively underestimate $j_{\rm bar}$ at low $M_{\rm bar}$. As mentioned above, their

dwarf galaxies lie close to our dwarfs in the $j_{\rm bar} - M_{\rm bar}$ plane.

In order to explain the idea of dwarfs having a higher $j_{\rm bar}$ than expected, Chowdhury & Chengalur (2017) and Kurapati et al. (2018) discussed two main possibilities: That the higher $j_{\rm bar}$ is a consequence of feedback processes that remove a significant amount of low-j gas, or that it is due to a significantly higher 'cold' gas accretion (see for instance Sancisi et al. 2008; Kereš et al. 2009) in dwarfs than in other galaxies. Kurapati et al. (2018), with similar results as Chowdhury & Chengalur (2017), already discussed that the former scenario is unlikely given the unrealistically high mass-loading factors that would be required, but they left open the possibility of the cold gas accretion. In this context, our results would suggest that these mechanisms are not needed to be particularly different in dwarfs compared with massive spirals as both group of galaxies lie in the same sequence; instead, they suggest that feedback and accretion processes act in a rather continuous way as a function of mass. This seems in agreement with the results we show in Sec. 5.5.4 regarding the retained fraction of angular momentum.

5.5.4 The retained fraction of angular momentum

In a ΛCDM context, the angular momentum of both dark matter and baryons is acquired by tidal torques (Peebles 1969). Considering the link between the specific angular momentum of the dark matter halo and its halo mass ($j_{\rm h} \propto \lambda M_{\rm h}^{2/3}$), the baryonic specific angular momentum is given by the expression (see e.g. Fall 1983; Romanowsky & Fall 2012; Obreschkow & Glazebrook 2014; P18)

$$\frac{j_{\rm bar}}{10^3 \text{ kpc km s}^{-1}} = 1.96 \left(\frac{\lambda}{0.035}\right) f_{\rm j,bar} \, f_{\rm M,bar}^{-2/3} \left(\frac{M_{\rm bar}}{10^{10} \text{ M}_\odot}\right)^{2/3} , \qquad (5.8)$$

with λ the halo spin parameter, $f_{\rm j,bar}$ the retained fraction of angular momentum ($j_{\rm bar}/j_{\rm h}$), and $f_{\rm M,bar}$ the global galaxy formation efficiency or baryonic-to-halo mass ratio ($M_{\rm bar}/M_{\rm h}$). Since λ is a parameter that is relatively well known from simulations ($\lambda \approx 0.035$, largely independent of halo mass, redshift, morphology and environment, e.g. Bullock et al. 2001a; Macciò et al. 2008), if the individual values of $M_{\rm h}$ were known, it would then be possible to measure $f_{\rm j,bar}$ for each individual galaxy.

Despite not knowing the precise value of $M_{\rm h}$ for all our galaxies, we can still investigate the behaviour of $f_{\rm j,bar}$ in a statistical way. For this, we can assume a stellar-to-halo mass relation to then find which value of $f_{\rm j,bar}$, as a function of mass, better reproduces the observed $j_{\rm bar} - M_{\rm bar}$ relation. We adopt the empirical stellar-to-halo mass relation for disc galaxies recently derived by Posti et al. (2020), by using accurate mass-decomposition models of SPARC and LITTLE THINGS galaxies (see also Read et al. 2017). The relation from Posti et al. (2020) follows a single power-law at all masses and deviates from relations derived with abundance matching especially at the high-mass end, where the abundance-matching relations would predict a break at around $M_{\rm h} \sim 10^{12}$ M$_\odot$

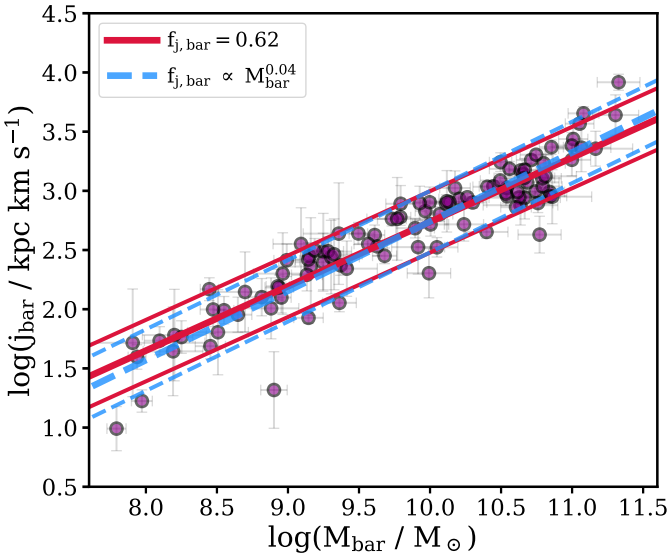

Figure 5.8: Observed $j_{\rm bar} - M_{\rm bar}$ plane (magenta points) compared with the outcome from Eq. 5.8 after assuming a constant (solid red line) or mass-dependent (dashed blue line) $f_{j,\rm bar}$. The lines below and above each relation show their scatter, coming from the scatter on λ and on the stellar-to-halo mass relation.

(e.g. Wechsler & Tinker 2018). As discussed in detail in Posti et al. (2019) and Posti et al. (2020), such an unbroken relation provides a better fit for disc galaxies.

Going back to Eq. 5.8, we explore two simple scenarios: One where the retained fraction of angular momentum is constant, $f_{\rm j,bar} = f_0$, and one where it is a simple function of $M_{\rm bar}$, $\log f_{\rm j,bar} = \alpha \log(M_{\rm bar}/{\rm M}_\odot) + f_1$, and we fit Eq. 5.8 for both of them. In the case of the constant retained fraction, we find $f_{\rm j,bar} = f_0 = 0.62$. The relation obtained by fixing this value in Eq. 5.8 is shown in Fig. 5.8 (solid red line), compared with the observational points. It is clear that the constant $f_{\rm j,bar}$ well reproduces the observed relation. In the case where $f_{\rm j,bar}$ is a function of $M_{\rm bar}$, the best-fitting coefficients are $\alpha = 0.04$ and $f_1 = -0.62$, and the resulting relation is shown in Fig. 5.8 with a dashed blue line.

Both scenarios for $f_{\rm j,bar}$ fit the data equally well, but the fit with a constant $f_{\rm j,bar}$ (having only one free parameter) is favoured by the BIC and AIC criteria. We also notice that the scatter in the relation can be almost entirely attributed to the scatter on λ (0.25 dex, Macciò et al. 2008) and on the stellar-to-halo mass relation (0.07 dex, Posti et al. 2020), without significant contribution from the scatter in $f_{\rm j,bar}$.

This provides observational evidence that despite different processes of mass and specific angular momentum gain and loss, the baryons in present-day disc galaxies have 'retained' a high fraction of the specific angular momentum of the

haloes, as required by early and recent models of galaxy formation (e.g. Fall & Efstathiou 1980; Fall 1983; Mo et al. 1998; Navarro & Steinmetz 2000; van den Bosch et al. 2001; Fall & Romanowsky 2013; Desmond & Wechsler 2015; Posti et al. 2018a; Irodotou et al. 2019). Our constant value for $f_{j,\mathrm{bar}}$ is somewhat smaller than predicted in some cosmological hydrodynamical simulations (e.g. Genel et al. 2015; Pedrosa & Tissera 2015), but it seems to be in good agreement with the outcome of the models from Dutton & van den Bosch (2012), once we account for the different assumptions in the stellar-to-halo mass relation.

As mentioned in the above references (see also Lagos et al. 2017; Cimatti et al. 2019), there are a number of reasons of why $f_{j,\mathrm{bar}}$ may be smaller or larger than 1. These include rather complex relations between biased cooling of baryons, angular momentum transfer from baryons to the dark halo via dynamical friction, feedback processes and past mergers. Thus, it remains somewhat surprising that despite all of these complexities, disc galaxies still find a way to inherit their most basic properties (mass and angular momentum) from their parent dark matter haloes in a rather simple fashion.

5.6 Conclusions

Using a set of high-quality rotation curves, H I surface density profiles, and near-infrared stellar profiles, we homogeneously studied the stellar, gas, and baryonic specific angular momentum−mass laws. Our sample (Fig. 5.1), representative of dwarf and massive regularly rotating disc galaxies, extends about five orders of magnitude in mass and four in specific angular momentum, providing the largest sample (in number and dynamic range) for which the three relations have been studied homogeneously. The specific angular momentum has been determined in a careful way, correcting the kinematics for both pressure-supported motions and stellar asymmetric drift (e.g. Fig. 5.3) and checking the individual convergence of each galaxy (Fig. 5.4).

Within the scatter of the data, the three relations can be characterised by unbroken power-laws (linear fits in log-log space) across all the mass range (Fig. 5.5), with dwarf and big spiral galaxies lying along the same relations. The stellar relation holds at lower masses than reported before, with a similar slope ($\alpha = 0.53$) and intrinsic scatter ($\sigma_\perp = 0.15$) as reported in previous literature. The gas relation has a slope about two times steeper ($\alpha = 1.02$) than the stellar slope and with a higher intercept. The baryonic relation has a slope $\alpha = 0.60$, relatively close to the value of the slope of the stellar relation, and it also has a similar intrinsic scatter as the stellar and gas $j - M$ laws ($\sigma_\perp = 0.14$). We provide the individual values of the mass and specific angular momentum for our galaxies (Table 5.1) as well as the best-fitting parameters for the three $j - M$ relations (Table 5.2).

The three laws also show some dependence on the optical disc scale length R_d and the gas fraction f_gas. The clearest trends are that at fixed M_* galaxies with higher j_* have larger R_d, while at fixed M_bar galaxies with lower f_gas have lower j_bar (Fig. 5.6 and 5.7).

When compared with theoretical predictions from ΛCDM, the $j_{\rm bar} - M_{\rm bar}$ scaling relation can be used to estimate the retained fraction of baryonic specific angular momentum, $f_{\rm j,bar}$. We find that a constant $f_{\rm j,bar} = 0.62$ reproduces well the $j_{\rm bar} - M_{\rm bar}$ law, with little requirement for scatter in $f_{\rm j,bar}$ (Fig. 5.8). In general, this provides empirical evidence of a relatively high ratio between the baryonic specific angular momentum in present-day disc galaxies, and the specific angular momentum of their parent dark matter halo. Overall, our results provide important constraints to (semi) analytic and numerical models of the formation of disc galaxies in a cosmological context. They are key for pinning down which physical processes are responsible for the partition of angular momentum into the different baryonic components of discs.

5.A Kinematic modelling of LVHIS, WHISP, and VLA-ANGST dwarfs

The Local Volume H I Survey (LVHIS, Koribalski et al. 2018), the Westerbork observations of neutral Hydrogen in Irregular and SPiral galaxies (WHISP, van der Hulst et al. 2001) and the Very Large Array-ACS Nearby Galaxy Survey Treasury (VLA-ANGST, Ott et al. 2012) projects, provide deep interferometric observations of a large set of gas−rich nearby galaxies. Full details on the characteristic of the surveys, including targets, observations and data reduction procedures can be found in the references above.

Given that highly reliable rotation curves are needed to estimate the specific angular momentum, we selected the dwarf galaxies in LVHIS, WHISP, and VLA-ANGST that were the most suitable to perform kinematic modelling on them (and in the case of WHISP, galaxies that are not already modelled by Swaters et al. 2002 and included in SPARC). We chose the best galaxies in terms of spatial resolution (at least five resolution elements) and undisturbed gas kinematics (galaxies without interacting neighbours or strong non-circular motions). We are mainly interested in dwarf galaxies with moderate rotation velocities, so we kept those galaxies with an observed velocity field suggesting rotation velocities below ~ 80 km s^{-1}.

We analysed the galaxies using the software ^{3D}BAROLO (Di Teodoro & Fraternali 2015), fitting the rotation velocity, velocity dispersion, inclination, and position angle. Initial estimates on inclination and position angle are determined by fitting the observed H I map, following the procedure described in Chapter 3. All the models converged with very good resemblance to the data. Importantly, we corrected the rotational speed $V_{\rm rot}$ for pressure-supported motions in the gas −often non-negligible in dwarf galaxies (e.g. Iorio et al. 2017). This is crucial as the circular speed ($V_{\rm c}^2 = V_{\rm rot}^2 + V_{\rm AD,gas}^2$) is needed to obtain the stellar rotation curve ($V_*^2 = V_{\rm c}^2 - V_{\rm AD,*}^2$), as described in Sec. 5.3.

After rejecting galaxies with inclinations below 30° (for which small uncertainties in inclination translate into big uncertainties in the deprojected rotation velocity) and above 75° (for which tilted-ring models are not well suited due to the overlapping of different line-of-sights), we ended up with 14 galaxies from LVHIS (LVHIS 9, 12, 20, 25, 26, 29, 30, 55, 60, 65, 72, 74, 78, and 80), four from VLA-ANGST (DDO 181, DDO 183, DDO 190, and NGC 4190) and three from WHISP (UGC 9649, UGC 10564, and UGC 12060). The galaxies have redshift-independent distance determinations from Karachentsev et al. (2007); Dalcanton et al. (2009); Tully et al. (2013) and Bouquin et al. (2018), coming mostly from the tip of the red giant branch. For those galaxies with kinematic parameters in the literature (e.g. Kirby et al. 2012; Kamphuis et al. 2015), the recovered projected rotation velocities are usually in good agreement with the values obtained with ^{3D}BAROLO, but the shape of our rotation curves are generally smoother.

Fig. 5.9 shows five representative galaxies fitted with ^{3D}BAROLO: Velocity field (observed and modelled), position-velocity diagram along the major axis

(observed and modelled), and the recovered rotation curve before and after correcting for asymmetric drift, as well as the velocity dispersion profile. The ring-by-ring parameters (rotation velocity, velocity dispersion, circular speed, and gas surface density) of the 21 galaxies as obtained from ^{3D}BAROLO are available upon request.

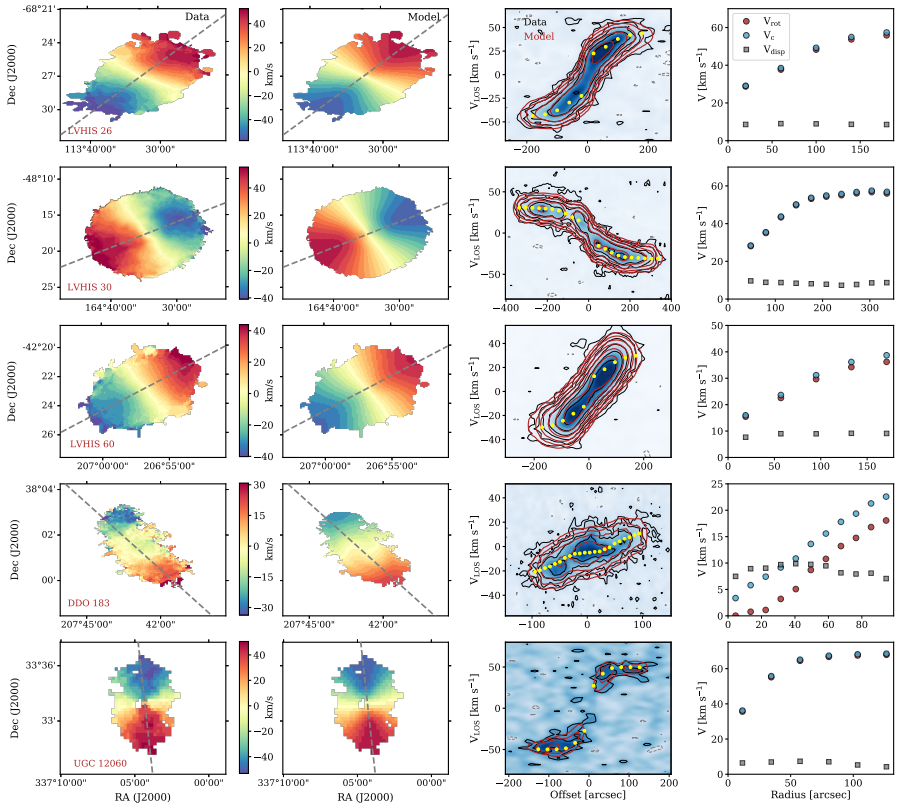

Figure 5.9: Kinematic models of five representative galaxies obtained with ^{3D}BAROLO. From *left* to *right*: 1) observed and 2) best-fitting model velocity field; the dashed grey line shows the average kinematic position angle, while the bar between the two panels show the colour scheme in both velocity fields. 3) Major axis position-velocity diagram: The data is shown in blue, while black contours enclose the data (grey for negative values) and red contours the best-fitting model. The contour levels are at -2, 2, 4, 8, 16, ... times the mean rms in the corresponding data cube. The recovered rotation velocities are shown in yellow. 4) Rotation velocity (red), circular speed (blue) and velocity dispersion (grey) profiles.

5.B Robustness of $j - M$ relations

5.B.1 Robustness against stellar-asymmetric drift correction

Since we made a series of assumptions while deriving $V_{\mathrm{AD}*}$ (and thus j_* and j_{bar}), it is important to understand how do changes in these assumptions affect the results shown in this work. We do not expect these assumptions to play a significant role in our determination of j_{bar}: At high M_{bar}, j_{bar} is dominated by the stellar component, but in that regime the asymmetric drift correction is often negligible (see for instance Fig. 5.3); at low M_{bar} the correction becomes more important, but then j_{bar} is dominated by the gas component, which is unaffected by $V_{\mathrm{AD}*}$. Therefore, the $j_{\mathrm{bar}} - M_{\mathrm{bar}}$ relation is robust against different ways of determining $V_{\mathrm{AD}*}$. Yet, the correction may play a role at the low j_*-regime of the $j_* - M_*$ relation, even if it not as strong as expected from the stellar rotation curve: $V_{\mathrm{AD}*}$ affects V_* more strongly at large radii, but j_* is also proportional to Σ_* (see Eq. 5.1), which decreases with radius. In the next paragraphs we investigate how these two facts affect j_*.

As mentioned before, our calculation of $V_{\mathrm{AD}*}$ is empirically motivated, and we used a floor value of 10 km s^{-1} for the stellar velocity dispersion $\sigma_{*,z}$. To test how much our measurements of j_* and j_{bar} would change by following different prescriptions, we perform two tests where we investigate two extreme scenarios. In the first scenario co-rotation of gas and stars is assumed, and this is we maximise j_* and j_{bar} by setting $V_{\mathrm{AD}*} = 0$. In the second scenario, we minimise j_* and j_{bar} by adopting a floor value for $\sigma_{*,z}$ of 15 km s^{-1}. This floor is clearly too high given the observed values of $\sigma_{*,z}$ in the outskirts of galaxies (e.g. Swaters 1999; Martinsson et al. 2013), but it is still interesting as an extreme case.

The result is shown in Fig. 5.10, where we compare our fiducial best-fitting stellar (left) and baryonic (right) $j - M$ laws (grey bands), as obtained in Sec. 5.4, with the values obtained from the two scenarios mentioned above: no asymmetric drift correction (top) and extreme asymmetric drift correction (bottom). We note that, as in Fig. 5.5, the galaxies in the left panels are not necessarily the same as in right panels.

We start by looking and the $j_* - M_*$ relation, shown in the left panels of Fig. 5.10. Both cases are still reasonably well fitted by the fiducial model, both in terms of slope and intercept and in terms of its intrinsic orthogonal scatter. The extreme scenario slightly reduces j_* for most of the galaxies, but it also makes a number (27) of them end up with unreliable j_* (and j_{bar}) because their stellar rotation curves have extremely large uncertainties and some are even compatible with zero. Because of this, 14 galaxies (the 14 with convergent profiles of the 27 affected galaxies, mostly dwarfs) were removed from the figure. Leaving aside this drawback, the main $j_* - M_*$ for the remaining galaxies is not strongly affected. A final caveat about this is that there are very few dwarf galaxies with both stellar and H I rotation curves, so testing how accurate is the

determination of the asymmetric drift correction (by comparing the stellar and neutral gas rotation curve) remains an open issue.

The right hand side panels of Fig. 5.10 show the $j_{\rm bar} - M_{\rm bar}$ laws considering the different j_* from the left hand side. It is clear that the baryonic relation is very robust against the asymmetric drift correction, as expected from our reasoning above. The points derived under both stellar asymmetric drift regimes are always well described by our fiducial best-fitting model. Fitting the points with Eq. 5.7 gives coefficients $\alpha = 0.59 \pm 0.02$, $\beta = 2.80 \pm 0.03$, and $\sigma_\perp = 0.18 \pm 0.02$ for the case of co-rotation of gas and stars, and $\alpha = 0.58 \pm 0.03$, $\beta = 2.81 \pm 0.03$, and $\sigma_\perp = 0.14 \pm 0.02$ for the strong $V_{\rm AD*}$. We can see then that even under extreme assumptions the $j_{\rm bar} - M_{\rm bar}$ relation is robust against the way of determining the asymmetric drift correction.

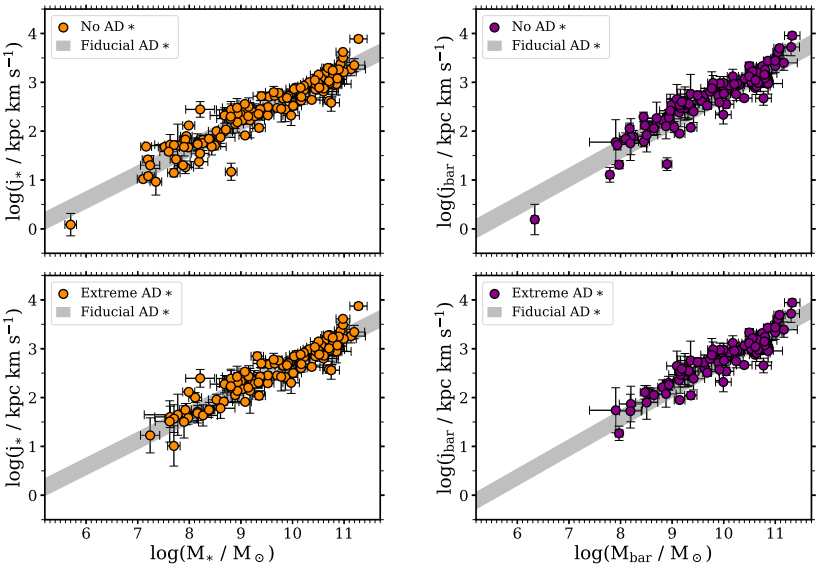

Figure 5.10: Stellar (*left*) and baryonic (*right*) $j - M$ relations under the assumption of none (*top*) or extreme (*bottom*) asymmetric drift correction. In all the panels, the grey band corresponds to the best-fitting relation found for our fiducial correction (see Table 5.2). Since we applied a convergence criterion, the galaxies are not exactly the same in all the panels.

As discussed before, the small differences were certainly expected for the $j_{\rm bar} - M_{\rm bar}$ relation, but not necessarily for the stellar component. To further investigate this, we compare the corrected (fiducial case) and non-corrected ($V_{\rm AD*} = 0$) values of j_* as a function of M_* for all the galaxies in our sample, as shown in Fig. 5.11. It becomes even clearer that the correction affects more low-M_* galaxies, as shown both by the observational points and by the running mean of the distribution (dashed blue line).

The median ratio between corrected and non-corrected j_* is 0.96. If we look

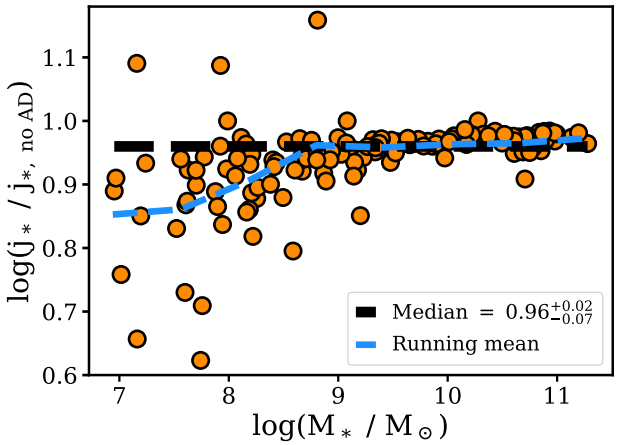

Figure 5.11: Ratio between values of the stellar specific angular moment obtained when the asymmetric drift correction is applied (j_*) or not ($j_{*,\mathrm{no\ AD}}$), i.e. co-rotation if stars and gas is assumed, as a function of M_*. Orange points show the ratios for each galaxy, while the dashed black and blue lines show the median of the distribution and the running mean, respectively. Three galaxies have a larger j_* when the asymmetric drift correction is applied. This is because those galaxies have a strong contribution of pressure-supported motions, such that the stellar rotation curve derived from the circular speed profile has a larger amplitude than the H I rotation curve.

at galaxies with $M_* < 10^9$ $M_\odot$ this ratio drops by $\sim 5\%$. Fig. 5.11 demonstrates that while the asymmetric drift correction does not strongly affect the j_* for the bulk of our galaxy sample, it is still important to correct on an individual basis because, for some of our dwarfs, the correction can account for a decrease in j_* of up to 40%.

5.B.2 Robustness against convergence criterion $\mathcal{R}$

We use the convergence criterion $\mathcal{R} \geq 0.8$ to select our final sample of galaxies (see Sec. 5.3.2). Based on tests using galaxies with clearly converging profiles we find that $\mathcal{R} \geq 0.8$ allows for sub−0.1 dex recoveries of j. In this appendix we explore how different assumptions on $\mathcal{R}$ affect the final shape of the $j_{\mathrm{bar}} - M_{\mathrm{bar}}$ relation. In particular, we explore the stricter case where $\mathcal{R} \geq 0.9$, and the extreme case of $\mathcal{R} > 0$ (and this is not applying any convergence criterion for our sample). Fig. 5.12 presents the $j_{\mathrm{bar}} - M_{\mathrm{bar}}$ law under these test assumptions: The left and right panel show the relation for $\mathcal{R} \geq 0.9$ and $\mathcal{R} > 0$, respectively.

In the case of $\mathcal{R} \geq 0.9$, by fitting the points with Eq. 5.7 we find the best-fitting parameters (not shown in Fig. 5.12) $\alpha = 0.56 \pm 0.03$, $\beta = 2.74 \pm 0.03$, and $\sigma_\perp = 0.12 \pm 0.02$, very similar to the values found for $\mathcal{R} \geq 0.8$ (Table 5.2). The sample is reduced, especially at M_{bar} below $10^{9.5}$ $M_\odot$, which contributes to a marginal decrease (but still consistent within uncertainties) in the slope of the relation.

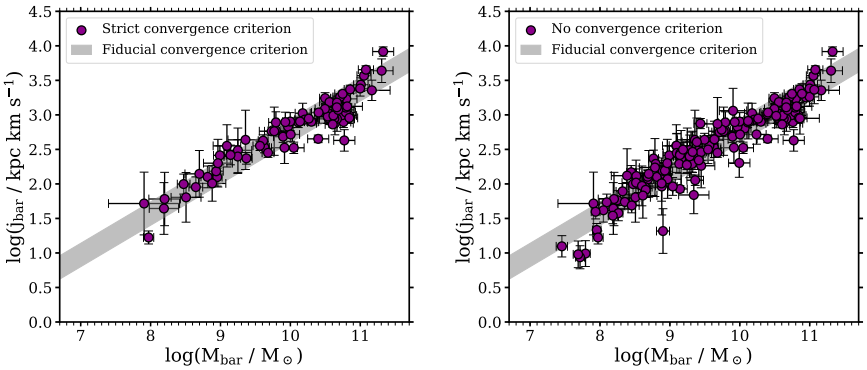

Figure 5.12: $j_{\rm bar} - M_{\rm bar}$ law under different assumptions for the convergence criterion. The *left* panel shows the galaxies that meet $\mathcal{R} \geq 0.9$, while the *right* panel shows the case where no criterion convergence is applied ($\mathcal{R} > 0$). In both panels, the grey band shows the best-fitting power-law found in Sec. 5.4 for the fiducial convergence criterion $\mathcal{R} \geq 0.8$.

For the case where no convergence criterion is applied we find $\alpha = 0.61 \pm 0.02$, $\beta = 2.83 \pm 0.03$, and $\sigma_\perp = 0.14 \pm 0.01$ (not shown in Fig. 5.12). The slope is slightly steeper than for the cases $\mathcal{R} \geq 0.8$ and $\mathcal{R} \geq 0.9$, but consistent within uncertainties. The intercept is also slightly higher, and the intrinsic scatter remains basically the same. We can see, however, that while the best-fitting parameters are not significantly affected by the convergence criterion as the bulk of the sample is not affected (likely related with the large extent of our rotation curves and surface density profiles), there are a number of galaxies with lower $j_{\rm bar}$ than the average, as expected from removing the convergence criterion.

5.B.3 Robustness against the stellar mass-to-light ratio

It is well known that using near-infrared surface brightness profiles, as we do in this work, is important to accurately trace the mass distributions of galaxies (e.g. Verheijen & Sancisi 2001; Lelli et al. 2016b). While j_* and $j_{\rm gas}$ do not depend on Υ, $j_{\rm bar}$ and $M_{\rm bar}$ do, since they depend on $f_{\rm gas}$. In this section we address how changes in Υ affect the $j_{\rm bar} - M_{\rm bar}$ relation. We note that our uncertainties in M_* (and thus our uncertainties in $f_{\rm gas}$, $M_{\rm bar}$, and $j_{\rm bar}$) always include an uncertainty term coming from Υ: $\sigma_\Upsilon = 0.11$ dex for the $3.6\mu m$ profiles (Lelli et al. 2016b) and $\sigma_\Upsilon = 0.3$ dex for the $H-$band profiles (Kirby et al. 2008; Young et al. 2014).

We performed two tests, building again the baryonic $j - M$ plane, but lowering and raising Υ by 1σ but keeping our convergence criterion of $\mathcal{R} \geq 0.8$. The results are shown in Fig. 5.13, where we compare the new sets of points with our fiducial best-fitting $j_{\rm bar} - M_{\rm bar}$ law (grey band, see Sec. 5.4). Naturally, the low$-\Upsilon$ generates a small shift towards lower masses with respect to the fiducial relation, while the high$-\Upsilon$ shifts galaxies rightwards. Fitting the low-

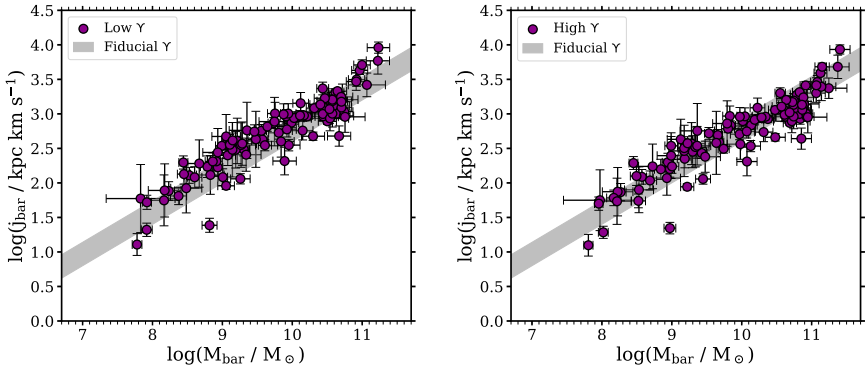

Figure 5.13: $j_{\rm bar} - M_{\rm bar}$ law under different assumptions for the mass-to-light ratio Υ for the convergence criterion. The *left* and *right* panels show the data points obtained by lowering and increasing our fiducial Υ by 1σ, respectively. In both panels, the grey band shows the best-fitting power-law found in Sec. 5.4 for the fiducial Υ.

and high-Υ $j_{\rm bar} - M_{\rm bar}$ relations gives best fitting parameters (α, β, $\sigma_\perp$) of (0.61, 2.82, 0.14) and (0.58, 2.75, 0.16), respectively. The fiducial Υ gives intermediate best-fitting parameters with respect to these two cases. Importantly, the slopes are compatible within their uncertainties, so we can conclude that the baryonic $j - M$ law is robust against the exact choice of the stellar mass-to-light ratio.

Chapter 6

A tight angular-momentum plane for disc galaxies

based on

– P. E. Mancera Piña, L. Posti, G. Pezulli et al., 2021 –

Published in Astronomy & Astrophysics (Letter to the Editor), A&A 651, L15

Abstract

The relations between the specific angular momenta (j) and masses (M) of galaxies are often used as a benchmark in analytic models and hydrodynamical simulations as they are considered to be amongst the most fundamental scaling relations. Using accurate measurements of the stellar (j_*), gas ($j_{\rm gas}$), and baryonic ($j_{\rm bar}$) specific angular momenta for a large sample of disc galaxies, we report the discovery of tight correlations between j, M, and the cold gas fraction of the interstellar medium ($f_{\rm gas}$). At fixed $f_{\rm gas}$, galaxies follow parallel power laws in 2D (j, M) spaces, with gas-rich galaxies having a larger j_* and $j_{\rm bar}$ (but a lower $j_{\rm gas}$) than gas-poor ones. The slopes of the relations have a value around 0.7. These new relations are amongst the tightest known scaling laws for galaxies. In particular, the baryonic relation ($j_{\rm bar} - M_{\rm bar} - f_{\rm gas}$), arguably the most fundamental of the three, is followed not only by typical discs but also by galaxies with extreme properties, such as size and gas content, and by galaxies previously claimed to be outliers of the standard 2D $j - M$ relations. The stellar relation ($j_* - M_* - f_{\rm gas}$) may be connected to the known $j_* - M_*-$bulge fraction relation; however, we argue that the $j_{\rm bar} - M_{\rm bar} - f_{\rm gas}$ relation can originate from the radial variation in the star formation efficiency in galaxies, although it is not explained by current disc instability models.

6.1 Introduction

Despite the remarkable diversity of galaxy properties observed in the present-day Universe, a number of physical parameters of galaxies appear to correlate with one another and form tight scaling laws. Such relations are of paramount importance in our quest to understand galaxy formation and evolution (e.g. Tully & Fisher 1977; Fall 1983; Burstein et al. 1997; McGaugh et al. 2000; Marconi & Hunt 2003; Cappellari et al. 2013a; Wang et al. 2016).
Since early models of galaxy formation were proposed, it has become clear that mass and angular momentum are two fundamental parameters controlling the evolution of galaxies (e.g. Fall & Efstathiou 1980; Dalcanton et al. 1997; Mo et al. 1998). From an observational point of view, starting from the work by Fall (1983), different authors have characterised the scaling relation between stellar mass (M_*) and stellar specific angular momentum ($j_* = J_*/M_*$, where J_* is the angular momentum), the $j_* - M_*$ or Fall relation (e.g. Romanowsky & Fall 2012; Obreschkow & Glazebrook 2014; Posti et al. 2018b). This $j_* - M_*$ law has been widely used in recent years to constrain and test both (semi-)analytic models and hydrodynamical simulations (e.g. Genel et al. 2015; Pedrosa & Tissera 2015; Obreja et al. 2016; Lagos et al. 2017; Tremmel et al. 2017; El-Badry et al. 2018; Stevens et al. 2018; Zoldan et al. 2018; Irodotou et al. 2019).

In Chapter 5 (i.e. Mancera Piña et al. 2021a), we derived accurate measurements of the stellar (j_*), (cold neutral) gas ($j_{\rm gas}$), and baryonic ($j_{\rm bar}$) specific angular momentum for a large sample of irregular spiral and dwarf galaxies (see also e.g. Obreschkow & Glazebrook 2014; Kurapati et al. 2018). They determined the $j - M$ relations for the three components and fitted them with unbroken power laws. They also noticed that the residuals from the best fitting relations correlate with the gas fraction ($f_{\rm gas} = M_{\rm gas}/M_{\rm bar}$, with $M_{\rm gas}$ and $M_{\rm bar}$ the gas and baryonic masses, respectively). These trends, also seen in a few semi-analytic models (e.g. Stevens et al. 2018; Zoldan et al. 2018), may indicate that the gas content plays an important role in the $j - M$ relations. In this chapter we build upon that result and report the discovery of new and very tight correlations between mass, specific angular momentum, and gas fraction. We show that disc galaxies across ~ 4 orders of magnitude in mass lie in very tight planes in the $(j, M, f_{\rm gas})$ spaces.

6.2 Definition of j and galaxy sample

The stellar and gas specific angular momenta of a galaxy are defined as

$$j_i(< R) = \frac{\int_0^R R'^2\ \Sigma_i(R')\ V_i(R')\ dR'}{\int_0^R R'\ \Sigma_i(R')\ dR'}\ , \tag{6.1}$$

with R being the galactocentric cylindrical radius, Σ_i the stellar or gas face-on surface density, and V_i the stellar or gas rotation velocity. Then, j_* and $j_{\rm gas}$

can be combined to obtain

$$j_{\rm bar} = f_{\rm gas} j_{\rm gas} + (1 - f_{\rm gas}) j_* \ . \tag{6.2}$$

For $f_{\rm gas} = M_{\rm gas}/M_{\rm bar}$, we assumed $M_{\rm bar} = M_* + M_{\rm gas}$, with $M_{\rm gas} = 1.33 M_{\rm HI}$, where $M_{\rm HI}$ is the mass of neutral atomic hydrogen and the factor 1.33 accounts for the presence of helium. While we neglected any contribution from molecular gas, in Appendix 6.A we show that its inclusion does not change the results found in this work.[1]

In Chapter 5 we compiled a high-quality sample of 157 nearby galaxies, predominantly discs. All the galaxies have near-IR photometry and extended H I rotation curves, allowing their stellar discs and rotation velocities to be traced robustly. The sample includes dwarf and massive galaxies, spanning the mass range $7 \lesssim \log(M_*/{\rm M}_\odot) \lesssim 11.5$, $6 \lesssim \log(M_{\rm gas}/{\rm M}_\odot) \lesssim 10.5$, $8 \lesssim \log(M_{\rm bar}/{\rm M}_\odot) \lesssim 11.5$, and with $0.01 < f_{\rm gas} < 0.97$ and a typical relative uncertainty, $\delta f_{\rm gas}/f_{\rm gas} \approx 0.2$ dex (median $\delta f_{\rm gas} \approx 0.05$). While not complete, the sample is representative of the population of regularly rotating nearby discs, like other large samples commonly used in the literature (e.g. Lelli et al. 2016a; Ponomareva et al. 2016). Using the near-IR photometry and H I rotation curves, in Chapter 5 we built cumulative radial profiles for j_* (applying a correction to convert $V_{\rm gas}$ into V_*), $j_{\rm gas}$, and $j_{\rm bar}$. By selecting only galaxies with radially convergent measurements of angular momentum, they built a sample of 130, 87, and 106 galaxies with accurate j_*, $j_{\rm gas}$, and $j_{\rm bar}$, respectively. For more details we refer the reader to Chapter 5, and in our associated data catalogues we provide the values of j, M, $f_{\rm gas}$, distance, and Hubble type for the galaxy sample.

In Chapter 5 we fitted the $j - M$ relations with power laws of the form

$$\log\left(\frac{j_i}{\rm kpc\ km\ s^{-1}}\right) = m_i[\log(M_i/{\rm M}_\odot) - 10] + n_i \ , \tag{6.3}$$

with the subscript i representing the stellar, gaseous, or baryonic component. The best fitting power laws have slopes m_i of about 0.5, 1.0, and 0.6 for stars, gas, and baryons, respectively, and an intrinsic scatter of 0.15 dex.

6.3 The $j - M - f_{\rm gas}$ planes

6.3.1 Best fitting planes

As shown in Fig. 5.6 in Chapter 5, there are systematic trends with $f_{\rm gas}$ in the residuals of the three $j - M$ laws. To see if introducing a dependence of the $j - M$ laws on $f_{\rm gas}$ can explain these trends, in this chapter we fitted the

[1] Our 'gas' refers only to the interstellar medium, and there is no attempt to include the largely unconstrained contribution of the gas outside galaxy discs. Although the sum of our gas and stars does not represent the 'whole' baryonic budget of a galaxy, we prefer to keep this nomenclature for the sake of consistency with the literature.

Table 6.1: Coefficients of the best fitting $j - M - f_{\rm gas}$ planes.

	α	β	γ	$\sigma_\perp$
Stars	0.67 ± 0.03	0.51 ± 0.08	-3.62 ± 0.23	0.10 ± 0.01
Gas	0.78 ± 0.03	-0.49 ± 0.04	-4.64 ± 0.25	0.08 ± 0.01
Baryons	0.73 ± 0.02	0.46 ± 0.05	-4.25 ± 0.19	0.08 ± 0.01

$(j, M, f_{\rm gas})$ data with planes. We fitted the data points with the model

$$\log\left(\frac{j_i}{\rm kpc\ km\ s^{-1}}\right) = \alpha_i \log(M_i/M_\odot) + \beta_i \log(f_{\rm gas}) \ + \gamma_i \ . \qquad (6.4)$$

Therefore, we assumed that, in contrast to Eq. 6.3, j_i also depends on $f_{\rm gas}$.[2] We performed the fit using the R package HYPER-FIT (Robotham & Obreschkow 2015), including a term for the intrinsic scatter $\sigma_\perp$. We assumed log-normal uncertainties in j, M, and $f_{\rm gas}$, and, using a Monte Carlo sampling method, we took into account the fact that uncertainties in the distance, inclination, and mass-to-light ratio of a given galaxy drive correlated uncertainties (also provided in our electronic tables) between $\log(M), \log(j)$, and $\log(f_{\rm gas})$. We stress that taking these correlations into account is important: Neglecting them can artificially lower the intrinsic scatter of the planes by a factor of two to three.

The best fitting coefficients are reported in Table 6.1. The orthogonal intrinsic scatter of our best fitting planes is significantly smaller than for the 2D relations. The log-marginal likelihood is also higher (i.e. better) for the 3D planes: by 27, 40, and 43 units for stars, gas, and baryons, respectively. We conclude that the inclusion of $f_{\rm gas}$ into the $j - M$ laws is statistically meaningful.

In Fig. 6.1 we compare the observed distribution of galaxies with our three best fitting planes; the figure shows the 3D $j - M - f_{\rm gas}$ planes projected into the 2D (j, M) spaces. Galaxies are colour-coded according to their $f_{\rm gas}$, and we overlay our lines of constant $f_{\rm gas}$ derived from our best fitting planes. The fits provide a very good description of the data, in line with the low intrinsic scatter we find for all the planes. By construction, the three $j - M - f_{\rm gas}$ planes are characterised by their M slopes (α_*, $\alpha_{\rm gas}$, and $\alpha_{\rm bar}$) and $f_{\rm gas}$ slopes (β_*, $\beta_{\rm gas}$, and $\beta_{\rm bar}$). Projected into the (j, M) spaces, the $f_{\rm gas}$ slopes act as a normalisation for j. At fixed M_* ($M_{\rm bar}$), gas-rich galaxies have a higher j_* ($j_{\rm bar}$) than gas-poor ones, while gas-poor galaxies show a higher $j_{\rm gas}$. For stars and

[2]Since our planes depend on $\log(f_{\rm gas})$, they become hard to interpret when $f_{\rm gas} \to 0$, preventing us from making extrapolations for galaxies with $f_{\rm gas} < 0.01$. Using $f_{\rm gas}$ instead of $\log(f_{\rm gas})$ produces less satisfactory fits when compared to the observations, so we prefer $\log(f_{\rm gas})$ despite its limitations when $f_{\rm gas} \to 0$. We also note that, given Eq. 6.2, the $j - M$ relations cannot all be exactly planes. However, fitting planes in the $(j, M, f_{\rm gas})$ spaces is a very useful empirical approach.

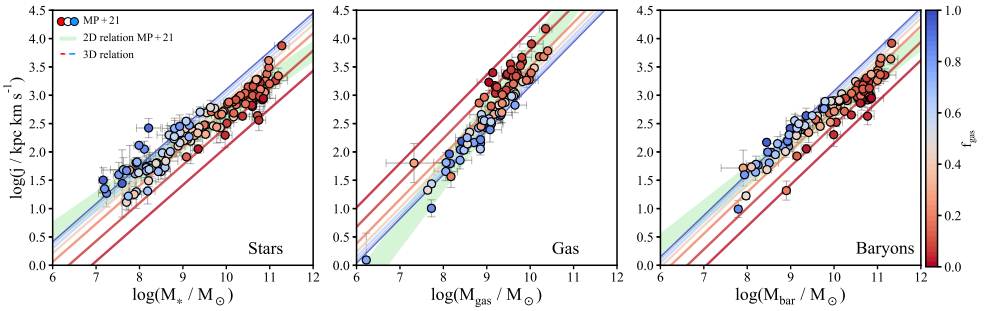

Figure 6.1: Stellar, gas, and baryonic $j - M - f_{\rm gas}$ planes, projected into the 2D (j, M) spaces. Galaxies are colour-coded according to their $f_{\rm gas}$ and are compared with lines of constant $f_{\rm gas}$ according to Eq. 6.4 and the best fitting coefficients of Table 6.1. From red to blue, the lines are at $f_{\rm gas} = 0.01, 0.05, 0.2, 0.4, 0.6, 0.8, 1$. For comparison, we show in green the best fitting 2D $j - M$ relations from Chapter 5 and their intrinsic scatter.

baryons, the 3D relations become steeper ($\alpha_* = 0.67 \pm 0.03, \alpha_{\rm bar} = 0.73 \pm 0.03$) than the 2D ones from Chapter 5 ($m_* = 0.53 \pm 0.02, m_{\rm bar} = 0.60 \pm 0.02$) once $f_{\rm gas}$ is taken into account, while the slope of the gas relation becomes shallower ($\alpha_{\rm gas} = 0.78 \pm 0.03, m_{\rm gas} = 1.02 \pm 0.04$). Given the different coefficients, the 2D $j - M$ relations (shown in Fig. 6.1 as green bands) differ from the projection of the 3D planes in the (j, M) spaces, especially at $M < 10^8$ M$_\odot$.

A remarkable property of our new scaling laws is their low intrinsic scatter. Given that the baryonic $j_{\rm bar} - M_{\rm bar} - f_{\rm gas}$ plane incorporates the stellar and cold gas components, we argue that this is likely the most fundamental of the three relations, although its intrinsic scatter is similar to the relation for the gas. Very few other scaling laws are thought to have a comparably low intrinsic scatter, for instance the H I mass-size relation (Wang et al. 2016) or the baryonic Tully-Fisher relation (BTFR; McGaugh et al. 2000; Ponomareva et al. 2017). In fact, our baryonic plane can in principle be used as a distance estimator, with an uncertainty $\delta D/D = (\delta j_{\rm bar}/j_{\rm bar})/|2\alpha_{\rm bar} - 1|$ at fixed $M_{\rm bar}$.

6.3.2 The similarities of the α slopes

The three α slopes of our $j - M - f_{\rm gas}$ planes are relatively close to one another and to the value 2/3 expected for their parent dark matter haloes (Fall 1983), which suggests some degree of structural self-similarity between different baryonic components and the dark matter halo. From a mathematical point of view, if we rewrite Eq. 6.2 in terms of $j_* = BM_*^{\alpha_*}$ (with B a function that depends only on $f_{\rm gas}$) and $M_* = M_{\rm bar}(1 - f_{\rm gas})$, we obtain

$$j_{\rm bar} = B\ (1 - f_{\rm gas})^{\alpha_*} \left[\frac{j_{\rm gas}}{j_*} f_{\rm gas} + (1 - f_{\rm gas}) \right] M_{\rm bar}^{\alpha_*}\ . \tag{6.5}$$

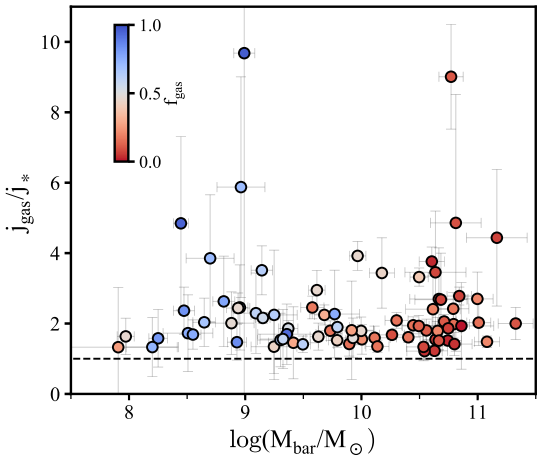

Figure 6.2: $j_{\rm gas}/j_*$ ratio as a function of $M_{\rm bar}$. Galaxies are colour-coded by their $f_{\rm gas}$, and the dashed black line corresponds to $j_{\rm gas}/j_* = 1$. Our galaxies (those with convergent j_* and $j_{\rm gas}$ from Chapter 5 cluster at $j_{\rm gas}/j_* \sim 2$ at all $M_{\rm bar}$, albeit with a significant scatter.

In a similar way, considering now $j_{\rm gas} = C M_{\rm gas}^{\alpha_{\rm gas}}$ (with C a function that depends only on $f_{\rm gas}$), we find

$$j_{\rm bar} = C\ f_{\rm gas}^{\alpha_{\rm gas}} \left[\frac{j_*}{j_{\rm gas}} (1 - f_{\rm gas}) + f_{\rm gas} \right] M_{\rm bar}^{\alpha_{\rm gas}} \ . \tag{6.6}$$

Therefore, at fixed $f_{\rm gas}$, the slope $\alpha_{\rm bar}$ of the baryonic $j - M - f_{\rm gas}$ plane is expected to be similar to α_* and $\alpha_{\rm gas}$, provided that the ratio $j_{\rm gas}/j_*$ is independent of $M_{\rm bar}$. As shown in Fig. 6.2, for our sample, $j_{\rm gas}/j_*$, which is always larger than 1 and mostly within a narrow range (the 16$^{\rm th}$ and 84$^{\rm th}$ percentiles are 1.5 and 3.2, respectively), does not seem to correlate with $M_{\rm bar}$, in line with the near-parallelism of the three relations shown in Fig. 6.1.

It is worth noticing that the $j_{\rm gas}/j_*$ ratio can be related to the relative extent of some characteristic size of the gaseous ($R_{\rm gas}$) and stellar (R_*) components of galactic discs, given that $j_{\rm gas}/j_* \approx R_{\rm gas} V_{\rm gas}/(R_* V_*) \approx R_{\rm gas}/R_*$. Although this is just an approximation, it can be useful in the physical interpretation of the $j - M - f_{\rm gas}$ relations (e.g. Sec. 6.4.2). In Appendix 6.B we show the expected dependence of $j_{\rm gas}/j_*$ on $M_{\rm bar}$ and $f_{\rm gas}$ derived from our best fitting $j_* - M_* - f_{\rm gas}$ and $j_{\rm gas} - M_{\rm gas} - f_{\rm gas}$ planes.

6.3.3 No outliers of the baryonic $j - M - f_{\rm gas}$ law

In Fig. 6.3 we plot again our baryonic plane, this time splitting the galaxies into bins of $f_{\rm gas}$. In each panel we plot lines covering the whole range of $f_{\rm gas}$ within that bin. This allows the tightness of our baryonic relation to be appreciated in more detail.

We now investigate whether any objects from known galaxy populations could be outliers of our baryonic plane. We do this by comparing our relation, derived using only our sample, with galaxies from the literature that have been argued to be outliers of the 2D $j - M$ relations or that could be outliers given their extreme properties in size, $f_{\rm gas}$, or rotation velocity.

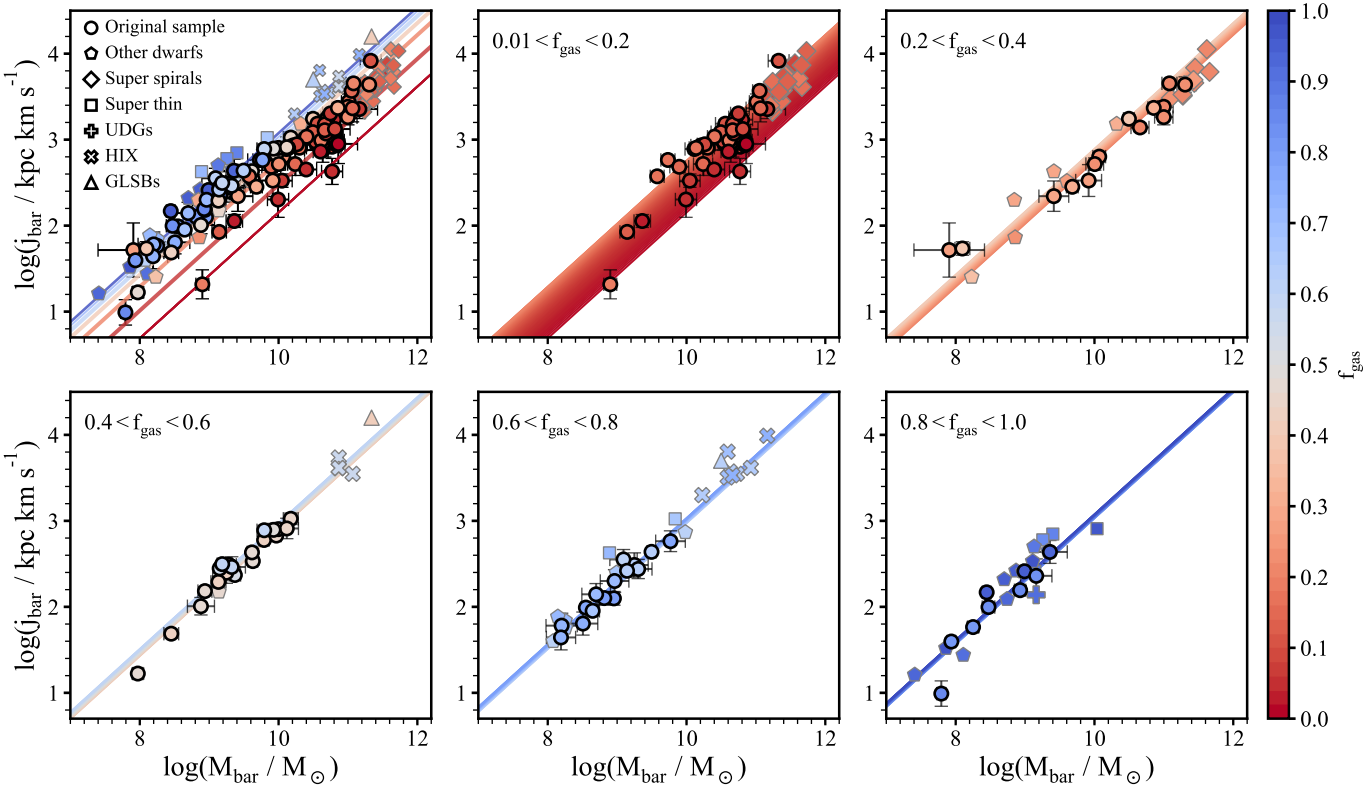

Figure 6.3: Baryonic $j_{\rm bar} - M_{\rm bar} - f_{\rm gas}$ plane for our original sample (circles) and a set of extreme galaxies (see text). The top left panel shows the relation for all the galaxies, while the remaining panels show the galaxies in bins of $f_{\rm gas}$ (given in the top left corner of each panel). On the first panel, the lines of constant $f_{\rm gas}$ are as in Fig. 6.1. In the remaining panels, the coloured areas enclose the region delimited by the whole $f_{\rm gas}$ bin. We remark that the coloured lines of our plane are derived by fitting only our data. The rest of the galaxies closely follow our fit.

First, we considered a set of dwarf galaxies from the literature, specifically those from Elson (2017) and Kurapati et al. (2018), that do not overlap with our sample. It was claimed by those authors that some of these galaxies are off the 2D $j_{\rm bar} - M_{\rm bar}$ relation. We also included the dwarf 'super thin' galaxies of Jadhav Y & Banerjee (2019), which have very high axis ratios and have been suggested to have higher j_* than other dwarfs. Next, we looked at the 'H I extreme galaxies' (HIXs) of Lutz et al. (2018), which have a particularly high $f_{\rm gas}$ for their M_* and are claimed to have higher $j_{\rm bar}$ than average. Moreover, we added a sample of 'super spiral' galaxies (Di Teodoro et al. 2021), which are very large discs with masses a factor of ten larger than L_* galaxies and were also claimed to be outliers of the $j_* - M_*$ relation (Ogle et al. 2019b).[3] Finally, we included the ultra-diffuse galaxies (UDGs) AGC 114905 (Chapter 4) and AGC 242019 (Shi et al. 2021)) and the giant low surface brightness galaxies (GLSBs) Malin 1 and NGC 7589 (Lelli et al. 2010). The UDGs are found to be outliers of the BTFR (Chapter 2 and 3), and both UDGs and GLSBs are extreme galaxies with very extended discs for their M_*. With the caveat that some of these galaxies have larger uncertainties than our sample, given the different data quality, we added all these sets of galaxies into the $j_{\rm bar} - M_{\rm bar} - f_{\rm gas}$ plane in Fig. 6.3. Remarkably, the location of all of these galaxies, given their $f_{\rm gas}$, is in very good agreement with the expectation of our scaling relation. We conclude that even extreme galaxies such as HIXs, UDGs, and GLSBs obey the $j_{\rm bar} - M_{\rm bar} - f_{\rm gas}$ law.

6.4 Discussion

6.4.1 Stellar relation: The link with bulge fraction

Previous works (e.g. Fall 1983; Romanowsky & Fall 2012; Cortese et al. 2016; Fall & Romanowsky 2018) found that the relation between j_* and M_* depends on the bulge-to-total mass fraction, $\mathcal{B}_*$. Fall & Romanowsky (2018, hereafter FR18), proposed a model in which discs and spheroids follow relations of the form $j_* \propto M_*^{0.67}$ but with different normalisation, with spheroids shifting downwards with respect to discs; any given galaxy then has a j_* that can be expressed as a linear superposition of a disc and a spheroid (a bulge).

The resemblance of our $j_* - M_* - f_{\rm gas}$ plane (where at fixed M_* a different $f_{\rm gas}$ produces a shift in j_*) with the $\mathcal{B}_*$ relation is clear. Both relations are valid for a variety of morphological types and are preserved along a broad mass span, and with a dependence of j_* on M_* with a slope of 2/3. The similarities are not unexpected since gas-poor galaxies usually have high $\mathcal{B}_*$, though the $f_{\rm gas} - \mathcal{B}_*$ relation is highly scattered. The above suggests that these two relations may be manifestations of a common physical mechanism. Finally, we note that the scatter is better quantified in the $j_* - M_* - f_{\rm gas}$ relation with respect to the $\mathcal{B}_*$

[3] Since $j_{\rm gas}$ is not available for the super spirals, we assumed $j_{\rm gas} = 1.9 j_*$, the median ratio found in the rest of our sample. This has little to no impact given their low gas content ($f_{\rm gas} \approx 0.15$).

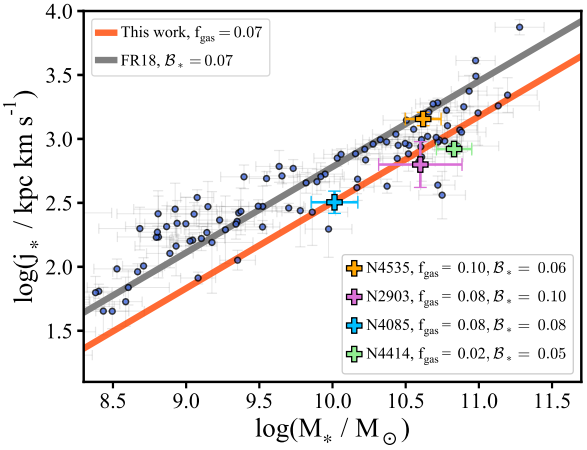

Figure 6.4: $j_* - M_*$ relation. Crosses show our galaxies with $(f_{\rm gas}, \mathcal{B}_*) \leq 0.1$. The black and red lines show the expectations from FR18 and this work, respectively. Only a fraction of our range in M_* is shown.

relation given that the uncertainties in $\mathcal{B}_*$ are difficult to estimate (Salo et al. 2015; FR18).

Interestingly, there is a regime in which the $f_{\rm gas}$ relation makes a different prediction from the $\mathcal{B}_*$ relation. For galaxies that are almost gas-free and almost bulge-less (we note that galaxies with $\mathcal{B}_* \lesssim 0.1 - 0.2$ host pseudo-bulges rather than classical bulges; see Fig. 3 in FR18), the $f_{\rm gas}$ relation expects them to have a lower-than-average j_*, while the $\mathcal{B}_*$ relation predicts a higher-than-average j_*. We tested this in Fig. 6.4 by looking at the four galaxies in our sample with $f_{\rm gas} \leq 0.1$ and $\mathcal{B}_* \leq 0.1$ (Salo et al. 2015). We also plot the expected lines given the average $\mathcal{B}_*$ and $f_{\rm gas}$ for these four galaxies. The points lie close to the $f_{\rm gas}$ relation and deviate from the $\mathcal{B}_*$ one. However, the evidence is not compelling given the low-number statistics. Finally, it is also important to mention that our galaxy sample is fairly different from that of FR18, with many more gas-dominated discs but a lack of early-type galaxies. These potential differences can be further explored with larger and more complete samples.

6.4.2 The origin of the baryonic relation

We then focused our attention on the $j_{\rm bar} - M_{\rm bar} - f_{\rm gas}$ relation. Its origin is likely related to different galaxy formation processes, such as variations in the angular momentum of the dark matter haloes, selective gas accretion within the discs, and different gas accretion histories from the intergalactic medium (Fall 1983; Posti et al. 2018b,a; Stevens et al. 2018; Zoldan et al. 2018). Evolutionary processes such as stellar and active galactic nucleus feedback, mergers, and angular momentum transfer between galaxies and their dark matter haloes are arguably also important (Leroy et al. 2008; Dutton & van den Bosch 2012; Romanowsky & Fall 2012; Lagos et al. 2017; Zoldan et al. 2018). Still, while a complex interplay between all these processes is expected, it all results in the tight $j_{\rm bar} - M_{\rm bar} - f_{\rm gas}$ law we observe. Therefore, it is interesting to check whether or not simple mechanisms are able to capture the dominant processes

that give rise to the $j_{\rm bar} - M_{\rm bar} - f_{\rm gas}$ relation.

Disc instability

We considered two models that have been proposed to explain the $j_{\rm bar} - f_{\rm gas}$ connection as a consequence of gravitational instability. First, Obreschkow et al. (2016) proposed a model that relates $f_{\rm gas}$ with $j_{\rm bar}$ via

$$f_{\rm gas} = \min\{1, 2.5q^{1.12}\}, \quad q = j_{\rm bar}\sigma_{\rm gas}/G\ M_{\rm bar}, \tag{6.7}$$

with q a stability parameter, $\sigma_{\rm gas}$ the gas velocity dispersion, and G the gravitational constant. Deviations from Eq. 6.7 may occur depending on the galaxy rotation curve, but they are expected to be small. These results were derived under a number of simplifying assumptions, but less idealised semi-analytic models are found to be in good agreement (Stevens et al. 2018). From Eq. 6.7, one has $\log(f_{\rm gas}) \propto\ 1.12[\log(j_{\rm bar}) -\ \log(M_{\rm bar})]$ and $j_{\rm bar} \propto M_{\rm bar}$ (this at fixed $f_{\rm gas}$ and assuming a constant $\sigma_{\rm gas}$). These dependences disagree with our best fitting plane, which has $\log(f_{\rm gas}) \propto 2.17\log(j_{\rm bar}) - 1.59\log(M_{\rm bar})$ and $j_{\rm bar} \propto M_{\rm bar}^{0.73}$ at fixed $f_{\rm gas}$. Projecting our baryonic plane into the $f_{\rm gas} - q$ diagram shows that galaxies of a given $M_{\rm bar}$ follow parallel sequences of the form $f_{\rm gas} \propto q^{1/\beta_{\rm bar}} = q^{2.22}$, instead of $f_{\rm gas} \propto q^{1.12}$. [4]

Also based on disc instability, Romeo (2020) proposed a set of scaling relations of the form $j_i\hat{\sigma}_i/(GM_i) \approx 1$, with i denoting stars or gas and $\hat{\sigma}$ a mass-weighted radial average of the velocity dispersion σ. This relation produces the scaling $j_* \propto M_*^{0.5}$ (for $\hat{\sigma}_* \propto M_*^{0.5}$, as proposed by Romeo 2020) and $j_{\rm gas} \propto M_{\rm gas}$, very similar to the values found in Chapter 5 for the 2D relations. To incorporate $f_{\rm gas}$, we rewrite the above expression (using $M_i = M_{\rm gas} = f_{\rm gas}M_{\rm bar}$) as

$$\frac{j_{\rm gas}}{M_{\rm bar}}\frac{\hat{\sigma}_{\rm gas}}{G} = f_{\rm gas}\ . \tag{6.8}$$

Assuming a constant $\hat{\sigma}_{\rm gas}$, as in Romeo (2020), this relation predicts $j_{\rm gas} \propto M_{\rm bar}$ at fixed $f_{\rm gas}$ and $j_{\rm gas} \propto f_{\rm gas}$ at fixed $M_{\rm bar}$. Instead, a corollary of our gas relation is that $j_{\rm gas} \propto M_{\rm bar}^{0.78}$ at fixed $f_{\rm gas}$ and that $j_{\rm gas} \propto f_{\rm gas}^{0.27}$ at fixed $M_{\rm bar}$. Therefore, the relation from Romeo (2020) also seems to depart from our data.

Star formation efficiency

A more general possibility is that the link between $j_{\rm bar}$, $M_{\rm bar}$, and $f_{\rm gas}$ is related to the star formation efficiency in galaxies, as we briefly discuss here. We started by noting that at fixed $M_{\rm bar}$ the larger the $j_{\rm bar}$ of a galaxy is, the more extended its baryonic distribution will be.[5] Also, it is well established that gas located in the outskirts of discs forms stars less efficiently than gas closer

[4] We note that assuming a non-constant $\sigma_{\rm gas}$ is not enough to alleviate the mentioned discrepancies. To match our relations, $\sigma_{\rm gas} \propto M_{\rm bar}^{\sim 0.25}$ is required; however, it is observed that $\sigma_{\rm gas} \propto M_{\rm bar}^{0.07}$ (e.g. Murugeshan et al. 2020).

[5] Second-order effects related to the concentration of the host halo might also be relevant in determining the galaxy sizes (Posti et al. 2020).

to the centre (e.g. Leroy et al. 2008). Thus, at fixed $M_{\rm bar}$, a galaxy with a large $j_{\rm bar}$ also has a large $f_{\rm gas}$ since a large portion of its mass is located in the less star-forming outer regions. Qualitatively, this is in agreement with the fact that for our entire galaxy sample $j_{\rm gas}/j_* \approx R_{\rm gas}/R_* > 1$ (see Sec. 6.3.2). All this suggests that the connection between $j_{\rm bar}$ and $f_{\rm gas}$ may be a reflection of the mechanism responsible for a radially declining star formation efficiency and a radially increasing $f_{\rm gas}$ in galaxy discs (e.g. Leroy et al. 2008; Krumholz et al. 2011; Bacchini et al. 2019a), but exploring this idea quantitatively (e.g. by investigating why the $j_{\rm gas}/j_*$ ratio is largely independent of $M_{\rm bar}$ and $f_{\rm gas}$; see Fig. 6.2 but also Fig. 6.5) is beyond the scope of the present study.

6.5 Conclusions

In this chapter we have used a high-quality sample of disc galaxies to study the relation between their specific angular momenta (j), masses (M), and gas fraction ($f_{\rm gas}$). The position of our galaxies in the $(j, M, f_{\rm gas})$ spaces can be described with planes such that galaxies with different $f_{\rm gas}$ follow parallel lines in the projected 2D (j, M) spaces. Remarkably, our planes are preserved along a wide range of mass and morphology with very small (≤ 0.1 dex) intrinsic scatter, which places the relations amongst the tightest scaling laws for disc galaxies. The $j_{\rm bar} - M_{\rm bar} - f_{\rm gas}$ plane is arguably the most fundamental, and it is even followed by populations of galaxies with extreme size, mass, and gas content, some of which were previously claimed to be outliers of the 2D $j - M$ relations.

The $j_* - M_* - f_{\rm gas}$ relation shows analogies with the $j_* - M_* - \mathcal{B}_*$ relation ($\mathcal{B}_*$ being the bulge-to-total mass fraction) previously discussed in the literature. Galaxies with fixed $f_{\rm gas}$ or $\mathcal{B}_*$ follow parallel relations of the form $j_* \propto M_*^{2/3}$. Most galaxies are well described by both the $f_{\rm gas}$ and $\mathcal{B}_*$ relations, while some discrepancies appear when looking at galaxies with low $f_{\rm gas}$ and low $\mathcal{B}_*$.

Finally, we show that models based purely on disc instability do not quantitatively reproduce the observed $j - M - f_{\rm gas}$ relations. We argue that the origin and behaviour of the $j_{\rm bar} - M_{\rm bar} - f_{\rm gas}$ law is closely related to the spatial distribution of gas and stars within galaxies, as well as to the radial variations in the star formation efficiency.

We stress that our relations offer a unique possibility to quantitatively test a variety of models, including hydrodynamical simulations and semi-analytic models, providing a powerful benchmark for theories on the formation of galactic discs. The slopes and intrinsic scatter of our $j - M - f_{\rm gas}$ planes are important requirements that hydrodynamical simulations and (semi-)analytic models should aim to reproduce.

6.A The role of molecular gas

In this chapter we have assumed $M_{\rm gas} = 1.33 M_{\rm HI}$ and $j_{\rm gas} = j_{\rm HI}$, neglecting any contribution from molecular (H_2) and ionised gas. Here we show that observationally motivated corrections to account for the presence of H_2 do not change our results.

To account for $M_{\rm H_2}$ in our estimates of $M_{\rm gas}$, we relied on the results from Catinella et al. (2018), who provide measurements of the ratio $M_{\rm H_2}/M_{\rm HI}$ as a function of M_* for a large sample of nearby galaxies. We fitted a linear relation to their binned measurements (see their Fig. 9 and Table 3), finding

$$\log(M_{\rm H_2}/{\rm M}_\odot) = 0.26 \log({\rm M}_*/{\rm M}_\odot) + \log({\rm M_{HI}}/{\rm M}_\odot) - 3.4. \quad (6.9)$$

The scatter is large, and we adopted an uncertainty of 50% in $M_{\rm H_2}$. With this, we redefined $M_{\rm gas} = 1.33(M_{\rm HI} + M_{\rm H_2})$ and updated $M_{\rm bar}$ and $f_{\rm gas}$ accordingly. For massive discs, the correction to $M_{\rm gas}$ is about 0.1 dex, which is smaller than the typical uncertainty in $M_{\rm gas}$ ($\sim$0.13 dex); the correction is even smaller for the dwarfs. The change in $f_{\rm gas}$ is of the same order, also being negligible at low masses and changing by up to 0.1 dex at the high-mass end; this change is also of the order of the typical uncertainty in $f_{\rm gas}$. Correspondingly, $M_{\rm bar}$ remains largely unchanged since the correction is smaller than 0.04 dex at all masses. Including H_2 can also affect $j_{\rm gas}$, as seen from the equation

$$j_{\rm gas} = f_{\rm atm} j_{\rm HI} + (1 - f_{\rm atm}) j_{\rm H_2} \ , \quad (6.10)$$

where $j_{\rm HI}$ and $j_{\rm H_2}$ are the specific angular momenta of the atomic and molecular gas components, respectively, and $f_{\rm atm}$ is the atomic-to-total gas ratio, $f_{\rm atm} = M_{\rm HI}/(M_{\rm HI} + M_{\rm H_2})$.

Obreschkow & Glazebrook (2014) provide measurements of $j_{\rm HI}$, $j_{\rm H_2}$, and $j_{\rm gas}$ for a sample of 16 spiral galaxies. In addition to this, we computed $j_{\rm HI}$ for four galaxies in our sample that have surface densities and CO rotation curves available from Bacchini et al. (2020a). The typical ratio between $j_{\rm gas}$ and $j_{\rm HI}$ is 0.85, which translates into a shift of 0.07 dex. Thus, on average, including H_2 implies a correction to $j_{\rm HI}$ such that $\log(j_{\rm gas}) = \log(j_{\rm HI}) - 0.07$. The correction is of the same order as the average uncertainty in $j_{\rm gas}$, 0.08 dex.

We fitted the 3D relations once again taking into account the above corrections to $M_{\rm gas}$, $f_{\rm gas}$, $j_{\rm gas}$, and $M_{\rm bar}$. The new coefficients for stars, gas, and baryons are listed in Table 6.2. As expected, they are fully consistent with those reported in Table 6.1 within the uncertainties. Therefore, we conclude that including H_2 does not have a significant effect on the derivation of the $j - M - f_{\rm gas}$ laws, and our results remain unchanged.

6.B The $j_{\rm gas}/j_*$ ratio from our best fitting planes

The $j_{\rm gas}/j_*$ ratio can be obtained directly from our individual galaxy measurements, as shown in Fig. 6.2. Nevertheless, $j_{\rm gas}/j_*$ can also be obtained by using

Table 6.2: Same as Table 6.1 but taking into account the presence of molecular gas.

	α	β	γ	$\sigma_\perp$
Stars	0.67 ± 0.03	0.55 ± 0.08	-3.57 ± 0.23	0.11 ± 0.01
Gas	0.75 ± 0.03	-0.50 ± 0.04	-4.46 ± 0.25	0.08 ± 0.01
Baryons	0.72 ± 0.02	0.42 ± 0.05	-4.23 ± 0.19	0.08 ± 0.01

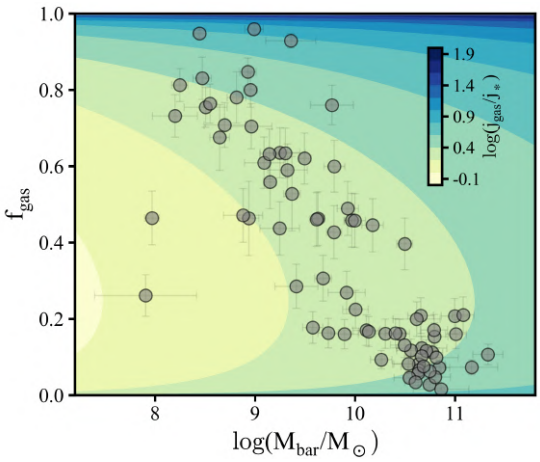

Figure 6.5: Relation between $M_{\rm bar}$, $f_{\rm gas}$, and the best fitting $j_{\rm gas}/j_*$ ratio according to Eq. 6.11. The background shows increasing levels of $j_{\rm gas}/j_*$ and the grey points show our galaxies with convergent measurements of $j_{\rm gas}$ and j_*.

our best fitting stellar and gas relations. This allows us to extrapolate $j_{\rm gas}/j_*$ to values of $f_{\rm gas}$ and $M_{\rm bar}$ beyond our observations and, in principle, to neglect the observational uncertainties since they are accounted for in our best fitting planes. Using Eq. 6.4 the ratio becomes

$$\log(j_{\rm gas}/j_*) = \alpha_{\rm gas}\log(f_{\rm gas}M_{\rm bar}) - \alpha_*\log[(1-f_{\rm gas})M_{\rm bar}] + (\beta_{\rm gas}-\beta_*)\log(f_{\rm gas}) + \gamma_{\rm gas} - \gamma_* \ , \quad (6.11)$$

and the corresponding surface according to Table 6.1 is shown in Fig. 6.5. As can be seen, most of our galaxies lie within a region where $j_{\rm gas}/j_* \sim 2$. It will be interesting to see where other large samples of galaxies would lie in Fig. 6.5 and whether they also follow the expected dependence of $j_{\rm gas}/j_*$ on $M_{\rm bar}$ and $f_{\rm gas}$.

Chapter 7

The impact of gas disc flaring on rotation curve decomposition and revisiting baryonic and dark-matter relations for nearby galaxies

based on

– P. E. Mancera Piña, F. Fraternali, T. Oosterloo et al., 2022 –

MNRAS, in press.

Abstract

Gas discs of late-type galaxies are flared, with scale heights increasing with the distance from the galaxy centres and often reaching kpc scales. We study the effects of gas disc flaring on the recovered dark matter halo parameters from rotation curve decomposition. For this, we carefully select a sample of 32 dwarf and spiral galaxies with high-quality neutral gas, molecular gas, and stellar mass profiles, robust H I rotation curves obtained via 3D kinematic modelling, and reliable bulge-disc decomposition. By assuming vertical hydrostatic equilibrium, we derive the scale heights of the atomic and molecular gas discs and fit dark matter haloes to the rotation curves self-consistently. We find that the effect of the gas flaring in the rotation curve decomposition can play an important role only for the smallest, gas-dominated dwarfs, while for most of the galaxies the effect is minor and can be ignored. We revisit the stellar– and baryon–to–halo mass relations ($M_* - M_{200}$ and $M_{\rm bar} - M_{200}$). Both relations increase smoothly up to $M_{200} \approx 10^{12}$ $M_\odot$, with galaxies at this end having high M_*/M_{200} and $M_{\rm bar}/M_{200}$ ratios approaching the cosmological baryon fraction. At higher M_{200} the relations show a larger scatter. Most haloes of our galaxy sample closely follow the concentration–mass ($c_{200} - M_{200}$) relation resulting from N-body cosmological simulations. Interestingly, the galaxies deviating above and below the relation have the highest and lowest stellar and baryon factions, respectively, which suggests that the departures from the $c_{200} - M_{200}$ law are regulated by adiabatic contraction and an increasing importance of feedback.

7.1 Introduction

About 50 years have passed since the first set of works aiming to use rotation curve decomposition to study, and provide evidence for, the dark matter content of galaxies (e.g. Freeman 1970; Roberts & Rots 1973; Shostak 1973; Bosma 1978; Rubin et al. 1980; van Albada & Sancisi 1986; Begeman 1987, see also Bertone & Hooper 2018 for a historical review). The main idea is well known: provided the distribution of stars and gas within a galaxy, one can compare the contribution from these baryonic components to the gravitational potential against the total potential traced by the observed rotation curve of the galaxy, and infer the mass distribution of the host dark matter halo. Significant work has also been done using rotation curves decomposition to test alternative theories to dark matter (e.g. Milgrom 1983; Kent 1987; McGaugh & de Blok 1998; Famaey & McGaugh 2012).

The derivation of mass models has become significantly more accurate and detailed than in the first studies half a century ago. Nowadays, mass models use high quality data with high resolution kinematic measurements (typically H I data) and accurate near-IR photometry to study the dynamics of relatively large galaxy samples (e.g. de Blok et al. 2008; Frank et al. 2016; Lelli et al. 2016a), using robust statistical techniques such as Bayesian inference (e.g. Read et al. 2016b; Posti et al. 2019), and testing a variety of dark matter haloes and even different types of dark matter (e.g. Ren et al. 2019; Li et al. 2020; Zentner et al. 2022). These models are used on a daily basis for a variety of applications on galaxy evolution and near-field cosmology.

A limitation of almost all the mass models available in the literature, is that they assume that the gas (and sometimes also the stars) is distributed in razor-thin discs. Yet, it has been well established observationally that gas discs are not only thick, but they are also flared, with a scale height increasing with galactocentric distance, as expected for systems in vertical hydrostatic equilibrium (e.g. Romeo 1992; Olling 1995; Yim et al. 2014; Cimatti et al. 2019).

Other than in the Milky Way (e.g. Nakanishi & Sofue 2003; Kalberla & Dedes 2008; Marasco & Fraternali 2011; Marasco et al. 2017), the flaring of gas discs can be measured directly only in highly-inclined galaxies, although this is challenging as there are degeneracies between the thickness of the discs and the inclination of galaxies, warps along the line of sight, or the presence of layers of extra-planar gas (e.g. Kerr et al. 1957; Sancisi & Allen 1979; Merrifield 1992; Oosterloo et al. 2007; O'Brien et al. 2010; Yim et al. 2014). Notwithstanding, the scale height of any galaxy can also be obtained by solving the equations of vertical hydrostatic equilibrium (i.e. assuming that the gas pressure is in balance with the gravitational pull) given the galactic potential (see for instance van der Kruit 1981; Romeo 1992; Olling 1995; Iorio 2018; Bacchini et al. 2019a, 2020b; Patra 2020a,b). In general, evidence shows clearly that in both dwarfs and massive late-type galaxies, the scale heights of gas discs at the outermost observed radii increase typically by a factor $2-10$ with respect to the innermost

regions, often reaching values $\gtrsim 1$ kpc.

Understanding the real geometry of gas discs has important implications for our understanding of star formation, turbulence, and feedback processes (e.g. Romeo 1992; Bacchini et al. 2019a; Utomo et al. 2019; Bacchini et al. 2020a). The flaring of the discs can also play a role when deriving the rotation curve decomposition and mass models of galaxies. Given that the circular speed profiles of discs will depend on their gravitational potential and more specifically on the radial acceleration at the midplane, a varying scale height will produce a different circular speed than razor-thin discs and even than thick discs with constant thickness (e.g. Binney & Tremaine 2008). The effects are systematic and should be quantified.

In this chapter, we aim to investigate how significantly affected mass models are when taking into account the flared geometry of the gas discs. To the best of our knowledge, the effect of gas flaring in the mass models has not been studied in the literature in a systematic way for a sample of galaxies (see e.g. Olling 1996 for an individual case). So far, mass models that assume razor-thin discs have been used to derive the scale height of the H I and H_2 discs, but the impact of this on the recovered dark matter halo parameters themselves is yet to be explored. It is important to understand and quantify this, specially with the advent of large and systematic studies providing mass models. In this work, we start filling this gap by self-consistently deriving the gas flaring and dark matter halo parameters for a sample of galaxies.

7

Accurate computations of scale heights require detailed kinematic modelling of interferometric H I and CO data, together with robust bulge-disc decomposition. As we detailed below, we have collected such data. This also allow us to revisit important scaling relations, namely the stellar- and baryon–to–halo mass relation, and the dark matter halo concentration–mass relation. While these relations have been recently explored using mass models of large galaxy samples (e.g. Posti et al. 2019; Li et al. 2020), some questions remain open. For instance, *i)* the shape of the stellar–to–halo mass relation at the lowest and highest stellar mass regime is not fully established (e.g. Moster et al. 2013; Posti et al. 2020), *ii)* the baryon–to–halo mass relation remains somewhat unexplored as mass models do only rarely include both the atomic and molecular gas content, and *iii)* it has been claimed that the dark matter concentration–mass relation from N-body cosmological simulations (e.g. Dutton & Macciò 2014; Ludlow et al. 2014) is not followed by the data unless imposed as a prior (e.g. Katz et al. 2017; Li et al. 2020). In addition to this, it is unknown whether the flaring of the discs can affect these relations. Gaining insight into these scaling laws is essential in the quest of understanding galaxy evolution. Besides encoding dynamical information, these relations are subject to baryonic physics and thus we can use them to constrain processes like feedback and adiabatic contraction, which are expected to impact the properties of the dark matter haloes (e.g. Mo et al. 2010; Cimatti et al. 2019). We will therefore take advantage of our analysis and data to revisit these relations.

The structure of this work is as follows. In Sec. 7.2 we present our galaxy sample, explain its selection criteria, and describe the type of data used for each of our galaxies. In Sec. 7.3 we detail our methodology to derive the gas discs scale heights and mass models for each galaxy. In Sec. 7.4 we present our main findings, showing our mass models and scale heights. In Sec. 7.5 we discuss the implications of our results for the scaling relations between halo mass and concentration, stellar mass, and baryonic mass; we also discuss the main caveats of our study and compare with previous works. Finally, in Sec. 7.6 we summarise our main findings.

7.2 Sample selection and data

To investigate the effects of the gas thickness on mass models, circular speeds, gas velocity dispersions, and mass profiles are needed. This makes it essential to select galaxies with high-quality data, mapping their gas and stellar distributions. In the case of the gas surface density profiles, deep, extended, and high-spatial resolution data (typically H I or CO emission-line observations) are needed. For the stellar component, near-IR data is desirable to trace the underlying stellar discs. Concerning the kinematics, the H I and CO data also allow to obtain the gas rotation velocity and velocity dispersion, which can then be used to obtain the circular speed. As we describe below, our sample consists of galaxies with these kind of data and with detailed kinematic models available in the literature.

7.2.1 Dwarf galaxies

Kinematics

We selected a subsample of the LITTLE THINGS galaxies (Hunter et al. 2012) studied by Iorio et al. (2017). Those authors provide the H I velocity dispersion ($\sigma_{\rm HI}$) as well as the circular speed ($V_{\rm c}$) of the galaxies after correcting the observed rotation velocities ($V_{\rm rot}$) for asymmetric drift (see Sec. 4.3 in Iorio et al. 2017). These parameters[1] were derived using $^{\rm 3D}$BAROLO (Di Teodoro & Fraternali 2015), a software that fits non-parametric tilted ring models to emission-line data cubes. Effectively, $^{\rm 3D}$BAROLO creates 3D realisations of rotating gas discs and chooses the model that better reproduces the emission-line data, velocity channel by velocity channel, after taking into account the beam (PSF) of the observations through a convolution operation. For large disc galaxies traditional 2D methods fitting the velocity field (e.g. de Blok et al. 2008; Frank et al. 2016) and $^{\rm 3D}$BAROLO yield similar results. However, dwarf galaxies (and low-resolution observations in general) may suffer from beam smearing, which can significantly modify the shape of the velocity fields (e.g. Begeman 1987; Swaters 1999; Di Teodoro & Fraternali 2015), making 2D

[1] All the kinematic data on LITTLE THINGS galaxies studied in Iorio et al. (2017) is publicly available at `https://www.filippofraternali.com/downloads`

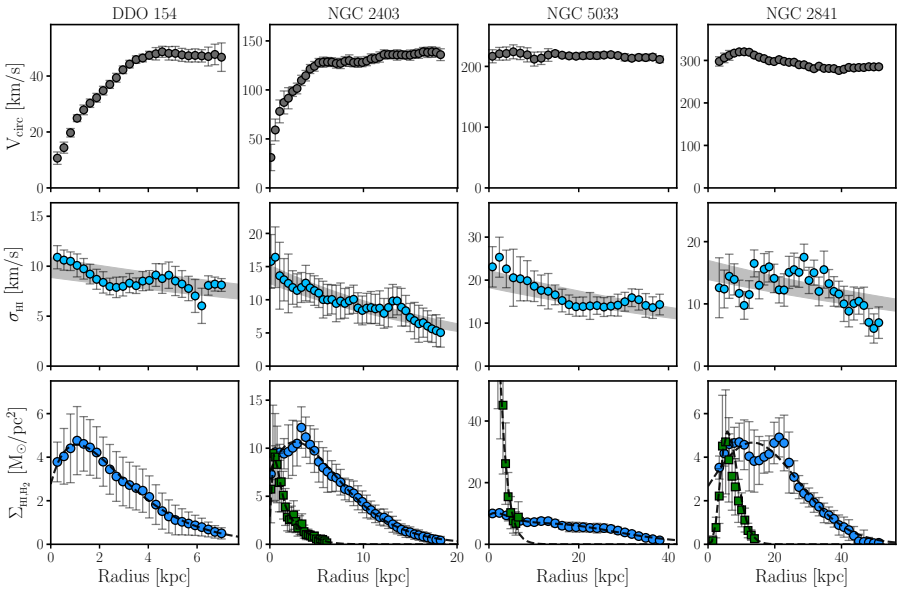

Figure 7.1: Data for four representative galaxies in our sample spanning our full circular speed range. *Top:* Circular speed profiles. *Middle:* H I velocity dispersion profiles. The gray band shows an exponential fit to the data (blue) with an uncertainty of ± 10 per cent in its normalisation. *Bottom:* H I (blue circles) and H_2 (green squares) surface density profiles, including helium correction. The dwarf DDO 133 has no available CO data and it likely hosts no significant H_2 reservoirs. The curves on top of the data show the functional forms fit to obtain the corresponding contributions to the total circular speed (see Sec. 7.3.1). In all the panels for NGC 2403 and NGC 2841 we plot one data point for every two, except for the H_2 surface density profiles.

methods unreliable to recover the intrinsic kinematics. The 3D approach of ^{3D}BAROLO is thus mostly necessary when deriving the kinematics of dwarfs, as it largely mitigates the effects of beam smearing. Moreover, 3D methods have also the advantage of constraining simultaneously the rotation of the galaxy as well as the gas velocity dispersion.

Out of the 17 systems studied by Iorio et al. (2017), we remove the galaxies DDO 47, DDO 50, DDO 53, DDO 101, DDO 133, DDO 216, and NGC 1569. As discussed in detail by Read et al. (2017), the above galaxies are subject of concern regarding their dynamical state, distance estimation, or inclination determination, so we prefer to keep them out of our analysis, ending up with ten dwarfs. It is worth mentioning that all the galaxies have inclination angles larger than 30 degrees, which is important as uncertainties in low inclination angles translate into big uncertainties in the deprojected rotation velocities.

Gas and NIR optical surface densities

The H I surface densities are taken directly from Iorio et al. (2017), and we only apply a multiplicative factor of 1.36 to account for the presence of helium. Stellar 3.6 μm surface brightness profiles are available from the S4G Survey (Bouquin et al. 2018, see also Sheth et al. 2010) and from Zhang et al. (2012). Molecular gas is not detected in these dwarfs (e.g. Leroy et al. 2008; Bigiel et al. 2010) as it often happens with low-mass galaxies, probably due to their low metallicities (see Hunt et al. 2015 and references therein). Recently, Hunter et al. (2021) attempted to infer the molecular gas content of LITTLE THINGS galaxies based on their FUV emission. Those authors report an average H_2–to–H I fraction of about 0.2. Given that these are not direct measurements of H_2 and that the H_2–to–H I fraction of Hunter et al. (2021) is relatively small, in our analysis we do not attempt to include the molecular gas contribution in dwarf galaxies.

7.2.2 Spiral galaxies

Kinematics

To define our spiral galaxy sample, we built on the work by Di Teodoro & Peek (2021), who also used ^{3D}BAROLO to derive the H I kinematics of a sample of nearby spiral galaxies. Broadly speaking, and as detailed below, we chose their best galaxies in terms of spatial resolution, undisturbed kinematics, available bulge-disc NIR photometric decomposition, and ancillary CO observations.

Among all the galaxies from Di Teodoro & Peek (2021), we make a first selection cut and keep only those with a spatial resolution better than 1 kpc, to ensure good sampling of the rotation curve and velocity dispersion profiles. Next, we selected against galaxies with inclinations below 30°. After this, we also eliminate the galaxies NGC 3031, NGC 3521, M83, which met the above criteria but show very perturbed kinematics or interactions with neighbors and thus it is not granted that their gas kinematics fully trace their potential wells.

Regarding the kinematics of the galaxies, we took the values from Di Teodoro & Peek (2021) for $V_{\rm rot}$[2] and converted them to $V_{\rm c}$ following the same asymmetric drift correction prescriptions detailed in Iorio et al. (2017). This correction is extremely small and rather negligible for this sample of massive galaxies, but we undertook it for consistency with the LITTLE THINGS dwarfs (where the correction is significant in some cases). An additional kinematic parameter that we will need for the mass models and the derivation of the scale height of the H_2 discs is their velocity dispersion (see Section 7.3.2). The rotation curves of H I and H_2 (as traced by the CO line) show a very good agreement (Frank et al. 2016; Bacchini et al. 2020a) between each other. In contrast, the H_2 velocity dispersion ($\sigma_{\rm H_2}$) and $\sigma_{\rm HI}$ are not the same. Bacchini et al. (2020a, see also e.g. Mogotsi et al. 2016) found that the ratio between $\sigma_{\rm H_2}$ and $\sigma_{\rm HI}$ among

[2]For a few galaxies we have removed a couple of data points near their centres where it is unclear whether there is actually emission (e.g. the centre of NGC 2841), or on the outer regions if the galaxies show a strong warp or an asymmetric rotation curve (e.g. NGC 3621).

late-type galaxies has a median value of 0.6, i.e. $\sigma_{\rm H_2} \approx 0.6\ \sigma_{\rm HI}$. In principle, one could derive the velocity dispersion of the molecular gas from the CO data (see below). However, this would require the CO kinematic modelling and for some galaxies the CO emission is patchy and the measurement of $\sigma_{\rm H_2}$ is not well constrained and has large uncertainties. For the sake of homogeneity and to avoid these complications, we use the empirical results of Bacchini et al. (2020a) and we assume $\sigma_{\rm H_2} = 0.6\ \sigma_{\rm HI}$; we have checked that reasonable variations of this equality do not impact our results on the mass models significantly.

Gas surface densities

The H I surface density profiles are taken from Di Teodoro & Peek (2021), and we apply the helium multiplicative factor of 1.36. In the case of the molecular gas, we derive H_2 profiles from a set of CO($J = 2-1$) and CO($J = 1-0$) total intensity maps; the existence of CO ancillary observations was one of the main criteria when selecting our sample. For this, we take advantage of following archival observations. The CO maps of the galaxies NGC 253, NGC 3351, NGC 3621, NGC 4535, and NGC 4536, come from the PHANGS-ALMA survey (Leroy et al. 2021b,a). The maps of NGC 2403, NGC 2841, NGC 3198, NGC 4559, NGC 4725, NGC 4736, and NGC 5055 come from the HERACLES survey (Leroy et al. 2009). The maps of NGC 5005 and NGC 5033 come from the BIMA project (Helfer et al. 2003), and of NGC 4651 and NGC 4698 from the VERTICO survey (Brown et al. 2021). The CO map of NGC 3486 comes from Rahman et al. (2012). As the CO map of NGC 3675 is not available, we extracted the published CO profile shown in Young et al. (1995) using a digitising software (Rohatgi et al. 2018). Finally, the galaxies NGC 1313 and NGC 3992 have no significant CO detection in the available data (Bajaja et al. 1995 and Helfer et al. 2003, respectively) and CO data for NGC 3898 and NGC 5350 do not seem to exist. These last two galaxies have, however, high circular speeds (about 250 km/s and 185 km/s, see Table 7.1) dominated in the inner regions by massive bulges and stellar discs, so we do not expect the lack of CO data to affect their rotation curve decomposition. The collected data have different sensitivity and spatial resolution, but overall they allow us to trace reasonably well the CO emission in the central regions of our sample.

Using the CO maps we build azimuthally averaged intensity maps using the same average geometric parameters as for the H I discs[3], and we convert the CO intensities $I_{\rm CO}^{(2-1)}$ to H_2 mass surface densities using

$$\frac{\Sigma_{\rm H_2}}{\rm M_\odot\ pc^{-2}} = \frac{\alpha_{\rm CO}^{(1-0)}}{\rm M_\odot\ pc^{-2}} \frac{1}{R_{21}} \frac{I_{\rm CO}^{(2-1)}}{\rm K\ km/s}, \tag{7.1}$$

where $\alpha_{\rm CO}^{(1-0)}$ is the CO–H_2 conversion factor (including the helium correction factor of 1.36) and R_{21} the CO$(2-1)$–to–CO$(1-0)$ intensity line ratio, for

[3]We note that there is an excellent agreement between the geometric parameters of the H I discs (Di Teodoro & Peek 2021) and the reported values for the CO discs (e.g. Leroy et al. 2021b; Brown et al. 2021).

which we assume a value of 0.7 (see e.g. Leroy et al. 2013; Sandstrom et al. 2013; Leroy et al. 2021b)[4]. While a handful of our galaxies have available $\alpha_{\rm CO}^{(1-0)}$ measurements from Sandstrom et al. (2013), the majority of our sample does not have available $\alpha_{\rm CO}^{(1-0)}$ values. This is not surprising given the difficulty in estimating $\alpha_{\rm CO}^{(1-0)}$ precisely. For consistency, for all our spiral galaxies we adopt $\alpha_{\rm CO}^{(1-0)} = 4.35$, the Milky Way reference value (e.g. Bolatto et al. 2013 and references therein), which is also in reasonable agreement with the average value measured by Sandstrom et al. (2013) in a sample of nearby spiral galaxies. Sandstrom et al. (2013) also found radial variations on the $\alpha_{\rm CO}^{(1-0)}$ of some galaxies in their sample. However, such variations are not always present nor seem to correlate significantly with other galaxy properties, and while most galaxies have somewhat lower values in the central regions, the scatter is large and trends with galactocentric distance are unclear. Given that molecular gas is not the dominant mass component of our galaxies at any radii we do not expect the potential uncertainties in $\alpha_{\rm CO}^{(1-0)}$ to have a strong effect in our rotation curve decomposition. In fact, this has already been shown by Frank et al. (2016).

NIR surface brightness and bulge-disc decomposition

Given that the bulge component will be relevant when deriving our mass models, we refined our selection by requiring that our spiral galaxies have available bulge-disc decompositions from the S4G data coming from Salo et al. (2015). Those authors performed a detailed decomposition of the 3.6 μm surface brightness profiles of the galaxies fitting an exponential disc and a Sérsic profile, and we stick to their decomposition for the sake of consistency. We also select against galaxies with a significant bar or central PSF-like component as determining their kinematics and potentials can be ambiguous (e.g. NGC 4548). For three galaxies in our sample (NGC 2403, NGC 3198, NGC 3621) we do not use the S4G bulge-disc decomposition. The first and the last are not in the sample of Salo et al. (2015), while the fit for NGC 3198 is not satisfactory (e.g. the Sérsic index is 10, the maximum allowed value by the fitting routine of Salo et al. 2015). These three galaxies have, however, 3.6 μm S4G and optical surface brightness profiles without evidence of a bulge (Kent 1987; Muñoz-Mateos et al. 2009). Because of this, and since the galaxies have exquisite H I and CO data and are prototypical well-studied nearby galaxies, we include them in our final sample.

7.2.3 Final galaxy sample

In the end, our final sample consists of ten dwarf galaxies with $15 \lesssim V_{\rm c}/({\rm km/s}) \lesssim 60$ and 22 more massive spirals with $V_{\rm c}$ as high as ~ 300 km/s. Table 7.1 lists our final galaxy sample, and gives the distance to the galaxies (taken form Di

[4]The CO data for NGC 3486, NGC 3675, NGC 5005, and NGC 5033 are for the transition $J = 1 - 0$, and so we take R_{21}=1 in Eq. 7.1.

Teodoro & Peek 2021 and Chapter 5), their morphological type taken from NED[5], and their characteristic circular speed at the outer radii $V_{\rm c,out}$. For the spiral galaxies this characteristic speed is computed following the algorithm of Lelli et al. (2016b, see their Eq. 1 and 2), i.e. by requiring that the circular speeds are flat within ~ 5 per cent over at least the last three measured points (but often many more points are included). The reported uncertainties correspond to the standard deviation in the values considered to estimate the flat speed. In the case of the dwarfs, where some of them have fewer than three points consistent with flat rotation, we use the mean outer velocity reported by Iorio et al. (2017). Fig. 7.1 shows the circular speeds, H I velocity dispersions, and gas surface densities for four representative galaxies in our sample spanning our full circular speed range.

We would like to highlight that although the galaxies in our sample have data coming from different studies, they all have the same type of data and have been analysed with the same methods and thus the sample is fairly homogeneous: 1) the H I kinematics for all the galaxies are derived using ^{3D}BAROLO on data cubes, 2) all the H I and H_2 surface density profiles are based on azimuthal averages of H I and CO maps, and 3) all the galaxies have 3.6 μm photometry and are either bulgeless or have available bulge-disc decomposition derived with the same methodology. This sample is not complete, but as similar samples often used in the literature (e.g. Lelli et al. 2016a; Ponomareva et al. 2016; Chapter 5), it is representative of the regularly rotating nearby galaxy population.

7.3 Obtaining the disc thickness and dark matter halo

The general idea of mass modelling from rotation curve decomposition is that the observed circular speed profile $V_{\rm c}$ is the sum in quadrature of the circular speed profiles of the baryonic and dark matter components

$$V_{\rm c}^2 = \Upsilon_{\rm d} V_{\rm d}|V_{\rm d}| + \Upsilon_{\rm b} V_{\rm b}|V_{\rm b}| + V_{\rm HI}|V_{\rm HI}| + V_{\rm H_2}|V_{\rm H_2}| + V_{\rm DM}|V_{\rm DM}| \ , \qquad (7.2)$$

with $V_{\rm d}$, $V_{\rm b}$, $V_{\rm HI}$, $V_{\rm H_2}$, and $V_{\rm DM}$ the contributions to the circular speed by the stellar disc, stellar bulge, H I disc, H_2 disc, and dark-matter halo, respectively, and with $\Upsilon_{\rm d}$ ($\Upsilon_{\rm b}$) the disc (bulge) mass-to-light ratio.

Our approach will be to fit $V_{\rm c}$ and obtain the dark matter halo by constraining $V_{\rm DM}$ (assuming a functional form with free parameters, see below) together with $\Upsilon_{\rm d}$ and $\Upsilon_{\rm b}$. The key novelty with respect to previous studies is that the thickness of the gas discs is derived self-consistently using an iterative procedure (and thus changing $V_{\rm HI}$ and $V_{\rm H_2}$). In the rest of this section we explain the general steps followed to obtain our final mass models.

[5]The NASA/IPAC Extragalactic Database (NED) is operated by the Jet Propulsion Laboratory, California Institute of Technology, under contract with the National Aeronautics and Space Administration.

Table 7.1: Galaxy sample used in this work. The first column gives the names of the galaxies, the second column their distance, the third column their morphological classification, and the fourth column their characteristic circular speed at the outermost radii.

Name	Distance [Mpc]	Morphology	$V_{c,out}$ [km/s]
Dwarf galaxies			
CV n I dwA	3.6 ± 0.2	Im	22 ± 4
DDO 52	10.3 ± 0.5	Im	51 ± 6
DDO 87	7.4 ± 2.2	Im	50 ± 9
DDO 126	4.9 ± 0.4	IBm	39 ± 3
DDO 154	3.7 ± 0.1	IB(s)m	47 ± 5
DDO 168	4.3 ± 0.3	IBm	56 ± 7
DDO 210	0.9 ± 0.1	IB(s)m	16 ± 10
NGC 2366	3.4 ± 0.3	SB(s)b	58 ± 5
UGC 8508	2.6 ± 0.2	IAm	34 ± 6
WLM	1.0 ± 0.1	IB(s)m	39 ± 3
Spiral galaxies			
NGC 0253	3.6 ± 0.3	SAB(s)c	198 ± 2
NGC 1313	4.2 ± 0.4	SB(s)d	127 ± 3
NGC 2403	3.2 ± 0.3	SAB(s)cd	136 ± 2
NGC 2841	14.1 ± 1.9	SA(r)b	286 ± 6
NGC 3198	13.8 ± 1.1	SB(rs)c	150 ± 3
NGC 3351	10.5 ± 0.8	SB(r)b	177 ± 4
NGC 3486	12.7 ± 2.8	SAB(r)c	155 ± 3
NGC 3621	6.7 ± 0.5	SA(s)d	145 ± 2
NGC 3675	14.4 ± 3.1	SA(s)b	213 ± 4
NGC 3898	22.1 ± 6.1	SA(s)ab	246 ± 5
NGC 3992	17.1 ± 4.7	SB(rs)bc	231 ± 3
NGC 4535	15.8 ± 1.3	SAB(s)c	225 ± 6
NGC 4536	15.2 ± 1.9	SAB(rs)bc	165 ± 4
NGC 4559	8.9 ± 0.8	SAB(rs)cd	123 ± 3
NGC 4651	16.8 ± 4.6	SA(rs)c	185 ± 3
NGC 4698	19.6 ± 4.2	SA(s)ab	214 ± 5
NGC 4725	12.4 ± 1.1	SAB(r)ab	211 ± 3
NGC 4736	4.4 ± 0.4	(R)SA(r)ab	148 ± 2
NGC 5005	18.4 ± 2.1	SAB(rs)bc	269 ± 6
NGC 5033	19.0 ± 2.7	SA(s)c	217 ± 3
NGC 5055	8.9 ± 0.7	SA(rs)bc	184 ± 6
NGC 5350	30.9 ± 5.5	SB(r)b	184 ± 2

7.3.1 From gas and stellar surface densities to circular speed profiles

Once the geometry and surface density of a matter component are known, its circular speed profile can be obtained from its gravitational potential. To derive the circular speed profiles from the surface densities, we use the software GALPYNAMICS (Iorio 2018). In the case of galactic discs, GALPYNAMICS computes the gravitational potential of a given mass distribution of density ρ via numerical integration of the expression (cf. Cuddeford 1993)

$$\Phi(R,z) = -\frac{2\,G}{\sqrt{R}} \int_{-\infty}^{\infty} dl \int_{0}^{\infty} du\ \sqrt{u\ y}\ K(\sqrt{y})\rho(u,l)\ , \tag{7.3}$$

where R and z are the radial and vertical coordinates, G is the gravitational constant, K the complete elliptical integral of the first kind, and y defined as:

$$y = \frac{2}{1+x},\ \text{with}\ x = \frac{R^2+u^2+(z-l)^2}{2Ru}\ . \tag{7.4}$$

The circular speed is then obtained via the derivative of the potential evaluated at the midplane

$$V_{\rm c}^2(R) = R\left[\frac{\partial\Phi(R,z)}{\partial R}\right]_{z=0}\ . \tag{7.5}$$

In the case of a spherical distribution the value of $V_{\rm c}$ is simply $\sqrt{GM(r)/r}$. While deriving $V_{\rm c}$ for a given component, GALPYNAMICS uses functional forms to describe its surface density profile. Because of this, we fit the observed gas and stellar surface densities with functional forms as described below.

Dwarfs: HI distribution

The surface density profiles of the H I discs of the dwarfs are well described by a function of the form

$$\Sigma_{\rm HI}(R) = \Sigma_{0,\rm HI}\ e^{-R/{\rm R}_1}(1+R/{\rm R}_2)^{\alpha}\ , \tag{7.6}$$

with Σ_0, R_1, R_2 and α the fitting parameters. This function has a characteristic shape that mimics very well the surface density profiles observed in gas-rich galaxies, which often show a plateau or central depression in the inner regions, then they increase, and then fall almost exponentially in the outskirts (e.g. Swaters 1999; Martinsson et al. 2016; Wang et al. 2016), as illustrated in Fig. 7.1 for DDO 133, NGC 2403, and NGC 2841.

Regarding the vertical distribution, while in a first step we assume the disc is razor-thin, the final scale height and its flaring are determined at the same time as the dark matter halo parameters, as we describe in Sec. 7.3.4.

Dwarfs: stellar discs

All our dwarf galaxies have stellar disc distributions that are very well fitted by exponential discs, with minimal departures. Therefore, we fit the stellar 3.6 μm profiles as exponential discs following

$$\Sigma_*(R) = \Sigma_{0,*}\ e^{-R/R_\mathrm{d}}\ , \tag{7.7}$$

with $\Sigma_{0,*}$ and R_d the stellar central surface density and disc scale length, respectively.

To fully define the stellar disc distribution, we also need to specify the vertical structure. We assume that the stellar disc follows a sech^2 profile along the vertical direction, and that it has a constant thickness $z_\mathrm{d} = 0.196 R_\mathrm{d}^{0.633}$, as found in low-inclination star forming galaxies (e.g. Bershady et al. 2010; see also van der Kruit & Freeman 2011). With this, the shape of V_d for the dwarfs is fully determined, and during our fitting technique we will obtain Υ_d (i.e. its normalisation). We remind the reader that there are no bulges present in our dwarfs, neither do the galaxies have significant H_2, and thus in practice $V_\mathrm{b} = V_{H_2} = 0$.

Spirals: H I and H_2 distributions

As for the dwarf galaxies, we fit some of the H I and H_2 profiles (including the helium content) of our spirals using Eq. 7.6. Some of the spirals, however, have gas surface density profiles with a more complex behavior. For these cases, following Bacchini et al. (2019a), we fit a 'poly-exponential' profile of third degree

$$\Sigma_{\mathrm{HI,H_2}}(R) = \Sigma_{0,\mathrm{pex}}\ e^{-R/R_\mathrm{pex}}\ (1 + c_1 R + c_2 R^2 + c_3 R^3)\ , \tag{7.8}$$

with $\Sigma_{,\mathrm{pex}}, R_\mathrm{pex}, c_1, c_2, c_3$ the fitting parameters. The galaxies for which we use a poly-exponential fit are NGC 3621, NGC 4535, NGC 4736, and NGC 5033, in the case of H I, and NGC 2403, NGC 3198, NGC 3351, NGC 4535, NGC 4725, NGC 5005, NGC 5033, and NGC 5055, in the case of H_2.

In a similar way as for the dwarfs, the gas discs of the spirals are also assumed to be thin in a preliminary step, but their final scale heights are obtained through our main fitting routine.

Spirals: stellar bulge and disc

As mentioned before, most of our galaxies have bulge-disc decomposition available from Salo et al. (2015). Those authors used a parametric modelling software (GALFIT, Peng et al. 2010) to decompose the 3.6 μm surface brightness profiles into different components. In a few cases we have neglected the contribution (less than 5 per cent of the total flux) from a PSF-like or bar component. In particular, we chose the parametrisations using an exponential disc plus a Sérsic component. Some galaxies (NGC 3486, NGC 3675, NGC 4651, NGC 4736, NGC 5033, and NGC 5055) were modeled using two exponential discs to mimic a more complex behavior of their surface brightness profiles. We obtain the

circular speed profile of our discs (up to the normalisation $\Upsilon_{\rm d}$) with GALPYNAMICS using an exponential profile (Eq. 7.7) with parameters coming from Salo et al. 2015. In the case of NGC 2403, NGC 3198, and NGC 3621, for which have no bulge-disc decomposition but the galaxies look bulgeless, we take the S4G 3.6 μm surfaces brightness profiles from Muñoz-Mateos et al. (2009) and we fit two exponential discs (needed to reproduce the observed features in the profiles) following Salo et al. (2015). For all the galaxies with double stellar disc profiles we obtain their total V_* by summing the individual contributions in quadrature. For the vertical distribution of all the stellar discs we make the same assumptions as for the stellar component of the dwarfs, assuming a sech^2 profile and a thickness $z_{\rm d} = 0.196 R_{\rm d}^{0.633}$ constant with radius. For the galaxies with two exponential discs we do not assume each has their own $z_{\rm d}(R_{\rm d})$ because usually one of the components has a low density and very large $R_{\rm d}$ (typically reproducing breaks/tails in surface brightness profiles). Instead, we combine both disc contributions and compute a half-light radius $R_{\rm eff}$, which is then transformed into a pseudo $R_{\rm d}$ using $R_{\rm eff} = 1.678 R_{\rm d}$; we then assume this pseudo $R_{\rm d}$ when computing $z_{\rm d} = 0.196 R_{\rm d}^{0.633}$. We note that the use of the expression $R_{\rm eff} = 1.678 R_{\rm d}$ is not fully justified as it is only valid for exponential discs, but we consider it a reasonable mass-weighted compromise. In any case, this assumption does not alter our results below.

For the bulge components the situation is less straightforward. The Sérsic profile describes surface densities with a flat (2D) geometry, while in practice bulges are spheroidal. Taking this into account is relevant because the force generated by a flattened distribution is different (stronger in the midplane) than that of an spheroid, and thus it can affect the recovery of the best-fitting dark matter halo parameters and the computation of the gas discs scale height. To obtain a realistic bulge component we assume that the bulges in our galaxies are spherical[6] and with a volume density described by a double power-law of the form:

$$\rho(r, z) = \frac{\rho_c}{(r/r_{\rm s})^{\alpha}(1 + (r/r_{\rm s}))^{\beta - \alpha}} \ , \tag{7.9}$$

with $r = \sqrt{R^2 + z^2}$ the spherical radius, $\rho_{\rm c}$ and $r_{\rm s}$ a characteristic density and radius, respectively, and α and β the power-law exponents. In practice, we obtain the best set ($\rho_{\rm c}$, $r_{\rm s}$, α, β), using an MCMC routine based on the python package `emcee` (Foreman-Mackey et al. 2013), such that the resulting spherical bulge has a projected 2D surface density matching the Sérsic profile reported by Salo et al. (2015). The resulting bulge is then given to GALPYNAMICS to obtain $V_{\rm b}$, while $\Upsilon_{\rm b}$ is obtained during our fitting routine. Fig. 7.2 shows the comparison between the Sérsic profiles (circles) for the bulges of NGC 5033 and NGC 2814 and the surface density of the best-fitting spherical bulges we obtain (black curves). We find a similarly good agreement for our full sample.

[6] We assume spherical symmetry for simplicity, but GALPYNAMICS can also deal with flattened spheroidal components.

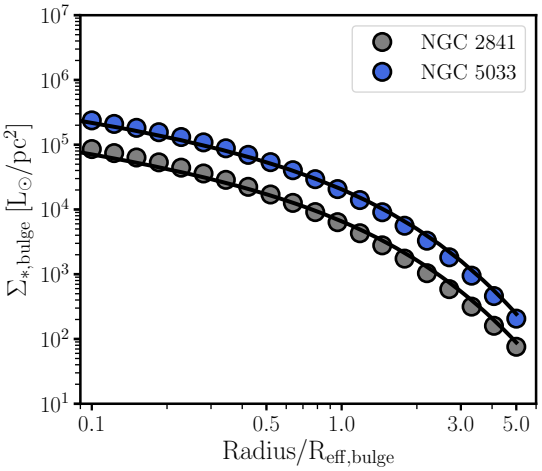

Figure 7.2: Comparison between the Sérsic profiles of NGC 2841 (grey) and NGC 5033 (blue) as derived by Salo et al. (2015), and the projected surface density of our best-fitting spherical bulges for those galaxies (black curves). The x-axis is normalised to the effective radii of the bulges ($R_{\mathrm{eff,bulge}}$). We only show distances up to $5R_{\mathrm{eff,bulge}}$ to ease the comparison, but a good agreement remains at all radii.

7.3.2 Deriving the thickness and flaring of the gas discs

Given an external mass distribution (e.g. a dark matter halo and a stellar disc), GALPYNAMICS is able to compute the gravitational potential of an additional galaxy component (e.g. a gas disc) and estimate its scale height under the assumption of vertical hydrostatic equilibrium. This is done iteratively taking into account the external gravitational potential and the self-gravity of the additional component through an iterative process (Iorio 2018). For the interested reader, extensive and detailed discussion on the use of GALPYNAMICS to estimate scale heights can be found in Iorio (2018); Bacchini et al. (2019a, 2020b).

Effectively, GALPYNAMICS solves numerically the following expression (see Bacchini et al. 2019a; Patra 2019), which describes the 3D density profile $\rho(R, z)$ of the distribution whose scale height we aim to derive

$$\rho(R, z) = \rho(R, 0) \exp\left[-\frac{\Phi(R, z) - \Phi(R, 0)}{\sigma^2(R)}\right] . \tag{7.10}$$

In the above equation, $\rho(R, 0)$ is the density profile of the gas (i.e. the radial profile of its volume density) evaluated in the disc midplane. In a similar way, $\Phi(R, 0)$ is the total (dark matter plus stars plus gas disc(s)) gravitational potential $\Phi(R, z)$ evaluated in the midplane. Finally, $\sigma(R)$ is the radial profile of the gas velocity dispersion, assumed to be isotropic. Following Bacchini et al. (2019a, 2020b), we fit the observed $\sigma(R)$ profiles with an exponential function $\sigma(R) = \sigma_0 e^{-R/R_\sigma}$, which provides a very good representation of the data and has the advantage of smoothing out small irregularities in the observed profiles, as shown in Fig. 7.1. The scale height $h(R)$ is defined as the standard deviation of Eq. 7.10, and thus it can be obtained once Φ and $\sigma(R)$ are known. Note that some authors report the scale heights as the half width at half maximum of the vertical profiles, which should then be divided by a factor 1.777 if comparing with h, as we assume a Gaussian profile for the vertical distribution. In Sec. 7.3.4

we explain how do we derive the thickness of the gas discs together with the best-fitting dark matter halo in a consistent way.

7.3.3 Fitting the dark matter halo and mass-to-light ratios

We assume that the dark matter haloes can be described by two different profiles depending on the galaxy mass. For the massive spirals we use a Navarro-Frenk-White (NFW, Navarro et al. 1997) profile, while for the dwarfs we fit the so-called coreNFW profile (Read et al. 2016a,b).

The density profile of the NFW profile is

$$\rho_{\rm NFW}(r) = \frac{4\rho_{\rm s}}{(r/r_{\rm s})(1+r/r_{\rm s})^2} \ , \tag{7.11}$$

where $r = \sqrt{R^2+z^2}$, $r_{\rm s}$ is a scale radius, and $\rho_{\rm s}$ the volume density at $r_{\rm s}$. This volume density can be written as

$$\rho_{\rm s} = \frac{M_{200}}{16\pi r_{\rm s}^3[\ln(1+c_{200}) - c_{200}/(1+c_{200})]} \ , \tag{7.12}$$

with M_{200} the dark matter mass within a radius R_{200} where the average density is 200 times the critical density of the universe, and $c_{200} \equiv R_{200}/r_{\rm s}$ is the concentration; N-body simulations find a clear anti-correlation between M_{200} and c_{200} (e.g. Dutton & Macciò 2014; Ludlow et al. 2014).

The coreNFW profile allows the classical NFW profile to develop a core if this is needed to provide a better fit to slowly rising rotation curves. This is typically the case for dwarf galaxies and the well-known cusp-core problem (see Bullock & Boylan-Kolchin 2017 for a recent review).

The density profile of the coreNFW halo is

$$\rho_{\rm coreNFW}(r) = f^n \rho_{\rm NFW}(r) + \frac{n f^{n-1}(1-f^2)}{4\pi r^2 r_{\rm c}} M_{\rm NFW}(r) \ , \tag{7.13}$$

where $\rho_{\rm NFW}$ and $M_{\rm NFW}$ are the conventional density and mass for a NFW halo at a given radius, but $f = \tanh(r/r_{\rm c})$ is a function that generates a core of size $r_{\rm c} = 2.94\ R_{\rm d}$. The parameter n controls how strong is the transformation from cusp to core: $n = 0$ means no core, recovering the NFW halo, and $n = 1$ means a completely cored density profile. In practice, n is defined as $n = \tanh(\kappa t_{\rm SF}/t_{\rm dyn})$, with $\kappa = 0.04$, $t_{\rm SF}$ the time whilst the galaxy has been forming stars (assumed to be 14 Gyr), and $t_{\rm dyn}$ the NFW dynamical time at the scale radius $r_{\rm s}$. For further details on all these parameters we refer the reader to Read et al. (2016a,b, 2017). In the end, following the above prescriptions, the coreNFW halo has the same two free parameters as the classic NFW halo: the mass M_{200} and the concentration c_{200}.

Together with the mass-to-light ratio for the stellar disc and the bulge, the dark matter halo parameters M_{200} and c_{200} are fitted using a MCMC routine

based on `emcee`. Our scripts explores the parameter space looking for trial dark matter haloes and Υ to find the best set of values to minimise Eq. 7.2 using χ^2 function.

For $\Upsilon_{\rm d}$, we use a Gaussian prior centered at $\Upsilon_{\rm d} = 0.5$ $\rm M_\odot/L_\odot$, with a standard deviation of 0.11 dex, and with boundaries $0.1 < \Upsilon_{\rm d}/(\rm M_\odot/L_\odot) < 1.5$. Instead of fitting directly $\Upsilon_{\rm b}$, we define a parameter f such that $\Upsilon_{\rm b} = f\Upsilon_{\rm d}$. We impose a Gaussian prior centered on $f = 1.4$ with standard deviation of 0.1 dex and with boundaries $1 < f < 2$. These priors aim to break the degeneracy between disc, bulge, and halo in the centre of galaxies using values motivated by stellar population synthesis models (e.g. McGaugh & Schombert 2014; Meidt et al. 2014; Querejeta et al. 2015).

For the priors on M_{200} and c_{200}, we investigate two different scenarios. In the first one, both M_{200} and c_{200} have flat and wide priors ($8 < \log(M_{200}/\rm M_\odot) < 14$ and $2 < c_{200} < 50$). In the second case, using the same boundary limits, we impose a Gaussian prior for $\rm c_{200}$ which is centered on the $c_{200} - M_{200}$ relation of Dutton & Macciò (2014)

$$\log(c_{200}) = 0.905 - 0.101 \log\left(\frac{0.7 M_{200}}{10^{12}\ \rm M_\odot}\right) , \tag{7.14}$$

with a 1σ standard deviation of 0.11 dex and assuming a Hubble parameter $h = 0.7$. We note that our boundaries for the parameter space of c_{200} are motivated by cosmological arguments (see McGaugh et al. 2003).

The approach detailed above allows us to check whether or not the $c_{200} - M_{200}$ is recovered from the data, or if it has to be imposed to obtain physically meaningful dark matter haloes. We discuss the results of these experiments in Section 7.5.3.

7.3.4 Self-consistent derivation of the thickness and dark matter halo

We now proceed to explain how we estimate the thickness of the gas discs and the best-fitting dark matter halo for each galaxy in our sample. This is done through an iterative processes based on GALPYNAMICS and our MCMC routine. The steps are as follows.

1. Making use of GALPYNAMICS and assuming $\Upsilon_{\rm d} = \Upsilon_{\rm b} = 1$, $V_{\rm d}$, $V_{\rm b}$ and the corresponding gravitational potentials $\Phi_{\rm d}$ and $\Phi_{\rm b}$ are derived from the stellar density profiles. We also assume that the H I and $\rm H_2$ discs are razor-thin to obtain a first estimate of $\Phi_{\rm HI}$ and $\Phi_{\rm H_2}$ and their corresponding $V_{\rm HI}$ and $V_{\rm H_2}$.

2. Using $V_{\rm d}$, $V_{\rm b}$, $V_{\rm HI}$, and $V_{\rm H_2}$, we fit $V_{\rm c}$ and we obtain a preliminary set ($\log(M_{200})$, c_{200}, $\Upsilon_{\rm d}$, f). Therefore, we can now update $\Phi_{\rm d}$ and $\Phi_{\rm b}$, and obtain $\Phi_{\rm DM}$. Traditional rotation curve decompositions would stop here.

3. GALPYNAMICS computes the thickness of the H I disc by solving numerically Eq. 7.10 while taking into account $\Phi_{\rm DM}$, $\Phi_{\rm d}$, $\Phi_{\rm b}$, $\Phi_{\rm H_2}$ (for a razor-thin $\rm H_2$

disc) and the H I disc self-gravity. This allow us to obtain a new estimate of $\Phi_{\rm HI}$.

4. GALPYNAMICS computes the thickness of the H_2 disc taking into account $\Phi_{\rm DM}$, $\Phi_{\rm d}$, $\Phi_{\rm b}$, $\Phi_{\rm HI}$ (derived in the previous step), and the H_2 disc self-gravity.

5. Step 3 and 4 are repeated iteratively until the changes in both scale heights, at all radii, are at least smaller than 10 per cent with respect to the previous iteration, which is a sensible choice given that the uncertainty in the scale height can be defined as the fractional error of the gas velocity dispersion ($\Delta h = h\Delta\sigma(R)/\sigma(R)$, see appendix E in Bacchini et al. 2019a), for which 10 per cent is an appropriate uncertainty (see Fig. 7.1). Once these iterations converge, we end up with scale heights (and Φ) for the H I and H_2 discs that were derived taking into account each other plus the stellar disc, the bulge, and the dark matter halo.

6. With all the new potentials, our MCMC routine finds a new best-fitting ($\log(M_{200})$, c_{200}, $\Upsilon_{\rm d}$, f) set, updating the mass model and generating a new set of potentials.

7. Steps $3-6$ are repeated iteratively until ($\log(M_{200})$, c_{200}, $\Upsilon_{\rm d}$, f) converge. We adopt a convergence criterion such that the change in M_{200}, c_{200}, $\Upsilon_{\rm d}$, and f between the last and penultimate iteration has to be less than 3 per cent. For most of our galaxies $2-3$ iterations are enough to reach convergence.

Due to our iterative process, the scale height of the gas discs, the disc and bulge stellar mass-to-light ratios, and the parameters of the dark matter halo, are derived in a fully consistent way taking into account the gravitational effects of each other.

7.4 Results

7.4.1 Mass models

In Fig. 7.3, we show the results of our rotation curve decomposition for the four representative galaxies displayed in Fig. 7.1. The figure corresponds to the case when c_{200} was obtained using the prior on Eq. 7.14. For each galaxy we show two mass models, one that assumes that the H I and H_2 (if present) discs are razor-thin as in traditional methods, and one showing our final model after taking into account the flaring of the discs. Similar plots of the mass models (and corresponding posterior distributions) for our whole sample, for both types of priors on c_{200}, are available in Appendix 7.C.

We obtain successful fits for all our sample when we use a prior on the $c_{200} - M_{200}$ relation: the best-fitting $V_{\rm c}$ faithfully reproduces the observations, and the posterior distributions of the best-fitting parameters are well behaved

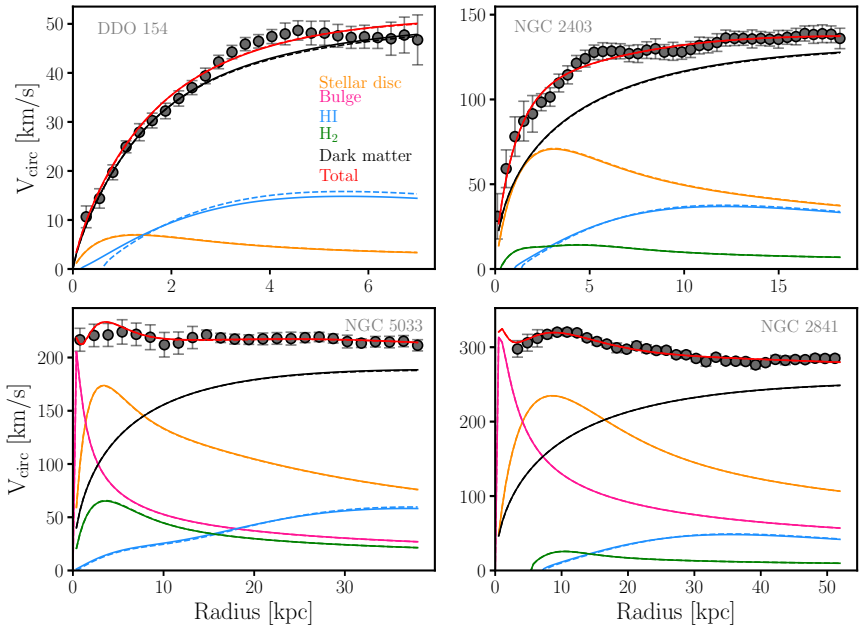

Figure 7.3: Mass models for the same representative galaxies as in Fig. 7.1. The models correspond to the case where c_{200} is obtained with a prior on Eq. 7.14. The points represent the circular speed profile of the galaxies (one out of each two points are shown for NGC 2403 and NGC 2841). The orange, pink, blue, green, and dark lines show the contribution to the circular speed by the stellar disc, bulge, H I disc, H_2 disc, and dark matter halo, respectively. Dashed lines show the first iteration of our MCMC (with razor-thin gas discs), while solid lines show our final model (with flared gas discs). Similar plots for all our galaxies are available in Appendix 7.C.

with a Gaussian or nearly Gaussian shape. When we use the flat prior on c_{200} the fits are seemingly equally good, but for some galaxies (CVn I dwA, NGC 253, NGC 3486, NGC 3898, NGC 4535, NGC 5350, and UGC 8505) their c_{200} values are not well constrained, as their posterior distributions go towards our lower bound $c_{200} = 2$. In the following figures such galaxies are shown with different symbols to emphasise that their mass models are not fully reliable. As we discuss below, for the rest of the galaxies the mass models obtained under our two $c_{200}-$priors are in very good agreement with each other.

Fig. 7.3 shows that most of the time the overall effect of including the flaring of the gas discs is minor. This is not fully surprising: in the high-mass regime the potential of the galaxies in the inner regions is heavily dominated by the stellar components, where most of the gas mass resides. In the dwarf galaxies the gas dominates the baryonic content, but the dark matter haloes are more important from a dynamical point of view. In the case of DDO 154 (top left panel in Fig. 7.3), one can appreciate that by not using the razor-thin disc assumption the 'negative' velocities often seen in the circular speed of H I discs (e.g. de Blok

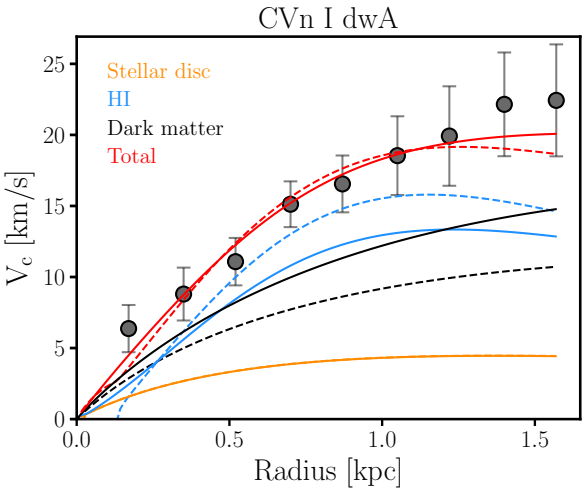

Figure 7.4: Mass model of the dwarf galaxy CVn I dwA. The solid (dashed) lines show the mass model when a flared (razor-thin) H I disc is used. The large effect of the flaring on the mass model is clear.

et al. 2008; Frank et al. 2016) are gone. While in practice those velocities are considered negative (which is why the absolute values in Eq. 7.2 are needed), in the presence of H I discs with a central depression, a test particle in the midplane would feel an outward acceleration due to the mass at larger radii. Because of this, the radial acceleration in the midplane is negative, and thus $|V_{\rm HI}|V_{\rm HI}$ is negative (see Eq. 7.5). Including the gas flaring strongly mitigates this effect: even when the central mass depression is there, the mass in the outer parts is distributed in a thicker disc, and thus a test particle in the midplane feels a weaker outwards acceleration, bringing $|V_{\rm HI}|V_{\rm HI}$ closer to zero and even to positive values. This is an interesting local effect only visible when considering the real geometry of the gas discs.

In a few galaxies the effects of the flaring are important. In Fig. 7.4 we show the mass model for the dwarf galaxy CVn I dwA, which shows the most extreme changes when including the H I disc flaring within our sample. The flaring not only gets rid of the negative $|V_{\rm HI}|V_{\rm HI}$ in the innermost regions, but it also decreases the contribution of the gas disc at larger radii, allowing for a dark matter halo about three times more massive.

We note here that our methodology described in Sec. 7.3.4 does not take into account the uncertainty in the distances of our galaxy sample. While the distance could be included as a nuisance parameter in the MCMC fitting (e.g. with a Gaussian prior, see Li et al. 2020; Chapter 4), this is computationally prohibitive for our sample in our methodology as it would be required to compute the potential of each component on each iteration of the MCMC, and for each of these iterations to compute our scale heights. In practice, the distance to the galaxies tends to simply follow its prior and it only helps as a nuisance parameter to obtain appropriate uncertainties in the other quantities being fitted (see Li et al. 2020), we decided to follow a simplistic approach. We repeat our steps

Table 7.2: Results of our rotation curve decomposition for the case when a prior on Eq. 7.14 is imposed. The columns give our fiducial values (the median of the posterior distributions) and their upper and lower uncertainties (corresponding to the $16^{\rm th}$ and $84^{\rm th}$ percentiles). Only galaxies with bulges have values of f. Note that all these quantities include the contribution from distance uncertainties.

Name	$\log(M_{200}/\mathrm{M}_\odot)$			c_{200}			$\Upsilon_\mathrm{d}(\mathrm{M}_\odot/\mathrm{L}_\odot)$			f		
	$50^{\rm th}$ pctl	$\sigma-$	$\sigma+$	$50^{\rm th}$ pctl	$\sigma-$	$\sigma+$	$50^{\rm th}$ pctl	$\sigma-$	$\sigma+$	$50^{\rm th}$ pctl	$\sigma-$	$\sigma+$
CVn I dwA	8.80	−0.26	+ 0.26	18.08	−4.57	+ 6.11	0.50	−0.11	+ 0.11	–	–	–
DDO 52	10.36	−0.16	+ 0.20	12.69	−3.18	+ 4.02	0.50	−0.11	+ 0.11	–	–	–
DDO 87	10.38	−0.19	+ 0.36	12.66	−3.74	+ 5.48	0.52	−0.11	+ 0.11	–	–	–
DDO 126	9.95	−0.14	+ 0.17	13.42	−2.85	+ 3.29	0.46	−0.11	+ 0.11	–	–	–
DDO 154	10.40	−0.08	+ 0.09	9.23	−0.95	+ 1.02	0.44	−0.11	+ 0.11	–	–	–
DDO 168	10.56	−0.16	+ 0.20	12.37	−2.64	+ 3.01	0.43	−0.11	+ 0.11	–	–	–
DDO 210	8.35	−0.57	+ 0.57	20.02	−5.42	+ 7.30	0.50	−0.11	+ 0.11	–	–	–
NGC 0253	12.31	−0.23	+ 0.30	6.60	−1.61	+ 2.01	0.32	−0.03	+ 0.03	1.40	−0.10	+ 0.10
NGC 1313	11.91	−0.12	+ 0.16	8.51	−1.41	+ 1.47	0.30	−0.08	+ 0.08	1.38	−0.10	+ 0.10
NGC 2366	10.47	−0.09	+ 0.11	15.19	−2.97	+ 3.30	0.50	−0.11	+ 0.11	–	–	–
NGC 2403	11.60	−0.05	+ 0.06	11.07	−1.40	+ 1.54	0.42	−0.07	+ 0.07	–	–	–
NGC 2841	12.52	−0.05	+ 0.05	8.81	−1.28	+ 1.69	0.84	−0.08	+ 0.08	1.37	−0.09	+ 0.09
NGC 3198	11.62	−0.02	+ 0.03	12.24	−1.36	+ 1.47	0.40	−0.07	+ 0.07	–	–	–
NGC 3351	11.78	−0.13	+ 0.16	8.22	−1.88	+ 2.36	0.56	−0.05	+ 0.05	1.41	−0.09	+ 0.09
NGC 3486	12.30	−0.15	+ 0.18	4.60	−0.89	+ 1.11	0.35	−0.08	+ 0.10	1.41	−0.10	+ 0.10
NGC 3621	11.62	−0.04	+ 0.05	11.80	−1.38	+ 1.50	0.22	−0.05	+ 0.05	–	–	–
NGC 3675	12.25	−0.13	+ 0.15	8.66	−1.86	+ 2.43	0.46	−0.10	+ 0.14	–	–	–
NGC 3898	12.85	−0.15	+ 0.17	4.76	−1.11	+ 1.89	0.63	−0.11	+ 0.19	1.42	−0.10	+ 0.11
NGC 3992	11.83	−0.05	+ 0.05	20.55	−6.41	+ 12.18	0.76	−0.10	+ 0.10	1.41	−0.10	+ 0.10
NGC 4535	12.62	−0.20	+ 0.26	6.62	−1.61	+ 1.93	0.52	−0.08	+ 0.08	1.43	−0.10	+ 0.10
NGC 4536	11.99	−0.14	+ 0.17	7.43	−1.47	+ 1.66	0.27	−0.04	+ 0.05	1.37	−0.10	+ 0.10
NGC 4559	11.41	−0.06	+ 0.07	9.63	−1.58	+ 1.81	0.36	−0.08	+ 0.08	1.39	−0.10	+ 0.10
NGC 4651	11.61	−0.09	+ 0.09	17.89	−4.53	+ 7.47	0.62	−0.13	+ 0.16	1.43	−0.10	+ 0.10
NGC 4698	12.17	−0.09	+ 0.10	10.07	−2.08	+ 2.70	0.50	−0.09	+ 0.12	1.38	−0.10	+ 0.10
NGC 4725	11.84	−0.06	+ 0.08	12.65	−2.76	+ 3.36	0.67	−0.08	+ 0.08	1.40	−0.10	+ 0.10
NGC 4736	11.33	−0.09	+ 0.12	17.97	−3.37	+ 3.72	0.21	−0.03	+ 0.03	1.28	−0.10	+ 0.10
NGC 5005	12.21	−0.24	+ 0.32	9.01	−2.51	+ 3.24	0.50	−0.06	+ 0.08	1.36	−0.09	+ 0.09
NGC 5033	12.07	−0.05	+ 0.05	11.25	−1.41	+ 1.60	0.31	−0.05	+ 0.07	1.40	−0.09	+ 0.10
NGC 5055	12.01	−0.04	+ 0.04	9.14	−1.02	+ 1.14	0.37	−0.04	+ 0.04	–	–	–
NGC 5350	12.22	−0.11	+ 0.13	5.05	−1.03	+ 1.27	0.47	−0.08	+ 0.10	1.46	−0.10	+ 0.10
UGC 8508	10.43	−0.39	+ 0.43	12.64	−3.60	+ 5.23	0.50	−0.11	+ 0.11	–	–	–
WLM	10.33	−0.22	+ 0.24	8.83	−1.80	+ 2.34	0.50	−0.11	+ 0.11	–	–	–

$1-7$ detailed in Sec. 7.3.4, but assuming the upper and lower 1σ uncertainties in the distance as reported in Table 7.1 (note that this also implies making the appropriate changes in the surface density profiles of the baryonic components). Then, for each galaxy we combine the three posterior distributions (one for each distance) of our parameters $(\log(M_{200}), c_{200}, \Upsilon_\mathrm{d}, f)$, and we re-obtain the $16^{\rm th}$, $50^{\rm th}$, and $84^{\rm th}$ percentiles of the final total distributions, which we use to define the final ($\log(M_{200})$, c_{200}, Υ_d, f) set and its uncertainties. We report these values in Table 7.2 for the case imposing the $c_{200} - M_{200}$ relation as a prior, and in Table 7.3 for the flat prior.

In Fig. 7.5 the effects of the gas flaring can be seen more clearly, as we show the comparison between the values of M_{200}, c_{200}, Υ_d, and f recovered using razor-thin and flared gas discs, as a function of M_{200}. The left panels show the comparison for our uninformative prior on c_{200} while the right panel shows it for the prior on c_{200} following the $c_{200} - M_{200}$ relation of Dutton & Macciò (2014). The parameters in the figure are obtained after considering the distance uncertainty as described in the previous paragraph.

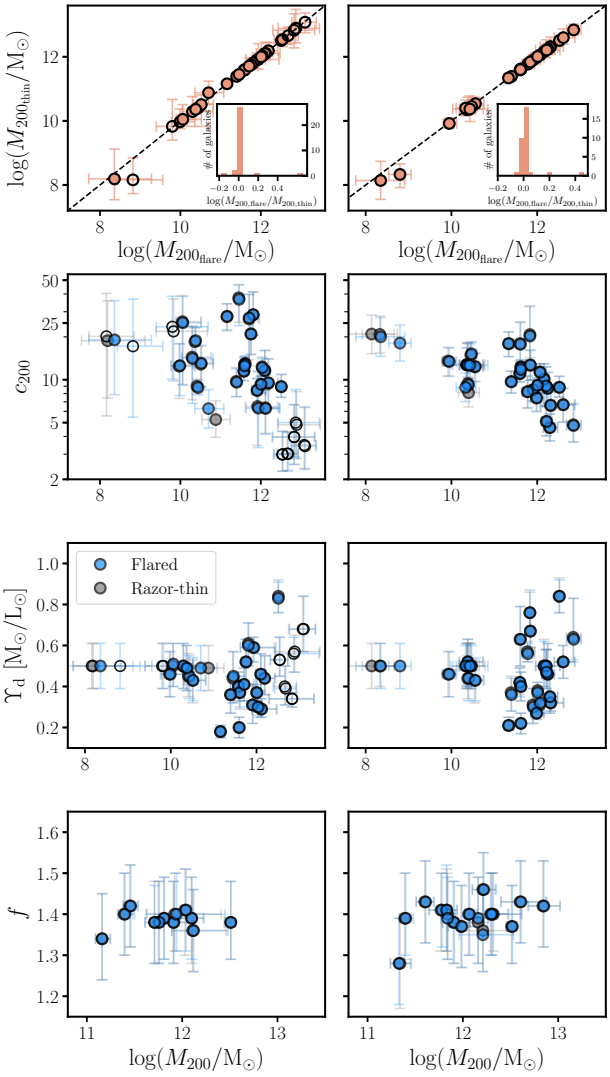

Figure 7.5: Comparison between the recovered parameters from our mass modelling when the gas discs are considered razor-thin (gray circles) and when the flaring is considered (blue circles); most of the time the values overlap. Empty symbols correspond to those galaxies for which we do not obtain well-constrained dark matter halo parameters when using a flat prior on c_{200}. Panels on the *left* concern the results obtained with a flat prior on c_{200}, while the *right* panels correspond to the results obtained assuming the prior on Eq. 7.14. The *top* panels show a direct comparison so there is no distinction between blue and grey circles; the dashed line indicates the 1:1 relation, while the insets show the distribution of the differences between M_{200} when derived with the flared and razor-thin gas discs.

Regarding M_{200}, the values derived with both razor-thin and flared discs are compatible with the 1:1 relation. As shown in the inset, the differences between the two derivations are close to zero. The two galaxies with a difference larger than +0.2 dex are dwarfs (the most extreme one being CVn I dwA; Fig. 7.4), where the flaring is expected to be more important as H I dominates the baryonic budget of the galaxies. No systematic trends as a function of M_{200} are clearly visible in the data, but this should be studied more carefully with larger samples of low-mass galaxies.

The second row of panels in Fig. 7.5 shows the recovered concentration parameters. Again, within the uncertainties the razor-thin- and flared-derived values are compatible. When using a flat prior, the concentration of some galaxies at high M_{200} tend towards $c_{200} = 2$, the lower limit of our priors. However, those galaxies also have low c_{200} values when imposing the prior on Eq. 7.14, and in general the values obtained using both priors are in agreement with each other. In Section 7.5.3 we discuss in detail the dark matter concentration-halo mass relation.

The third row shows the disc mass-to-light ratios. Motivated by stellar population synthesis models, we used a Gaussian prior centered at $\Upsilon_{\rm d} = 0.5 \pm 0.1$ $\rm M_\odot/L_\odot$. Interestingly, the values of $\Upsilon_{\rm d}$ show significant spread (which does not correlate with optical colours[7]) at $M_{200} \gtrsim 10^{11}$ $\rm M_\odot$ (i.e. for all the massive disc galaxies). At these masses, the median value for our flat (Eq. 7.14) prior scenario is is 0.41 (0.46) $\rm M_\odot/L_\odot$, with a standard deviation of 0.15 (0.17) $\rm M_\odot/L_\odot$ and values in the range 0.18 (0.21) − 0.83 (0.84) $\rm M_\odot/L_\odot$. We checked with our two most extreme galaxies in terms of $\Upsilon_{\rm d}$ (NGC 2841 with $\Upsilon_{\rm d} = 0.83$ $\rm M_\odot/L_\odot$ and NGC 4736 with $\Upsilon_{\rm d} = 0.18$ $\rm M_\odot/L_\odot$) the consequences of assuming a value of $\Upsilon_{\rm d} = 0.5$ $\rm M_\odot/L_\odot$ often assumed when studying scaling relations (e.g. Lelli et al. 2016b; Chapter 5). In the case of NGC 2841 one obtains a similar M_{200} but the fit to the rotation curve is slightly worse than in Fig. 7.3; moreover, the concentration of the galaxy moves away from the $c_{200} - M_{200}$ relation (see below). For NGC 4736 the mass model always overestimates the observed circular speed. This shows that the value of $\Upsilon_{\rm d} = 0.5$ $\rm M_\odot/L_\odot$ is representative, but for some galaxies in our sample it would bias the estimation of the stellar mass (and concentration) by a significant amount (see also the discussion in Ponomareva et al. 2018 on estimating $\Upsilon_{\rm d}$ with different methods). For smaller galaxies, Fig. 7.5 may give the impression that $\Upsilon_{\rm d} = 0.5$ $\rm M_\odot/L_\odot$ is perfectly appropriate. However, it should be noted that their posterior distributions on $\Upsilon_{\rm d}$ simply follow their Gaussian priors. This is because the contribution of $V_{\rm d}$ to the mass models of dwarfs is small, and thus our MCMC fitting loses constraining power on $\Upsilon_{\rm d}$; because of this, it is likely that the real uncertainties in the $\Upsilon_{\rm d}$ for the dwarfs are underestimated by 20 − 40 per cent. The effects of the gas discs flaring are negligible (up to the uncertainties just described for the dwarf galaxies), as seen from the overlap of grey and blue circles in the third panels of Fig. 7.5.

[7]We checked this by recovering the $(B - V)$ colours of our sample from the HyperLeda database (Makarov et al. 2014).

Finally, the bottom panels of Fig. 7.5 show the values of f as a function of M_{200}; note the different range in the x-axis with respect to the other panels, as f is only a parameter for the massive galaxies with bulge. There are no visible differences between values derived with razor-thin or flared gas discs, and within the uncertainties the prior of $f = 1.4 \pm 0.1$ provides satisfactory fits to the data.

7.4.2 Scale heights

Fig. 7.6 shows the H I (blue line and band) and H_2 (green line and band) scale heights for the same four representative galaxies as before. Fig. 7.7 shows the scale heights for our full sample, and tables giving the scale heights are available in the published article corresponding to this chapter. Naturally, the scale heights increase with increasing galactocentric distance. At all radii the scale height of the H I discs is larger than for the H_2 discs. This is expected given that the velocity dispersion of H I is higher.

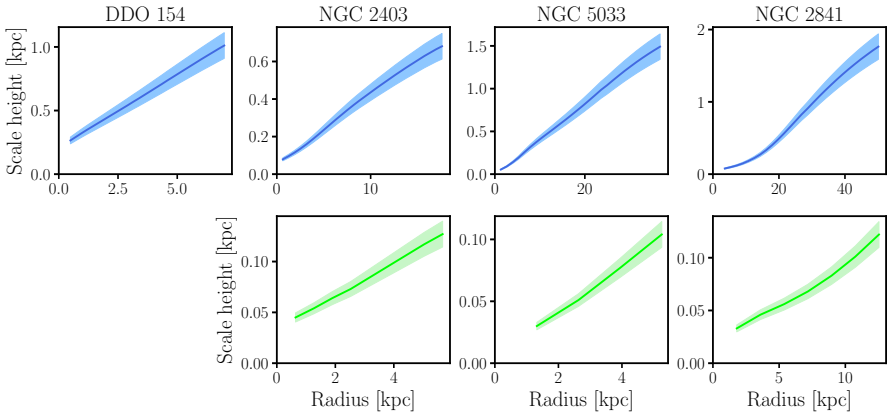

Figure 7.6: Example of H I (*top*) and H_2 (*bottom*) scale heights in our sample. The solid blue and green lines show our estimations, while the colour bands show the assumed uncertainty of 10 per cent, motivated by the uncertainty in the gas velocity dispersion (see Fig. 7.1). We only show the scale heights for our mass models with a prior on the $c_{200} - M_{200}$ relation, but the profiles obtained with the flat prior largely overlap.

While the overall behavior of the flaring is the same in all our galaxies, the steepness and normalisation change from galaxy to galaxy (see Fig. 7.7). Previous observational works have postulated a 'universality' of the H I and H_2 scale heights in late-type galaxies when normalised to characteristic scales (Patra 2019, 2020a,b). In particular, using a sample of disc galaxies Patra (2019, 2020b) with R normalised to units of R_{25} (the radius at which a $B-$band isophote reaches 25 mag/arcsec^2), and $h(R)$ to be unity at a radius of $0.3R_{25}$. Patra (2020a) instead adopted a pseudo-isothermal parameterisation to fit to a set of rotation curves of dwarf galaxies, and used the 'core radius' to normalise R.

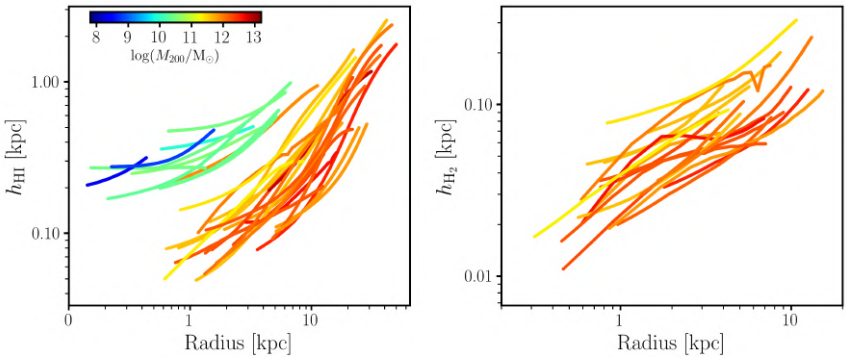

Figure 7.7: H I (*left*) and H_2 (*right*) scale heights for our galaxy sample. Galaxies are colour-coded according to the mass of their dark matter haloes.

The normalised $h(R)$ values seem to have a linear dependency on the normalised radial scale, although the scatter is fairly large. The logic behind using R_{25} or the core radius is that the claimed universal shape of the $h(R)$ profiles is a dynamical effect. Thus, it is appropriate to re-scale using characteristic scales related to the radii at which the stellar or dark matter component are dominant. On the other hand using $0.3R_{25}$ as a normalisation factor of $h(R)$ seems less justified.

In Fig. 7.7 we plot the scale heights for our galaxy sample colour-coded by the halo mass. There is a general trend of low-mass galaxies having thicker discs than their more massive counterparts, as expected given their weaker potentials. At fixed M_{200} the profiles are somewhat homogeneous, although the scatter is always large. We explore introducing the above normalisations as well as more dynamically-motivated values such as normalising the radius to a fraction of the virial radius and the re-scale $h(R)$ according to the virial velocities, but significant scatter remains. We thus find little evidence for a universal $h(R)$ profile. This is not fully surprising as $h(R)$ depends strongly on the gas velocity dispersion, the dark matter halo, the stellar mass-to-light ratio, and the bulge-to-total mass ratio, which show a large spread in our sample. While there are a number of significant differences between the derivation of $h(R)$ by Patra (2019, 2020a,b) and ours (see for instance the discussion in Bacchini et al. 2020b), it is likely that the different conclusions arise mostly from our larger sample with a wider variety in gas kinematics, halo mass, bulge ratio, and mass-to-light ratio.

7.5 Implications and discussion

Our data and the parameters we recover from our fitting procedure allow us to revisit some of the most important scaling relations concerning the connection between galaxies and their dark matter haloes. In this section, we discuss three of them: the stellar–to–halo mass relation, the baryon–to–halo mass relation,

and the halo concentration–mass relation.

7.5.1 Stellar–to–halo mass relation

The stellar–to–halo mass relation (SHMR) has been widely studied in the context of understanding the star formation efficiency as a function of the halo mass (e.g. Moster et al. 2013; Rodríguez-Puebla et al. 2015; Wechsler & Tinker 2018; Posti et al. 2020; Romeo et al. 2020). The classical picture based on abundance-matching techniques is that the SHMR increases monotonically from the dwarf regime till $M_* \approx 5 \times 10^{11}$ $M_\odot$, where it flattens. The relation, however, might be different if galaxies are split in quenched and star-forming (Rodríguez-Puebla et al. 2015; Posti & Fall 2021).

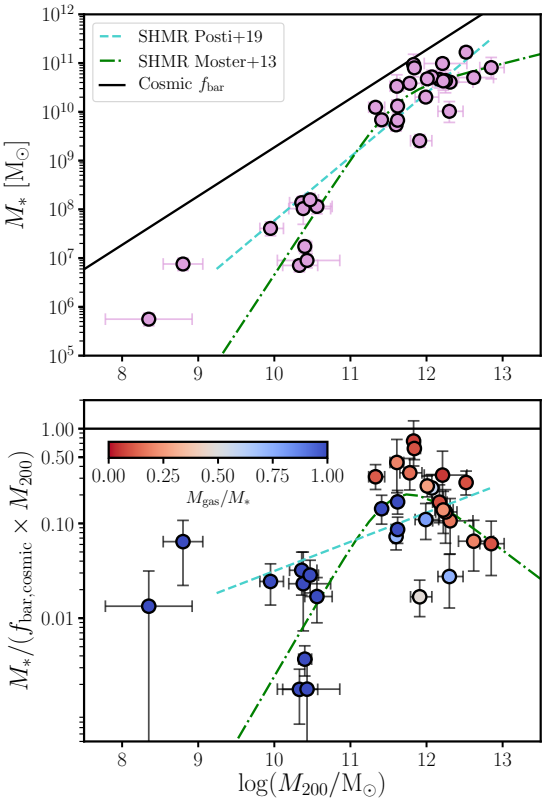

Figure 7.8: *Top:* Stellar-to-halo mass relation for our galaxy sample. *Bottom:* M_*/M_{200} ratio normalised to the cosmological baryon fraction vs. M_{200}. Galaxies are colour-coded according to their stellar-to-cold gas content $M_{\rm gas}/M_*$. In both panels the black solid line shows the cosmological baryon fraction $f_{\rm bar,cosmic}$. For comparison, we plot with a green semi-dashed curve the SHMR relation from Moster et al. (2013), while the teal dashed line shows a fit to the analysis by Posti et al. (2019).

To compute M_* for our sample, we integrate the luminosity profiles of the bulge and disc components up to R_{200}. We do this rather than integrating to infinity in order to measure the mass of the different baryonic and dark components within the same observed radius. In any case, this integration limit has very little impact in the integrated stellar mass as the luminosity profiles have values close to zero at such large distances, and it has no repercussion on our results. Once the total luminosity of disc and bulge is estimated, we

multiply by the corresponding $\Upsilon_{\rm d}$ and by $f\Upsilon_{\rm d}$ in the case of the bulge, and we add the mass of both components. The uncertainties in all the quantities are estimated using Monte Carlo realisations, including distance and best-fitting parameters uncertainties. The mass of the baryonic components of our galaxies are listed in Table 7.4.

In the top panel of Fig. 7.8 we show the SHMR for our galaxy sample, using the values derived with our prior on the $c_{200} - M_{200}$ relation. The black solid lines show the cosmic limit, given by $M_{200}/f_{\rm bar,cosmic}$. We can see that M_* increases with M_{200} rather linearly (in log-log space), although the scatter at high M_{200} is large. We compare our measurements with the abundance matching-based SHMR from Moster et al. (2013), and with a linear fit to the data from Posti et al. (2019), who performed the rotation curve decomposition of galaxies in the SPARC data base (Lelli et al. 2016a). Our data points appear to scatter around both SHMRs, but our low-number statistics prevent us from drawing conclusions on this, albeit the scatter is likely real as it is also present when studying larger samples (Posti & Fall 2021).

In the bottom panel of Fig. 7.8 we show the M_*/M_{200} ratio normalised to the average cosmological baryon fraction ($f_{\rm bar,cosmic} = \Omega_{\rm b}/\Omega_{\rm m} \approx 0.187$, Planck Collaboration et al. 2020). We can see that at fixed M_{200} galaxies with lower $M_{\rm gas}/M_*$ ratios have higher M_*/M_{200} values. In addition to this, the disc galaxies with the largest M_{200} have M_*/M_{200} as low as dwarf galaxies, despite their much lower $M_{\rm gas}/M_*$. We can see from both panels that at the high-mass regime four spiral galaxies have baryon fractions between $\sim 50 - 100$ percent of $f_{\rm bar,cosmic}$. The existence of galaxies with nearly all of their baryons in the form of stars at $M_* \sim 10^{11}$ M$_\odot$ was in fact suggested recently by Posti et al. (2019).

To see this more clearly, in Fig. 7.9 we plot the stellar mass fraction now as a function of M_*. We find that those galaxies with the highest stellar masses have also the highest M_*/M_{200} ratios. This is in qualitative agreement with the results from Posti et al. (2019, 2020) and Posti & Fall (2021), and deviates significantly from the abundance-matching predictions.

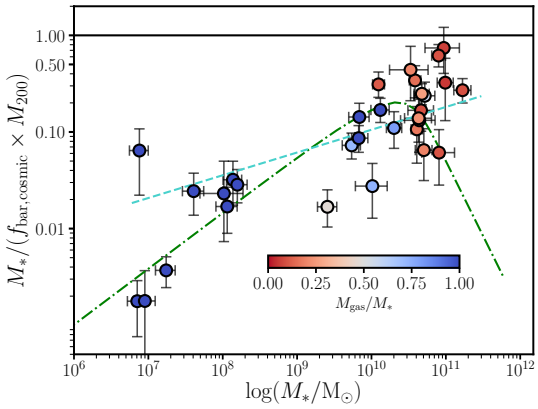

Figure 7.9: M_*/M_{200} ratio normalised to the cosmological baryon fraction vs. M_*. Colours and curves are as in Fig. 7.8.

7.5.2 Baryon–to–halo mass relation

We now focus on the baryon–to–halo mass relation (BHMR). Arguably, the BHMR is more fundamental than the SHMR, as it incorporates simultaneously the stellar and gas content. It is also more robust, especially at the low-mass regime since dwarf irregular galaxies are gas-dominated.

To compute the baryonic mass we consider the stellar mass as defined before, together with the neutral and molecular gas content. Similarly as for M_*, we compute $M_{\rm HI}$ and $M_{\rm H_2}$ by integrating the functional forms fitted to the observed surface densities, from 0 to R_{200}. Strictly speaking, our $M_{\rm bar}$ is not the total baryonic mass as it neglects the mass of the warm and hot ionised gas. This assumption is commonly made given that the warm and hot ionised gas are not expected to contribute significantly to the whole baryonic budget near galaxy discs, and because it is extremely challenging to obtain reliable mass measurements of these gas phases. Under the same logic, our $M_{\rm gas}$ values should be seen as the mass of the cold ISM gas.

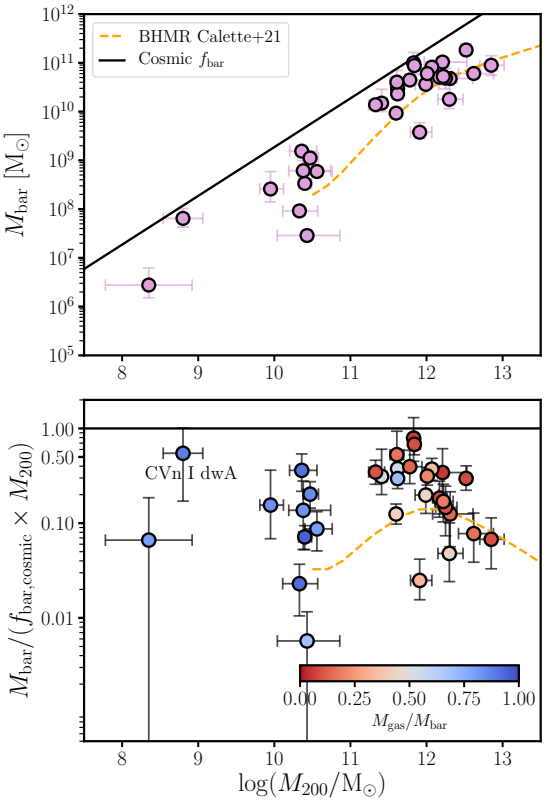

Figure 7.10: *Top:* Baryon–to–halo mass relation for our galaxy sample. *Bottom:* $M_{\rm bar}/M_{200}$ ratio normalised to the cosmological baryon fraction vs. M_{200}. Galaxies are colour-coded according to their stellar-to-cold gas content $M_{\rm gas}/M_*$. In both panels the black solid line shows the cosmological baryon fraction $f_{\rm bar,cosmic}$, and the orange dashed curve shows the semi-empirical relation from Calette et al. (2021) for comparison.

The top panel of Fig. 7.10 shows the $M_{\rm bar} - M_{200}$ relation for our galaxy sample, while the bottom panel shows the $M_{\rm bar}/M_{200}$ ratio normalised to the cosmic mean. Again, we show the results obtained with the prior on Eq. 7.14.

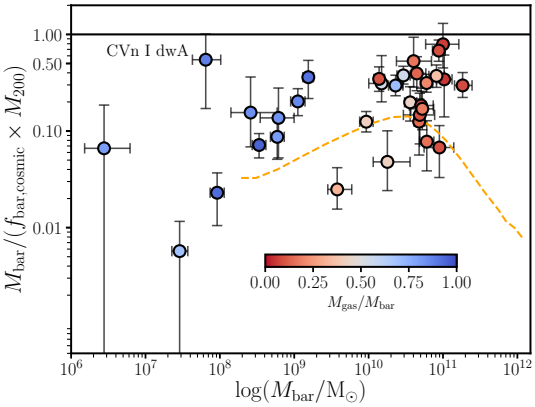

Figure 7.11: $M_{\rm bar}/M_{200}$ ratio normalised to the cosmological baryon fraction vs. $M_{\rm bar}$. Colours and curves are as in Fig. 7.10.

As expected, the picture of the BHMR does not change with respect to the SHMR for the massive galaxies, dominated by the stellar component. Instead, there are substantial changes for the dwarf galaxies once their major baryonic budget is added. Overall, $M_{\rm bar}/M_{200}$ has significant scatter and does not show clear trends as a function of M_{200}. A similar behavior is seen in Fig. 7.11 but as a function of $M_{\rm bar}$.

For comparison, in Figs. 7.10 and 7.11 we plot the BHMR from Calette et al. (2021), which is based on abundance matching to link M_* with M_{200} and in empirical correlations to link M_* to $M_{\rm gas}$; in this case they consider $M_{\rm gas} = 1.4M_{\rm HI}$. Predictions from similar semi-empirical approaches overlap with each other (Rodríguez-Puebla et al. 2011). The relation follows approximately the trends described by the data in the $M_{\rm bar}/(f_{\rm bar,cosmic} \times M_{200})$ vs. M_{200} plane, although at all M_{200} it appears to have lower $M_{\rm bar}$ values than most points. Similarly to what happens in the stellar relation, abundance matching does not seem to capture fully the behavior of the $M_{\rm bar}/(f_{\rm bar,cosmic} \times M_{200})$ vs. $M_{\rm bar}$ plane.

Finally, we note the peculiar position of the galaxy CVn I dwA in the above figures. At $M_{200} \approx 10^{8.8}$, CVn I dwA has a higher-than-average $M_{\rm bar}/M_{200}$ with a median value of about 50 per cent the cosmological baryon fraction, although the uncertainties are large. CVn I dwA, is a low surface brightness dwarf with an extremely low metallicity (van Zee 2000). It would be interesting to further study this galaxy in the future, in the context of recent results that suggest the existence of a number of extended diffuse dwarf galaxies with baryon fractions comparable to the cosmological average (e.g. Chapters 2 and 4).

Overall, our analysis presents empirical $M_* - M_{200}$ and $M_{\rm bar} - M_{200}$ relations spanning five orders of magnitude in M_*, $M_{\rm bar}$ and M_{200}, taking into account the mass from the atomic and molecular gas, as well as the stellar disc and bulge. These relations can be used to directly test the outcome and predictions from models and simulations, setting constraints on e.g. the gas-to-stellar mass ratio, the efficiency of star formation, and the ability of galaxies to retain their

baryons within their discs.

7.5.3 Concentration–mass relation

N-body simulations find a clear anti-correlation between M_{200} and c_{200} (e.g. Bullock et al. 2001a; Dutton & Macciò 2014; Ludlow et al. 2014). Observational work on rotation curve decomposition, however, reports that this relation is not present in the data unless it is assumed as a prior during the fitting, especially when considering NFW haloes over other more flexible density profiles (see discussion in Di Cintio et al. 2014; Katz et al. 2017; Li et al. 2020 and references therein). To explore this with the best possible data, in this work we performed our rotation curve decomposition by allowing c_{200} to have 1) an uninformative flat prior, and 2) a prior following the $c_{200} - M_{200}$ of Dutton & Macciò (2014, see our Eq. 7.14).

In Fig. 7.12 we show the location of our galaxies in the $c_{200} - M_{200}$ plane, for both cases of priors on c_{200}. As mentioned before, some of our galaxies do not have a well constrained mass model when using a flat prior on c_{200}, and so we show them with crosses rather than circles; the values for these galaxies are merely indicative. We compare our measurements against the theoretical expectation from Dutton & Macciò (2014), i.e. Eq. 7.14.

Unsurprisingly, when Eq. 7.14 is imposed as a prior (left panel of Fig 7.12) we recover very well the $c_{200} - M_{200}$ relation. Remarkably, even when we consider an uninformative prior on c_{200} (right panel of Fig 7.12), galaxies appear to follow the $c_{200} - M_{200}$ relation albeit with larger scatter and larger individual uncertainties with respect to the case when Eq. 7.14 is used as a prior. Note that the galaxies for which their dark matter halo parameters are less well constrained still follow the same trends when imposing the $c_{200} - M_{200}$ relation on the left panel. Specifically, the most massive galaxies tend to deviate towards low values of c_{200} regardless of the prior.

Our results suggest that the $c_{200} - M_{200}$ relation can actually emerge from the data, provided they are of good enough quality. This is not necessarily expected given that the $c_{200} - M_{200}$ relation is obtained from cosmological N-body simulations, while baryonic physics can modify the structure of dark matter haloes. In particular, adiabatic contraction due to the baryon cooling and collapse, together with stellar/AGN feedback are expected to modify the inner density profiles (and thus the concentration) of the primordial dark matter haloes. In principle, dynamical friction between baryons and dark matter can also affect c_{200}, but its effects are expected to be minor for galaxies without extreme bars and where the baryons have retained a large fraction of their angular momentum (Sellwood 2008, see also Nipoti & Binney 2015). Since our sample was chosen not to have significant bars, and the discs have retained a large fraction of the angular momentum of the dark matter halo (Chapter 5), we expect dynamical friction to be inefficient at affecting c_{200} significantly. Adiabatic contraction tends to increase c_{200}, since the halo contracts as response of the deeper potential owed to the central baryon condensation (e.g. Blumenthal

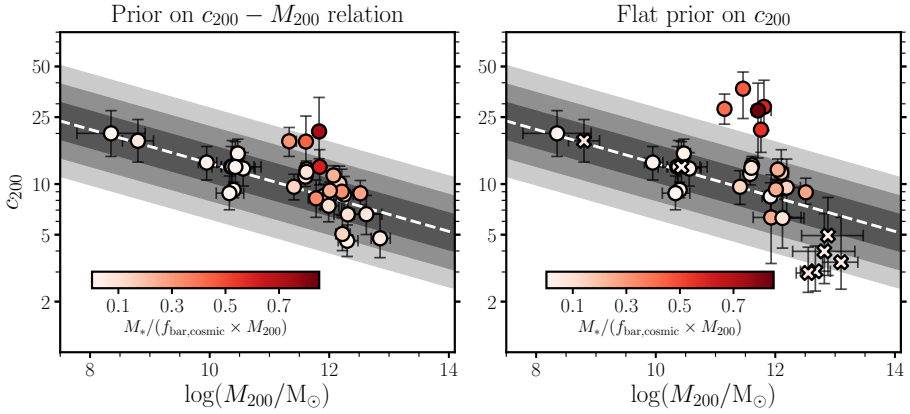

Figure 7.12: Concentration–mass relation for the dark matter haloes of our galaxy sample. On the *left* panel we display the results considering the prior on Eq. 7.14, while the *right* panel shows the results from the flat prior on c_{200}. In both panels we show the $c_{200} - M_{200}$ relation (white line) from the cosmological N-body simulations by Dutton & Macciò (2014), together with its 1, 2, 3σ scatter (grey bands). Galaxies are colour-coded according to their $M_*/(f_{\mathrm{bar,cosmic}} \times M_{200})$ fraction. The crosses in the right panel correspond to galaxies for which their mass models are less reliable given their posterior distributions.

et al. 1986; Duffy et al. 2010; Katz et al. 2014). The modification to c_{200} is not straightforward to estimate as it might depend on the individual assembly histories (e.g. Gnedin et al. 2004; Tissera et al. 2010). Feedback, on the other hand, mitigates the effects of halo contraction as it can lead to lower central dark matter densities (Navarro et al. 1996; Read & Gilmore 2005; Pontzen & Governato 2012). This is particularly true if metal-line radiative cooling is efficient (as it eases the collapse of the baryons), but the exact quantification of the effect is highly dependent on the feedback prescriptions (e.g. Sellwood 2008; Duffy et al. 2010; Bryan et al. 2013; Di Cintio et al. 2014; Katz et al. 2017).

Our results indicate that despite the above phenomena, the overall $c_{200} - M_{200}$ relation appears to hold reasonably well for most galaxies in our sample across a mass large range. Recently, Beltz-Mohrmann & Berlind (2021) analysed hydrodynamical simulations and obtained similar results. However, simulations also show that the inclusion of baryons can generate 'wiggles' in the $c_{200} - M_{200}$ relation due to the interplay of different feedback processes (Lovell et al. 2018; Anbajagane et al. 2022). Interestingly, such deviations seem to be present in our data, at similar M_{200} as in the simulations; namely, the higher concentrations at about $M_{200} \sim 5 \times 10^{11}$ $\mathrm{M}_\odot$ (where adiabatic contraction is efficient the most), and lower concentrations at $M_{200} \sim 10^{13}$ $\mathrm{M}_\odot$. Note that when we impose the prior of Eq. 7.14 on c_{200} the deviations are reduced but still present.

While the comparisons with the results of hydrodynamical simulations are complex and out of the scope of this chapter, we can speculate on a qualitative

explanation for the trends in our data. With this in mind, in Fig. 7.12 we colour-code the galaxies in terms of their M_*/M_{200} fraction normalised to $f_{\rm bar,cosmic}$. As it turns out, the galaxies showing a systematically higher c_{200} are those with the largest M_*/M_{200}. Based on this, we argue that the galaxies with high M_*/M_{200} have larger c_{200} precisely because they converted most of their gas into stars; in fact these galaxies have $M_{\rm bar}/M_{200}$ fractions comparable to the cosmological average host overall higher baryon fractions than galaxies of similar M_{200} (see Fig. 7.10).

Posti et al. (2019) has discussed the elevated baryon fractions in some spiral galaxies in detail, arguing for a 'failed feedback' scenario where feedback was not efficient enough to eject a significant amount of gas before the galaxies built their stellar mass. In the framework of adiabatic contraction, the high central stellar mass densities could then be responsible for the higher concentrations. Under this scenario, below $M_{200} \sim 5 \times 10^{11}$ M$_\odot$ the effects of adiabatic contraction and stellar feedback fully compensate each other (or are both negligible). According to our figure, at $M_{200} \gtrsim 5 \times 10^{12}$ M$_\odot$ it would be required that feedback overpowers halo contraction, lowering the concentration and also the global baryon- and stellar-to halo mass fractions. In fact, AGN feedback has been found to be able to lower c_{200} as well as the baryon fraction in galaxies according to simulations (e.g. Duffy et al. 2010; Bryan et al. 2013). Moreover, semi-empirical models also find that AGN feedback becomes more efficient at such masses and it manages to reproduce the SHMR (Marasco et al. 2021, see also e.g. Fabian 2012; Choi et al. 2015). Despite the scenario we sketch being merely qualitative, it seems in line with expectations of feedback processes and adiabatic contraction models. However, all this should be tested by repeating the experiment of using a flat prior on c_{200} for larger samples, and ideally complementing it with stellar rotation curves to trace at high resolution the innermost regions of the most massive galaxies, which largely determine their c_{200} parameters. In general, the above trends between M_{200}, c_{200}, and M_*/M_{200} can be exploited to further understand the connection between dark matter haloes and feedback and the build-up of mass in galaxies, providing key constraints to both analytic models and simulations.

7.5.4 Comparison with previous work and caveats

Comparison of mass models with previous works

Some galaxies in our sample have been recently studied by other authors performing standard rotation curve decomposition. Specifically, Posti et al. (2019) has mass models for seven of our massive galaxies and Li et al. (2020) for eight, while Read et al. (2017) studied our ten dwarfs. We find reasonably good agreement with all of their results. Below we quantify the comparison. When quoting differences, we refer to the operation of subtracting their values from ours.

First, we compare against Posti et al. (2019), who fitted NFW haloes using a Gaussian prior on the same $c_{200} - M_{200}$ relation as us, and a flat prior on $\Upsilon_{\rm d}$,

and $\Upsilon_{\rm b} = 1.4\Upsilon_{\rm d}$. Given this, for the comparison we use our results from the $c_{200} - M_{200}$ prior. Our mean (median) difference in M_{200} with respect to Posti et al. (2019) is 0.009 (-0.01) dex, with a standard deviation of 0.17 dex. Our mean (median) difference in c_{200} is of 0.06 (0.03) dex, with a standard deviation of 0.22 dex (mostly driven by NGC 3992 for which we find a higher c_{200} by 0.5 dex). For $\Upsilon_{\rm d}$ the mean (median) difference is -0.07 (-0.04) with a standard deviation of 0.08 dex.

Second, also for the massive galaxies, we compare our fiducial results (i.e. with the flat prior on c_{200}) with the values obtained by Li et al. (2020), derived using the same prior on $\Upsilon_{\rm d}$ as us, a flat prior on c_{200}, and a prior on $\Upsilon_{\rm b}$ centered at 0.7 with standard deviation of 0.1 dex (which is similar to our prior on f). Regarding M_{200}, the mean (median) difference is -0.14 (0.06) dex with a standard deviation of 0.56 dex, largely driven by NGC 5055 for which our M_{200} is 1.5 dex lower than the Li. et al. value (0.86×10^{12} $\mathrm{M}_{\odot}$ vs. 18.6×10^{12} $\mathrm{M}_{\odot}$). The mean (median) difference in c_{200} is 0.06 (0.09) dex, with a standard deviation of 0.32. The mean (median) difference in $\Upsilon_{\rm d}$ is -0.03 (-0.08) dex, with standard deviation 0.09 dex. Finally, for $\Upsilon_{\rm b}$ the mean (median) difference is 0.31 (0.32) dex, with standard deviation 0.34 dex. We note here that the bulge-disc decomposition for our sample is more robust than the decomposition used in Li et al. (2020), which is based on a visual fit (Lelli et al. 2016a).

Lastly, we compared the results for the dwarfs against the values from Read et al. (2017), who used a flat prior on c_{200} and fitted M_* with a Gaussian prior with center and standard deviation according to the values by Zhang et al. (2012), who obtained M_* using SED fitting. The mean (median) difference in M_{200} is 0.1 (0.2) dex, with a standard deviation of 0.34 dex. There seems to be a systematic trend as a function of M_{200}, with our more massive galaxies having larger values with respect to Read et al. (2017), but the scatter and low number statistics do not allow to make strong conclusions. For c_{200}, the mean (median) difference is 0.1 (0.1) dex, with standard deviation 0.16 dex and our values being lower on average, without clear systematic trends. Overall, taking into account that the approaches of Posti et al. (2019), Li et al. (2020), and Read et al. (2017) differ significantly from ours (e.g. different rotation curves, inclinations, priors, fitting parameters, assumed geometry and shape of the stellar and gas profiles), the agreement in the recovered parameters is fairly good.

Caveats

Our mass models and the interpretation of our results are based on a number of assumptions. Here we focus on the two main assumptions that could affect our results the strongest: the premise of vertical hydrostatic equilibrium and the kinematic modelling on which our results rely.

Regarding the former, it is expected that regularly rotating galaxies (as those selected to be in our final sample) without recent strong interactions have their gas pressure in balance with the gravitational pull from the midplane (e.g. Mo et al. 2010; Cimatti et al. 2019). Measurements in the Milky Way seem

to indicate that some fraction of the atomic gas might have 50% larger scale height than expected from hydrostatic equilibrium within ~ 5 kpc, although the agreement improves at larger radii (see Marasco et al. 2017; Bacchini et al. 2019b for a detailed discussion). In general, in order to test the validity of hydrostatic equilibrium it is of primary interest to measure both the gas velocity dispersion and the gas scale height in other galaxy discs directly from observations, but there is no robust method to do so yet. Note that given our finding that the scale height influences very little the mass models except for the lowest mass galaxies, small deviations from vertical hydrostatic equilibrium would have no impact on our results regarding the SHMR, BHMR, or the $c_{200} - M_{200}$ relation.

Regarding our second assumption, one of the main motivations and strength of our work is the argument that we self-consistently derive our mass models and scale heights taking into account each other given our iterative approach. However, the kinematic modelling from which our rotation curves and velocity dispersion profiles are derived is not consistent with the fact that gas discs are flared. The 3D kinematic modelling technique of ^{3D}BAROLO fits thin tilted-ring models (Rogstad et al. 1974) to the data cubes. This represents an improvement over fitting tilted-ring models to the velocity fields, but neither approach takes into account the increase of the scale height with radius. This is because for thick/flared discs, line of sights contain emission coming from different rings, and the ring-by-ring approach of the tilted-ring technique cannot to account for this. Despite this, the effects of assuming a thin disc when a thick disc is appropriate are known. As discussed in Iorio (2018) and Di Teodoro et al. (2019), there are three main effects due to the mixing of different disc layers in the same line of sight. By considering a thin disc instead of a thick disc: *i)* the recovered surface density profiles are shallower than in reality, *ii)* the velocity dispersion tends to be overestimated, and *iii)* the rotation velocities at large (low) radii can be slightly overestimated (underestimated). These effects are expected to be negligible for massive spiral galaxies, but somewhat more important for dwarfs, as their potential wells are shallower and their thickness are larger both in their overall value and relative to their $R_{\rm max,HI}$ (see Fig. 7.7). Nevertheless, as shown by Iorio (2018), even for three of the least massive galaxies in our sample (DDO 210, NGC 2366, and WLM) the kinematic parameters derived with ^{3D}BAROLO are well consistent with the values estimated considering a thick disc, and the flaring is a subdominant source of uncertainty in the kinematic modelling compared to, for instance, instrumental limitations and non-circular motions. All of the above indicates that the kinematic parameters derived with the tilted-ring modelling are reliable (but see also Roper et al. 2022), even if this technique cannot fully take into account the flaring of discs. In conclusion, this partial inconsistency in our methodology does not significantly affect our results.

7.6 Conclusions

Mass models of galaxies obtained through their rotation curve decomposition are often derived assuming that the neutral (HI) and molecular (H_2) gas discs are razor-thin. In reality, gas discs are flared, which can affect the mass models given the different gravitational effects of a flared geometry with respect to a razor-thin disc. In this chapter we set out to investigate the effects of the flaring on the best-fitting parameters from rotation curve decomposition, namely the stellar mass-to-light ratios (Υ), the mass of the halo (M_{200}), and its concentration (c_{200}). This is the first time that such an investigation is carried out systematically.

To this end, we use a sample of 32 late-type galaxies with the best possible data quality. Our sample has H I and CO resolved interferometric observations, bulge-disc decomposition based on deep NIR imaging, and available 3D kinematic modelling providing their gas velocity dispersion and circular speed (V_c). The sample spans about six orders of magnitude in stellar mass (M_*), including very small ($V_c \approx 20$ km/s) and very massive ($V_c \approx 290$ km/s) galaxies. Under the assumption of vertical hydrostatic equilibrium we use an iterative approach combined with a Bayesian fitting technique to simultaneously derive the scale height of the gas discs and the mass models (using NFW and coreNFW profiles). The NFW and coreNFW profiles provide an excellent fit to the observations of our massive and dwarf galaxies, respectively. All our mass models converge with reasonable values of Υ, M_{200} and c_{200} (Fig. 7.3). For most of our galaxies the fits are equally satisfactory by fitting c_{200} using a flat prior or by imposing a reference $c_{200} - M_{200}$ relation from N-body cosmological simulations, although for some of them the $c_{200} - M_{200}$ relation is necessary to set robust constraints on the mass models. In addition to the derivation of the gas discs flaring and the analysis of its effects, we use our detailed mass models to explore the stellar–to–halo (SHMR), baryon–to–halo (BHMR), and $c_{200} - M_{200}$ relations. Our main results can be summarised as follows.

- In the majority of our sample the effects of the flaring of the gas discs on the recovered best-fitting parameters is very minor given the larger dynamical contribution of the stellar and dark matter components. However, the effects are significant for the smallest and gas-richest dwarf galaxies, where the lower gas circular speeds of a flared disc gives room to considerably more massive haloes (Figs. 7.3, 7.4, 7.5).

- The scale heights of both H I and CO discs are monotonically increasing with radius in the vast majority of cases. As expected from their lower gas velocity dispersion, CO discs are considerably thinner than the H I discs. Additionally, low-mass galaxies have thicker discs than more massive ones (Figs. 7.6 and 7.7). We find little evidence of a 'universal' scale height profile (Fig. 7.7), contrary to previous claims.

- We explore the stellar–to–halo mass relation for our sample (Fig. 7.8). At fixed M_{200}, galaxies with higher stellar-to-gas ratios ($M_*/M_{\rm gas}$) have higher M_*/M_{200}. Some galaxies around $M_{200} \approx 10^{12}$ $M_\odot$ have very

high M_*/M_{200} ratios approaching the cosmological baryon fraction, in agreement with previous findings. Nearly at all masses the galaxies scatter between a linear monotonically increasing relation and a broken power-law following abundance-matching expectations. As a function of M_*, the M_*/M_{200} ratios increase nearly monotonically (Fig. 7.9).

- The baryon–to–halo mass relation of our sample (Fig. 7.10) is similar to the stellar–to–halo mass relation at high baryonic masses ($M_{\rm bar}$) but it is shallower in the low-mass regime given the high gas masses in dwarf galaxies. In general, the $M_{\rm bar}/M_{200}$ ratio of is more homogeneous, though with large scatter, than M_*/M_{200} (Figs. 7.10 and 7.11).

- The $c_{200}-M_{200}$ relation of our dark matter haloes follows well the expected relation from N-body cosmological simulations. This is trivial when the $c_{200}-M_{200}$ relation is imposed, but the relation appears to hold relatively well even when using an uninformative prior on c_{200} (Fig. 7.12). That galaxies follow the $c_{200}-M_{200}$ relation is not necessarily expected given that adiabatic contraction and feedback processes can modify the inner distribution of the dark matter density profile.

- Despite the overall $c_{200}-M_{200}$ relation being preserved, galaxies with $M_{200}\approx 5\times10^{11}$ M$_\odot$ and $M_{200}\approx 10^{13}$ M$_\odot$ seem to lie systematically above and below the relation, respectively. Interestingly, the galaxies above the relation show also the highest stellar and baryon mass fractions, opposite to the galaxies below the relation (Fig. 7.12). We argue that these deviations could be attributed to adiabatic contraction and AGN feedback, respectively.

We provide the largest sample for which the gas scale heights have been derived homogeneously using the hydrostatic equilibrium condition, allowing us to derive most detailed mass models. Our analysis is relevant in the context of the H I kinematics and mass modeling from the upcoming large-volume H I surveys. Moreover, our results can be directly used to test the outcome and predictions of both models and hydrodynamical simulations, with the goal of achieving a more complete picture of the physics regulating the shape of galaxies as well as the galaxy-halo connection and the efficiency of feedback processes.

7.A Mass models with a flat prior on c_{200}

Table 7.3 lists the best-fitting parameters of our rotation curve decomposition obtained using a flat prior on c_{200}.

7.B Baryon content of our galaxy sample

Table 7.4 presents the estimates of the visible mass in our galaxies. The mass of the gas includes H I and H_2 (when available), while the stellar mass includes

Table 7.3: Results of our rotation curve decomposition for the case when c_{200} has a flat prior. The columns give our fiducial values (the median of the posterior distributions) and their upper and lower uncertainties (corresponding to the 16$^{\text{th}}$ and 84$^{\text{th}}$ percentiles, including the contribution from distance uncertainties. Only galaxies with bulges have values of f. Note that the posterior distributions of the galaxies CVn I dwA, DDO 210, NGC 253, NGC 3486, NGC 3898, NGC 4535, NGC 5350, and UGC 8505, are not Gaussian, and thus the reported percentiles are not as reliable as in the case of the prior on Eq. 7.14, but we report them here for completeness.

Name	$\log(M_{200}/\mathrm{M}_\odot)$			c_{200}			$\Upsilon_\mathrm{d}(\mathrm{M}_\odot/\mathrm{L}_\odot)$			f		
	50$^{\text{th}}$ pctl	$\sigma-$	$\sigma+$	50$^{\text{th}}$ pctl	$\sigma-$	$\sigma+$	50$^{\text{th}}$ pctl	$\sigma-$	$\sigma+$	50$^{\text{th}}$ pctl	$\sigma-$	$\sigma+$
CVn I dwA	8.82	−0.40	+ 0.74	17.19	−11.74	+ 19.64	0.50	−0.11	+ 0.11	–	–	–
DDO 52	10.30	−0.26	+ 0.51	14.07	−7.25	+ 9.51	0.50	−0.11	+ 0.11	–	–	–
DDO 87	10.06	−0.17	+ 0.46	25.10	−15.93	+ 13.32	0.51	−0.11	+ 0.11	–	–	–
DDO 126	9.99	−0.21	+ 0.37	12.56	−4.81	+ 5.30	0.46	−0.11	+ 0.11	–	–	–
DDO 154	10.44	−0.09	+ 0.10	8.82	−0.99	+ 1.07	0.45	−0.11	+ 0.11	–	–	–
DDO 168	10.52	−0.20	+ 0.30	13.06	−4.06	+ 4.41	0.43	−0.11	+ 0.11	–	–	–
DDO 210	8.36	−0.64	+ 0.92	19.05	−11.18	+ 16.86	0.50	−0.11	+ 0.11	–	–	–
NGC 0253	12.82	−0.53	+ 0.51	3.98	−1.42	+ 2.69	0.34	−0.03	+ 0.03	1.40	−0.10	+ 0.10
NGC 1313	11.92	−0.14	+ 0.20	8.44	−1.75	+ 1.75	0.31	−0.09	+ 0.09	1.38	−0.10	+ 0.10
NGC 2366	10.38	−0.09	+ 0.12	18.81	−4.38	+ 4.52	0.49	−0.11	+ 0.11	–	–	–
NGC 2403	11.58	−0.06	+ 0.07	11.49	−1.62	+ 1.81	0.40	−0.07	+ 0.07	–	–	–
NGC 2841	12.51	−0.06	+ 0.05	8.93	−1.35	+ 1.90	0.83	−0.07	+ 0.08	1.38	−0.09	+ 0.09
NGC 3198	11.61	−0.02	+ 0.03	12.93	−1.53	+ 1.66	0.37	−0.07	+ 0.07	–	–	–
NGC 3351	11.93	−0.30	+ 0.50	6.33	−2.96	+ 5.02	0.59	−0.06	+ 0.05	1.40	−0.09	+ 0.09
NGC 3486	12.67	−0.25	+ 0.25	3.03	−0.72	+ 1.25	0.39	−0.08	+ 0.10	1.40	−0.10	+ 0.10
NGC 3621	11.60	−0.05	+ 0.05	12.49	−1.59	+ 1.69	0.20	−0.05	+ 0.05	–	–	–
NGC 3675	12.19	−0.17	+ 0.23	9.53	−3.14	+ 4.55	0.43	−0.08	+ 0.11	–	–	–
NGC 3898	13.10	−0.31	+ 0.28	3.43	−1.06	+ 2.91	0.67	−0.11	+ 0.16	1.42	−0.11	+ 0.11
NGC 3992	11.81	−0.05	+ 0.06	28.77	−7.96	+ 12.64	0.60	−0.10	+ 0.10	1.39	−0.10	+ 0.10
NGC 4535	12.88	−0.44	+ 0.59	4.94	−2.08	+ 3.38	0.56	−0.10	+ 0.08	1.44	−0.10	+ 0.10
NGC 4536	12.12	−0.23	+ 0.36	6.28	−2.12	+ 2.34	0.29	−0.04	+ 0.05	1.36	−0.10	+ 0.10
NGC 4559	11.41	−0.07	+ 0.09	9.63	−2.06	+ 2.37	0.36	−0.09	+ 0.09	1.40	−0.10	+ 0.10
NGC 4651	11.46	−0.07	+ 0.08	36.89	−12.36	+ 9.46	0.45	−0.13	+ 0.12	1.42	−0.10	+ 0.10
NGC 4698	12.10	−0.11	+ 0.12	11.68	−3.14	+ 4.32	0.45	−0.08	+ 0.09	1.38	−0.10	+ 0.10
NGC 4725	11.76	−0.05	+ 0.06	21.06	−5.63	+ 6.07	0.51	−0.10	+ 0.10	1.38	−0.10	+ 0.10
NGC 4736	11.15	−0.07	+ 0.08	28.00	−5.30	+ 6.28	0.18	−0.03	+ 0.03	1.35	−0.10	+ 0.10
NGC 5005	11.71	−0.10	+ 0.22	27.39	−13.12	+ 12.41	0.41	−0.08	+ 0.08	1.38	−0.10	+ 0.10
NGC 5033	12.04	−0.05	+ 0.05	12.18	−1.70	+ 1.92	0.30	−0.05	+ 0.07	1.41	−0.10	+ 0.10
NGC 5055	12.01	−0.04	+ 0.04	9.30	−1.17	+ 1.31	0.37	−0.04	+ 0.04	–	–	–
NGC 5350	12.55	−0.20	+ 0.19	2.96	−0.69	+ 1.25	0.53	−0.08	+ 0.11	1.46	−0.10	+ 0.10
UGC 8508	9.80	−0.40	+ 0.88	23.54	−13.45	+ 15.03	0.50	−0.11	+ 0.11	–	–	–
WLM	10.70	−0.34	+ 0.38	6.27	−1.70	+ 2.25	0.49	−0.11	+ 0.11	–	–	–

the contribution of disc and bulge (when available). The baryonic mass is the sum of the gas and stellar mass. Note that M_* has been derived using the mass-to-light ratios obtained with the prior on Eq. 7.14.

7.C Rotation curve decomposition

This appendix presents the mass models of our galaxy sample and their corresponding posterior distributions. Figs. 7.13 and 7.15 show the models and posteriors for the case when Eq. 7.14 is imposed as a prior, while Figs. 7.14 and 7.16 correspond to the flat prior on c_{200}.

Table 7.4: Stellar, gas, and baryonic (stars+gas) mass of our galaxy sample. The stellar mass has been derived using the mass-to-light ratios from our mass models considering the prior on the $c_{200} - M_{200}$ relation.

Name	$\log(M_*/\mathrm{M}_\odot)$			$\log(M_{\mathrm{gas}}/\mathrm{M}_\odot)$			$\log(M_{\mathrm{bar}}/\mathrm{M}_\odot)$		
	50^{th} pctl	$\sigma-$	$\sigma+$	50^{th} pctl	$\sigma-$	$\sigma+$	50^{th} pctl	$\sigma-$	$\sigma+$
CVn I dwA	6.88	-0.13	0.12	7.76	-0.21	0.22	7.81	-0.18	0.20
DDO 52	8.14	-0.13	0.12	9.15	-0.08	0.08	9.19	-0.07	0.07
DDO 87	8.02	-0.32	0.26	8.71	-0.31	0.24	8.79	-0.25	0.21
DDO 126	7.61	-0.15	0.13	8.34	-0.34	0.40	8.41	-0.26	0.36
DDO 154	7.24	-0.14	0.12	8.50	-0.10	0.10	8.53	-0.09	0.09
DDO 168	8.06	-0.15	0.13	8.68	-0.11	0.11	8.77	-0.09	0.09
DDO 210	5.75	-0.14	0.12	6.34	-0.36	0.41	6.44	-0.26	0.35
NGC 0253	10.61	-0.08	0.08	9.85	-0.15	0.20	10.68	-0.07	0.08
NGC 1313	9.41	-0.13	0.13	9.09	-0.35	0.42	9.58	-0.13	0.20
NGC 2366	8.20	-0.15	0.13	8.98	-0.11	0.11	9.05	-0.10	0.10
NGC 2403	9.73	-0.13	0.12	9.59	-0.13	0.14	9.97	-0.09	0.09
NGC 2841	11.22	-0.12	0.11	10.21	-0.41	0.52	11.26	-0.11	0.13
NGC 3198	10.12	-0.13	0.12	10.21	-0.13	0.13	10.47	-0.09	0.09
NGC 3351	10.59	-0.08	0.08	9.77	-0.30	0.48	10.65	-0.07	0.12
NGC 3486	10.01	-0.23	0.2	9.88	-0.43	0.51	10.25	-0.19	0.30
NGC 3621	9.83	-0.14	0.12	10.21	-0.13	0.12	10.36	-0.09	0.10
NGC 3675	10.64	-0.25	0.21	9.69	-0.24	0.37	10.69	-0.22	0.20
NGC 3898	10.91	-0.23	0.21	9.93	-0.29	0.23	10.95	-0.21	0.19
NGC 3992	10.97	-0.25	0.21	9.80	-0.61	0.69	11.00	-0.23	0.21
NGC 4535	10.70	-0.11	0.11	10.00	-0.11	0.11	10.78	-0.10	0.10
NGC 4536	10.30	-0.10	0.10	10.21	-0.12	0.14	10.56	-0.08	0.09
NGC 4559	9.84	-0.14	0.13	9.91	-0.35	0.43	10.17	-0.17	0.28
NGC 4651	10.53	-0.28	0.24	9.83	-0.43	0.55	10.60	-0.23	0.24
NGC 4698	10.67	-0.18	0.17	9.65	-0.26	0.43	10.71	-0.16	0.16
NGC 4725	10.90	-0.09	0.09	9.90	-0.16	0.16	10.94	-0.08	0.09
NGC 4736	10.09	-0.08	0.08	9.15	-0.11	0.12	10.14	-0.07	0.07
NGC 5005	10.99	-0.11	0.11	9.75	-0.18	0.38	11.02	-0.10	0.11
NGC 5033	10.72	-0.14	0.14	10.47	-0.15	0.15	10.91	-0.10	0.11
NGC 5055	10.68	-0.10	0.10	10.10	-0.10	0.10	10.78	-0.08	0.08
NGC 5350	10.63	-0.19	0.17	9.98	-0.25	0.24	10.72	-0.15	0.15
UGC 8508	6.95	-0.15	0.14	7.30	-0.14	0.14	7.46	-0.10	0.11
WLM	6.85	-0.13	0.12	7.93	-0.10	0.10	7.96	-0.09	0.09

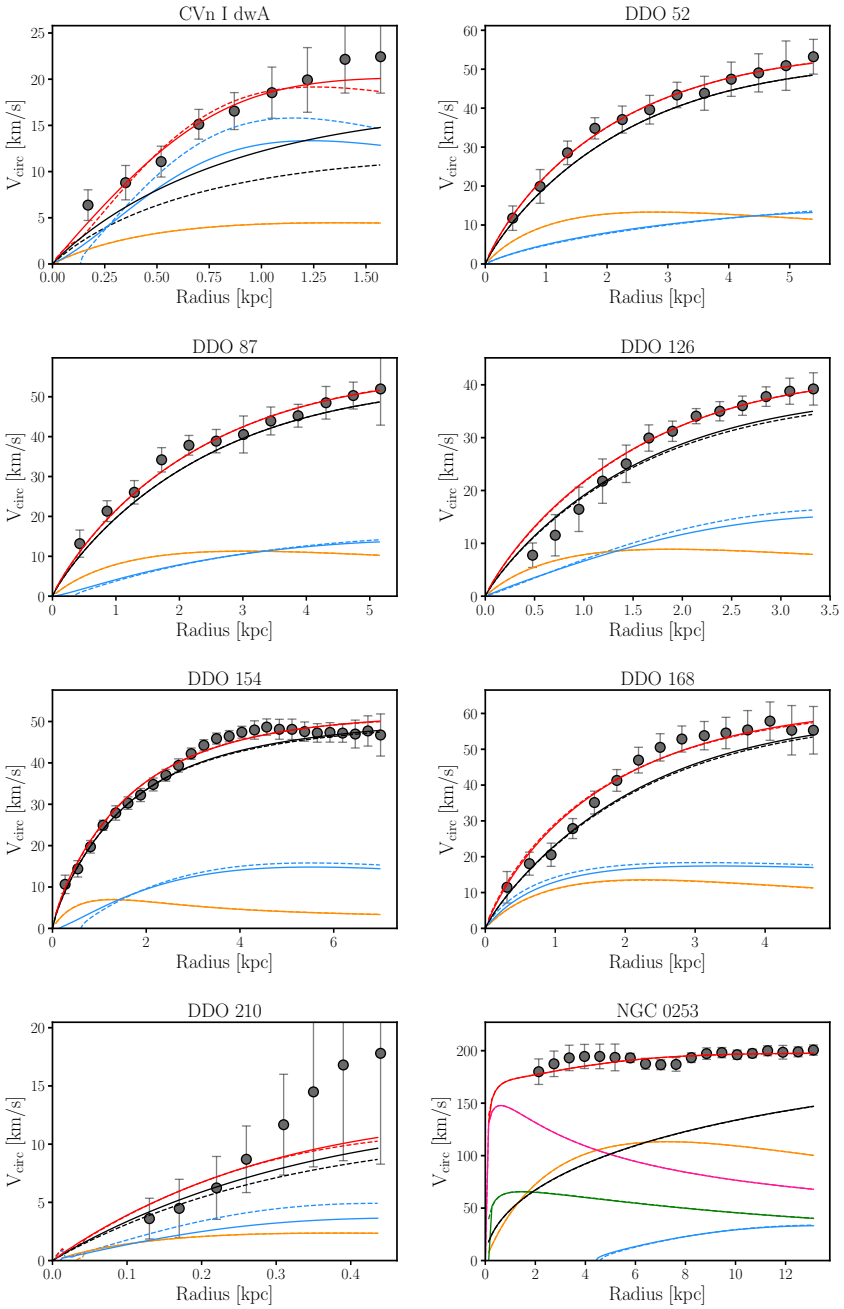

Figure 7.13: Mass models for our galaxy sample under the prior of Eq. 7.14. Observed circular speeds are shown with grey points. The blue, green, pink, orange, and black lines correspond to the contribution to the total circular speed (red line) from the H I, H_2, stellar disc, bulge, and dark matter halo, respectively.

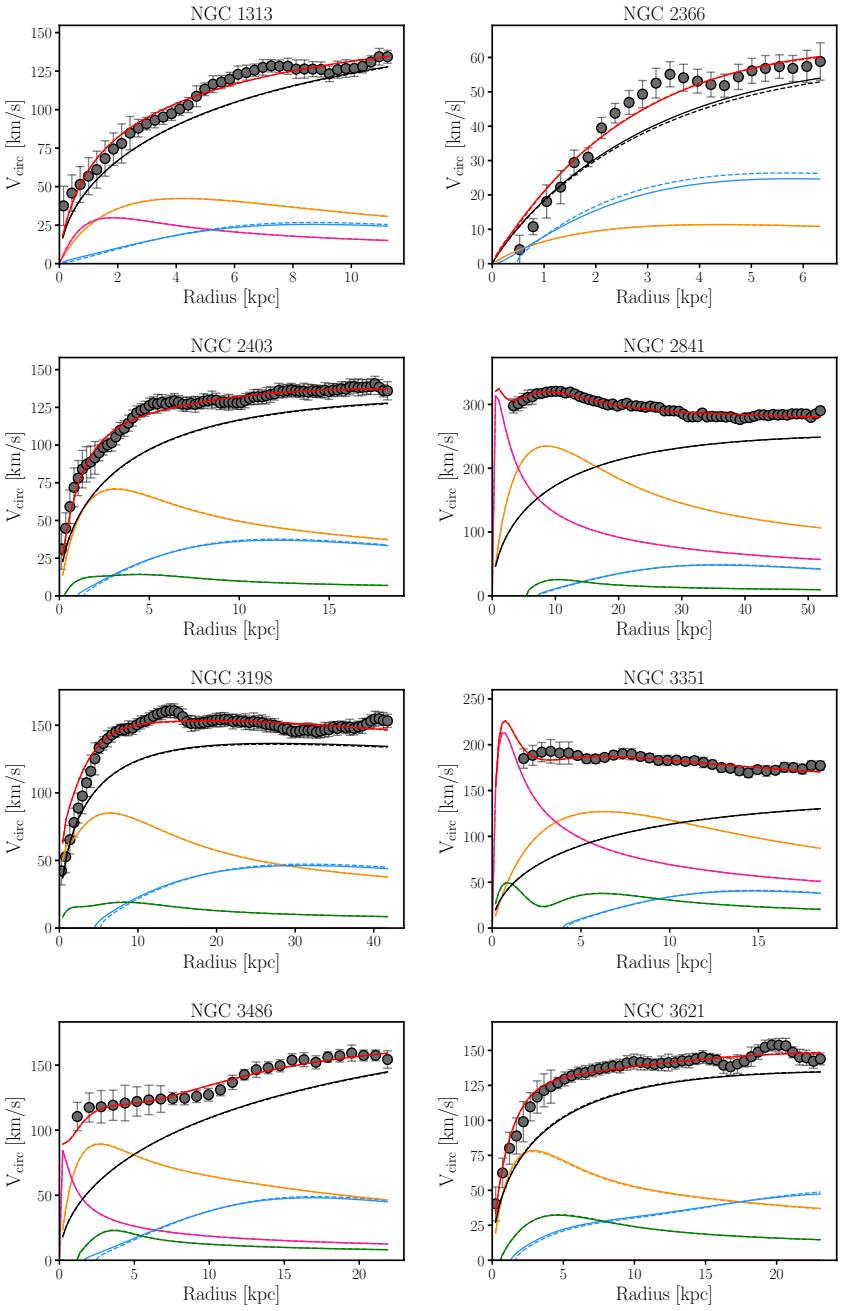

Figure 7.13: Continuation.

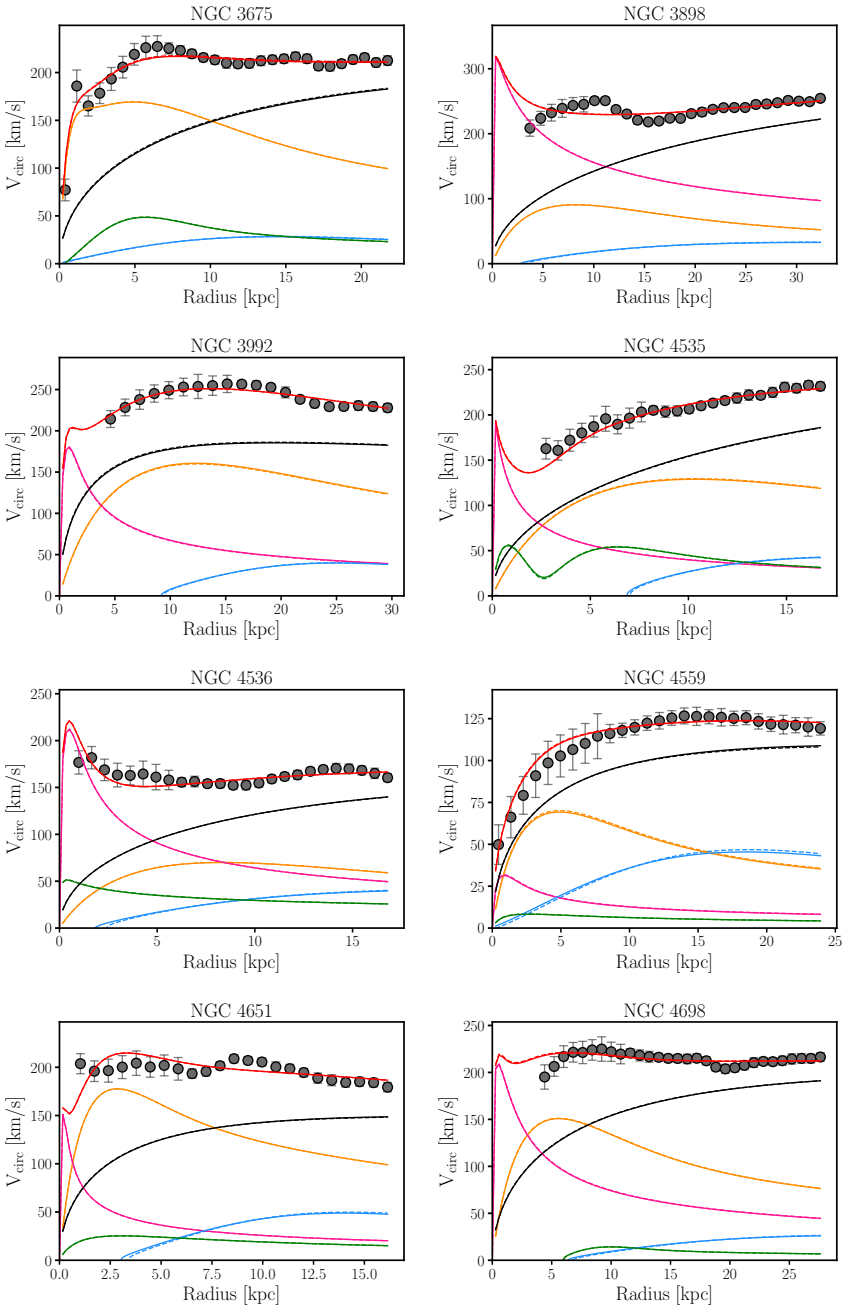

Figure 7.13: Continuation.

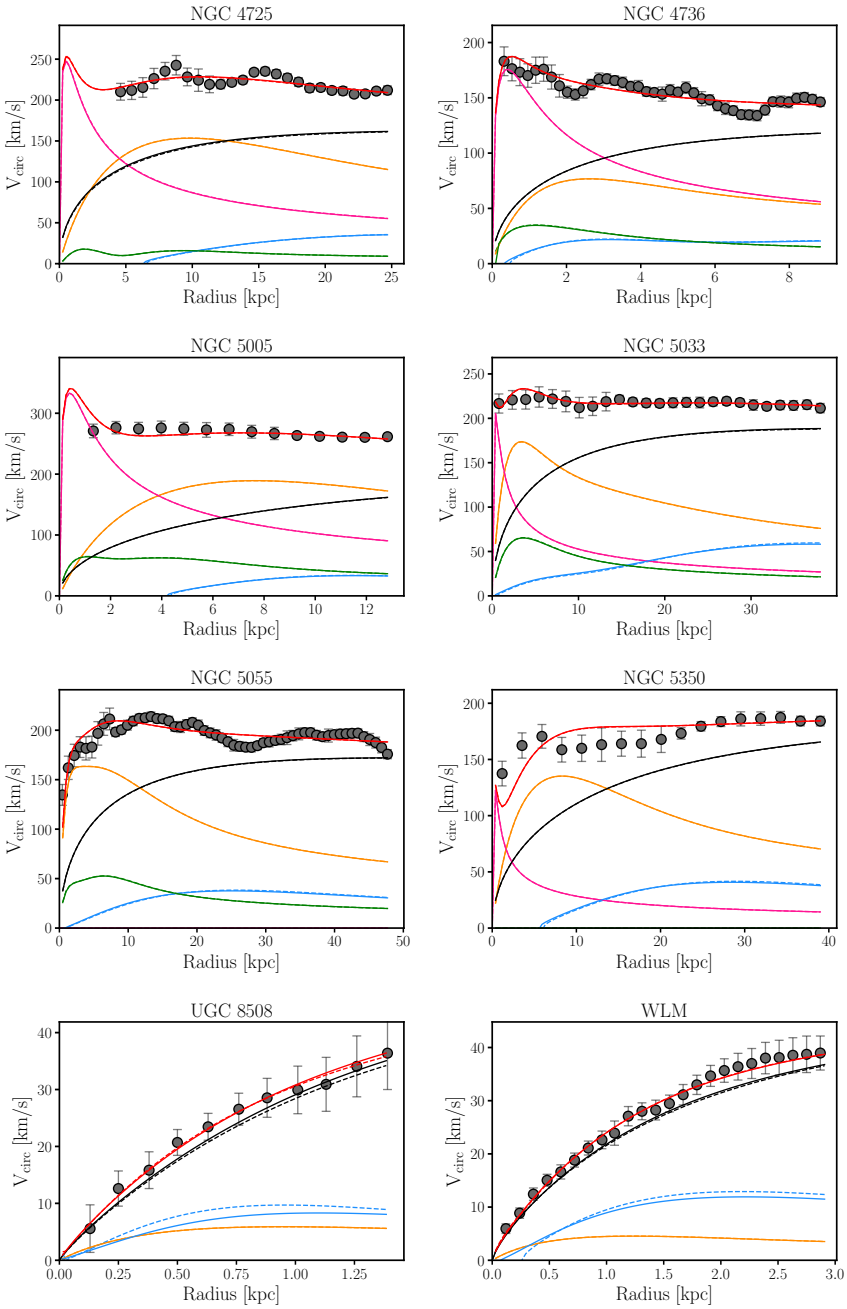

Figure 7.13: Continuation.

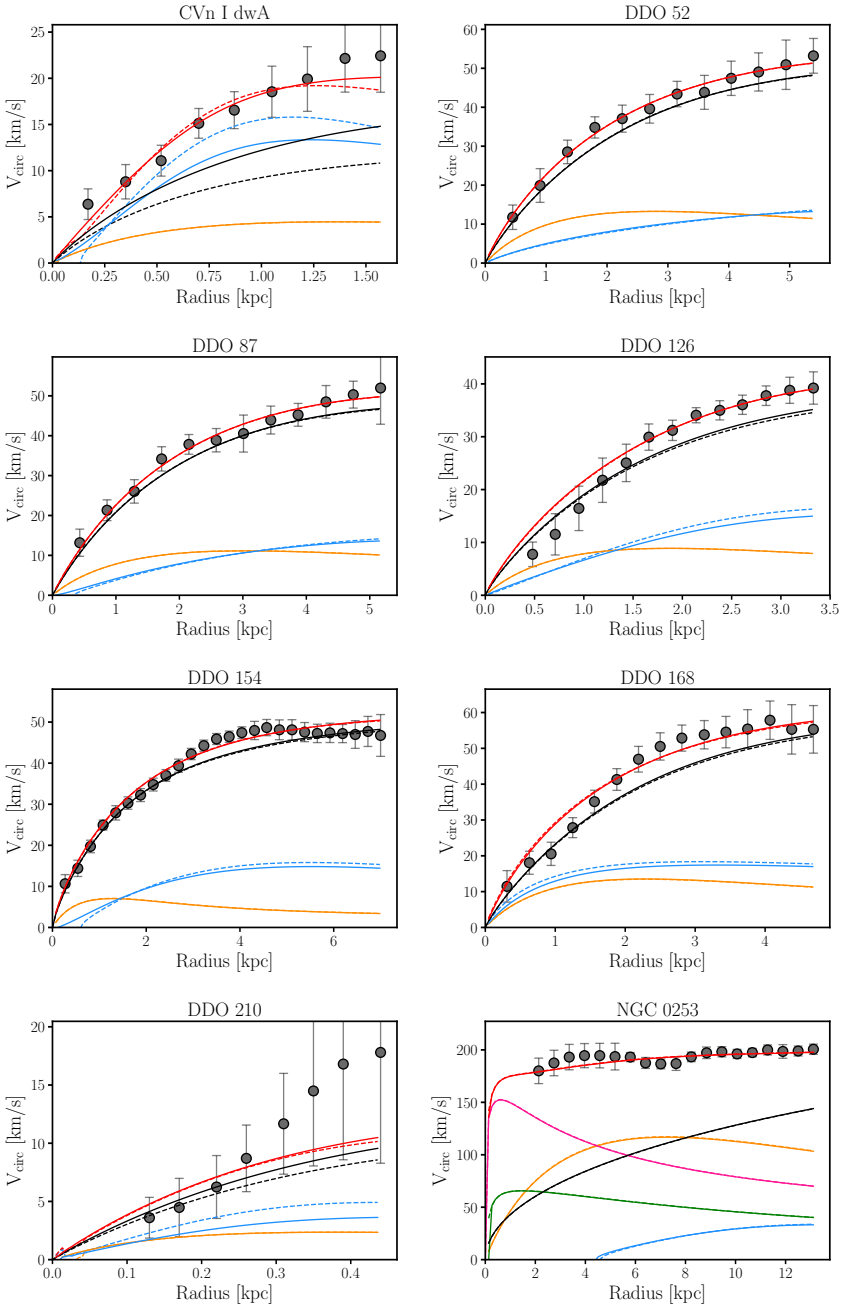

Figure 7.14: Mass models for our galaxy sample under the flat prior on c_{200}. Symbols and colors are as in Fig. 7.13.

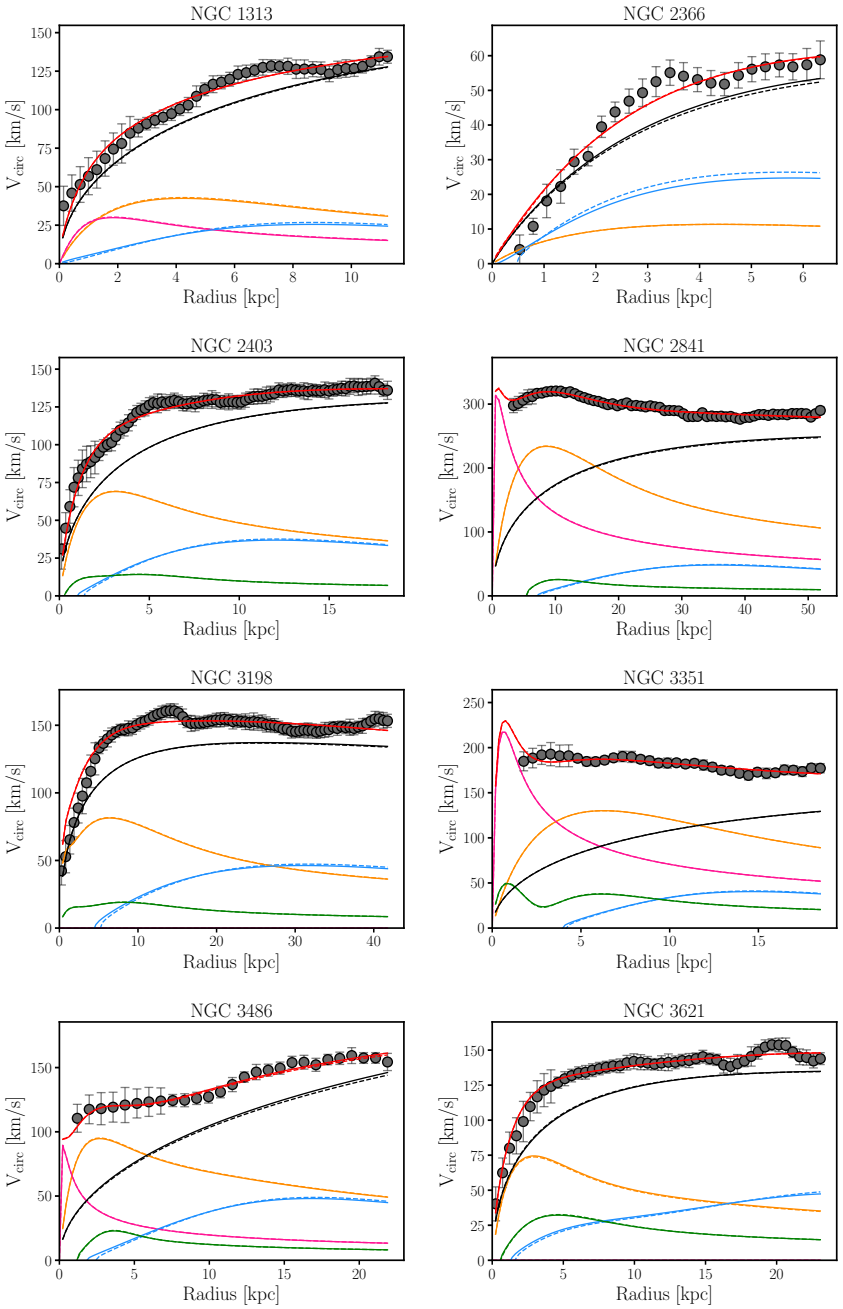

Figure 7.14: Continuation.

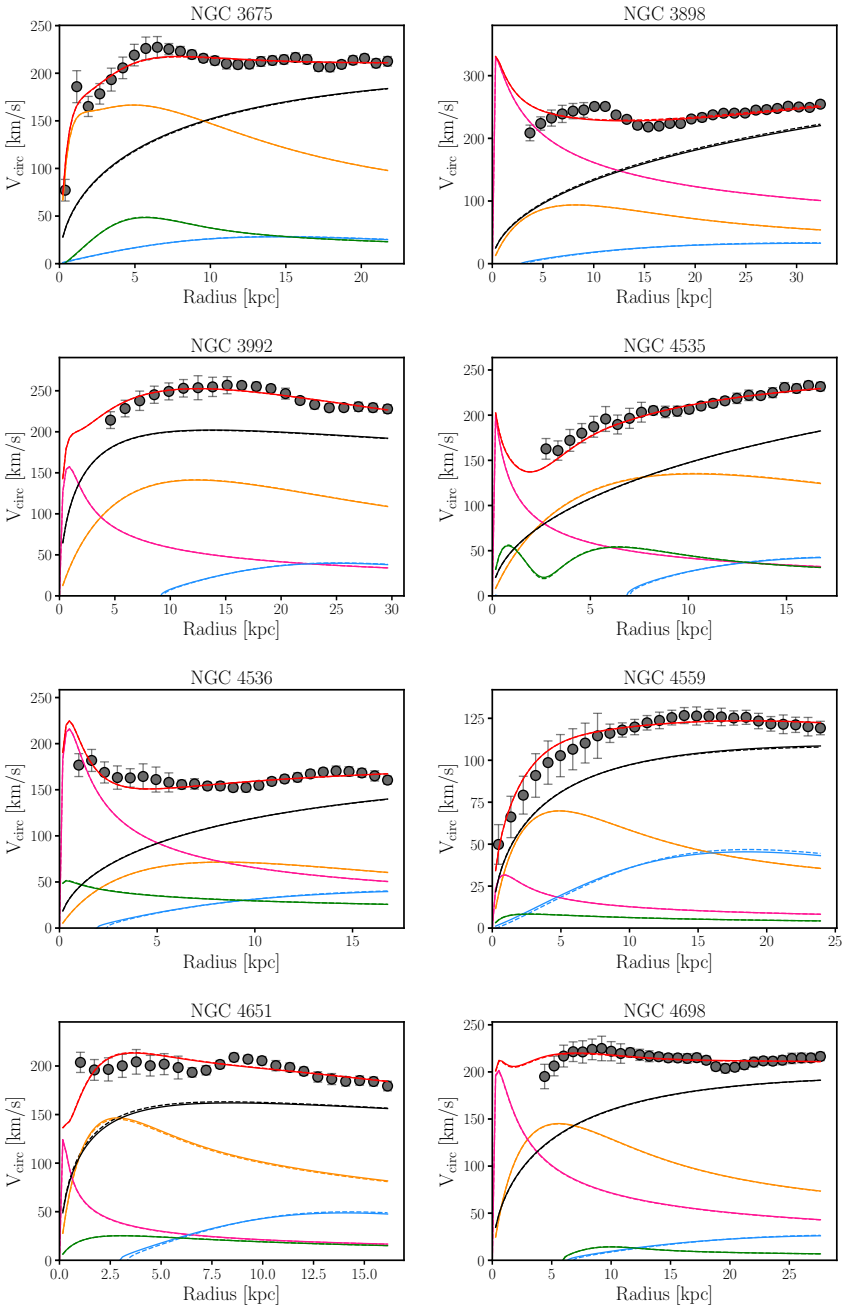

Figure 7.14: Continuation.

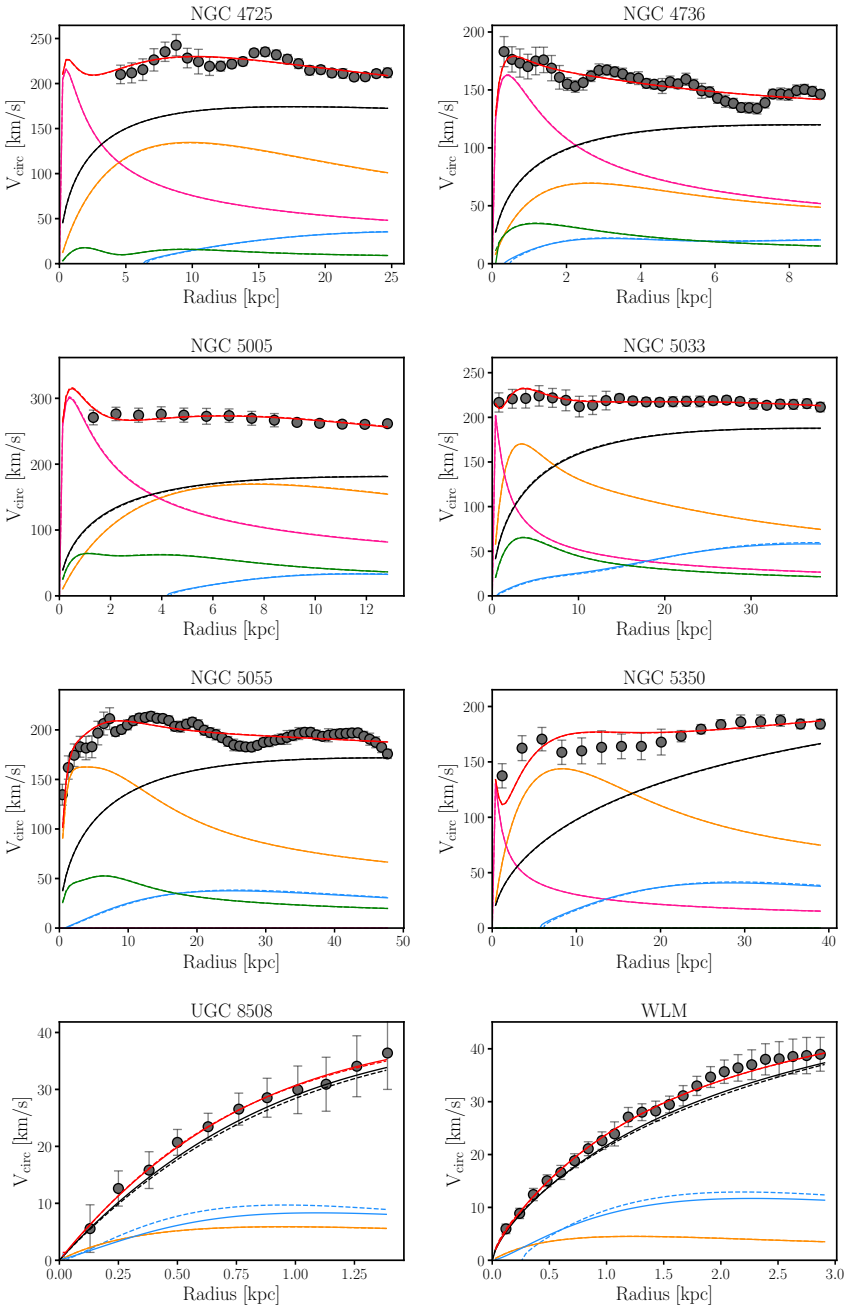

Figure 7.14: Continuation.

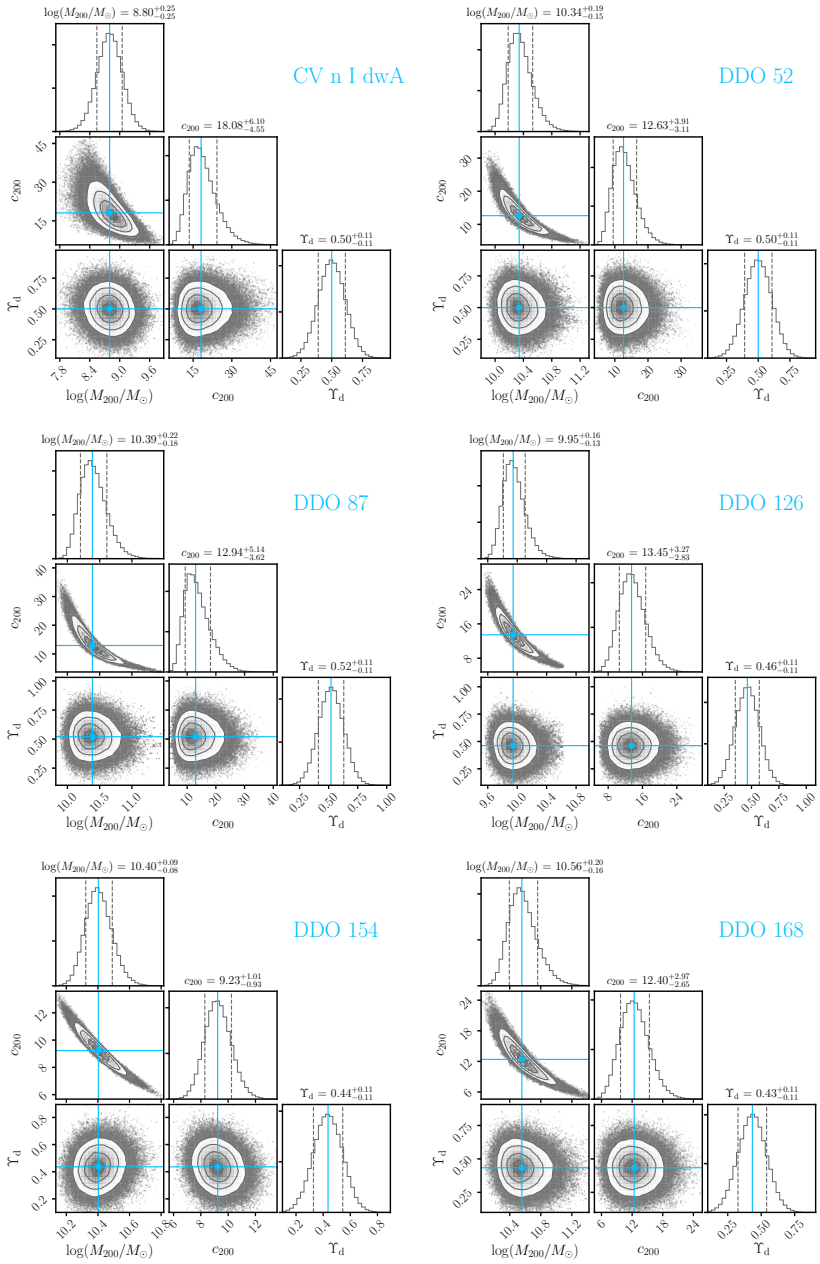

Figure 7.15: MCMC posterior distributions for the mass models for our galaxy sample under the prior of Eq. 7.14. These posterior distributions correspond to the mass models from Fig. 7.13.

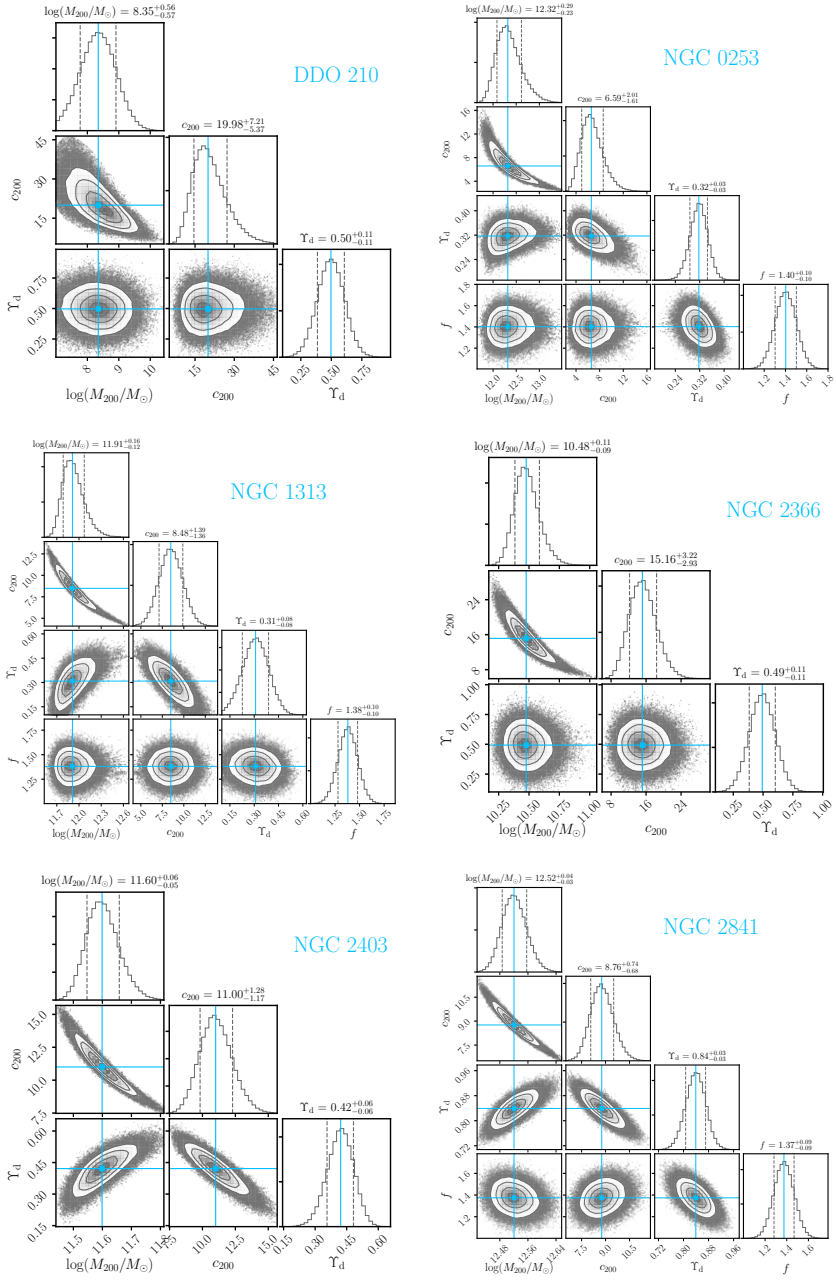

Figure 7.15: Continuation.

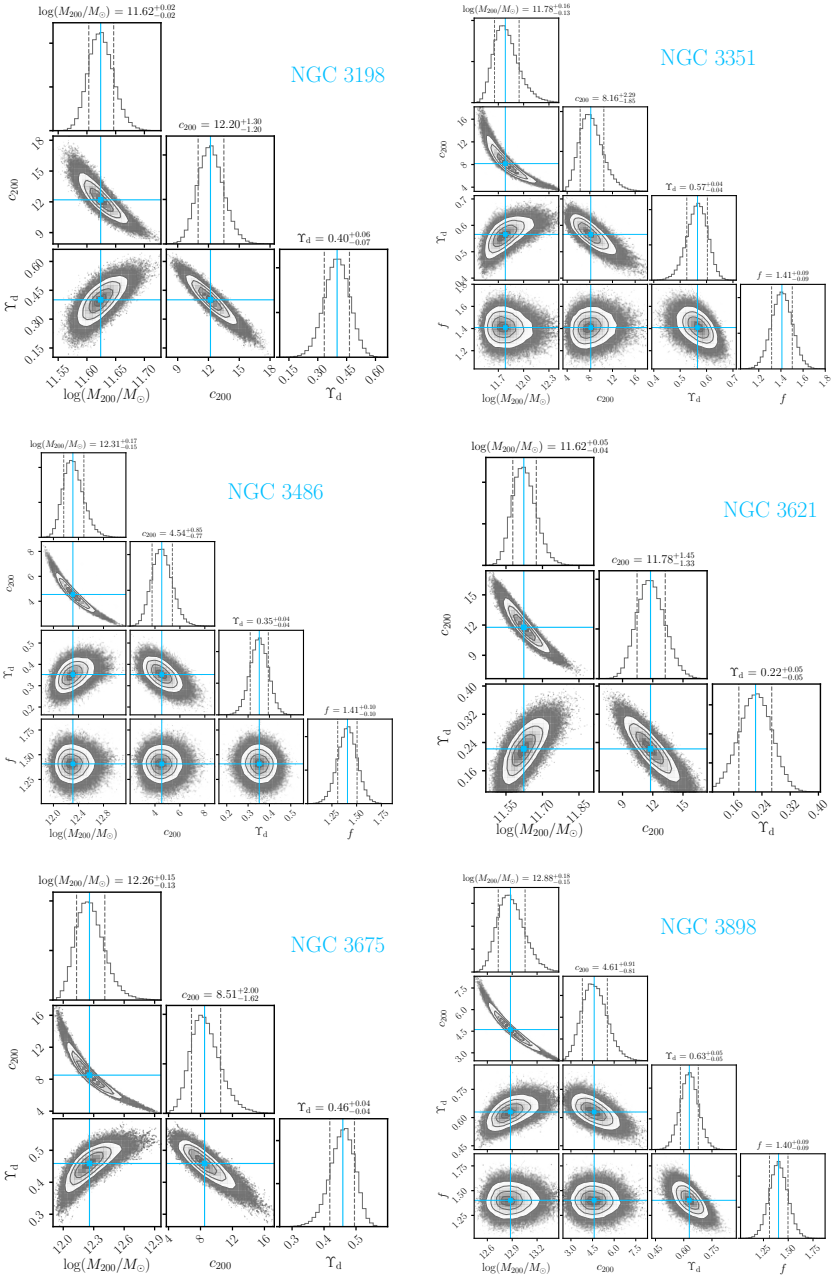

Figure 7.15: Continuation.

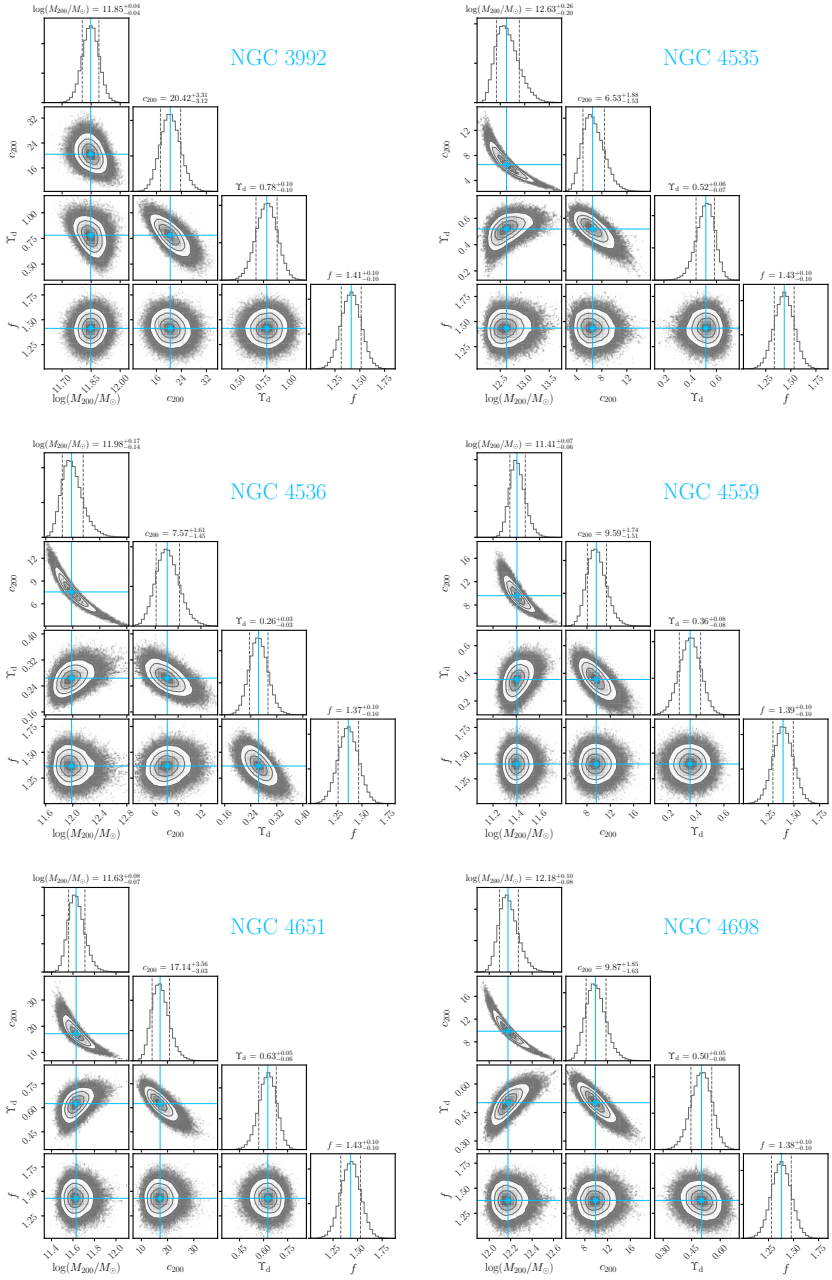

Figure 7.15: Continuation.

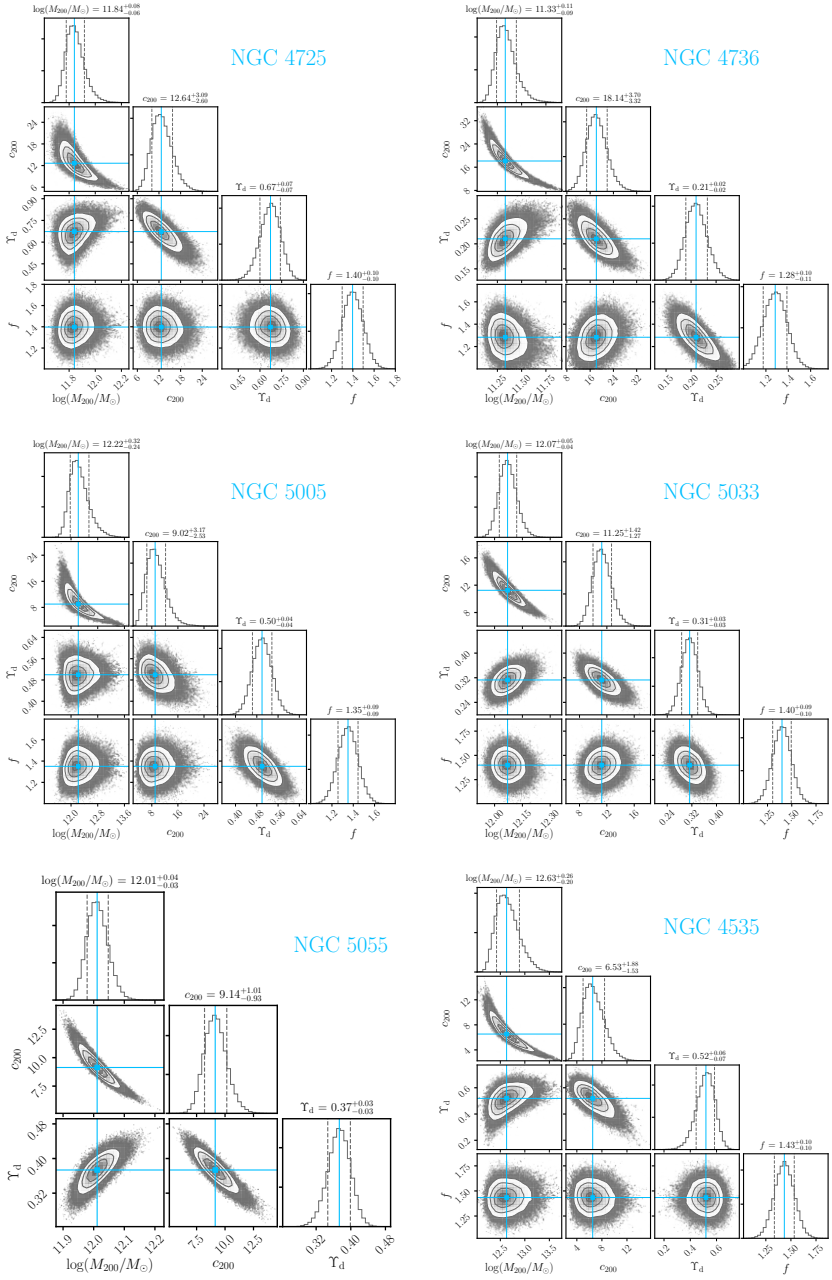

Figure 7.15: Continuation.

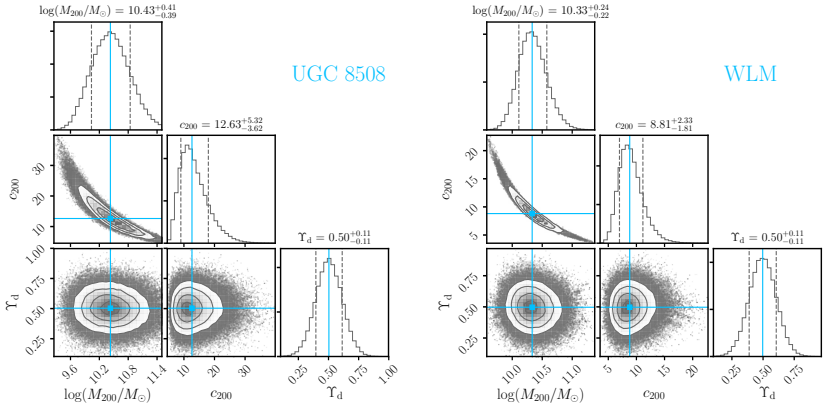

Figure 7.15: Continuation.

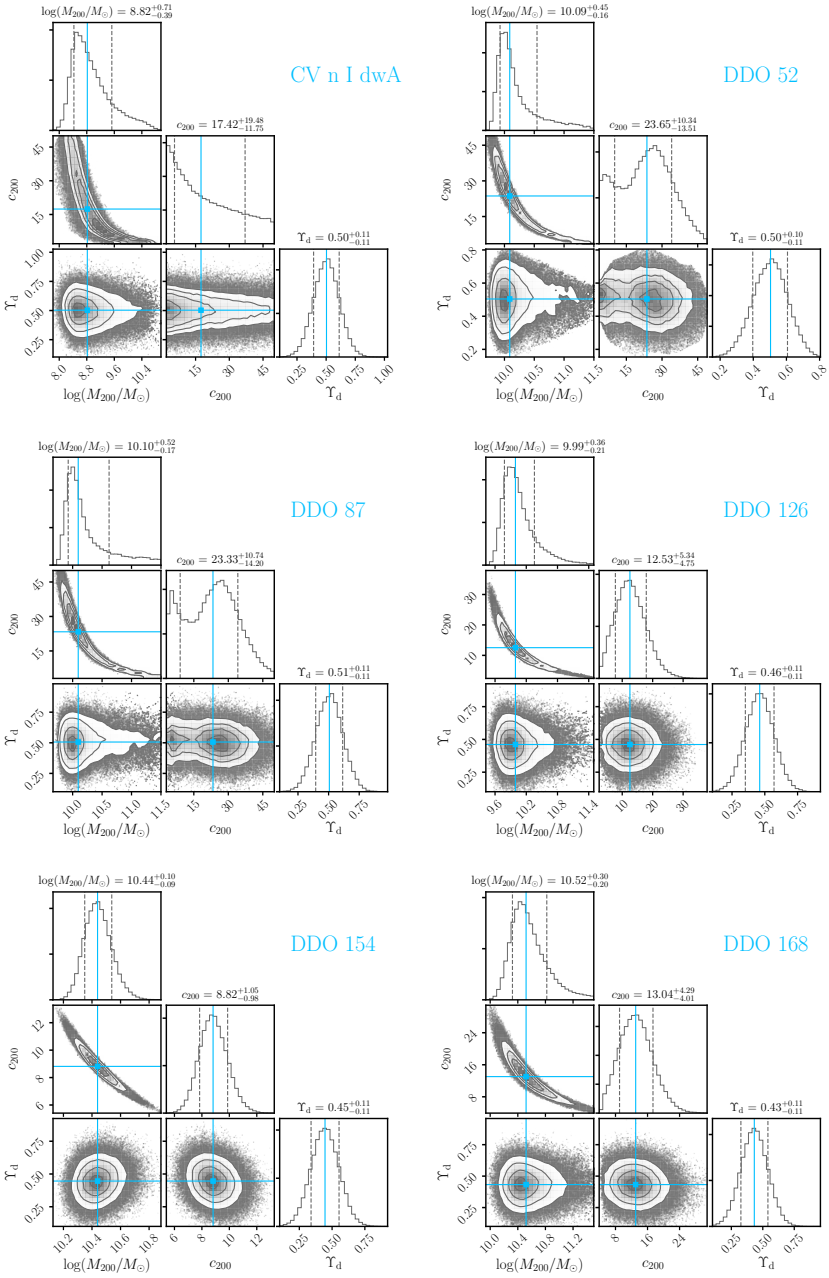

Figure 7.16: MCMC posterior distributions for the mass models for our galaxy sample under the flat prior on c_{200}. These posterior distributions correspond to the mass models from Fig. 7.14.

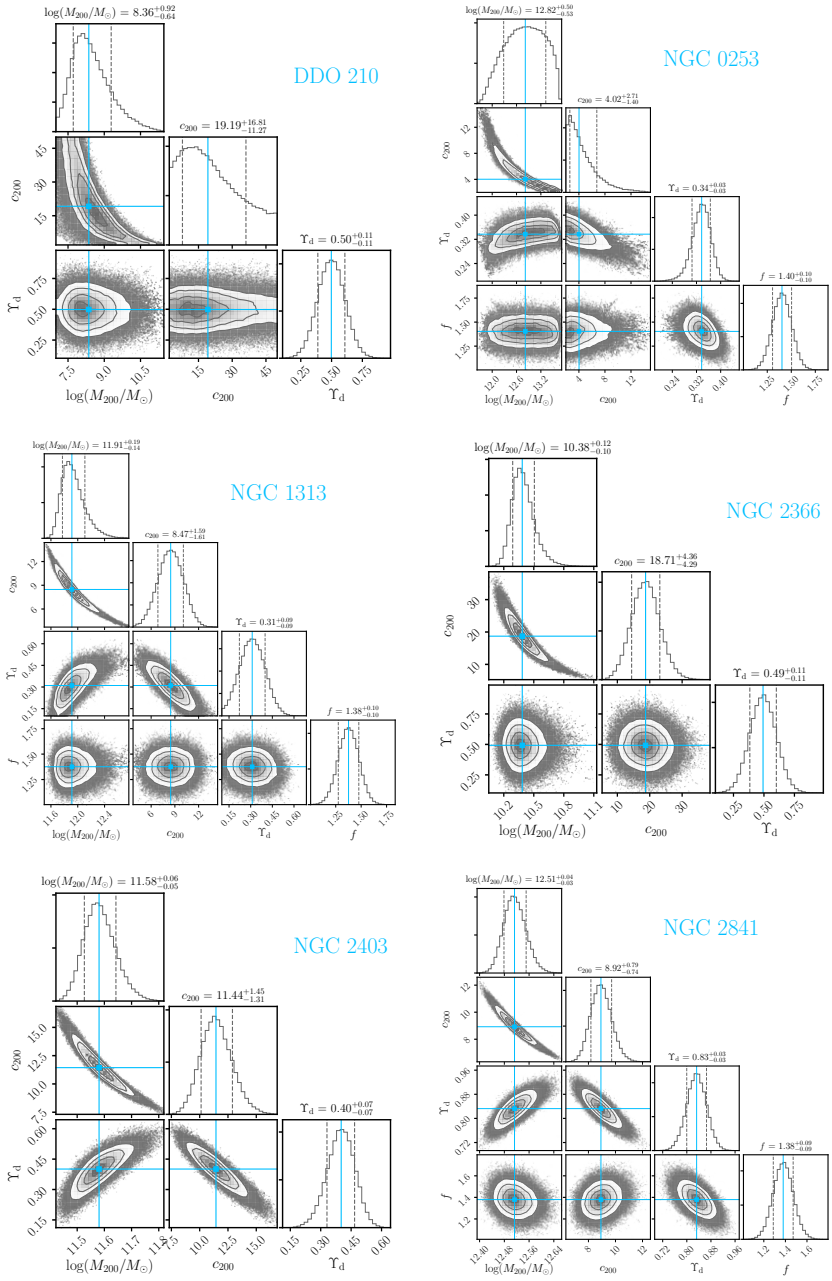

Figure 7.16: Continuation.

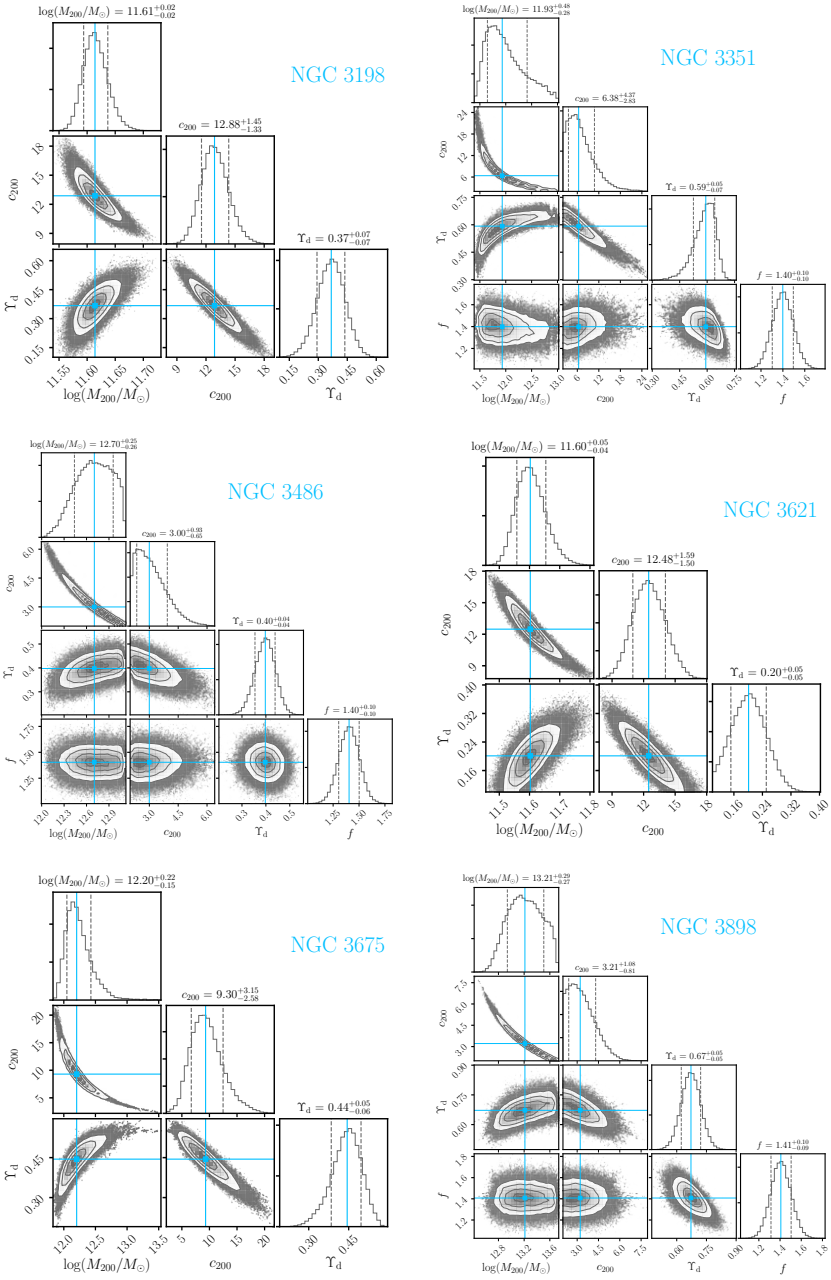

Figure 7.16: Continuation.

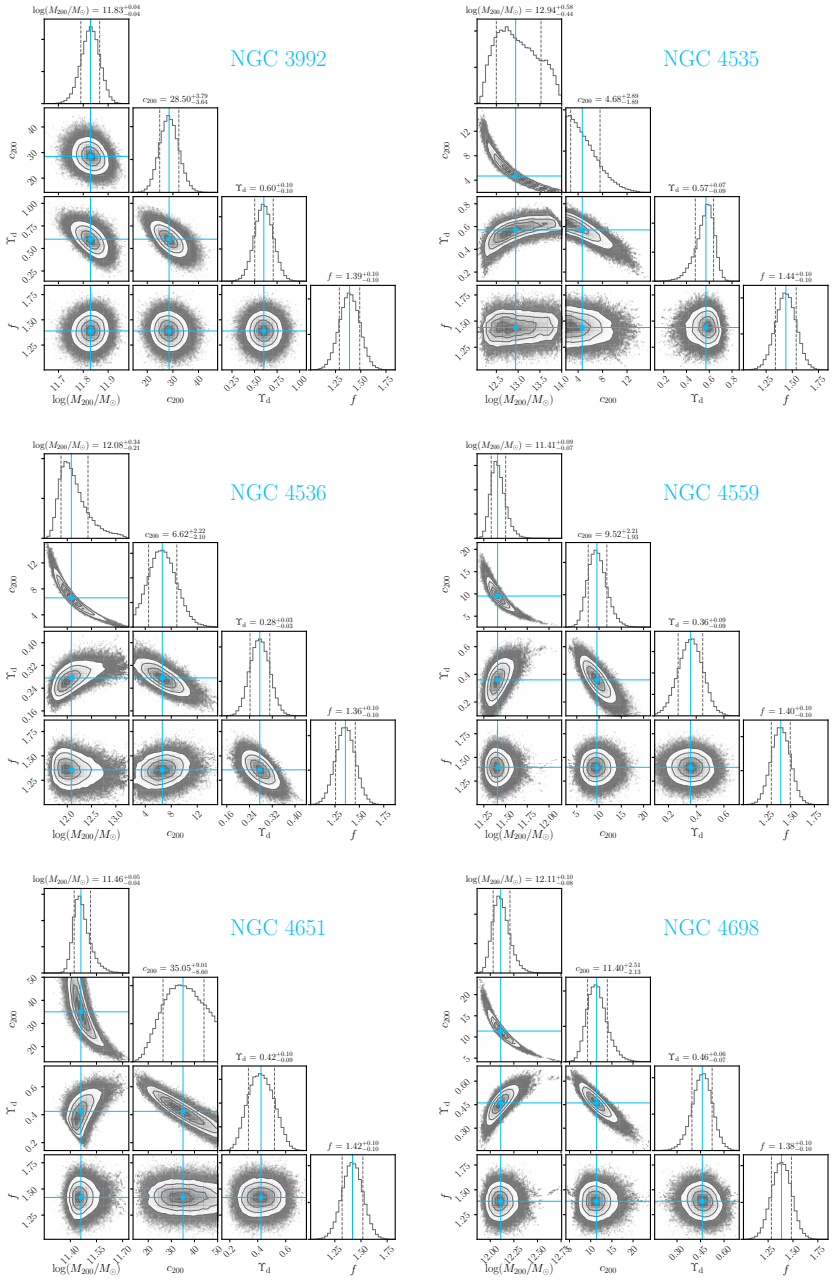

Figure 7.16: Continuation.

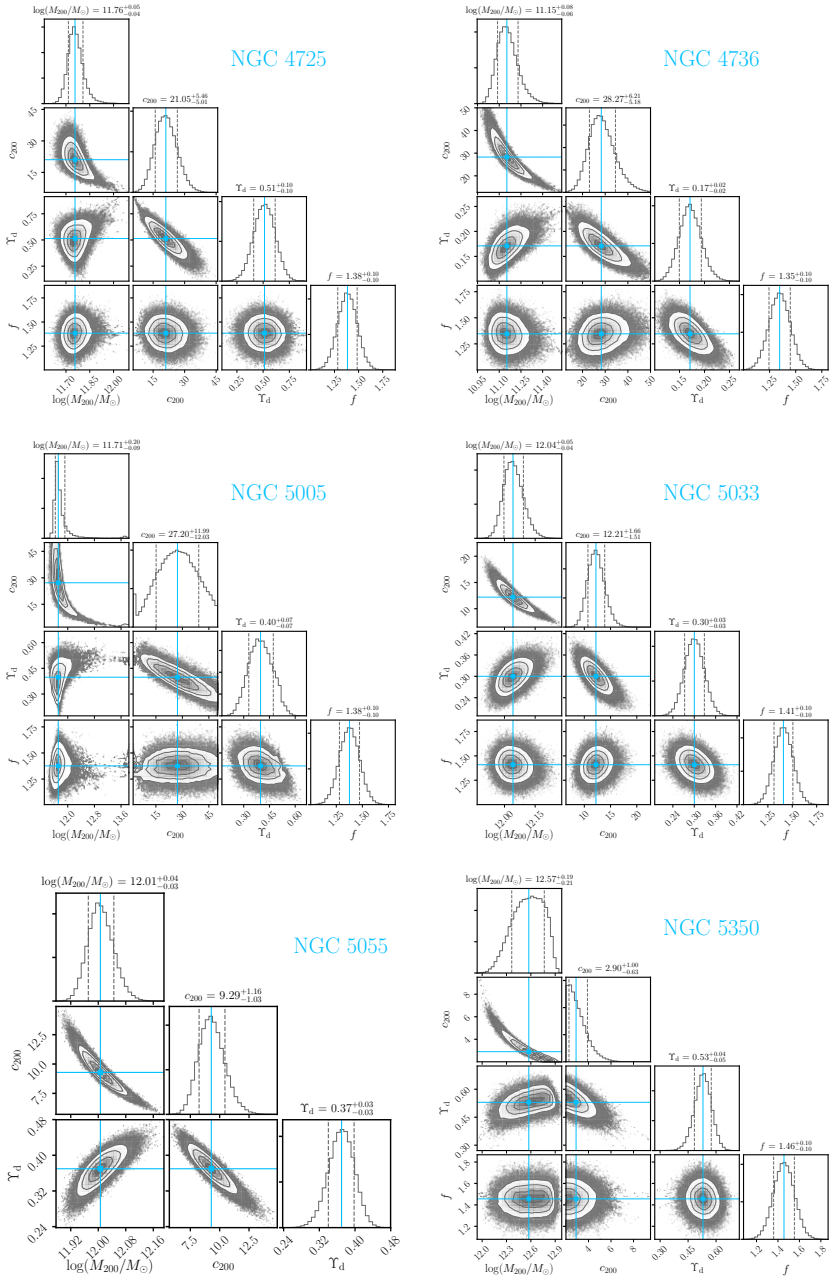

Figure 7.16: Continuation.

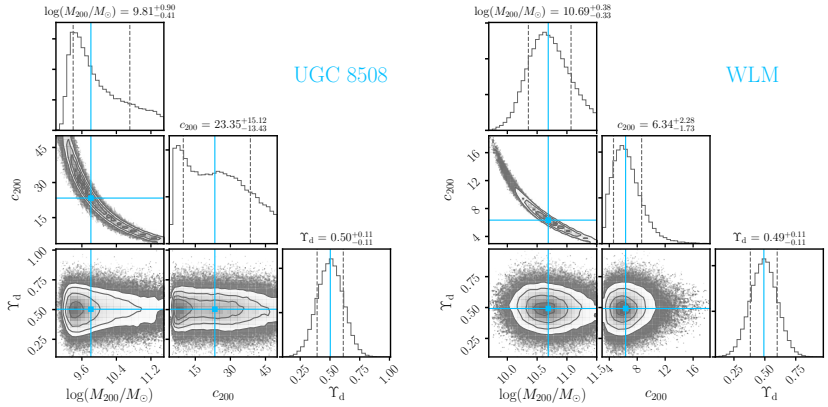

Figure 7.16: Continuation.

Chapter 8

Conclusions and prospects for future research

In this Ph.D. dissertation we set out to investigate the dark matter and angular momentum content of a wide variety of disc galaxies, from ultra-diffuse dwarfs to massive spirals. For this, we took advantage of H I (spectral line at 21 cm) interferometric data of the highest possible quality, state-of-the-art kinematic modelling techniques, and robust analysis tools. In this concluding chapter, we summarise the main findings of this work, focusing on the questions highlighted in Sec. 1.4, and we present potential prospects for future research.

8.1 Remarks and conclusions

8.1.1 Ultra-diffuse galaxies

The first part of this thesis has been dedicated to the study ultra-diffuse galaxies (UDGs, see e.g. van Dokkum et al. 2015, see also Sandage & Binggeli 1984; Conselice 2018). UDGs are puzzling galaxies since their stellar masses are typical of dwarfs ($M_* \sim 10^8$ M$_\odot$) but their effective radii are as large as for large spiral galaxies like the Milky Way ($R_e \gtrsim 1.5$ kpc). Current simulations and

models have proposed, broadly speaking, two different formation mechanisms to explain the optical properties of UDGs (but see also e.g. Wright et al. 2021 and references therein for more mechanisms). One idea is that stellar feedback, which creates dark matter cores (e.g. Navarro et al. 1996; Pontzen & Governato 2012), is also responsible for the extended stellar body (Di Cintio et al. 2017; Chan et al. 2018; Cardona-Barrero et al. 2020). The other proposed explanation is that UDGs have large effective radii because of high angular momentum (Amorisco & Loeb 2016; Rong et al. 2017).

To gain insight into the nature of UDGs, it is essential to accurately derive their kinematics. A subset of the UDG population that is particularly suited for this task is that of isolated UDGs, as they are found to host significant cold gas reservoirs ($M_{\rm gas} \sim 10^{8-9}$ M$_\odot$) and to show kinematic signatures of rotation (Leisman et al. 2017; Spekkens & Karunakaran 2018). In this context, in Chapters 2 and 3 we studied a small sample of six isolated, gas-rich UDGs. We exploited low-resolution (two independent resolution elements) observations from two radio interferometers, the Very Large Array (VLA) and the Westerbork Synthesis Radio Telescope (WSRT), to obtain, for the first time, resolved measurements of the gas rotation velocity and the gas velocity dispersion of UDGs. For this, we paid special attention to our kinematic modelling, carefully performed by using the software $^{\rm 3D}$Barolo (Di Teodoro & Fraternali 2015), especially designed to deal with low-resolution observations, and to different sources of uncertainty such as the estimation of the inclination angles.

We found that all our galaxies are outliers of the baryonic Tully-Fisher relation (BTFR, McGaugh et al. 2000), with baryonic masses a factor $10-100$ larger than other galaxies rotating at similar speeds ($V_{\rm c} \approx 20-40$ km/s). While unresolved measurements had already suggested low rotation velocities (Leisman et al. 2017), our spatially-resolved data and analysis leaves little room for a reconciliation of UDGs with the BTFR. The offset from the BTFR is fairly unexpected given that no other known galaxy population is found to be off this scaling law, and the relation is claimed to have an extremely small intrinsic scatter ($\sigma_{\rm int} \approx 0.05$ dex, see Lelli et al. 2016b; Ponomareva et al. 2018). The combination of high baryonic mass and low circular speed is so extreme that our galaxies have baryon fractions consistent with the cosmological average, unlike other dwarf galaxies (e.g. Geha et al. 2006; Iorio et al. 2017). Looking in more detail at the low circular speed regime (below ~ 50 km/s) of the BTFR, we also found that the mass offset from it appears to correlate with the optical disc scale length (or effective radius): galaxies with larger effective radii deviate towards higher baryonic masses with respect to galaxies with more compact sizes. We conjectured that this trend and the offset from the BTFR are related via a 'weak feedback' mechanism where at similar circular speeds and star formation rates, galaxies with large sizes have lower star formation rate surface densities than more compact objects. The low star formation rate surface densities would prevent galaxies from ejecting gas out of their virial radius, allowing them to keep a high baryon fraction. Although merely speculative and qualitative, this scenario seems in line with recent results from observations and simulations,

that suggest that dwarfs and spiral galaxies do not lose as much mass in the form of outflows, and then external mechanisms are required to lower their baryon fractions (e.g. Lelli et al. 2014b; Emerick et al. 2018; McQuinn et al. 2019; Romano et al. 2019).

Our kinematic measurements also gave us an estimate of the dynamical masses of the galaxies, which are found to be very similar to the measured baryonic masses, suggesting a low dark matter content in regions as extended as 10 kpc. These low dark matter fractions could be explained by either a dark matter halo with a mass much lower than expected ($M_{200} \ll 10^{10}$ $M_\odot$), or by normal haloes in terms of mass but with extremely low concentration parameters.

We found that the low dark matter fractions are in tension with the UDG-like galaxies produced via stellar feedback in the hydrodynamical simulations by Di Cintio et al. (2017), which are found to be dark-matter dominated and with normal concentration parameters (see Di Cintio et al. 2017; Jiang et al. 2019). On the other hand, we obtained tentative evidence that the galaxies may have a higher-than-average stellar specific angular momentum, which could explain the extended light distributions. We note, however, that a high stellar specific angular momentum does not necessarily imply the high angular momentum dark matter halo proposed by the semi-analytic model of Amorisco & Loeb (2016).

In Chapter 4, we used high-resolution (five independent resolution elements) VLA data to map in detail the H I distribution and kinematics of AGC 114905, which is the galaxy that, among our six UDGs, shows the largest deviation from the BTFR. Our results are in very good agreement with those obtained from the low-resolution data. We found that the circular speed profile of the galaxy can be largely explained by the gravitational contribution of the stellar and gas discs, with little room for a dark matter halo. If a dark matter halo that follows cold dark matter (CDM) expectations is imposed, the total circular speed fails at reproducing the observations by a large margin. The only way to fit a halo with a reasonable mass comes at the expense of using an extremely low concentration parameter ($c_{200} \lesssim 1$), significantly off the standard CDM predictions ($c_{200} \approx 12$, e.g. Dutton & Macciò 2014; Ludlow et al. 2014). The inclination of AGC 114905, which we measured using the shape of the total H I intensity map and independently of our modelling, is relatively low ($\approx 32°$) and remains the largest source of uncertainty in our analysis (e.g. Karunakaran et al. 2020; Sellwood & Sanders 2022). However, the associated errors do not appear to be large enough to explain the atypical properties of the galaxy.

Chapters 2, 3, and 4 provide the most detailed kinematic characterisation of gas-rich UDGs to date. With this, we have provided important insights to the questions posed in Sec. 1.4. Regarding the behavior of the BTFR at low circular speeds, we discovered that some low-mass galaxies appear to deviate upwards when their disc scale lengths are extended. Concerning the question on the dark matter content of UDGs, we found that they seem to have atypical dark matter haloes and to be baryon-dominated in regions as extended as 10 kpc. We have not been able to provide a definitive answer to the question 'What

is the origin of UDGs?', although we find some indications of UDGs having a higher-than-average stellar specific angular momentum, which could explain their extended light distributions. Formation mechanisms aiming to explain the origin of UDGs must be able to reproduce the set of unusual properties our analysis has unveiled.

8.1.2 The baryonic specific angular momentum of disc galaxies

At different cosmic times, the angular momentum content of galaxies plays an important role at shaping their morphologies (e.g. Fall 1983; Romanowsky & Fall 2012; Marasco et al. 2019; Bouché et al. 2021). In addition, angular momentum has a central position within the currently-favoured cosmological model, ΛCDM, via the tidal torque theory (e.g. Peebles 1969; Doroshkevich 1970; Fall 1983). Observational constraints have been compared with simulations and models in order to learn about different processes such as stellar feedback and outflows, angular momentum transfer between galaxy and halo, and the impact of galaxy mergers, to name a few (Steinmetz & Navarro 1999; Dutton & van den Bosch 2012; Pedrosa & Tissera 2015; Teklu et al. 2015; Lagos et al. 2017, 2018; El-Badry et al. 2018; Posti et al. 2018a; Stevens et al. 2018).

While the relation between stellar specific angular momentum and stellar mass ($j_* - M_*$) has been widely studied for large galaxy samples (e.g. Romanowsky & Fall 2012; Obreschkow & Glazebrook 2014; Fall & Romanowsky 2018; Posti et al. 2018b; Sweet et al. 2018), the relation for the cold gas ($j_{\rm gas} - M_{\rm gas}$) has been less explored (see e.g. Kurapati et al. 2018, 2021). Without information on the cold gas component, the underlying baryonic relation ($j_{\rm bar} - M_{\rm bar}$) cannot be studied in detail, preventing us from obtaining a global picture of the angular momentum content of galaxies. In Chapters 5 and 6 we contributed at filling this gap by focusing on the derivation and analysis of the baryonic specific angular momentum of disc galaxies.

In Chapter 5, we compiled a high-quality sample of about 160 nearby galaxies with extended H I rotation curves and surface density profiles, and near-infrared (NIR) stellar surface brightness profiles. With our sample, we homogeneously studied the stellar, gas, and baryonic specific angular momentum–mass ($j - M$) relations of disc galaxies. We note here that by 'gas' we refer mostly to H I, but we have demonstrated (see Sec. 6.A) that the inclusion of H_2 has only a minor effect and does not alter the nature of our conclusions discussed below. Although a few earlier studies had looked into the three $j - M$ relations (e.g. Obreschkow & Glazebrook 2014; Elson 2017; Kurapati et al. 2018; Murugeshan et al. 2020), our work presents the largest sample for which the three relations have been studied simultaneously.

From a purely empirical point of view, the three relations are well characterised by unbroken power laws of the form $j \propto M^{\alpha}$ with slopes α of about 0.5, 1, and 0.6 for stars, gas, and baryons, respectively. The intrinsic scatter of each relation is around 0.15 dex. By comparing with theoretical expectations,

we found that the baryons in disc galaxies have retained about 60% of the original angular momentum of their dark matter halo, in agreement with some semi-analytical models (e.g. Dutton & van den Bosch 2012) and somewhat lower than reported in hydrodynamical simulations (Genel et al. 2015; Pedrosa & Tissera 2015).

While the intrinsic scatter of the three relations is relatively low, close inspection of the residuals from the best-fitting relations revealed systematic trends with the gas fraction $f_{\rm gas} = M_{\rm gas}/(M_* + M_{\rm gas})$. In Chapter 6, we further explored this by looking at the precise distribution of galaxies in the $j - M - f_{\rm gas}$ spaces. We found that the three relations can be well fitted by planes of the form $j \propto M^{\alpha} f_{\rm gas}^{\beta}$. In this case, the three α coefficients affecting M are all around 0.7, following rather closely the value of 2/3 expected from the tidal torque theory (e.g. Fall 1983; Shaya & Tully 1984; White 1984; Heavens & Peacock 1988). Remarkably, the intrinsic scatter of the best-fitting planes is $\lesssim 0.1$ dex, making these scaling laws some of the tightest scaling relations for late-type galaxies. Among the three laws, we argue that the baryonic relation is the most fundamental, and we have shown that it is followed not only by our calibration sample, but also by galaxies (including UDGs) with extreme properties in terms of size, mass, star formation, kinematics, or gas content. We also showed that the $j - M - f_{\rm gas}$ relations have similarities will the well known relation between j_*, M_*, and B/T, the bulge-to-total mass fraction, although the relations have different 'predictions' regarding gas-poor, bulgeless galaxies. Finally, we argued that our relations can be used as stringent tests for the predictions of models and simulations. As an example of this, we showed that current galaxy evolution models purely based on disc stability arguments (e.g. Obreschkow et al. 2016; Romeo 2020) do not manage to fully capture our scaling laws.

Overall, we have performed one of the most complete investigations in the literature regarding the angular momentum content of late-type galaxies. As detailed above, albeit that some aspects remain unknown, our study largely allowed to answer the question 'What is the behavior of the stellar, gas, and baryonic $j - M$ relations?' posed in Sec. 1.4 for galaxies across about five orders of magnitude in stellar mass and with a vast range of properties.

8.1.3 Gas scale heights and galaxy-halo connection from robust rotation curve decomposition

One of the most robust empirical ways to determine the dark matter distribution of galaxies is by looking at the kinematics of their diffeent baryonic components, which trace the underlying total gravitational potential. In the specific case of disc galaxies, H I rotation curve decomposition has been used for the last 50 years to infer the properties of the host dark matter haloes (e.g. Freeman 1970; Roberts & Rots 1973; Bosma 1978; Rubin et al. 1980; Begeman 1987; Verheijen 1997; de Blok et al. 2008; Read et al. 2017).

When deriving the contribution of the gas discs to the total circular speed profile of disc galaxies, it is almost invariably assumed that gas discs are razor-

thin. However, abundant observational evidence exists against this assumption, as gas discs are found to be flared, with a scale height increasing with radius and often reaching kpc sizes at the outermost observed radii (e.g. Sancisi & Allen 1979; Kalberla & Dedes 2008; Marasco & Fraternali 2011; Yim et al. 2014; Bacchini et al. 2019a). This may affect rotation curve decompositions because discs of different thickness will exert a different gravitational force in the midplane (cf. Cuddeford 1993; Binney & Tremaine 2008).

In Chapter 7, we set out to quantify how much gas disc flaring affects mass models with respect to the standard razor-thin discs. For this, we built a sample of galaxies with the highest possible data quality. Specifically, we studied 32 disc galaxies, from dwarfs to massive spirals in the range $M_* \approx (5\times10^6 - 5\times10^{11})$ $M_\odot$, with archival deep H I and CO interferometric observations, accurate kinematic modelling, and robust NIR bulge-disc decompositions.

Under the assumption of vertical hydrostatic equilibrium and using a Bayesian framework, we performed rotation curve decomposition, obtaining the best-fitting dark matter halo parameters (namely the mass M_{200} and concentration c_{200}) simultaneously with the flaring of the gas discs. We found that the effects of the gas flaring are negligible for most galaxies in our sample. Only the smallest, most gas-rich dwarf galaxies are affected in a significant way. Since the contribution to the total circular speed by a flared disc is weaker than for a razor-thin disc, including the flaring allows for a more massive dark matter halo to be fitted.

The gas discs of dwarf galaxies are thicker than in more massive spirals, showing a broad trend with halo mass. For the spirals, H I discs are significantly thicker than the H_2 discs, as expected from the larger H I velocity dispersion. While in every galaxy the scale heights increase with radius, the way they increase is fairly diverse, and we do not find evidence for a 'universal' scale height profile as suggested in the literature (e.g. Patra 2020a,b). The absence of a single universal profile is not surprising given the strong dependence of the scale height on the velocity dispersion, the mass-to-light ratio, and the bulge fraction of galaxies, all of which vary significantly within our galaxy sample.

Our high-quality data and robust analysis put us in a good position to revisit important dynamical scaling laws involving the mass of the dark matter haloes with stellar mass, baryonic mass, and the concentration parameter. We find that the stellar masses of our sample increase roughly linearly (in log-log space) with increasing halo mass, albeit that the scatter is large, especially at the high-mass regime ($M_* \gtrsim 5\times10^{10}$ $M_\odot$). The galaxies with the highest stellar masses of our sample show very high M_*/M_{200} ratios, some of which even approach to the average cosmological baryon fraction. This confirms previous findings showing that the most massive spiral galaxies have virtually no 'missing baryons' (Posti et al. 2019). Inspection of the M_*/M_{200} ratio as a function of M_* reveal a linearly (again in log-log space) increasing relation which deviates from the predictions of abundance-matching (Moster et al. 2013) at high M_* values. This adds up to results in the literature suggesting that late- and early-type galaxies follow different sequences in the stellar-to-halo mass relation (e.g. Rodríguez-

Puebla et al. 2015; Posti & Fall 2021). The baryon-to-halo relation presents a similar picture, with $M_{\rm bar}$ increasing smoothly with M_{200}. Correlations based on abundance-matching (e.g. Calette et al. 2021) follow a similar trend in shape, but their normalisation (i.e. their $M_{\rm bar}/M_{200}$ ratios) is somewhat lower than in our observations. Both as a function of $M_{\rm bar}$ and M_{200}, the $M_{\rm bar}/M_{200}$ ratios of our galaxy sample show large scatter and no clear trends, in contrast to M_*/M_{200} which is much higher for massive spirals than for dwarfs.

Regarding the $c_{200} - M_{200}$ relation, we find it to be followed reasonably well by the dark matter haloes of our galaxy sample. Some galaxies around $M_{200} \sim 5 \times 10^{11}$ M$_\odot$ show moderate deviations towards higher values than expected, while the most massive galaxies with $M_{200} \gtrsim 10^{12}$ M$_\odot$ deviate towards low concentrations. Interestingly, the galaxies with higher-than-average concentrations are those with the highest stellar fractions relative to the cosmological baryon fraction. We speculate that the small departures from the average concentration-mass relation could be arising from baryonic physics. On the one hand, adiabatic contraction (e.g. Blumenthal et al. 1986; Katz et al. 2014) could be responsible for the high concentration in those spirals with very high stellar fractions. On the other hand, feedback could be behind the low concentrations of the most massive spirals, which also show relatively low baryon fractions. Dynamical friction between baryons and dark matter halo may also imprint changes in the dark matter density distribution, but these effects are expected to be negligible for our galaxy sample (e.g. Sellwood 2008; Nipoti & Binney 2015).

In Sec. 1.4 we presented the question 'How important is the dynamical effect of the flaring of the gas discs for rotation curve decomposition?'. The work developed in Chapter 7 has allowed us to answer in good measure this question, showing that except for the smallest dwarfs the effects of the flaring can be neglected.

8.2 Future prospects

There are different lines of research than can be pursued to further our understanding on the subjects studied in this dissertation. In this section, we present an overview on some of these subjects, focusing mostly on the potential of current and future observational facilities to test galaxy formation theories.

8.2.1 UDGs

The origin and evolutionary pathways of UDGs are yet to be fully understood. An essential step will be to increase the number of systems with resolved gas kinematics. Exploiting larger samples (especially using blind selections in forthcoming H I surveys, see Sec. 8.2.2), even at relatively low resolution, would help to clarify whether the offset from the BTFR can be ascribed to the optical disc scale length of the galaxies and their star formation rate surface densities, as speculated in Chapter 3. With data at a high spatial resolution

it would also be possible to provide a more definitive answer on whether or not gas-rich UDGs have extended light distributions because of a higher-than-average j_* (Chapter 3), even if their $j_{\rm bar}$ values do not seem to be atypically high (Chapter 6). High-resolution H I data for multiple UDGs would additionally help to overcome the concerns regarding the inclination of individual systems. We note however that obtaining these data can be very time-consuming with current facilities such as the VLA (Chapter 4). The new MeerKAT radio interferometer (Booth et al. 2009) already represents an improvement in terms of sensitivity but not in spatial resolution, for which we will have to wait for the Square Kilometre Array (SKA) interferometer (Dewdney et al. 2009).

On a broader astrophysical frame, high-resolution H I data will also be crucial to investigate the properties of the dark matter haloes of UDGs. This is relevant as we have shown that the halo of AGC 114905 seems to be quite atypical for dwarf (and any other type of) galaxies, with a concentration parameter significantly below CDM expectations. Therefore, UDGs are emerging as a promising class of galaxies where to test different dark matter theories (e.g. Yang et al. 2020; Bechtol et al. 2022), potentially helping to address one of the most urgent questions of modern astrophysics.

Work along these lines is underway. We have recently obtained new high-resolution VLA data for another UDG studied in Chapters 2 and 3, AGC 248945. While we are only starting to study this object, our preliminary kinematic modelling, shown in Fig. 8.1, is promising, and we should be able to provide estimates of the dark matter halo parameters of this galaxy in the upcoming months.

Related to the mass models of gas-rich UDGs, we are also carrying out an investigation fitting the low-resolution data of Chapter 3 and comparing the outcome with cosmological simulations. One of the main results of the analysis (Kong et al. 2022) is that indeed UDGs seem to have very shallow haloes with low c_{200}. For a given $M_{\rm halo}$, the low concentrations are significantly below the average value expected from the concentration-mass relation (Dutton & Macciò 2014), although haloes in the (dark-matter only) cosmological simulation IllustrisTNG-50 (Nelson et al. 2019) exist with similarly low concentrations, as shown in the left panel of Fig. 8.2. While it is promising that such haloes exist in simulations, their dark matter densities at larger scales do not match the densities of real gas-rich UDGs. This can be seen in the right panels of Fig. 8.2: the circular speeds of the simulated low-concentration haloes within 2 and 8 kpc are systematically higher than the speeds of the best-fitting haloes of the UDGs. As mentioned in Kong et al. (2022), potential solutions to this tension include stellar feedback or dark matter self-interactions, highlighting once again the potential of UDGs to study the intrinsic properties of dark matter. These results and future similar analyses will benefit significantly from large samples of UDGs with high-quality interferometric observations.

In parallel to the above, we should obtain estimates of the halo masses of UDGs with different tracers. For instance, nearby galaxies follow a correlation between their number of globular clusters and their total dynamical mass (see

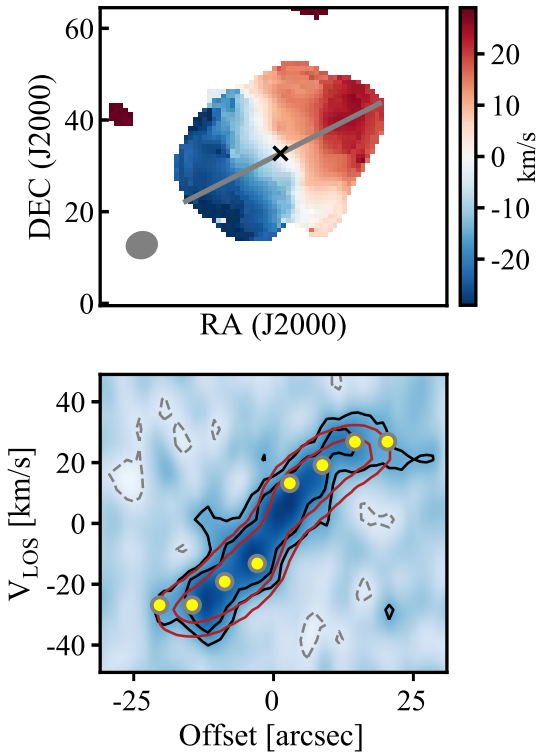

Figure 8.1: Preliminary new VLA data of AGC 248945. *Top*: observed velocity field; the grey ellipse shows the beam of the observations, the grey line the kinematic major axis, and the black cross the kinematic centre. *Middle:* Major-axis PV diagram; data are shown in blue background and black contours (grey for negative values), and the preliminary best-fitting ^{3D}Barolo azimuthal model in red contours. The contours are at $-2, 2, 4$ times the r.m.s. noise of the PV diagram. The yellow points show the recovered rotation velocities.

Burkert & Forbes 2020 and references therein). This relation has been used to estimate dynamical masses of a few UDGS (e.g. van Dokkum et al. 2016; Saifollahi et al. 2022), but whether UDGs actually follow the relation is still debated (e.g. Müller et al. 2021). In order to constrain this open issue, we have applied for observing time at the Hubble Space Telescope (HST) to benchmark the relation between the number of globular clusters and the dynamical mass in gas-rich UDGs. This will enable independent mass estimates of UDGs without detailed interferometric observations. Studying the properties of the globular clusters of UDGs can also be a useful tool to test models that make direct predictions on some of their properties such as their number, spatial distribution, sizes, and luminosities (e.g. Trujillo-Gomez et al. 2022; Bar et al. 2022; Danieli et al. 2022).

Finally, we would like to emphasise how relevant it would be to study the stellar content of gas-rich UDGs in more detail, in order to obtain star-formation histories and stellar kinematics. Accurate star formation histories are key to study the possibility that UDGs experienced strong episodic bursts of star formation as proposed in some models (e.g. Di Cintio et al. 2017), albeit that one would need exquisite observations to have a robust comparison with simulations (Ruiz-Lara et al. 2018). In addition to this, if UDGs have truly low concentrations, one would expect a late assembly time (Wechsler & Tinker 2018),

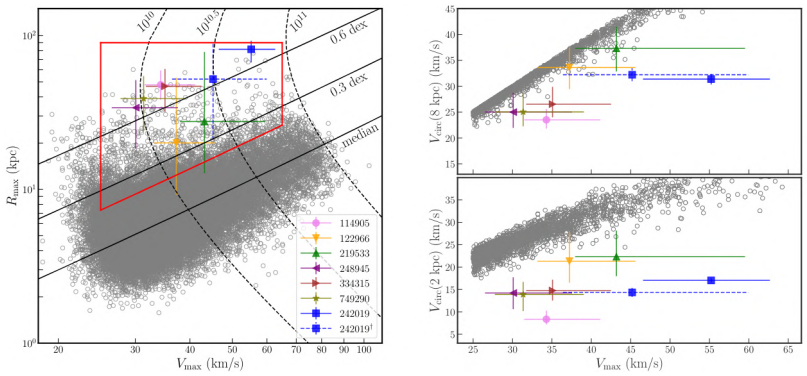

Figure 8.2: Comparison between the dark matter haloes of gas-rich UDGs and haloes in the IllustrisTNG-50 simulation. *Left:* Relation between the maximum circular speed of the dark matter haloes (a proxy for M_{200}) and the radius at which this velocity is reached (a proxy for c_{200}). The grey circles represent simulated dark matter haloes, while the coloured symbols show the best-fitting haloes of gas-rich UDGs. The red box encloses the low-concentration haloes shown in the right panel. *Right:* Circular speed at 8 and 2 kpc. The simulated haloes are too dense with respect to the real UDGs, especially in the innermost 2 kpc. Figure from Kong et al. (2022).

which could be tested with the star formation histories. Studying the kinematics of their stellar discs is also a crucial ingredient to understand UDGs, as only with stellar kinematics we can directly measure j_* and its link with the large size distributions. Hydrodynamical simulations are also starting to make predictions on the stellar kinematics of UDGs (Cardona-Barrero et al. 2020), thus setting observational constraints is timely. Unfortunately, due to their low surface brightness obtaining extended stellar kinematics with high signal–to–noise ratios is extremely time-consuming even with efficient instruments like the Multi-Unit Spectroscopic Explorer (MUSE) at the Very Large Telescope (VLT), and we may need to wait for larger telescopes like the Extremely Large Telescope (ELT) or the currently-called James Webb Space Telescope (JWST) to investigate in detail the resolved stellar kinematics of gas-rich UDGs.

8.2.2 Angular momentum

To further understand the behavior of the $j-M$ laws it is desirable to improve our measurements of the specific angular momentum (j) and to study its evolution with redshift. This will likely help at understanding the origin of the tight $j - M - f_{\rm gas}$ correlations we observe in Chapters 5 and 6 in nearby galaxies, but also to gain insight on how the angular momentum is linked to other scaling relations such as the Tully-Fisher and the mass-size relations, and to phenomena like gas accretion, assembly histories, and mergers.

Regarding the improvement of the measurements, it is particularly important to analyse the Fall relation using directly stellar kinematics (e.g. Cortese et al.

2016; Rizzo et al. 2018; Falcón-Barroso et al. 2019). Usually, when computing j_*, it is assumed that the rotation velocity of the stars is the same as the rotation of the gas, while this is not necessarily the case. One option is to apply a stellar asymmetric drift correction to account for this (e.g. Posti et al. 2018b; Chapter 5). As shown in Fig. 5.11 in Chapter 5, the correction is expected to be significant for dwarf galaxies, and it is thus critical to apply it accurately. However, asymmetric drift corrections are estimated using theoretical and at best semi-empirical prescriptions which are not fully tested. The only way to overcome this is by measuring extended gas and stellar rotation curves of dwarf and massive galaxies, as this would allow to calibrate the correction. Obtaining a sample with high quality H I and stellar kinematics is not completely straightforward. Currently, stellar kinematics are usually available only within one effective radius (e.g. Sánchez et al. 2012; Cortese et al. 2016), and therefore deeper data are needed. For this, exploiting instruments such as MUSE (in the Southern hemisphere) is key, but might be problematic as galaxies with high quality H I data that are observable in the South are usually very nearby (e.g. Hunter et al. 2012), with sizes much larger than the field of view of MUSE. The situation will improve with dedicated programmes starting to collect resolved stellar and H I data (e.g. Lopez-Sanchez 2019) but especially with the advent of large-volume H I surveys (in both hemispheres) such as those that have been carried out with the APERture Tile In Focus (Apertif) instrument at WSRT (Oosterloo et al. 2010; Adams & van Leeuwen 2019), and observations with the SKA and its pathfinders like the Australian Square Kilometre Array Pathfinder (ASKAP, Johnston et al. 2008) and MeerKAT. These promising H I data sets will be nicely complemented with powerful IFUs as those planned for the ELT in the South (Ramsay et al. 2021), and with current instruments in the North such as the Multi-Espectrógrafo en GTC de Alta Resolución para Astronomía (MEGARA, Gil de Paz et al. 2012) at the Gran Telescopio Canarias and the WHT Enhanced Area Velocity Explorer (WEAVE, Dalton et al. 2012) at the William Herschel Telescope (first-light expected in 2022), both at the Roque de los Muchachos Observatory.

Closely related to the above, it would also be interesting to study the $j - M$ relations in galaxies of very different gas fractions. For instance, we have shown in Chapter 6 that our best-fitting $j - M - f_{\rm gas}$ planes expect a break in the observed 2D relations at low and high masses once galaxies of all different gas fractions at fixed mass are studied. This would provide stringent tests to models and simulations that should aim to reproduce the observed correlations.

Finally, we would like to highlight that it would be important to extend our gas and baryonic $j - M$ relations to higher redshift. This would complement existing studies of the Fall relation at $z = 1 - 2$ (e.g. Marasco et al. 2019; Sweet et al. 2019; Bouché et al. 2021) and help to better understand the interplay between angular momentum and different physical processes. For example, there is no full consensus on whether or not the Fall relation evolves with redshift, nor has the relation with gas fraction ever been studied. There are inherent complications on studying the gas and baryonic relations as neutral atomic gas

can currently be observed in emission for samples of galaxies only at $z \lesssim 0.2$ (e.g. Gogate et al. 2020; Ponomareva et al. 2021), so one often relies on the ionised gas to trace the kinematics (e.g. Wisnioski et al. 2015; Di Teodoro et al. 2016) even if it has a large velocity dispersion. Exploiting IFUs (including the Near InfraRed Spectrograph NIRSpec on JWST) and the Atacama Large Millimeter/submillimeter Array (ALMA) to obtain stellar and molecular gas kinematics will be very helpful, and will give crucial input to galaxy formation models.

8.2.3 Gas scale heights and mass models

As shown in Chapter 7, the smallest and most gas-rich of the dwarfs in our studied sample were the only galaxies for which the gas disc flaring played a role when deriving the properties of their dark matter haloes. In order to fully quantify these effects, understand if they are systematic, and assess whether or not we need to consider them when deriving mass models, future works should utilise larger samples of gas-rich dwarfs, reaching down to masses as low as possible. Forthcoming H I observations as those described above will play a crucial role in this regard.

The method we have used to incorporate the gas flaring in the derivation of mass models heavily depends on the assumption of vertical hydrostatic equilibrium. Therefore, it would be desirable to quantify how well this assumption holds within different galaxies, as it has been tested in the Milky Way (e.g. Marasco et al. 2017; Bacchini et al. 2019b), and understand any deviations from it. As discussed in Chapter 7, a few galaxies in the literature have direct estimates of the flaring of their discs (e.g. Olling 1995; Yim et al. 2014), although the measurements are challenging due to different degeneracies between the gas thickness and e.g. disc inclination or warps (Swaters 1999). Still, as multi-wavelength observations and analysis tools develop, it will become feasible to test the assumption of vertical hydrostatic equilibrium in more external galaxies.

A critical work will be to observationally estimate robust concentration parameters of dark matter haloes. This will move forwards investigations on the departures from the halo concentration-mass relation predicted by N-body cosmological simulations (e.g. Bullock et al. 2001a; Dutton & Macciò 2014). Since the concentration strongly depends on the innermost regions of galaxies, combining stellar and gas kinematics will be essential. Near their centres, galaxies are often devoid of gas (atomic but sometimes also molecular, e.g. Leroy et al. 2008; Bigiel & Blitz 2012; Schinnerer et al. 2019). Even when gas is present in the central regions, it might be disturbed, making it hard to interpret the kinematics. Stars instead, dominate the inner potential and are less easily disturbed than the gas. In addition to this, stellar kinematics can typically be obtained at a spatial resolution much higher than gas interferometric observations, which is crucial to trace the central dark matter densities and thus the concentration parameters. Stellar kinematics are therefore a necessary complement to gas kinematics. The facilities described in Sec. 8.2.2 should allow us to use this combination to provide

strong observational constraints on the concentration parameters of the haloes of disc galaxies. As discussed in Chapter 7 and references therein, the outcome of mass models can be used for a wide variety of applications. For instance, they can be used in near-field cosmology to test the nature of dark matter (e.g. Bullock & Boylan-Kolchin 2017; Tulin & Yu 2018; Ren et al. 2019; Zentner et al. 2022), but also to study the effects of baryonic physics in the haloes (e.g. Blumenthal et al. 1986; Nipoti & Binney 2015; Katz et al. 2014; Lazar et al. 2020).

Overall, these are promising times for the community interested in the dark matter and angular momentum content of galaxies. The prospects discussed in this section will be studied in the upcoming years and will hopefully provide answers to questions of paramount importance as those highlighted in this chapter. However, given the plethora of data of exquisite quality that will soon be available, we will most likely end up investigating and learning the most from aspects that we are not even considering at the moment, and that is exciting.

Bibliography

Abadi M. G., Moore B., Bower R. G., 1999, MNRAS, 308, 947

Adams E. A. K., Oosterloo T. A., 2018, A&A, 612, A26

Adams E. A. K., van Leeuwen J., 2019, Nature Astronomy, 3, 188

Agnes P., et al., 2018, Phys. Rev. Lett., 121, 081307

Alam S., et al., 2015, ApJS, 219, 12

Amorisco N. C., 2018, MNRAS, 475, L116

Amorisco N. C., Loeb A., 2016, MNRAS, 459, L51

Anbajagane D., Evrard A. E., Farahi A., 2022, MNRAS, 509, 3441

Avila-Reese V., Zavala J., Firmani C., Hernández-Toledo H. M., 2008, AJ, 136, 1340

Bacchini C., Fraternali F., Iorio G., Pezzulli G., 2019a, A&A, 622, A64

Bacchini C., Fraternali F., Pezzulli G., Marasco A., Iorio G., Nipoti C., 2019b, A&A, 632, A127

Bacchini C., Fraternali F., Iorio G., Pezzulli G., Marasco A., Nipoti C., 2020a, A&A, 641, A70

Bacchini C., Fraternali F., Pezzulli G., Marasco A., 2020b, A&A, 644, A125

Bajaja E., Wielebinski R., Reuter H. P., Harnett J. I., Hummel E., 1995, , 114, 147

Banerjee A., Jog C. J., Brinks E., Bagetakos I., 2011, MNRAS, 415, 687

Bar N., Danieli S., Blum K., 2022, arXiv e-prints, p. arXiv:2202.10179

Barat D., D'Eugenio F., Colless M., Sweet S. M., Groves B., Cortese L., 2020, MNRAS,

Barbosa C. E., et al., 2020, ApJS, 247, 46

Battaglia G., Fraternali F., Oosterloo T., Sancisi R., 2006, A&A, 447, 49

Beasley M. A., Trujillo I., 2016, ApJ, 830, 23

Bechtol K., et al., 2022, arXiv e-prints, p. arXiv:2203.07354

Begeman K. G., 1987, PhD thesis, Kapteyn Astronomical Institute, University of Groningen

Begum A., Chengalur J. N., 2004, A&A, 424, 509

Bellstedt S., et al., 2016, MNRAS, 460, 2862

Beltz-Mohrmann G. D., Berlind A. A., 2021, ApJ, 921, 112

Benítez-Llambay A., Frenk C. S., Ludlow A. D., Navarro J. F., 2019, MNRAS, 488, 2387

Bennet P., Sand D. J., Zaritsky D., Crnojević D., Spekkens K., Karunakaran A., 2018, ApJ, 866, L11

Bernstein-Cooper E. Z., et al., 2014, AJ, 148, 35

Bershady M. A., Verheijen M. A. W., Westfall K. B., Andersen D. R., Swaters R. A., Martinsson T., 2010, ApJ, 716, 234

Bertone G., Hooper D., 2018, Reviews of Modern Physics, 90, 045002

Bertone G., Tait T. M. P., 2018, Nature, 562, 51

Bertone G., Hooper D., Silk J., 2005, , 405, 279

Bigiel F., Blitz L., 2012, ApJ, 756, 183

Bigiel F., Leroy A., Walter F., Blitz L., Brinks E., de Blok W. J. G., Madore B., 2010, AJ, 140, 1194

Binney J., 1977, ApJ, 215, 483

Binney J. J., Evans N. W., 2001, MNRAS, 327, L27

Binney J., Tremaine S., 2008, Galactic Dynamics: Second Edition

Binney J., Gerhard O., Silk J., 2001, MNRAS, 321, 471

Blumenthal G. R., Faber S. M., Primack J. R., Rees M. J., 1984, Nature, 311, 517

Blumenthal G. R., Faber S. M., Flores R., Primack J. R., 1986, ApJ, 301, 27

Bolatto A. D., Wolfire M., Leroy A. K., 2013, ARA&A, 51, 207

Boomsma R., 2007, PhD thesis, Kapteyn Astronomical Institute, University of Groningen

Booth R. S., de Blok W. J. G., Jonas J. L., Fanaroff B., 2009, arXiv e-prints, p. arXiv:0910.2935

Bosma A., 1978, PhD thesis, Kapteyn Astronomical Institute, University of Groningen

Bottema R., 1993, A&A, 275, 16

Bouché N., Carfantan H., Schroetter I., Michel-Dansac L., Contini T., 2015, AJ, 150, 92

Bouché N. F., et al., 2021, A&A, 654, A49

Bouquin A. Y. K., et al., 2018, ApJS, 234, 18

Braine J., Duc P. A., Lisenfeld U., Charmandaris V., Vallejo O., Leon S., Brinks E., 2001, A&A, 378, 51

Broeils A. H., 1992, PhD thesis, Kapteyn Astronomical Institute, University of Groningen

Broeils A. H., Rhee M. H., 1997, A&A, 324, 877

Brook C. B., Stinson G., Gibson B. K., Roškar R., Wadsley J., Quinn T., 2012a, MNRAS, 419, 771

Brook C. B., Stinson G., Gibson B. K., Wadsley J., Quinn T., 2012b, MNRAS, 424, 1275

Brook C. B., Santos-Santos I., Stinson G., 2016, MNRAS, 459, 638

Brown T., et al., 2021, ApJS, 257, 21

Bryan S. E., Kay S. T., Duffy A. R., Schaye J., Dalla Vecchia C., Booth C. M., 2013, MNRAS, 429, 3316

Bullock J. S., Boylan-Kolchin M., 2017, ARA&A, 55, 343

Bullock J. S., Kolatt T. S., Sigad Y., Somerville R. S., Kravtsov A. V., Klypin A. A., Primack J. R., Dekel A., 2001a, MNRAS, 321, 559

Bullock J. S., Dekel A., Kolatt T. S., Kravtsov A. V., Klypin A. A., Porciani C., Primack J. R., 2001b, ApJ, 555, 240

Burkert A., Forbes D. A., 2020, AJ, 159, 56

Burstein D., Bender R., Faber S., Nolthenius R., 1997, AJ, 114, 1365

Butler K. M., Obreschkow D., Oh S.-H., 2017, ApJ, 834, L4

Calette A. R., Avila-Reese V., Rodríguez-Puebla A., Hernández-Toledo H., Papastergis E., 2018, , 54, 443

Calette A. R., Rodríguez-Puebla A., Avila-Reese V., Lagos C. d. P., 2021, MNRAS, 506, 1507

Calvi R., Poggianti B. M., Fasano G., Vulcani B., 2012, MNRAS, 419, L14

Cappellari M., et al., 2013a, MNRAS, 432, 1709

Cappellari M., et al., 2013b, MNRAS, 432, 1862

Cardona-Barrero S., Di Cintio A., Brook C. B. A., Ruiz-Lara T., Beasley M. A., Falcón-Barroso J., Macciò A. V., 2020, MNRAS, 497, 4282

Carleton T., Errani R., Cooper M., Kaplinghat M., Peñarrubia J., Guo Y., 2019, MNRAS, 485, 382

Casertano S., 1983, MNRAS, 203, 735

Catinella B., et al., 2018, MNRAS, 476, 875

Cebrián M., Trujillo I., 2014, MNRAS, 444, 682

Chamba N., Trujillo I., Knapen J. H., 2020, A&A, 633, L3

Chan T. K., Kereš D., Wetzel A., Hopkins P. F., Faucher-Giguère C. A., El-Badry K., Garrison-Kimmel S., Boylan-Kolchin M., 2018, MNRAS, 478, 906

Choi E., Ostriker J. P., Naab T., Oser L., Moster B. P., 2015, MNRAS, 449, 4105

Chowdhury A., Chengalur J. N., 2017, MNRAS, 467, 3856

Cimatti A., Fraternali F., Nipoti C., 2019, Introduction to Galaxy Formation and Evolution: From Primordial Gas to Present-Day Galaxies. Cambridge University Press

Conselice C. J., 2018, Research Notes of the American Astronomical Society, 2, 43

Cortese L., Catinella B., Boissier S., Boselli A., Heinis S., 2011, MNRAS, 415, 1797

Cortese L., et al., 2016, MNRAS, 463, 170

Courteau S., Dutton A. A., van den Bosch F. C., MacArthur L. A., Dekel A., McIntosh D. H., Dale D. A., 2007, ApJ, 671, 203

Cuddeford P., 1993, MNRAS, 262, 1076

D'Onghia E., Burkert A., Murante G., Khochfar S., 2006, MNRAS, 372, 1525

Dalcanton J. J., 2007, ApJ, 658, 941

Dalcanton J. J., Spergel D. N., Summers F. J., 1997, ApJ, 482, 659

Dalcanton J. J., et al., 2009, ApJS, 183, 67

Dalton G., et al., 2012, in McLean I. S., Ramsay S. K., Takami H., eds, Society of Photo-Optical Instrumentation Engineers (SPIE) Conference Series Vol. 8446, Ground-based and Airborne Instrumentation for Astronomy IV. p. 84460P, doi:10.1117/12.925950

Danieli S., van Dokkum P., Conroy C., Abraham R., Romanowsky A. J., 2019, ApJ, 874, L12

Danieli S., et al., 2022, ApJ, 927, L28

Davis M., Summers F. J., Schlegel D., 1992, Nature, 359, 393

de Blok W. J. G., 1997, PhD thesis, Kapteyn Astronomical Institute, Groningen, The Netherlands

de Blok W. J. G., Walter F., 2000, ApJ, 537, L95

de Blok W. J. G., Walter F., Brinks E., Trachternach C., Oh S. H., Kennicutt R. C. J., 2008, AJ, 136, 2648

den Heijer M., et al., 2015, A&A, 581, A98

Desmond H., Wechsler R. H., 2015, MNRAS, 454, 322

Dewdney P. E., Hall P. J., Schilizzi R. T., Lazio T. J. L. W., 2009, IEEE Proceedings, 97, 1482

Di Cintio A., Brook C. B., Macciò A. V., Stinson G. S., Knebe A., Dutton A. A., Wadsley J., 2014, MNRAS, 437, 415

Di Cintio A., Brook C. B., Dutton A. A., Macciò A. V., Obreja A., Dekel A., 2017, MNRAS, 466, L1

Di Cintio A., Brook C. B., Macciò A. V., Dutton A. A., Cardona-Barrero S., 2019, MNRAS, 486, 2535

Di Teodoro E. M., 2015, PhD thesis, University of Bologna

Di Teodoro E. M., Fraternali F., 2014, A&A, 567, A68

Di Teodoro E. M., Fraternali F., 2015, MNRAS, 451, 3021

Di Teodoro E. M., Peek J. E. G., 2021, ApJ, 923, 220

Di Teodoro E. M., Fraternali F., Miller S. H., 2016, A&A, 594, A77

Di Teodoro E. M., et al., 2019, MNRAS, 483, 392

Di Teodoro E. M., Posti L., Ogle P. M., Fall S. M., Jarrett T., 2021, MNRAS, 507, 5820

Dickey J. M., Kazes I., 1992, ApJ, 393, 530

Doppel J. E., Sales L. V., Navarro J. F., Abadi M. G., Peng E. W., Toloba E., Ramos-Almendares F., 2021, MNRAS, 502, 1661

Doroshkevich A. G., 1970, Astrophysics, 6, 320

Dressler A., 1980, ApJ, 236, 351

Dressler A., 1986, ApJ, 301, 35

Du W., Cheng C., Zheng Z., Wu H., 2020, AJ, 159, 138

Duc P. A., Mirabel I. F., 1998, A&A, 333, 813

Duc P.-A., Paudel S., McDermid R. M., Cuillandre J.-C., Serra P., Bournaud F., Cappellari M., Emsellem E., 2014, MNRAS, 440, 1458

Duffy A. R., Schaye J., Kay S. T., Dalla Vecchia C., Battye R. A., Booth C. M., 2010, MNRAS, 405, 2161

Dutton A. A., 2012, MNRAS, 424, 3123

Dutton A. A., Macciò A. V., 2014, MNRAS, 441, 3359

Dutton A. A., van den Bosch F. C., 2012, MNRAS, 421, 608

El-Badry K., et al., 2018, MNRAS, 473, 1930

Elmegreen B. G., Hunter D. A., 2015, ApJ, 805, 145

Elson E. C., 2017, MNRAS, 472, 4551

Emerick A., Bryan G. L., Mac Low M.-M., 2018, ApJ, 865, L22

Emsellem E., et al., 2019, A&A, 625, A76

Faber S. M., Jackson R. E., 1976, ApJ, 204, 668

Fabian A. C., 2012, ARA&A, 50, 455

Falcón-Barroso J., et al., 2011, MNRAS, 417, 1787

Falcón-Barroso J., et al., 2019, A&A, 632, A59

Fall S. M., 1983, in Athanassoula E., ed., IAU Symposium Vol. 100, Internal Kinematics and Dynamics of Galaxies. pp 391–398

Fall S. M., Efstathiou G., 1980, MNRAS, 193, 189

Fall S. M., Romanowsky A. J., 2013, ApJ, 769, L26

Fall S. M., Romanowsky A. J., 2018, ApJ, 868, 133

Famaey B., McGaugh S. S., 2012, Living Reviews in Relativity, 15, 10

Fattahi A., et al., 2016, MNRAS, 457, 844

Fernández Lorenzo M., Sulentic J., Verdes-Montenegro L., Argudo-Fernández M., 2013, MNRAS, 434, 325

Field G. B., 1965, ApJ, 142, 531

Fierlinger K. M., Burkert A., Ntormousi E., Fierlinger P., Schartmann M., Ballone A., Krause M. G. H., Diehl R., 2016, MNRAS, 456, 710

Ford A. B., Davé R., Oppenheimer B. D., Katz N., Kollmeier J. A., Thompson R., Weinberg D. H., 2014, MNRAS, 444, 1260

Foreman-Mackey D., Hogg D. W., Lang D., Goodman J., 2013, , 125, 306

Frank B. S., de Blok W. J. G., Walter F., Leroy A., Carignan C., 2016, AJ, 151, 94

Franx M., de Zeeuw T., 1992, ApJ, 392, L47

Fraternali F., van Moorsel G., Sancisi R., Oosterloo T., 2002, AJ, 123, 3124

Fraternali F., Sancisi R., Kamphuis P., 2011, A&A, 531, A64

Fraternali F., Karim A., Magnelli B., Gómez-Guijarro C., Jiménez-Andrade E. F., Posses A. C., 2021, A&A, 647, A194

Freeman K. C., 1970, ApJ, 160, 811

Frenk C. S., White S. D. M., Davis M., Efstathiou G., 1988, ApJ, 327, 507

Gallimore J. F., et al., 2016, ApJ, 829, L7

Gault L., et al., 2021, ApJ, 909, 19

Geha M., Blanton M. R., Masjedi M., West A. A., 2006, ApJ, 653, 240

Genel S., Fall S. M., Hernquist L., Vogelsberger M., Snyder G. F., Rodriguez-Gomez V., Sijacki D., Springel V., 2015, ApJ, 804, L40

Gentile G., 2008, ApJ, 684, 1018

Gil de Paz A., et al., 2012, in McLean I. S., Ramsay S. K., Takami H., eds, Society of Photo-Optical Instrumentation Engineers (SPIE) Conference Series Vol. 8446, Ground-based and Airborne Instrumentation for Astronomy IV. p. 84464Q, doi:10.1117/12.925739

Giovanelli R., et al., 2005, AJ, 130, 2598

Gnedin O. Y., Kravtsov A. V., Klypin A. A., Nagai D., 2004, ApJ, 616, 16

Gogate A. R., Verheijen M. A. W., Deshev B. Z., van Gorkom J. H., Montero-Castaño M., van der Hulst J. M., Jaffé Y. L., Poggianti B. M., 2020, MNRAS, 496, 3531

Goldsmith D. W., Habing H. J., Field G. B., 1969, ApJ, 158, 173

Gooch R., 1996, in Jacoby G. H., Barnes J., eds, Astronomical Society of the Pacific Conference Series Vol. 101, Astronomical Data Analysis Software and Systems V. p. 80

Governato F., Willman B., Mayer L., Brooks A., Stinson G., Valenzuela O., Wadsley J., Quinn T., 2007, MNRAS, 374, 1479

Greco J. P., et al., 2018, ApJ, 857, 104

Guo Q., et al., 2020, Nature Astronomy, 4, 246

Harbeck D. R., et al., 2014, in Ramsay S. K., McLean I. S., Takami H., eds, Society of Photo-Optical Instrumentation Engineers (SPIE) Conference Series Vol. 9147, Ground-based and Airborne Instrumentation for Astronomy V. p. 91470P, doi:10.1117/12.2056651

Haslbauer M., Dabringhausen J., Kroupa P., Javanmardi B., Banik I., 2019a, A&A, 626, A47

Haslbauer M., Dabringhausen J., Kroupa P., Javanmardi B., Banik I., 2019b, A&A, 626, A47

Haurberg N. C., Salzer J. J., Cannon J. M., Marshall M. V., 2015, ApJ, 800, 121

Haynes M. P., et al., 2011, AJ, 142, 170

Haynes M. P., et al., 2018, ApJ, 861, 49

He M., Wu H., Du W., Wicker J., Zhao P., Lei F., Liu J., 2019, ApJ, 880, 30

Heavens A., Peacock J., 1988, MNRAS, 232, 339

Heiles C., Troland T. H., 2003, ApJ, 586, 1067

Helfer T. T., Thornley M. D., Regan M. W., Wong T., Sheth K., Vogel S. N., Blitz L., Bock D. C. J., 2003, ApJS, 145, 259

Hermosa Muñoz L., et al., 2020, A&A, 634, A10

Hernandez X., Park C., Cervantes-Sodi B., Choi Y.-Y., 2007, MNRAS, 375, 163

Herrmann K. A., Hunter D. A., Zhang H.-X., Elmegreen B. G., 2016, AJ, 152, 177

Hidalgo-Gámez A. M., 2004, , 40, 37

Holwerda B. W., Pirzkal N., Cox T. J., de Blok W. J. G., Weniger J., Bouchard A., Blyth S. L., van der Heyden K. J., 2011, MNRAS, 416, 2426

Hopkins P. F., et al., 2018, MNRAS, 480, 800

Huang S., Haynes M. P., Giovanelli R., Brinchmann J., 2012, ApJ, 756, 113

Hubble E. P., 1926, ApJ, 64, 321

Hunt L. K., et al., 2015, A&A, 583, A114

Hunter D. A., Elmegreen B. G., Baker A. L., 1998, ApJ, 493, 595

Hunter D. A., Hunsberger S. D., Roye E. W., 2000, ApJ, 542, 137

Hunter D. A., Rubin V. C., Swaters R. A., Sparke L. S., Levine S. E., 2005, ApJ, 634, 281

Hunter D. A., et al., 2012, AJ, 144, 134

Hunter D. A., Elmegreen B. G., Berger C. L., 2019, AJ, 157, 241

Hunter D. A., et al., 2021, AJ, 161, 71

Impey C., Bothun G., Malin D., 1988, ApJ, 330, 634

Iorio G., 2018, PhD thesis, alma, `http://amsdottorato.unibo.it/8449/`

Iorio G., Fraternali F., Nipoti C., Di Teodoro E., Read J. I., Battaglia G., 2017, MNRAS, 466, 4159

Irodotou D., Thomas P. A., Henriques B. M., Sargent M. T., Hislop J. M., 2019, MNRAS, 489, 3609

Jackson R. A., et al., 2021, MNRAS, 502, 1785

Jadhav Y V., Banerjee A., 2019, MNRAS, 488, 547

Janowiecki S., Jones M. G., Leisman L., Webb A., 2019, MNRAS, 490, 566

Jiang F., Dekel A., Freundlich J., Romanowsky A. J., Dutton A. A., Macciò A. V., Di Cintio A., 2019, MNRAS, 487, 5272

Johnson M. C., Hunter D., Wood S., Oh S.-H., Zhang H.-X., Herrmann K. A., Levine S. E., 2015, AJ, 149, 196

Johnston S., et al., 2008, Experimental Astronomy, 22, 151

Jones M. G., Papastergis E., Pandya V., Leisman L., Romanowsky A. J., Yung L. Y. A., Somerville R. S., Adams E. A. K., 2018, A&A, 614, A21

Józsa G. I. G., Kenn F., Klein U., Oosterloo T. A., 2007, A&A, 468, 731

Kado-Fong E., et al., 2021, ApJ, 920, 72

Kalberla P. M. W., Dedes L., 2008, A&A, 487, 951

Kamphuis P., Józsa G. I. G., Oh S. . H., Spekkens K., Urbancic N., Serra P., Koribalski B. S., Dettmar R. J., 2015, MNRAS, 452, 3139

Kaplinghat M., Ren T., Yu H.-B., 2020, , 2020, 027

Karachentsev I. D., et al., 2007, AJ, 133, 504

Karunakaran A., Spekkens K., Zaritsky D., Donnerstein R. L., Kadowaki J., Dey A., 2020, ApJ, 902, 39

Katz H., McGaugh S. S., Sellwood J. A., de Blok W. J. G., 2014, MNRAS, 439, 1897

Katz H., Lelli F., McGaugh S. S., Di Cintio A., Brook C. B., Schombert J. M., 2017, MNRAS, 466, 1648

Kaviraj S., Darg D., Lintott C., Schawinski K., Silk J., 2012, MNRAS, 419, 70

Kennicutt Robert C. J., 1989, ApJ, 344, 685

Kennicutt R. C., Evans N. J., 2012, ARA&A, 50, 531

Kent S. M., 1987, AJ, 93, 816

Kereš D., Katz N., Fardal M., Davé R., Weinberg D. H., 2009, MNRAS, 395, 160

Kerr F. J., Hindman J. V., Carpenter M. S., 1957, Nature, 180, 677

Kirby E. M., Jerjen H., Ryder S. D., Driver S. P., 2008, AJ, 136, 1866

Kirby E. M., Koribalski B., Jerjen H., López-Sánchez Á., 2012, MNRAS, 420, 2924

Komatsu E., et al., 2011, ApJS, 192, 18

Kong D., Kaplinghat M., Yu H.-B., Fraternali F., Mancera Piña P. E., 2022, arXiv e-prints, p. arXiv:2204.05981

Koribalski B. S., et al., 2018, MNRAS, 478, 1611

Kormendy J., Kennicutt Robert C. J., 2004, ARA&A, 42, 603

Kourkchi E., Tully R. B., Courtois H. M., Dupuy A., Guinet D., 2022, MNRAS,

Kovács O. E., Bogdán Á., Canning R. E. A., 2019, ApJ, 879, L12

Krajnović D., et al., 2013, MNRAS, 432, 1768

Krumholz M. R., Leroy A. K., McKee C. F., 2011, ApJ, 731, 25

Kulier A., Galaz G., Padilla N. D., Trayford J. W., 2020, MNRAS, 496, 3996

Kurapati S., Chengalur J. N., Pustilnik S., Kamphuis P., 2018, MNRAS, 479, 228

Kurapati S., Chengalur J. N., Verheijen M. A. W., 2021, MNRAS, 507, 565

Kuzio de Naray R., McGaugh S. S., de Blok W. J. G., 2008, ApJ, 676, 920

Lagos C. d. P., Theuns T., Stevens A. R. H., Cortese L., Padilla N. D., Davis T. A., Contreras S., Croton D., 2017, MNRAS, 464, 3850

Lagos C. d. P., et al., 2018, MNRAS, 473, 4956

Lange R., et al., 2015, MNRAS, 447, 2603

Laporte C. F. P., Agnello A., Navarro J. F., 2019, MNRAS, 484, 245

Larson R. B., 1981, MNRAS, 194, 809

Lazar A., et al., 2020, MNRAS, 497, 2393

Leaman R., et al., 2012, ApJ, 750, 33

Lee J. H., Kang J., Lee M. G., Jang I. S., 2020, ApJ, 894, 75

Leisman L., et al., 2017, ApJ, 842, 133

Lelli F., Fraternali F., Sancisi R., 2010, A&A, 516, A11

Lelli F., Verheijen M., Fraternali F., 2014a, MNRAS, 445, 1694

Lelli F., Fraternali F., Verheijen M., 2014b, A&A, 563, A27

Lelli F., et al., 2015, A&A, 584, A113

Lelli F., McGaugh S. S., Schombert J. M., 2016a, AJ, 152, 157

Lelli F., McGaugh S. S., Schombert J. M., 2016b, ApJ, 816, L14

Lelli F., McGaugh S. S., Schombert J. M., Desmond H., Katz H., 2019, MNRAS, 484, 3267

Leroy A. K., Walter F., Brinks E., Bigiel F., de Blok W. J. G., Madore B., Thornley M. D., 2008, AJ, 136, 2782

Leroy A. K., et al., 2009, AJ, 137, 4670

Leroy A. K., et al., 2013, AJ, 146, 19

Leroy A. K., et al., 2021a, ApJS, 255, 19

Leroy A. K., et al., 2021b, ApJS, 257, 43

Li P., Lelli F., McGaugh S., Schombert J., 2020, ApJS, 247, 31

Liao S., et al., 2019, MNRAS, 490, 5182

Lilly S. J., Carollo C. M., Pipino A., Renzini A., Peng Y., 2013, ApJ, 772, 119

Lopez-Sanchez A., 2019, in Linking Galaxies from the Epoch of Initial Star Formation to Today. p. 60, doi:10.5281/zenodo.2635319

Lovell M. R., et al., 2018, MNRAS, 481, 1950

Ludlow A. D., Navarro J. F., Angulo R. E., Boylan-Kolchin M., Springel V., Frenk C., White S. D. M., 2014, MNRAS, 441, 378

Lutz K. A., et al., 2018, MNRAS, 476, 3744

Mac Low M.-M., Klessen R. S., 2004, Reviews of Modern Physics, 76, 125

Macciò A. V., Dutton A. A., van den Bosch F. C., Moore B., Potter D., Stadel J., 2007, MNRAS, 378, 55

Macciò A. V., Dutton A. A., van den Bosch F. C., 2008, MNRAS, 391, 1940

Makarov D., Prugniel P., Terekhova N., Courtois H., Vauglin I., 2014, A&A, 570, A13

Mancera Piña P. E., Peletier R. F., Aguerri J. A. L., Venhola A., Trager S., Choque Challapa N., 2018, MNRAS, 481, 4381

Mancera Piña P. E., Aguerri J. A. L., Peletier R. F., Venhola A., Trager S., Choque Challapa N., 2019a, MNRAS, 485, 1036

Mancera Piña P. E., et al., 2019b, ApJ, 883, L33

Mancera Piña P. E., et al., 2020, MNRAS, 495, 3636

Mancera Piña P. E., Posti L., Fraternali F., Adams E. A. K., Oosterloo T., 2021a, A&A, 647, A76

Mancera Piña P. E., Posti L., Pezzulli G., Fraternali F., Fall S. M., Oosterloo T., Adams E. A. K., 2021b, A&A, 651, L15

Marasco A., Fraternali F., 2011, A&A, 525, A134

Marasco A., Fraternali F., van der Hulst J. M., Oosterloo T., 2017, A&A, 607, A106

Marasco A., Oman K. A., Navarro J. F., Frenk C. S., Oosterloo T., 2018, MNRAS, 476, 2168

Marasco A., Fraternali F., Posti L., Ijtsma M., Di Teodoro E. M., Oosterloo T., 2019, A&A, 621, L6

Marasco A., Posti L., Oman K., Famaey B., Cresci G., Fraternali F., 2020, A&A, 640, A70

Marasco A., Cresci G., Posti L., Fraternali F., Mannucci F., Marconi A., Belfiore F., Fall S. M., 2021, MNRAS, 507, 4274

Marconi A., Hunt L. K., 2003, ApJ, 589, L21

Marshall M. A., Mutch S. J., Qin Y., Poole G. B., Wyithe J. S. B., 2019, MNRAS, 488, 1941

Martín-Navarro I., et al., 2019, MNRAS, 484, 3425

Martinsson T. P. K., Verheijen M. A. W., Westfall K. B., Bershady M. A., Schechtman-Rook A., Andersen D. R., Swaters R. A., 2013, A&A, 557, A130

Martinsson T. P. K., Verheijen M. A. W., Bershady M. A., Westfall K. B., Andersen D. R., Swaters R. A., 2016, A&A, 585, A99

Masters K. L., 2005, PhD thesis, Cornell University

McGaugh S. S., 2005, ApJ, 632, 859

McGaugh S. S., 2012, AJ, 143, 40

McGaugh S. S., Schombert J. M., 2014, AJ, 148, 77

McGaugh S. S., de Blok W. J. G., 1998, ApJ, 499, 66

McGaugh S. S., Schombert J. M., Bothun G. D., de Blok W. J. G., 2000, ApJ, 533, L99

McGaugh S. S., Rubin V. C., de Blok W. J. G., 2001, AJ, 122, 2381

McGaugh S. S., Barker M. K., de Blok W. J. G., 2003, ApJ, 584, 566

McGaugh S. S., Schombert J. M., de Blok W. J. G., Zagursky M. J., 2010, ApJ, 708, L14

McNichols A. T., et al., 2016, ApJ, 832, 89

McQuinn K. B. W., van Zee L., Skillman E. D., 2019, ApJ, 886, 74

Meidt S. E., et al., 2014, ApJ, 788, 144

Merrifield M. R., 1992, AJ, 103, 1552

Mihos J. C., McGaugh S. S., de Blok W. J. G., 1997, ApJ, 477, L79

Mihos J. C., et al., 2015, ApJ, 809, L21

Milgrom M., 1983, ApJ, 270, 365

Mo H. J., Mao S., White S. D. M., 1998, MNRAS, 295, 319

Mo H., van den Bosch F. C., White S., 2010, Galaxy Formation and Evolution

Mogotsi K. M., de Blok W. J. G., Caldú-Primo A., Walter F., Ianjamasimanana R., Leroy A. K., 2016, AJ, 151, 15

Monelli M., Trujillo I., 2019, ApJ, 880, L11

Montes M., Infante-Sainz R., Madrigal-Aguado A., Román J., Monelli M., Borlaff A. S., Trujillo I., 2020, ApJ, 904, 114

Moore B., Lake G., Katz N., 1998, ApJ, 495, 139

Moster B. P., Naab T., White S. D. M., 2013, MNRAS, 428, 3121

Muñoz-Mateos J. C., et al., 2009, ApJ, 703, 1569

Müller O., et al., 2019, A&A, 624, L6

Müller O., et al., 2021, ApJ, 923, 9

Murugeshan C., Kilborn V., Obreschkow D., Glazebrook K., Lutz K., Džudžar R., Dénes H., 2019, MNRAS, 483, 2398

Murugeshan C., Kilborn V., Jarrett T., Wong O. I., Obreschkow D., Glazebrook K., Cluver M. E., Fluke C. J., 2020, MNRAS, 496, 2516

Nadler E. O., et al., 2021, , 126, 091101

Nakanishi H., Sofue Y., 2003, , 55, 191

Navarro J. F., Steinmetz M., 2000, ApJ, 538, 477

Navarro J. F., Eke V. R., Frenk C. S., 1996, MNRAS, 283, L72

Navarro J. F., Frenk C. S., White S. D. M., 1997, ApJ, 490, 493

Navarro J. F., et al., 2010, MNRAS, 402, 21

Nelson D., et al., 2019, MNRAS, 490, 3234

Nipoti C., Binney J., 2015, MNRAS, 446, 1820

Noordermeer E., 2006, PhD thesis, Kapteyn Astronomical Institute, University of Groningen

Noordermeer E., Merrifield M. R., Aragón-Salamanca A., 2008, MNRAS, 388, 1381

O'Brien J. C., Freeman K. C., van der Kruit P. C., 2010, A&A, 515, A62

Obreja A., Stinson G. S., Dutton A. A., Macciò A. V., Wang L., Kang X., 2016, MNRAS, 459, 467

Obreschkow D., Glazebrook K., 2014, ApJ, 784, 26

Obreschkow D., Glazebrook K., Kilborn V., Lutz K., 2016, ApJ, 824, L26

Ogle P. M., Lanz L., Appleton P. N., Helou G., Mazzarella J., 2019a, ApJS, 243, 14

Ogle P. M., Jarrett T., Lanz L., Cluver M., Alatalo K., Appleton P. N., Mazzarella J. M., 2019b, ApJ, 884, L11

Oh S.-H., et al., 2015, AJ, 149, 180

Olling R. P., 1995, AJ, 110, 591

Olling R. P., 1996, AJ, 112, 481

Oman K. A., et al., 2015, MNRAS, 452, 3650

Oman K. A., Navarro J. F., Sales L. V., Fattahi A., Frenk C. S., Sawala T., Schaller M., White S. D. M., 2016, MNRAS, 460, 3610

Oman K. A., Marasco A., Navarro J. F., Frenk C. S., Schaye J., Benítez-Llambay A., 2019, MNRAS, 482, 821

Oosterloo T., Fraternali F., Sancisi R., 2007, AJ, 134, 1019

Oosterloo T., Verheijen M., van Cappellen W., 2010, in van Leeuwen J., ed., ISKAF2010 Science Meeting. p. 43 (`arXiv:1007.5141`)

Osterbrock D. E., 1989, Astrophysics of gaseous nebulae and active galactic nuclei

Ott J., et al., 2012, AJ, 144, 123

Papastergis E., Adams E. A. K., van der Hulst J. M., 2016, A&A, 593, A39

Patra N. N., 2019, MNRAS, 484, 81

Patra N. N., 2020a, MNRAS, 495, 2867

Patra N. N., 2020b, MNRAS, 499, 2063

Pedrosa S. E., Tissera P. B., 2015, A&A, 584, A43

Peebles P. J. E., 1969, ApJ, 155, 393

Peebles P. J. E., 1971, A&A, 11, 377

Peng C. Y., Ho L. C., Impey C. D., Rix H.-W., 2010, AJ, 139, 2097

Pezzulli G., Fraternali F., Binney J., 2017, MNRAS, 467, 311

Planck Collaboration et al., 2020, A&A, 641, A6

Ponomareva A. A., Verheijen M. A. W., Bosma A., 2016, MNRAS, 463, 4052

Ponomareva A. A., Verheijen M. A. W., Peletier R. F., Bosma A., 2017, MNRAS, 469, 2387

Ponomareva A. A., Verheijen M. A. W., Papastergis E., Bosma A., Peletier R. F., 2018, MNRAS, 474, 4366

Ponomareva A. A., et al., 2021, MNRAS, 508, 1195

Pontzen A., Governato F., 2012, MNRAS, 421, 3464

Posti L., Fall S. M., 2021, A&A, 649, A119

Posti L., Pezzulli G., Fraternali F., Di Teodoro E. M., 2018a, MNRAS, 475, 232

Posti L., Fraternali F., Di Teodoro E. M., Pezzulli G., 2018b, A&A, 612, L6

Posti L., Fraternali F., Marasco A., 2019, A&A, 626, A56

Posti L., Famaey B., Pezzulli G., Fraternali F., Ibata R., Marasco A., 2020, A&A, 644, A76

Press W. H., Schechter P., 1974, ApJ, 187, 425

Prole D. J., et al., 2019a, MNRAS, 484, 4865

Prole D. J., van der Burg R. F. J., Hilker M., Davies J. I., 2019b, MNRAS, 488, 2143

Querejeta M., et al., 2015, ApJS, 219, 5

Rahman N., et al., 2012, ApJ, 745, 183

Ramsay S., et al., 2021, The Messenger, 182, 3

Read J. I., Gilmore G., 2005, MNRAS, 356, 107

Read J. I., Agertz O., Collins M. L. M., 2016a, MNRAS, 459, 2573

Read J. I., Iorio G., Agertz O., Fraternali F., 2016b, MNRAS, 462, 3628

Read J. I., Iorio G., Agertz O., Fraternali F., 2017, MNRAS, 467, 2019

Ren T., Kwa A., Kaplinghat M., Yu H.-B., 2019, Physical Review X, 9, 031020

Rhee M. H., 1996, PhD thesis, Kapteyn Astronomical Institute, University of Groningen

Rickard L. J., Palmer P., Morris M., Zuckerman B., Turner B. E., 1975, ApJ, 199, L75

Rizzo F., Fraternali F., Iorio G., 2018, MNRAS, 476, 2137

Roberts M. S., Rots A. H., 1973, A&A, 26, 483

Robotham A. S. G., Obreschkow D., 2015, , 32, e033

Rodríguez-Puebla A., Avila-Reese V., Firmani C., Colín P., 2011, , 47, 235

Rodríguez-Puebla A., Avila-Reese V., Yang X., Foucaud S., Drory N., Jing Y. P., 2015, ApJ, 799, 130

Rodríguez-Puebla A., Behroozi P., Primack J., Klypin A., Lee C., Hellinger D., 2016, MNRAS, 462, 893

Rogstad D. H., Lockhart I. A., Wright M. C. H., 1974, ApJ, 193, 309

Rohatgi A., Rehberg S., ZlatanStanojevic 2018, Ankitrohatgi/Webplotdigitizer: Version 4.1 Of Webplotdigitizer, doi:10.5281/zenodo.1137880

Román J., Trujillo I., 2017a, MNRAS, 468, 703

Román J., Trujillo I., 2017b, MNRAS, 468, 4039

Román J., Beasley M. A., Ruiz-Lara T., Valls-Gabaud D., 2019, MNRAS, 486, 823

Romano D., Calura F., D'Ercole A., Few C. G., 2019, A&A, 630, A140

Romanowsky A. J., Fall S. M., 2012, ApJS, 203, 17

Romeo A. B., 1992, MNRAS, 256, 307

Romeo A. B., 1994, A&A, 286, 799

Romeo A. B., 2020, MNRAS, 491, 4843

Romeo A. B., Falstad N., 2013, MNRAS, 433, 1389

Romeo A. B., Agertz O., Renaud F., 2020, MNRAS, 499, 5656

Rong Y., Guo Q., Gao L., Liao S., Xie L., Puzia T. H., Sun S., Pan J., 2017, MNRAS, 470, 4231

Roper F. A., Oman K. A., Frenk C. S., Benítez-Llambay A., Navarro J. F., Santos-Santos I. M. E., 2022, arXiv e-prints, p. arXiv:2203.16652

Rubin V. C., Ford W. K. J., Thonnard N., 1980, ApJ, 238, 471

Ruiz-Lara T., et al., 2018, MNRAS, 478, 2034

Saifollahi T., Zaritsky D., Trujillo I., Peletier R. F., Knapen J. H., Amorisco N., Beasley M. A., Donnerstein R., 2022, MNRAS, 511, 4633

Saintonge A., Catinella B., 2022, arXiv e-prints, p. arXiv:2202.00690

Saintonge A., et al., 2011, MNRAS, 415, 32

Saintonge A., et al., 2017, ApJS, 233, 22

Sales L. V., et al., 2017, MNRAS, 464, 2419

Sales L. V., Navarro J. F., Peñafiel L., Peng E. W., Lim S., Hernquist L., 2020, MNRAS, 494, 1848

Salo H., et al., 2015, ApJS, 219, 4

Sánchez Almeida J., Filho M., 2019, Research Notes of the American Astronomical Society, 3, 191

Sánchez S. F., et al., 2012, A&A, 538, A8

Sancisi R., Allen R. J., 1979, A&A, 74, 73

Sancisi R., Fraternali F., Oosterloo T., van der Hulst T., 2008, , 15, 189

Sandage A., Binggeli B., 1984, AJ, 89, 919

Sanders R. H., 1996, ApJ, 473, 117

Sanders R. H., McGaugh S. S., 2002, ARA&A, 40, 263

Sanders R. H., Verheijen M. A. W., 1998, ApJ, 503, 97

Sanders R. L., et al., 2016, ApJ, 816, 23

Sandstrom K. M., et al., 2013, ApJ, 777, 5

Sault R. J., Teuben P. J., Wright M. C. H., 1995, in Shaw R. A., Payne H. E., Hayes J. J. E., eds, Astronomical Society of the Pacific Conference Series Vol. 77, Astronomical Data Analysis Software and Systems IV. p. 433 (arXiv:astro-ph/0612759)

Sawala T., et al., 2015, MNRAS, 448, 2941

Schaye J., et al., 2015, MNRAS, 446, 521

Schinnerer E., et al., 2019, ApJ, 887, 49

Schoenmakers R. H. M., Franx M., de Zeeuw P. T., 1997, MNRAS, 292, 349

Schombert J., McGaugh S., Lelli F., 2020, AJ, 160, 71

Sellwood J. A., 2008, in Funes J. G., Corsini E. M., eds, Astronomical Society of the Pacific Conference Series Vol. 396, Formation and Evolution of Galaxy Disks. pp 341–346 (arXiv:0803.1574)

Sellwood J. A., Sanders R. H., 2022, arXiv e-prints, p. arXiv:2202.08678

Sengupta C., Scott T. C., Chung A., Wong O. I., 2019, MNRAS, 488, 3222

Serra P., et al., 2012, MNRAS, 422, 1835

Sersic J. L., 1968, Atlas de Galaxias Australes

Shaya E. J., Tully R. B., 1984, ApJ, 281, 56

Sheth K., et al., 2010, , 122, 1397

Shi Y., Zhang Z.-Y., Wang J., Chen J., Gu Q., Yu X., Li S., 2021, ApJ, 909, 20

Shin E.-j., Jung M., Kwon G., Kim J.-h., Lee J., Jo Y., Oh B. K., 2020, ApJ, 899, 25

Shostak G. S., 1973, A&A, 24, 411

Sicking F. J., 1997, PhD thesis, Kapteyn Astronomical Institute, University of Groningen

Silk J., 2019, MNRAS, 488, L24

Slipher V. M., 1914, Lowell Observatory Bulletin, 2, 66

Solanes J. M., Manrique A., García-Gómez C., González-Casado G., Giovanelli R., Haynes M. P., 2001, ApJ, 548, 97

Somerville R. S., et al., 2018, MNRAS, 473, 2714

Spekkens K., Giovanelli R., 2006, AJ, 132, 1426

Spekkens K., Karunakaran A., 2018, ApJ, 855, 28

Spekkens K., Sellwood J. A., 2007, ApJ, 664, 204

Starkenburg T. K., Sales L. V., Genel S., Manzano-King C., Canalizo G., Hernquist L., 2019, ApJ, 878, 143

Steinmetz M., Navarro J. F., 1999, ApJ, 513, 555

Stevens A. R. H., Croton D. J., Mutch S. J., 2016, MNRAS, 461, 859

Stevens A. R. H., Lagos C. d. P., Obreschkow D., Sinha M., 2018, MNRAS, 481, 5543

Stone C., Courteau S., Arora N., 2021, ApJ, 912, 41

Strickland D. K., Stevens I. R., 2000, MNRAS, 314, 511

Swaters R. A., 1999, PhD thesis, Kapteyn Astronomical Institute, University of Groningen

Swaters R. A., van Albada T. S., van der Hulst J. M., Sancisi R., 2002, A&A, 390, 829

Swaters R. A., Sancisi R., van Albada T. S., van der Hulst J. M., 2009, A&A, 493, 871

Sweet S. M., Fisher D., Glazebrook K., Obreschkow D., Lagos C., Wang L., 2018, ApJ, 860, 37

Sweet S. M., et al., 2019, MNRAS, 485, 5700

Sweet S. M., Glazebrook K., Obreschkow D., Fisher D. B., Burkert A., Lagos C. D. P., Espejo Salcedo J. M., 2020, MNRAS, 494, 5421

Tamburro D., Rix H. W., Leroy A. K., Mac Low M. M., Walter F., Kennicutt R. C., Brinks E., de Blok W. J. G., 2009, AJ, 137, 4424

Teich Y. G., et al., 2016, ApJ, 832, 85

Teklu A. F., Remus R.-S., Dolag K., Beck A. M., Burkert A., Schmidt A. S., Schulze F., Steinborn L. K., 2015, ApJ, 812, 29

Thomas D., Maraston C., Schawinski K., Sarzi M., Silk J., 2010, MNRAS, 404, 1775

Thornton K., Gaudlitz M., Janka H. T., Steinmetz M., 1998, ApJ, 500, 95

Tielens A. G. G. M., 2005, The Physics and Chemistry of the Interstellar Medium

Tissera P. B., White S. D. M., Pedrosa S., Scannapieco C., 2010, MNRAS, 406, 922

Toloba E., et al., 2018, ApJ, 856, L31

Tolstoy E., Hill V., Tosi M., 2009, ARA&A, 47, 371

Toomre A., 1964, ApJ, 139, 1217

Toomre A., 1981, in Fall S. M., Lynden-Bell D., eds, Structure and Evolution of Normal Galaxies. pp 111–136

Tremmel M., Karcher M., Governato F., Volonteri M., Quinn T. R., Pontzen A., Anderson L., Bellovary J., 2017, MNRAS, 470, 1121

Tremmel M., Wright A. C., Brooks A. M., Munshi F., Nagai D., Quinn T. R., 2020, MNRAS, 497, 2786

Trujillo-Gomez S., Kruijssen J. M. D., Reina-Campos M., 2022, MNRAS, 510, 3356

Trujillo I., Roman J., Filho M., Sánchez Almeida J., 2017, ApJ, 836, 191

Trujillo I., et al., 2019, MNRAS, 486, 1192

Trujillo I., Chamba N., Knapen J. H., 2020, MNRAS, 493, 87

Tulin S., Yu H.-B., 2018, , 730, 1

Tully R. B., Fisher J. R., 1977, A&A, 500, 105

Tully R. B., et al., 2013, AJ, 146, 86

Tumlinson J., Peeples M. S., Werk J. K., 2017, ARA&A, 55, 389

Utomo D., Blitz L., Falgarone E., 2019, ApJ, 871, 17

van Albada T. S., Sancisi R., 1986, Philosophical Transactions of the Royal Society of London Series A, 320, 447

van Dokkum P. G., Abraham R., Merritt A., Zhang J., Geha M., Conroy C., 2015, ApJ, 798, L45

van Dokkum P., et al., 2016, ApJ, 828, L6

van Dokkum P., et al., 2018, Nature, 555, 629

van Dokkum P., Danieli S., Abraham R., Conroy C., Romanowsky A. J., 2019, ApJ, 874, L5

van Zee L., 2000, ApJ, 543, L31

van de Hulst H. C., Muller C. A., Oort J. H., 1954, , 12, 117

van de Hulst H. C., Raimond E., van Woerden H., 1957, , 14, 1

van den Bosch F. C., Lewis G. F., Lake G., Stadel J., 1999, ApJ, 515, 50

van den Bosch F. C., Burkert A., Swaters R. A., 2001, MNRAS, 326, 1205

van der Burg R. F. J., Muzzin A., Hoekstra H., 2016, A&A, 590, A20

van der Hulst J. M., 1979, A&A, 71, 131

van der Hulst J. M., Terlouw J. P., Begeman K. G., Zwitser W., Roelfsema P. R., 1992, in Worrall D. M., Biemesderfer C., Barnes J., eds, Astronomical Society of the Pacific Conference Series Vol. 25, Astronomical Data Analysis Software and Systems I. p. 131

van der Hulst J. M., Skillman E. D., Smith T. R., Bothun G. D., McGaugh S. S., de Blok W. J. G., 1993, AJ, 106, 548

van der Hulst J. M., van Albada T. S., Sancisi R., 2001, in Hibbard J. E., Rupen M., van Gorkom J. H., eds, Astronomical Society of the Pacific Conference Series Vol. 240, Gas and Galaxy Evolution. p. 451

van der Kruit P. C., 1981, A&A, 99, 298

van der Kruit P. C., 1988, A&A, 192, 117

van der Kruit P. C., Freeman K. C., 2011, ARA&A, 49, 301

van der Kruit P. C., Searle L., 1981, A&A, 95, 105

van der Marel R. P., Alves D. R., Hardy E., Suntzeff N. B., 2002, AJ, 124, 2639

van der Wel A., Bell E. F., Holden B. P., Skibba R. A., Rix H.-W., 2010, ApJ, 714, 1779

Venhola A., et al., 2017, A&A, 608, A142

Venhola A., et al., 2018, A&A, 620, A165

Verheijen M. A. W., 1997, PhD thesis, Kapteyn Astronomical Institute, University of Groningen

Verheijen M. A. W., Sancisi R., 2001, A&A, 370, 765

Verlinde E., 2017, SciPost Physics, 2, 016

Viel M., Lesgourgues J., Haehnelt M. G., Matarrese S., Riotto A., 2005, , 71, 063534

Vogelsberger M., Genel S., Sijacki D., Torrey P., Springel V., Hernquist L., 2013, MNRAS, 436, 3031

Walter F., Brinks E., de Blok W. J. G., Bigiel F., Kennicutt Robert C. J., Thornley M. D., Leroy A., 2008, AJ, 136, 2563

Wang L., Dutton A. A., Stinson G. S., Macciò A. V., Penzo C., Kang X., Keller B. W., Wadsley J., 2015, MNRAS, 454, 83

Wang J., Koribalski B. S., Serra P., van der Hulst T., Roychowdhury S., Kamphuis P., Chengalur J. N., 2016, MNRAS, 460, 2143

Wang J., Yang K., Zhang Z.-Y., Fang M., Shi Y., Liu S., Li J., Li F., 2020, MNRAS, 499, L26

Wechsler R. H., Tinker J. L., 2018, ARA&A, 56, 435

Wen X.-Q., Wu H., Zhu Y.-N., Lam M. I., Wu C.-J., Wicker J., Zhao Y.-H., 2013, MNRAS, 433, 2946

White S. D. M., 1984, ApJ, 286, 38

White S. D. M., Rees M. J., 1978, MNRAS, 183, 341

Wisnioski E., et al., 2015, ApJ, 799, 209

Wolfire M. G., McKee C. F., Hollenbach D., Tielens A. G. G. M., 2003, ApJ, 587, 278

Wright A. C., Tremmel M., Brooks A. M., Munshi F., Nagai D., Sharma R. S., Quinn T. R., 2021, MNRAS, 502, 5370

Yang D., Yu H.-B., An H., 2020, , 125, 111105

Yim K., Wong T., Xue R., Rand R. J., Rosolowsky E., van der Hulst J. M., Benjamin R., Murphy E. J., 2014, AJ, 148, 127

York D. G., et al., 2000, AJ, 120, 1579

Young J. S., et al., 1995, ApJS, 98, 219

Young T., Jerjen H., López-Sánchez Á. R., Koribalski B. S., 2014, MNRAS, 444, 3052

Yun M. S., Ho P. T. P., Lo K. Y., 1994, Nature, 372, 530

Zanisi L., et al., 2020, MNRAS, 492, 1671

Zentner A., Dandavate S., Slone O., Lisanti M., 2022, arXiv e-prints, p. arXiv:2202.00012

Zhang H.-X., Hunter D. A., Elmegreen B. G., Gao Y., Schruba A., 2012, AJ, 143, 47

Zoldan A., De Lucia G., Xie L., Fontanot F., Hirschmann M., 2018, MNRAS, 481, 1376

Zwaan M. A., van der Hulst J. M., de Blok W. J. G., McGaugh S. S., 1995, MNRAS, 273, L35

Summary for non-experts

Present-day galaxies

Carl Sagan once said that we are a way for the cosmos to know itself. In fact, from our location within a star-forming galaxy, the Milky Way, we attempt to understand our own and other galaxies: when and how they formed, how they evolved until the present day, and what will their fate be in a future we will not be able to witness.

The main visible components of any galaxy are stars and gas. However, the population of galaxies we observe in the nearby Universe is richly diverse, showing a spread in a large number of properties like masses, gas content, size, and the rate at which stars form from their gas, among others. This wide diversity in present-day galaxies is the final product of their evolution through cosmic time, and we can therefore use observations to compare with theoretical models with the aim of understanding the physics of galaxy formation and evolution. While only 100 years ago the astronomical community was still debating whether there were other galaxies in the Universe besides the Milky Way, our knowledge, while yet incomplete, has increased significantly since then. We now have elaborate galaxy formation theories within a cosmological framework, starting from the Big Bang itself 14 billion years ago and making predictions for a distant future.

In our attempt to understand galaxies, it is necessary to classify them according to some common features. One of the most commonly-used classification schemes is the so-called Hubble diagram or Hubble fork, shown in Fig. I, which is based on the optical appearance of the galaxies. In general terms, galaxies are classified in two big families: early- and late-type galaxies (indicated with the letters E and S in Fig. I, respectively). Early-type galaxies, located in the left part of the Hubble diagram, have elliptical morphology (which is why they are also called elliptical galaxies), often have little rotational support, have small

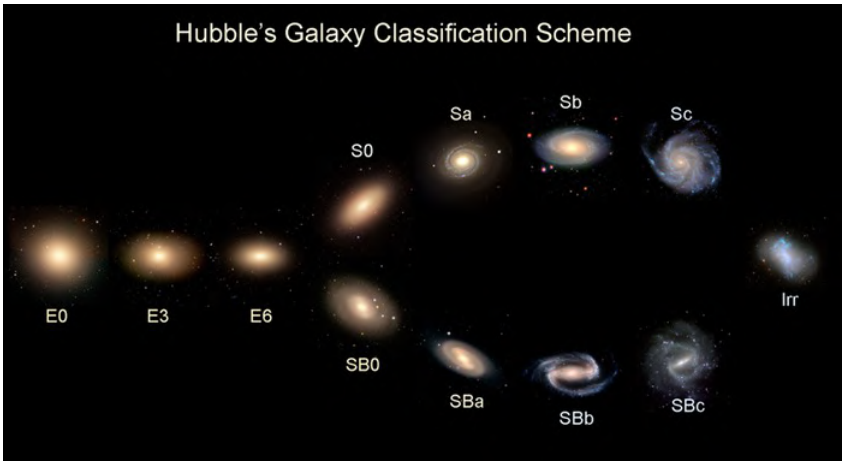

Figure I: Hubble morphological classification. Credits: University of Iowa.

gas reservoirs, and show very low star formation, with most of their stars being old, having formed in the past. On the other hand, the right side of the Hubble diagram shows late-type galaxies. Late-type systems have discy morphology (which is why they are also called disc galaxies), are supported by rotation, have significant gas reservoirs, relatively young stars, and active star formation; very often they also have spiral arms or central light concentrations with either an spheroidal (called bulge) or elongated (called bar) shapes. The fork in the Hubble diagram further splits late-type galaxies: on the top prong galaxies are ordered according to the decreasing prominence of their bulge and increasing prominence of the spiral arms, while on the bottom prong barred galaxies are ordered depending on the size of their bars and how open their spiral arms are. Galaxies that do not fit in the above sequences of the Hubble fork are called irregulars (Irr), often displayed at the end of the Hubble fork. It is important to notice that the Hubble diagram is *not* an evolutionary diagram showing the evolution of galaxies with time.

As mentioned above, late-type galaxies have large gas reservoirs. Together with a small amount of dust, the gas forms the so-called interstellar medium (ISM). Most of this gas is neutral atomic hydrogen, commonly called H I. In late-type systems, both stars (except for the bulge, which tends to be spheroidal) and H I are distributed in a disc configuration. H I is usually more extended than the stars, as depicted in Fig. II, where the stellar emission of a nearby spiral galaxy is shown in blue and yellow, while the H I disc is shown in orange. H I discs are thick and flared, with their thickness increasing with the distance from the galaxy centre. Still, their thickness is much smaller than their radial extension, so they are thin relative to their radial size.

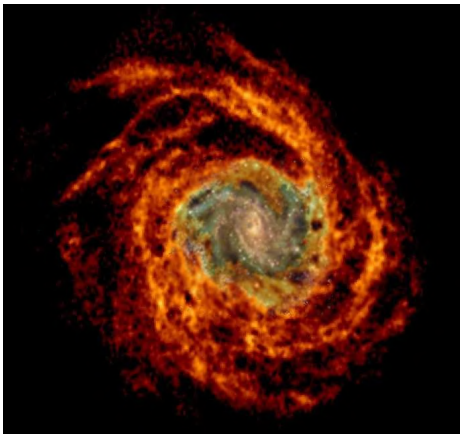

Figure II: Stellar (blue and yellow) and H I (orange) discs of a nearby disc galaxy. The H I is significantly more extended than the stars. Credits: Tom Oosterloo.

Dark matter and angular momentum

The visible component of galaxies (essentially stars and gas, generically called 'baryons') settles within more massive structures called dark matter haloes, as sketched in the left panel of Fig. III. In turn, these dark matter haloes are surrounded by the so-called intergalactic medium (IGM). The dark matter content is crucial at regulating the evolution of galaxies, as it is tightly linked with their capability to accrete gas from the IGM and with how frequently will galaxies merge with other surrounding galaxies. The distribution of dark matter within galaxies can be modified by the processes related to stars and gas. For instance, the explosion of stars into supernovae can modify the density distribution of the dark matter, and by measuring this density accurately we can estimate how powerful the supernovae explosions had to be. This is an example of how by studying the dark matter content of galaxies we can also learn about the physical processes involving stars and gas.

Quantifying the distribution of dark matter in galaxies is, therefore, of paramount importance. However, this is not an easy task. In contrast to ordinary matter, dark matter does not emit or reflect radiation, and thus it cannot be directly observed. Dark matter, however, interacts with baryons through gravity, allowing us to infer its presence even if invisible. Dark matter accounts for about 80% of all the mass in the Universe, compared to 20% of the baryons. Despite of this, what exactly dark matter is made of has remained an unsolved question for more than 50 years.

One of the clearest manifestations of the existence of dark matters comes from the observed kinematics of disc galaxies. As mentioned before, the stars and gas in disc galaxies rotate, and the amount of rotation is directly linked with the total mass distribution within the galaxy. Using different types of instruments and telescopes, we can measure the rotation of the stars and gas at different locations within galaxies. By doing so, we can build a so-called rotation curve, showing the average rotation velocity of galaxies as a function

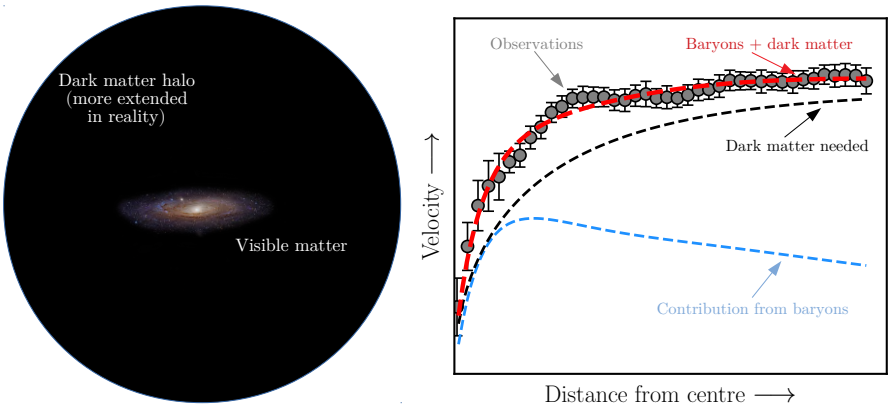

Figure III: *Left:* Sketch of a disc galaxy within its host dark matter halo. Note that the sketch is not at scale, in reality the dark halo is about 10 times more extended than the visible galaxy. The dark matter haloes are surrounded by the intergalactic medium (not shown). Credits for the optical image: HST/NASA. *Right:* Rotation curve (grey points) of a nearby spiral galaxy. The blue line show the velocity expected given the visible matter in the galaxy. In order to reproduced the observed rotation curve, an additional component is needed, the dark matter halo (black line). Once baryons and dark matter are considered jointly (red line) there is a good match with the observed rotation curve.

of the distance from their centres. H I is particularly useful for this as it allow us to measure rotation curves up to very large distances (see Fig. II). The H I rotation curve of a nearby disc galaxy is shown in the right-hand side of Fig. III (grey circles). Given the amount and distribution of stars and gas in galaxies, we can compute what should be the level of rotation of the system (blue line in Fig. III). Surprisingly, when one measures the actual rotation curve, it strongly differs from what we would expect given the mass in the baryons. In order to match the observations, an additional dark matter component is needed (black line in Fig. III).

The baryonic and dark matter content of galaxies have also been found empirically to correlate with each other via the so-called baryonic Tully-Fisher relation (BTFR), sketched in Fig. IV. This relation shows a link between the baryonic mass of galaxies and their rotation velocity; given that the latter depends both on the baryons and on the dark matter, the BTFR connects visible and dark masses in galaxies. The relation is very tight for massive spiral galaxies with high velocities, but its behavior is less clear for 'dwarf' galaxies with low masses and rotation speeds. Establishing the precise shape of the BTFR is important to learn about the amount of dark matter and the processes of mass loss within different galaxies. In fact, the BTFR is a powerful useful tool often used to asses

whether or not models and simulations of galaxy formation are realistic: a model or simulation that fails at reproducing the BTFR would, in principle, be falsified.

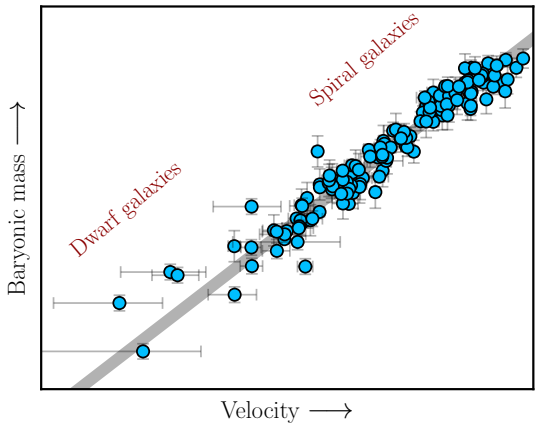

Figure IV: Sketch of the baryonic Tully-Fisher relation. This scaling law connects the visible mass in galaxies with their rotation velocity, which includes the contribution from the dark matter haloes. The points show a set of massive spirals and dwarf disc galaxies, and the grey line is a fit to the data. The behavior of the relation at low masses and low velocities is not as clear as for the high-mass and high-velocity regime.

Another key parameter governing galaxy evolution is angular momentum. Tightly related to the rotation curves of galaxies, angular momentum measures the amount of rotation within a galaxy given its mass distribution, and broadly speaking it is proportional to the product of the rotation velocity of galaxies times their sizes. For example, if two galaxies have the same rotation velocity but one of them is more extended, then that galaxy will have a larger angular momentum. Observations have found that angular momentum is strongly linked with galaxy morphology. As shown in Fig. V, at fixed stellar mass galaxies with different angular momentum (or to be more precise specific angular momentum, i.e. the angular momentum per unit mass) have remarkably different morphologies. The general trend of this relation, often called the Fall relation, is that at fixed stellar mass, the stars of late-type galaxies have a higher specific angular momentum than in early-types, with the intermediate groups from the Hubble fork such as S0 galaxies (also called lenticulars) lying among them (see Fig. I).

Despite having a general understanding of the relation between mass and angular momentum, several details are still missing. To name specific examples, it is not clear what is the behavior of the relation for low-mass galaxies, what is the impact of supernovae explosions in the angular momentum and morphology of galaxies, or what is the angular momentum of the gas component (and not only of the stars).

This thesis

The main goal of this thesis has been to investigate the dark matter and angular momentum content of nearby disc galaxies. For this, we have exploited observations of their H I kinematics, which enabled us to perform robust measurements

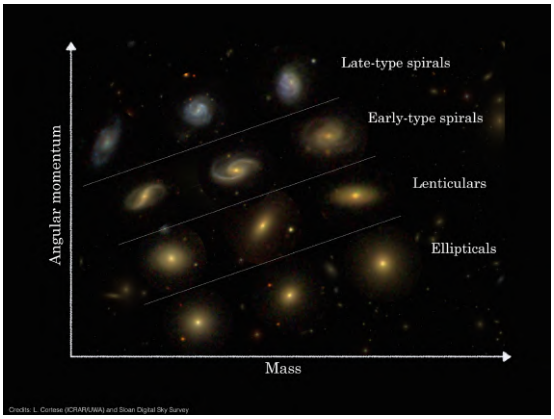

Figure V: Sketch of the relation between the mass and angular momentum of the stellar component of nearby galaxies (known as the Fall relation). Galaxies of similar stellar mass show strikingly diverse morphologies given their different angular momentum content. Credits: Luca Cortese.

of their dark matter and angular momentum content.

The first two chapters focused on a population of faint dwarf galaxies named ultra-diffuse galaxies (UDGs). UDGs are very peculiar systems because they have a light distribution as extended as big spiral galaxies like our Milky Way, but with about 1000 times fewer stars. Because of this their density of stars is very low, giving them a diffuse appearance at optical wavelengths. Albeit UDGs have been studied in detail in the last few years, the formation mechanisms of these faint but large galaxies are still unclear. A crucial piece of information largely missing is their kinematics, which in turn would give us information on their dark matter and angular momentum. In Chapters 2 and 3 we studied a sample of six UDGs with large H I reservoirs. For this, we exploited data from the Westerbork Synthesis Radio Telescope in the Netherlands and from the Very Large Array interferometer (also a set of radio antennas) in the USA. By looking at the motions of the H I in UDGs, we obtained the rotation velocity of the systems, enabling us to place them in the BTFR. Surprisingly, our six galaxies are strong outliers of the relation: their rotation velocities are much lower than expected given their mass in gas and stars, and thus they deviate upwards from the BTFR in the low-velocity regime. This is the first known population of galaxies to systematically deviate from the BTFR, and their position is challenging for current models of galaxy evolution. The total mass (baryons plus dark matter) inferred from the rotation of our UDGs is very similar to the measured mass of the baryons, which suggested the galaxies have low dark matter reservoirs. We also found tentative evidence that the specific angular momentum of UDGs is higher than that of other galaxies with similar stellar mass, which could explain why UDGs have more extended light distributions.

In Chapter 4 we studied one of our six UDGs (the galaxy AGC 114905) but with sharper data than before, which allowed us to trace the distribution of the gas and its motions in much more detail. We corroborated that AGC 114905 is off the BTFR. Moreover, by studying thoroughly its rotation curve, we found that there is very little room for dark matter: opposite to what happens in Fig. III, in the case of our UDG the observed rotation matches well the contribution

from the baryons. These results appear in tension with current dark matter models, and show the great potential UDGs have to test different theories and gain insight into the nature of dark matter.

In Chapters 5 and 6 we measured the angular momentum of stars, gas, and baryons (stars and gas together) in a sample of about 160 nearby late-type galaxies with the highest-available data quality. This is the largest sample of galaxies for which detailed measurements of the baryonic angular momentum have been performed. Overall, we found that the three relations (for stars, gas, and baryons) between mass and specific angular momentum are well described by unbroken power-laws from the regime of low-mass dwarf galaxies to the most massive spiral galaxies, without breaks previously suggested by other authors. In addition to this, we found that the gas fraction of galaxies (the mass in gas relative to the baryonic mass) is tightly correlated with mass and angular momentum. In a 3D space where the dimensions are mass, specific angular momentum, and gas fraction, galaxies define very tight planes. This new scaling relation is among the tightest (and therefore arguably among the most fundamental) known scaling laws of galaxies.

Finally, in Chapter 7 we used very detailed observations and robust analysis tools to infer the properties of the dark matter haloes in a sample of dwarf and massive nearby disc galaxies. The most innovative aspect of our analysis is that we took into account the real geometry of the gaseous discs of galaxies. Instead of assuming they have a small constant thickness, we obtained estimates of their true thickness and its changes with radius (and this is, its flaring). Changing the geometry changes the expected contribution of the baryons to the rotation curve, and therefore changing the dark matter needed to match the observations (see Fig. III). Our analysis showed that the flaring of the discs plays a role only for the smallest and most-gas rich dwarf galaxies, but can be safely ignored for massive systems. We found reasonably good agreement between the mass and distribution of dark matter in our observed galaxies with predictions from simulations. Moreover, our analysis corroborated previous findings that show that among late-type systems, the efficiency to convert gas into stars is higher for galaxies with high stellar masses.

Overall, in this thesis we have performed the most detailed kinematic characterisation of gas-rich UDGs to date, provided the most comprehensive analysis of the baryonic angular momentum of nearby disc galaxies and its relation with the gas content in the literature, and obtained some of the most thorough estimations of the dark matter haloes of dwarf and massive star-forming galaxies. The original observational results presented here have provided us with new insights on the role of dark matter and angular momentum at shaping the bewildering population of galaxies we observe today.

Samenvatting

Hedendaagse sterrenstelsels

Carl Sagan heeft ooit gezegd dat wij een manier zijn voor de kosmos om zichzelf te leren kennen. Vanuit onze positie binnen een stervormend sterrenstelsel, de Melkweg, proberen wij onze eigen en andere sterrenstelsels te begrijpen: wanneer en hoe zij zijn gevormd, hoe zij zich tot op heden hebben ontwikkeld en wat hun lot zal zijn in een toekomst waarvan wij geen getuige kunnen zijn.

De belangrijkste zichtbare componenten van elk sterrenstelsel zijn sterren en gas. De populatie van melkwegstelsels die we in het nabije heelal waarnemen, is echter zeer divers en vertoont spreiding in een groot aantal eigenschappen, zoals massa's, gasinhoud, grootte en de snelheid waarmee sterren uit hun gas worden gevormd, om er maar een paar te noemen. Deze grote diversiteit in de huidige melkwegstelsels is het eindproduct van hun evolutie door de kosmische tijd heen en we kunnen daarom waarnemingen gebruiken om te vergelijken met theoretische modellen met als doel de fysica van de vorming en evolutie van melkwegstelsels te begrijpen. Terwijl de astronomische gemeenschap nog maar 100 jaar geleden discussieerde over de vraag of er naast de Melkweg nog andere melkwegstelsels in het heelal waren, is onze kennis, hoewel nog onvolledig, sindsdien aanzienlijk toegenomen. We beschikken nu over uitgebreide theorieën over de vorming van sterrenstelsels binnen een kosmologisch kader, dat uitgaat van de oerknal zelf en voorspellingen doet voor een verre toekomst.

Om melkwegstelsels te begrijpen is het nodig ze in te delen aan de hand van enkele gemeenschappelijke kenmerken. Een van de meest gebruikte classificatieschema's is het zogeheten Hubble-diagram of de Hubble-vork, getoond in Fig. I en die gebaseerd is op de optische verschijningsvorm van de melkwegstelsels. In het algemeen worden melkwegstelsels ingedeeld in twee grote families: stelsels van het vroege en het late type (respectievelijk aangegeven met de letters E en S in Fig. I). Vroeg-type stelsels, die zich in het linkerdeel van het Hubble-diagram bevinden, hebben een elliptische vorm (daarom worden ze ook elliptische stelsels genoemd), de rotatie is relatief onbelangrijk, hebben kleine gasreservoirs en vertonen zeer weinig stervorming, terwijl de meeste van hun sterren oud zijn,

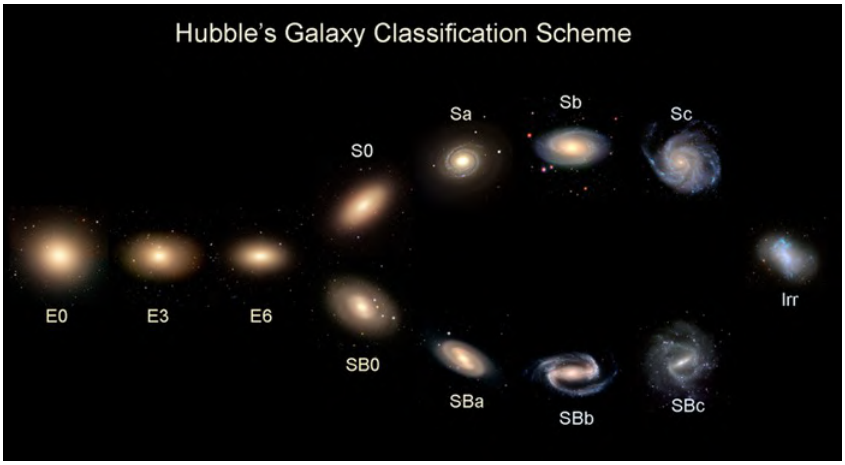

Figuur I: Hubble morfologische classificatie. Credits: Universiteit van Iowa.

omdat ze in het verleden zijn gevormd. Aan de rechterkant van het Hubble-diagram staan daarentegen stelsels van het late type. Laat-type stelsels hebben een schijfachtige vorm (daarom worden ze ook wel schijfstelsels genoemd), de rotatie van het stelsel is erg belangrijk, hebben aanzienlijke gasreservoirs, relatief veel jonge sterren en actieve stervorming; heel vaak hebben ze ook spiraalarmen of centrale lichtconcentraties met ofwel een sferoïdale (bulge genoemd) ofwel een langgerekte (balk genoemd) vorm. De vork in het Hubble-diagram splitst laat-type melkwegstelsels verder op: op de bovenste tak worden melkwegstelsels gerangschikt naar afnemende prominentie van hun bulge en toenemende prominentie van hun spiraalarmen, terwijl op de onderste tand balkvormige melkwegstelsels worden gerangschikt naar de grootte van hun balk en hoe open hun spiraalarmen zijn. Melkwegstelsels die niet in de bovenstaande volgordes van de Hubble-vork passen, worden onregelmatige stelsels (Irr) genoemd, die vaak aan het eind van de Hubble-vork worden weergegeven. Het is belangrijk op te merken dat het Hubble-diagram geen evolutiediagram is die de evolutie van sterrenstelsels in de tijd laat zien.

Zoals hierboven vermeld, hebben laat-type melkwegstelsels grote gasreservoirs. Samen met een kleine hoeveelheid stof vormt dit gas het zogenaamde interstellaire medium (ISM). Het grootste deel van dit gas bestaat uit neutrale atomaire waterstof, als H I aangeduid. In stelsels van het late type zijn zowel de sterren (behalve de bulge, die meestal sferoïdaal is) als het H I verdeeld in een schijfconfiguratie. De verdeling van H I is meestal uitgebreider dan de sterren, zoals te zien is in Fig. II, waar de stellaire emissie van een nabijgelegen spiraalvormig sterrenstelsel in blauw en geel is weergegeven, terwijl de H I-schijf in oranje wordt getoond. H I schijven zijn vrij dun, maar hun dikte neemt toe naar buiten toe en hun dikte neemt toe met de afstand tot het centrum van het melkwegstelsel. Toch is hun dikte veel kleiner dan hun radiale grootte.

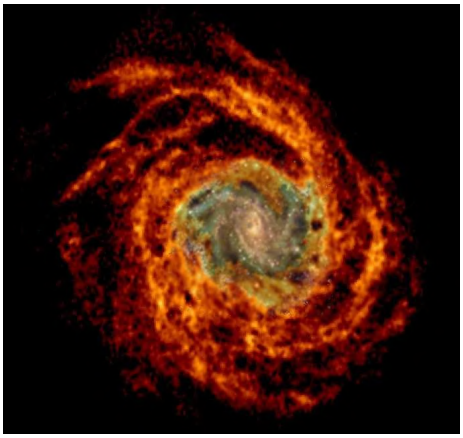

Figuur II: Stellaire (blauw en geel) en H I (oranje) schijven van een nabijgelegen schijfstelsel. De H I schijf is beduidend groter dan de sterren. Credits: Tom Oosterloo.

Donkere materie en impulsmoment

De zichtbare component van sterrenstelsels (in hoofdzaak sterren en gas, in het algemeen 'baryonen' genoemd) nestelt zich in grotere structuren die donkere materiehalo's worden genoemd, zoals geschetst in het linkerpaneel van Fig. III. Op hun beurt worden deze donkere materie halo's omgeven door het zogenaamde intergalactische medium (IGM). Het gehalte aan donkere materie is van cruciaal belang voor de evolutie van melkwegstelsels, omdat het nauw samenhangt met hun vermogen om gas uit het IGM op te nemen en met hoe vaak melkwegstelsels-samen zullen smelten met andere omringende melkwegstelsels. De verdeling van donkere materie binnen sterrenstelsels kan worden gewijzigd door de processen die verband houden met sterren en gas. Zo kan bijvoorbeeld de explosie van sterren in supernovae de dichtheidsverdeling van de donkere materie veranderen en door deze dichtheid nauwkeurig te meten kunnen we schatten hoe krachtig de supernovae-explosies moesten zijn. Dit is een voorbeeld van hoe we door het bestuderen van de verdeling van donkere materie in sterrenstelsels ook meer te weten kunnen komen over de fysische processen waarbij sterren en gas betrokken zijn.

Kwantificering van de verdeling van donkere materie in melkwegstelsels is daarom van groot belang. Dit is echter geen gemakkelijke taak. In tegenstelling tot gewone materie zendt donkere materie geen straling uit en reflecteert deze ook niet, zodat deze niet rechtstreeks kan worden waargenomen. Donkere materie interageert echter met baryonen door middel van de zwaartekracht, waardoor wij de aanwezigheid ervan kunnen afleiden, ook al is deze onzichtbaar. Ongeveer 80% van alle materie in het heelal is donker, slechts 20% bestaat uit baryonen Desondanks is de precieze samenstelling van donkere materie al meer dan 50 jaar een onopgeloste vraag.

Een van de duidelijkste bewijzen van het bestaan van donkere materie komt uit de waargenomen kinematica van schijfstelsels. Zoals gezegd roteren de sterren en het gas in schijfstelsels en de mate van rotatie houdt rechtstreeks verband met

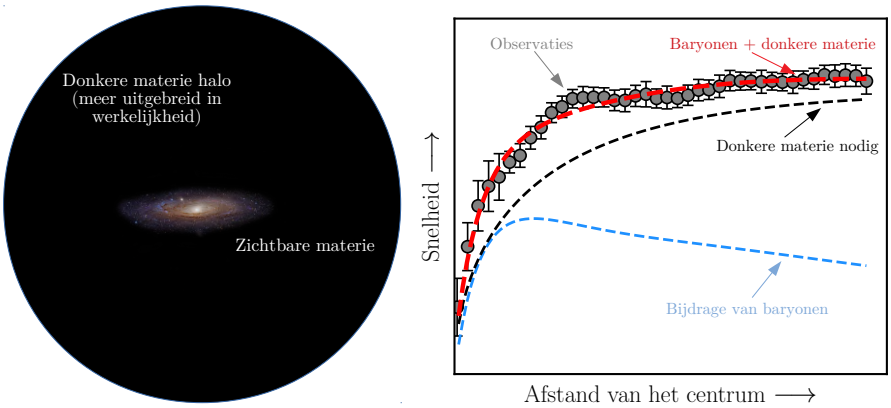

Figuur III: *Links:* Schets van een schijfstelsel binnen zijn halo van donkere materie. Merk op dat de schets niet op schaal is, in werkelijkheid is de donkere halo ongeveer 10 keer zo groot als het zichtbare melkwegstelsel. De donkere materie halo's zijn omgeven door het intergalactische medium (niet afgebeeld). Credits voor de optische afbeelding: HST/NASA. *Rechts*: Rotatiekromme (grijze punten) van een nabijgelegen spiraalvormig sterrenstelsel. De blauwe lijn toont de verwachte snelheid, gegeven de zichtbare materie in het melkwegstelsel. Om de waargenomen Rotatiekromme te reproduceren, is een extra component nodig, de donkere materie halo (zwarte lijn). Wanneer baryonen en donkere materie gezamenlijk worden beschouwd (rode lijn) is er een goede overeenkomst met de waargenomen rotatiekromme.

de totale massaverdeling binnen het sterrenstelsel. Met behulp van verschillende soorten instrumenten en telescopen kunnen we de rotatie van de sterren en het gas op verschillende plaatsen in melkwegstelsels meten. Op die manier kunnen we een zogenaamde rotatiekromme opstellen, die de gemiddelde rotatiesnelheid van sterrenstelsels toont als functie van de afstand tot hun centrum. H I is hiervoor bijzonder nuttig omdat we er rotatiekrommen mee kunnen meten tot op zeer grote afstanden van het centrum van het sterrenstelsel (zie Fig. II). De H I-rotatiekromme van een naburig schijfstelsel is te zien in het rechterdeel van Fig. III (grijze cirkels). Gegeven de hoeveelheid en verdeling van sterren en gas in sterrenstelsels, kunnen we berekenen wat de mate van rotatie van het stelsel zou moeten zijn (blauwe lijn in Fig. III). Verrassend genoeg wijkt de werkelijke rotatiekromme sterk af van wat we op grond van de massa van de baryonen zouden verwachten. Om aan de waarnemingen te voldoen, is een extra donkere materiecomponent nodig (zwarte lijn in Fig. III).

Ook is empirisch vastgesteld dat de baryonmassa en de donkere materie van melkwegstelsels met elkaar correleren via de zogenaamde baryonische Tully-Fisher relatie (BTFR), die in Fig. IV. Deze relatie toont een verband aan tussen de baryonische massa van een sterrenstelsel en zijn rotatiesnelheid; aangezien

deze laatste zowel van de baryonen als van de donkere materie afhangt, verbindt de BTFR de zichtbare en donkere massa's in sterrenstelsels. De relatie is zeer nauw voor spiraalstelsels met hoge snelheden, maar het gedrag is minder duidelijk voor 'dwerg' stelsels met lage massa's en rotatiesnelheden. Het vaststellen van de precieze vorm van de BTFR is belangrijk om meer te weten te komen over de hoeveelheid donkere materie en de processen van massaverlies binnen verschillende melkwegstelsels. In feite is de BTFR een krachtig instrument dat vaak wordt gebruikt om na te gaan of modellen en simulaties van de vorming van melkwegstelsels al dan niet realistisch zijn: een model of simulatie die er niet in slaagt de BTFR te reproduceren zou in principe fout zijn.

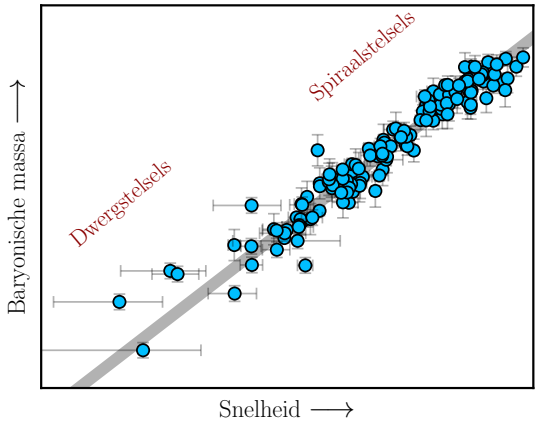

Figuur IV: Schets van de baryonische Tully-Fisher relatie. Deze schalingswet verbindt de zichtbare massa in melkwegstelsels met hun rotatiesnelheid, waarin de bijdrage van de donkere materie halo's is inbegrepen. De punten tonen een verzameling van massieve spiralen en dwergschijfgalaxieën en de grijze lijn is een fit met de gegevens. Het gedrag van de relatie bij lage massa's en lage snelheden is niet zo duidelijk als voor het regime van hoge massa's en hoge snelheden.

Een andere belangrijke parameter voor de evolutie van melkwegstelsels is het impulsmoment. Het impulsmoment, dat nauw verbonden is met de rotatiekrommen van melkwegstelsels, meet de hoeveelheid rotatie binnen een melkwegstelsel gegeven zijn massaverdeling en is in het algemeen evenredig met het product van de rotatiesnelheid van melkwegstelsels en hun grootte. Bijvoorbeeld, als twee melkwegstelsels dezelfde rotatiesnelheid hebben, maar één van hen is groter, dan zal dat melkwegstelsel een groter impulsmoment hebben. Waarnemingen hebben uitgewezen dat het impulsmoment sterk samenhangt met de morfologie van melkwegstelsels. Zoals te zien is in Fig. V hebben melkwegstelsels met een verschillend impulsmoment (of om precies te zijn een specifiek impulsmoment, d.w.z. het impulsmoment per massa-eenheid) bij een vaste stermassa opmerkelijk verschillende morfologieën. De algemene trend van deze relatie, die vaak de Fall relatie wordt genoemd, is dat bij een gegeven stellaire massa, de sterren van laat-typische melkwegstelsels een hoger specifiek impulsmoment hebben dan in vroeg-typische melkwegstelsels, waarbij de tussenliggende groepen uit de Hubble-vork, zoals S0-sterrenstelsels (ook wel lenticulars genoemd), ertussen liggen (zie Fig. I).

Hoewel we een algemeen begrip hebben van de relatie tussen massa en impulsmoment, ontbreken er nog verschillende details. Om enkele specifieke

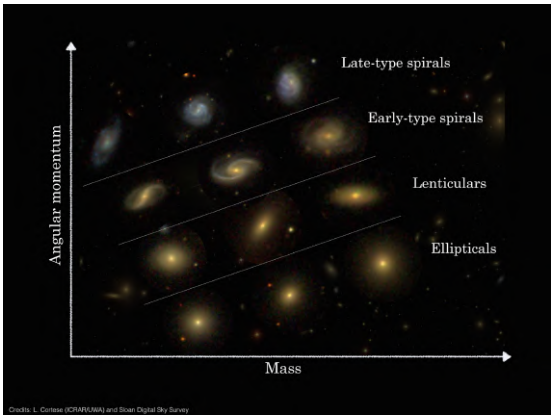

Figuur V: Schets van de relatie tussen de massa en het impulsmoment van de stellaire component van nabije melkwegstelsels (bekend als de Fall relatie). Melkwegstelsels met een vergelijkbare stellaire massa vertonen opvallend verschillende morfologieën, gezien hun verschillende impulsmomentinhoud. Credits: Luca Cortese.

voorbeelden te noemen: het is niet duidelijk hoe de relatie zich gedraagt voor melkwegstelsels met een lage massa, wat de invloed is van supernova-explosies op het impulsmoment en de morfologie van melkwegstelsels, of wat het impulsmoment is van het gas (en niet alleen van de sterren).

Dit proefschrift

Het hoofddoel van dit proefschrift was het onderzoeken van de inhoud van donkere materie en impulsmoment van nabije schijfsterrenstelsels. Hiervoor hebben we gebruik gemaakt van waarnemingen van hun H I kinematica, die ons in staat stelden robuuste metingen van hun donkere materie en impulsmoment inhoud uit te voeren.

De eerste twee hoofdstukken concentreerden zich op een populatie van zwakke dwergstelsels, ultra-diffuse galaxies (UDGs) genaamd. UDG's zijn zeer eigenaardige stelsels omdat zij een lichtverdeling hebben die even uitgebreid is als grote spiraalstelsels zoals onze Melkweg, maar met ongeveer 1000 maal minder sterren. Hierdoor is hun dichtheid aan sterren zeer laag, waardoor ze er bij optische golflengten zwak en diffuus uitzien. Hoewel UDG's de laatste jaren in detail zijn bestudeerd, zijn de vormingsmechanismen van deze zwakke maar grote sterrenstelsels nog steeds onduidelijk. Een cruciaal stuk informatie dat grotendeels ontbreekt is hun kinematica, die ons op zijn beurt informatie zou geven over hun donkere materie en hoekmomentum. In de Hoofdstukken 2 en 3 hebben we een steekproef van zes UDG's met grote H I reservoirs bestudeerd. Hiervoor hebben we gebruik gemaakt van gegevens van de Westerbork Synthese Radio Telescoop in Nederland en van de Very Large Array interferometer in de VS. Door naar de bewegingen van de H I in UDG's te kijken, verkregen we de rotatiesnelheid van de stelsels, waardoor we ze in de BTFR konden plaatsen. Verrassend genoeg zijn onze zes melkwegstelsels sterke uitschieters van deze relatie: hun rotatiesnelheden zijn veel lager dan verwacht gezien hun massa in gas en sterren en wijken dus ze in het lage-snelheidsregime naar boven

af van de BTFR. Dit is de eerste bekende populatie van melkwegstelsels die systematisch van de BTFR afwijkt en dit is een uitdaging voor de huidige modellen van de evolutie van melkwegstelsels. De totale massa (baryonen plus donkere materie) die uit de rotatie van onze UDG's wordt afgeleid is zeer vergelijkbaar met de gemeten massa van de baryonen, wat suggereert dat de melkwegstelsels kleine donkere materie reservoirs hebben. We hebben ook een indicatie gevonden dat het specifieke impulsmoment van UDGs hoger is dan dat van andere sterrenstelsels met vergelijkbare stellaire massa, wat zou kunnen verklaren waarom UDGs uitgebreidere lichtverdelingen hebben.

In Hoofdstuk 4 hebben we een van onze zes UDG's (het melkwegstelsel AGC 114905) bestudeerd, maar met scherpere gegevens dan voorheen, waardoor we de verdeling van het gas en zijn bewegingen gedetailleerder hebben kunnen achterhalen. We hebben bevestigd dat AGC 114905 niet op de BTFR ligt. Door zijn rotatiekromme grondig te bestuderen ontdekten we bovendien dat er weinig ruimte is voor donkere materie: in tegenstelling tot wat gebeurt in Fig. III, komt in het geval van onze UDG de waargenomen rotatie goed overeen met de bijdrage van de baryonen. Deze resultaten lijken op gespannen voet te staan met de huidige donkere materie modellen en tonen aan dat UDGs een groot potentieel hebben om verschillende theorieën te testen en inzicht te krijgen in de aard van donkere materie.

In de Hoofdstukken 5 en 6 hebben we het impulsmoment van sterren, gas en baryonen (sterren en gas samen) gemeten in een steekproef van ongeveer 160 nabije laat-typische melkwegstelsels met de hoogst beschikbare gegevenskwaliteit. Dit is de grootste steekproef van melkwegstelsels waarvoor gedetailleerde metingen van het baryonisch impulsmoment zijn uitgevoerd. In het algemeen vonden we dat de drie relaties (voor sterren, gas en baryonen) tussen massa en specifiek impulsmoment goed beschreven kunnen worden door ononderbroken machtswet van het regime van dwerggalaxieën met lage massa tot de meest massieve spiraalgalaxieën, zonder onderbrekingen die eerder door andere auteurs zijn voorgesteld. Bovendien vonden we dat de gasfractie van melkwegstelsels (de massa in gas ten opzichte van de totale baryonische massa) sterk gecorreleerd is met massa en impulsmoment. In een 3D-ruimte waarin de dimensies massa, specifiek impulsmoment en gasfractie zijn, definiëren sterrenstelsels zeer strakke vlakken. Deze nieuwe schalingsrelatie is een van de strakste (en daarom aantoonbaar een van de meest fundamentele) bekende schalingswetten van sterrenstelsels.

Tenslotte hebben we in Hoofdstuk 7 zeer gedetailleerde waarnemingen en robuuste analyse-instrumenten gebruikt om de eigenschappen van de donkere materie halo's af te leiden in een steekproef van dwerg- en massieve nabije schijfgalaxieën. Het meest innovatieve aspect van onze analyse is dat we rekening hebben gehouden met de werkelijke geometrie van de gasvormige schijven van melkwegstelsels. In plaats van aan te nemen dat ze een kleine, constante dikte hebben, hebben we schattingen van hun werkelijke dikte verkregen en het verloop met afstand tot het centrum van het sterrenstelse. Verandering van de geometrie verandert de verwachte bijdrage van de baryonen aan de rotatiekromme en

daardoor verandert ook de benodigde donkere materie (zie Fig. III). Onze analyse toonde aan dat het uitwaaieren van de schijven alleen een rol speelt voor de kleinste en meest gasrijke dwergstelses, maar genegeerd kan worden voor grote stelsels. Wij vonden een redelijk goede overeenkomst tussen de massa en de verdeling van donkere materie in onze waargenomen melkwegstelsels vergeleken met de voorspellingen uit simulaties. Bovendien bevestigde onze analyse eerdere bevindingen die aantonen dat bij laat-type stelsels de efficiëntie waarmee gas in sterren wordt omgezet hoger is voor stelsels met hoge stellaire massa's.

Om samen te vatten hebben we in dit proefschrift de meest gedetailleerde kinematische karakterisering van gasrijke UDG's tot nu toe uitgevoerd, de meest uitgebreide analyse van het baryonische impulsmoment van nabije schijfstelsels en de relatie daarvan met het gasgehalte gedaan en enkele van de meest nauwkeurige schattingen van de donkere materie halo's van dwerg- en massieve stervormingsgalaxieën verkregen. De waarneemresultaten die hier worden gepresenteerd hebben ons nieuwe inzichten verschaft over de rol van donkere materie en impulsmoment bij het vormen van de verbijsterend rijke populatie van melkwegstelsels die we vandaag waarnemen.

Resumen no académico

Galaxias el día de hoy

Carl Sagan dijo una vez que somos la forma en que el cosmos se descubre a sí mismo. En efecto, desde nuestra ubicación dentro de nuestra galaxia, la Vía Láctea, intamos entenderla no sólo a ella pero a todas las demás galaxias a nuestro alrededor: cómo y cuándo se formaron, cómo es que evolucionaron hasta el día de hoy, y cuál será su destino en un futuro lejano que no podremos presenciar.

Los principales componentes que podemos ver en cualquier galaxia son estrellas y gas. Sin embargo, la población de galaxias que observamos hoy día en el Universo cercano es multidiversa, con una vasta variedad de propiedades como su masa, tamaño, contenido de gas, y su tasa de formación estelar, entre otras. Esta diversidad el producto final de la evolución de las galaxias y podemos comparar observaciones de sus propiedades para comparar con modelos teóricos e intentar entender la física detrás de la formación y evolución de galaxias a través de la historia del Universo. Aunque hace solamente 100 años la comunidad astronómica aún debatía sobre si había otras galaxias en el Universo además de la Vía Láctea, nuestro conocimiento, si bien aún incompleto, ha incrementado considerablemente y ahora tenemos teorias de la evolución de galaxias dentro de un marco cosmológico, empezando con el Big Bang hace 14 mil millones de años y haciendo predicciones para un futuro también distante.

Para poder entender a las galaxias, es útil clasificarlas de acuerdo a propiedades en común. Uno de los esquemas de clasificación más usados es el llamado diagrama o diapazón de Hubble, mostrado en la Fig. I, el cual se basa en la apariencia de las galaxias a longitudes de onda opticas. En general, las galaxias son clasificadas en dos grandes familias: de tipo temprano y de tipo tardío (indicadas con las letras E y S en la Fig. I). Es importante mencionar que los adjetivos temprano y tardío se usan por razones históricas, pero no tiene ninguna relación con la evolución de galaxias (una galaxia temprana *no* se va a convertir en una tardía con el tiempo).

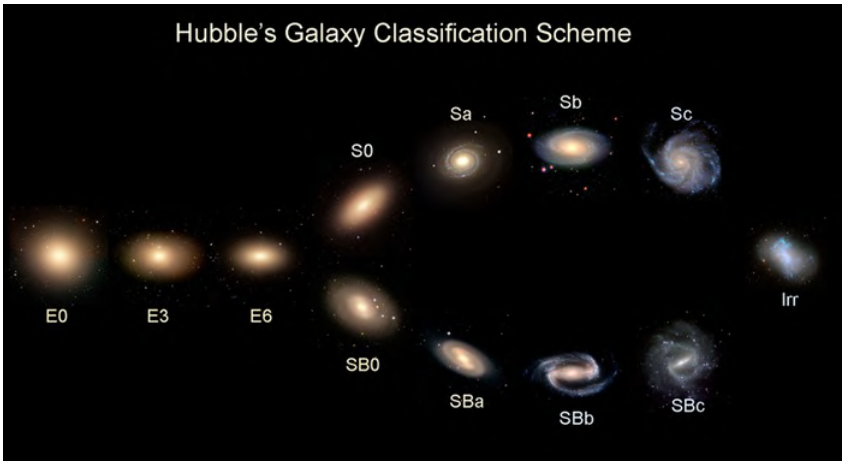

Figura I: Clasificación morfológica de Hubble. Galaxias de tipo temprano (E for su nombre en inglés) se ubican a la izquierda de las galaxias de tipo tardío (S). Creditos: Universidad de Iowa.

Las galaxias de tipo temprano, en la parte izquierda del diagrama de Hubble, tienen forma ellítica (por lo cual también se les llama galaxias elípticas), usualmente no rotan sobre su propio eje, tienen muy poco gas, baja formación estelar, y sus estrellas son viejas, pues se formaron hace mucho tiempo. Por otra parte, el lado derecho del diagrama de Hubble muestra las galaxias de tipo tardío. Éstas galaxias tienen forma the disco (por lo cual también se les llama galaxias disco), rotan, suelen tener grandes cantidades de gas, y siguen formando estrellas, por lo que sus poblaciones estelares son jóvenes. Frecuentemente las galaxias de disco tienen brazos espirales o concentraciones de luz en sus centros que pueden ser esferoidales (llamados bulbos) o elongadas (llamadas barras). El diapazón en el diagrama de Hubble divide a las galaxias de tipo tardío aún más: el brazo superior las ordena de acuerdo a cómo sus bulbos se van volviendo más débiles y los brazos espirales más fuertes, mientras que en el brazo inferior las galaxias son ordenadas dependiendo del tamaño de sus barras y qué tan abiertos son sus brazos espirales. Algunas galaxias no pueden ser clasificadas en estas dos grandes familias. En este caso se les nombra galaxias irregulares (Irr), y regularmente se muestran al final del diagrama de Hubble.

Como se mencionó anteriormente, las galaxias de tipo tardío tienen grandes candidates de gas. El gas y modestas cantidades de polvo forman lo que se conoce como el medio interestelar. La mayor parte del gas es hidrogeno atómico neutro, comunmente llamado H I. Así como las estrellas (excepto por los bulbos, que son esferoidales), el H I está también distribuido en forma de un disco. El disco de H I es usualmente más extenso que el disco estelar, como se muestra en la Fig. II donde las estrellas de una galaxia espiral cercana se muestran con color azul y amarillo y el disco de gas con color naranja. Los discos de H I son gruesos y acampanados, con su grosor aumentando con la distancia al centro de

la galaxia. Sin embargo, el grosor de los discos es pequeño comparado con su extensión horizontal.

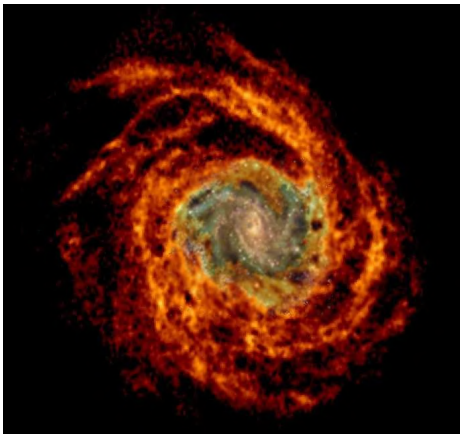

Figura II: Disco de estrellas (color azul y amarillo) y de gas (color naranja) en una galaxia cercana de tipo tardío. La distribución del gas es mucho más extendida que la distribución de las estrellas. Creditos: Tom Oosterloo.

Materia obscura y momento angular

Los componentes visibles de las galaxias (básicamente estrellas y gas, a los cuales nos referimos usualmente como 'bariones') están inmersos dentro de estructuras mucho más masivas llamadas halos de materia obscura, como se muestra en el panel izquierdo de la Fig. III. A su vez, los halos de materia obscura residen dentro del llamado medio intergaláctico. El contenido de materia obscura es un ingrediente crucial que regula la evolución de las galaxias, pues está intímamente ligado a su habilidad de acretar gas del medio intergaláctico y a qué tan frecuentemente las galaxias van a colisionar y crecer al fusionarse con otras galaxias a su alrededor. La distribución de materia obsura de las galaxias puede ser modificada por procesos que involucran a las estrellas y al gas. Por ejemplo, la exposión de estrellas en supernovas al final de su vida puede cambiar cómo está la materia obscura distribuida, y midiendo esa distribución podemos inferir qué tan fuerte tuvieron que ser las explosiones de las supernovas. Esto ilustra cómo estudiando la materia obscura podemos también aprender sobre los procesos físicos relacionados con las estrellas y el gas.

Como puede verse, cuantificar la distribución de materia obscura en galaxias es sumamente importante. Sin embargo no es una tarea fácil. En contraste con la materia ordinaria, la materia obscura no emite ni refleja radiación, y por lo tanto no puede ser observada directamente. Afortunadamente, la materia obscura sí interactúa con la materia bariónica a través de la fuerza de gravedad, lo que nos permite inferir su presencia incluso cuando es invisible a nuestros ojos. La materia obscura representa cerca del 80% de toda la masa en el Universo (el 20% restante son bariones). A pesar de ello, de qué exactamente está hecha la materia obscura ha permanecido como una pregunta sin respuesta por los últimos 50 años.

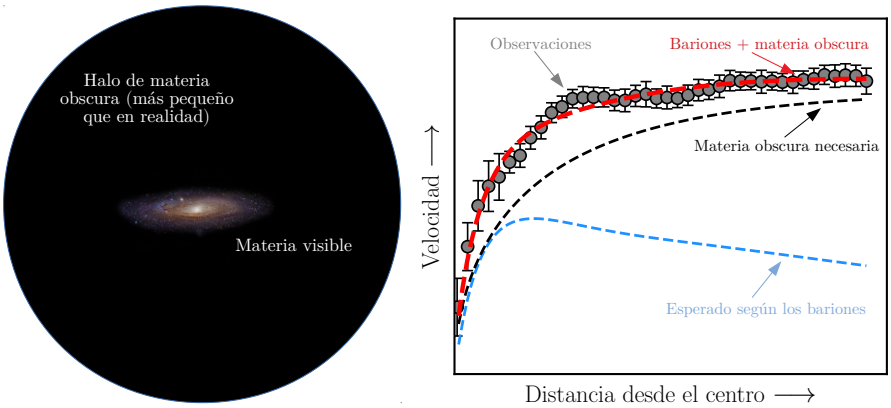

Figura III: *Izquierda:* Esquema de una galaxia de disco en su halo de materia obscura. El esquema no está a escala, en realidad el halo es aproximadamente 10 veces más extenso que la materia visible. Creditos de la imágen óptica: HST/NASA. *Derecha:* Curva de rotación (círculos grises) de una galaxia de disco cercana. La línea azul muestra la velocidad teórica que se espera considerando solamente la masa visible. Para poder reproducir la curva de rotación observada se necesita añadir un componente extra: el halo de materia obscura (línea negra). Una vez que la materia visible y obscura se consideran juntas (línea roja) se logra reproducir la curva de rotación.

Una de las manifestaciones más claras de que la materia obscura existe es la cinemática de galaxias de disco. Como se mencionó anteriormente, las estrellas y el gas en galaxias de disco giran, y la velocidad de rotación está directamente relacionada con la distribución total de masa. Utilizando distintos tipos de instrumentos y telescopios podemos medir la rotación de estrellas y gas en posiciones distintas dentro de cada galaxia, y así derivar una 'curva de rotación', que muestra la velocidad de rotación promedio a distintas distancias del centro. El H I es particularmente útil para esta tarea, pues nos permite medir curvas de rotación muy extensas (véase Fig. II). La curva de rotación de H I de una galaxia de disco cercana se muestra en el lado derecho de la Fig. III (círculos grises). Dada la distribución de masa de las estrellas y el gas, podemos calcular cuál debería de ser la rotación de la galaxia (línea azul en la Fig. III). Intrigantemente, las mediciones de la curva de rotatión son muy differentes a las expectativas teóricas basadas en la masa de los bariones. Para tener una mayor velocidad y poder reproducir las observaciones, es necesario añadir un componente adicional de materia obscura (línea negra en la Fig. III).

El contenido bariónico y de materia obscura en galaxias también se encuentran ligados por medio de una relación empírica llamada relación bariónica de Tully-Fisher (BTFR por sus siglas en inglés), esquematizada en la Fig. IV. La figura muestra la masa bariónica de las galaxias en función de su velocidad de

rotación; como la velocidad depende de la masa total (bariones más materia obscura), la BTFR conecta el contenido de materia visible y obscura. La relación es muy ceñida para galaxias espirales masivas, pero su comportamiento es menos claro cuando se mira a las galaxias enanas que tienen bajas masa y baja velocidad de rotación. Establecer la forma y características de la BTFR de forma precisa es importante para poder aprender acerca de la cantidad de materia obscura en galaxias y también sobre los procesos a través de los cuales las galaxias pueden perder masa. De hecho, la BTFR es una herramienta poderosa y frecuentemente usada para juzgar y valorar si modelos y simulaciones de galaxias son realísticos y adecuados: modelos o simulaciones que fallen en reproducir la BTFR serían, en principio, descartados.

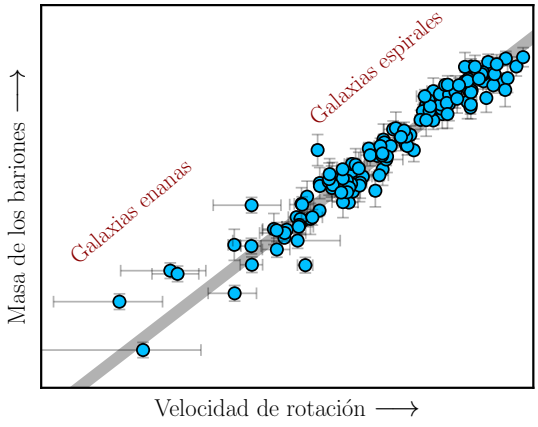

Figura IV: Esquema de la relación bariónica de Tully-Fisher. La relación conecta la masa visible de las galaxias con su velocidad de rotación, la cual incluye contribución del halo de materia obscura. Los círculos representan un conjunto de galaxias de disco masivas y enanas, y la banda gris es un ajuste a los datos. El comportamiento de la relación a bajas masas y bajas velocidades es menos claro que a masas y velocidades altas.

Otro parámetro clave que rige la evolución de las galaxias es el 'momento angular'. Estrechamente relacionado con las curvas de rotación, el momento angular mide la cantidad de rotación dentro de una galaxia dada su distribución de masas, y en términos generales es proporcional al producto de la velocidad de rotación de las galaxias y sus tamaños. Por ejemplo, si dos galaxias tienen la misma velocidad de rotación pero una de ellas está más extendida, esa galaxia tendrá un momento angular mayor. Observacionalmente se ha descubierto que el momento angular está estrechamente relacionado con la morfología de las galaxias. Como se muestra en la Fig. V, galaxias con diferente momento angular (o para ser más precisos momento angular específico, es decir el momento angular por unidad de masa) tienen morfologías notablemente diferentes. La tendencia general de esta relación, a menudo llamada relación de Fall por su descubridor, es que a masa estelar fija, las galaxias de tipo tardío tienen un momento angular específico mayor que en las de tipo temprano, encontrándose entre ellas los grupos intermedios del diapazón de Hubble como las galaxias S0 (también llamadas lenticulares) (véase Fig. I).

A pesar de tener una comprensión global de cómo funciona la relación entre la masa y el momento angular, todavía hay varios detalles que no entendemos

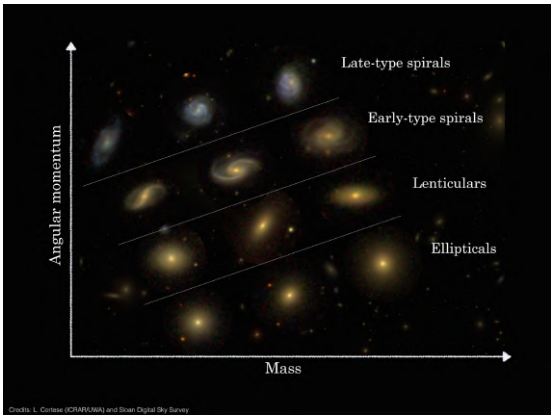

Figura V: Esquema de la relación entre masa y momento angular de la componente estelar de las galaxias cercanas (conocida como relación de Fall). Galaxias de masa estelar similar muestran morfologías sorprendentemente diversas dado su diferente momento angular. Credito: Luca Cortese.

totalmente. Por citar ejemplos concretos, no está claro cuál es el comportamiento de la relación para las galaxias enanas de baja masa, cuál es el impacto de las explosiones de supernovas en el momento angular y la morfología de las galaxias, o cuál es el momento angular del gas H I (y no sólo de las estrellas).

Esta tesis

El objetivo principal de esta tesis doctoral ha sido investigar el contenido de materia obscura y momento angular de las galaxias de disco cercanas. Para ello, hemos explotado observaciones de la cinemática de su gas H I, lo que nos ha permitido realizar mediciones robustas del contenido de materia obscura y momento angular.

Los dos primeros capítulos se centraron en el estudio de una población de galaxias enanas débiles denominadas galaxias ultra difusas (UDGs for sus siglas en inglés). Las UDGs son sistemas muy peculiares porque tienen una distribución de luz tan extendida como grandes galaxias espirales como la Vía Láctea, pero con unas 1000 veces menos estrellas. Por ello, su densidad de estrellas es muy baja, lo que les confiere un aspecto difuso en longitudes de onda ópticas. Aunque se han estudiado en detalle en los últimos años, los mecanismos de formación de estas débiles pero grandes galaxias aún no están claros. Una pieza crucial de información aún poco explorada es la cinemática de las UDGs, que a su vez nos daría información sobre su materia obscura y su momento angular. En los Capítulos 2 y 3 estudiamos una muestra de seis UDGs con un alto contenido de gas H I. Para ello, explotamos datos del Radiotelescopio de Westerbork en los Países Bajos y del interferómetro (también un conjunto de antenas de radio) Very Large Array en los Estados Unidos. Observando los movimientos del H I en las UDGs, obtuvimos la velocidad de rotación de los sistemas, lo que nos permitió situarlos en la BTFR. Sorprendentemente, nuestras seis galaxias se desvían significativamente de la relación: sus velocidades de rotación son mucho más bajas de lo esperado dada su masa en gas y estrellas, y por tanto se desvían

hacia arriba de la BTFR en el régimen de bajas velocidades. Esta es la primera población conocida de galaxias que se desvía sistemáticamente de la BTFR, y su posición es un reto para los modelos actuales de evolución de galaxias. La masa total (bariones más materia obscura) inferida a partir de la rotación de nuestras UDGs es muy similar a la masa medida de los bariones, lo que sugiere que las galaxias tienen bajas reservas de materia obscura. También encontramos pruebas tentativas de que el momento angular específico de las UDG es mayor que el de otras galaxias con una masa estelar similar, lo que podría explicar por qué las UDG tienen distribuciones de luz más extendidas.

En el Capítulo 4 estudiamos una de nuestras seis UDGs (la galaxia AGC 114905) pero con datos más nítidos que antes, lo que nos permitió trazar la distribución del gas y sus movimientos con mucho más detalle. Corroboramos que AGC 114905 no obedece la BTFR. Además, al estudiar a fondo su curva de rotación, descubrimos que la galaxia no parece albergar grandes cantidades de materia obscura: en contraste con lo que ocurre en la Fig. III, en el caso de nuestra UDG la rotación observada coincide bien con la contribución de los bariones. Estos resultados parecen estar en tensión con los modelos actuales de materia obscura, y muestran el gran potencial que tienen las UDGs para poner a prueba diferentes teorías y obtener nueva información sobre la naturaleza de la materia obscura.

En los Capítulos 5 y 6 medimos el momento angular de las estrellas, el gas y los bariones (estrellas y gas juntos) en una muestra de unas 160 galaxias cercanas de tipo tardío. Esta es la mayor muestra de galaxias para la que se han realizado mediciones detalladas del momento angular bariónico. En general, encontramos que las tres relaciones (para las estrellas, el gas y los bariones) entre la masa y el momento angular específico están bien descritas por leyes de potencia ininterrumpidas desde el régimen de las galaxias enanas de baja masa hasta las galaxias espirales más masivas, sin rupturas o desviaciones previamente sugeridas por otros autores. Además, encontramos que la fracción de gas de las galaxias (la masa en gas respecto a la masa bariónica) está estrechamente correlacionada con la masa y el momento angular. En un espacio 3D donde las dimensiones son la masa, el momento angular específico y la fracción de gas, las galaxias definen planos muy estrechos. Esta nueva relación que hemos descubierto se encuentra entre las leyes de las galaxias más estrechas y ajustadas (y, por tanto, podría decirse que entre las más fundamentales) que se conocen.

Por último, en el Capítulo 7 utilizamos observaciones muy detalladas y herramientas de análisis robustas para inferir las propiedades de los halos de materia obscura en una muestra de galaxias de disco enanas y masivas cercanas. El aspecto más innovador de nuestro análisis es que tomamos en cuenta la geometría y grosor real de los discos gaseosos de las galaxias. En lugar de suponer que tienen un pequeño espesor constante, obtuvimos estimaciones de su verdadero espesor, el cual es acampanado. Al considerar una geometría distinta, la contribución esperada de los bariones a la curva de rotación cambia, y por lo tanto cambia también la materia obscura necesaria para explicar las observaciones (véase la Fig. III). Nuestro análisis demostró que el ensanchamiento

de los discos desempeña un papel importante solamente para las galaxias enanas más pequeñas y ricas en gas, pero puede ignorarse para los sistemas más masivos. Encontramos un acuerdo razonablemente bueno entre la masa y la distribución de la materia obscura observadas en nuestras galaxias y predicciones de ciertas simulaciones. Además, nuestro análisis corroboró hallazgos anteriores que muestran que, entre los sistemas de tipo tardío, la eficiencia para convertir el gas en estrellas es mayor para las galaxias con masas estelares elevadas.

En general, en esta tesis hemos llevado a cabo la caracterización cinemática más detallada de UDGs ricas en gas hasta la fecha, hemos proporcionado el análisis más completo del momento angular bariónico de las galaxias de disco cercanas y su relación con el contenido de gas, y hemos obtenido algunas de las estimaciones más completas de los halos de materia obscura de las galaxias de disco enanas y masivas. Los originales resultados presentados en esta tesis han brindado nuevos conocimientos sobre el papel de la materia obscura y el momento angular en la formación de la multidiversa población de galaxias que observamos hoy en día en el Universo.

Acknowledgments

'And now we get to the hard part. The endings, the farewells, and the famous last words. If you don't hear from me often, remember that you're in my thoughts.'

Moon Palace, Paul Auster

The wild journey of completing a PhD is not always easy. In fact, it can easily get complicated and unpleasant. I was fortunate, during the last four years I had the best time. Sure, there were lows and highs, but I never felt in despair as I never felt alone. I was always understood, supported, and encouraged. In the next few paragraphs I want to dedicate a few words, certainly insufficient, to thank those wonderful people that have been with me during the last years. This thesis may have only my name in the cover, but its merit is shared with all of you.

The first person I need to mention is *Filippo*. Filippo, your acknowledgment is the last one I am writing because it is very hard for me to find the words to express all I would like to tell you. I really do not know where to start. You have been the best-possible supervisor ever. I think it says a lot that after you won the prize for the best supervisor of the faculty they did not allow your PhD students to vote the next year because you would have won it again. I am sure you would win the prize every single time. Thanks for inviting me to work with you; choosing your project, and you as a supervisor, has undoubtedly been one of the best choices of my life. I definitely did not make a mistake, and I hope you think you did not either! You have truly been a fantastic mentor in many different aspects. First, I should mention how inspiring your curiosity and excitement towards science are. Luckily, they are also contagious and I see some signs of them in me. Your rigor and desire to understand every small detail have also impacted the way in which I do research, making me a much better scientist. You found the perfect combination to give me the freedom to learn by myself and to pursue what I found interesting the most, but at the same time to guide me and not leaving alone rumbling in the limbo wasting time. Working with you is not only interesting but it is also fun and easy. You are

always super fast giving feedback and answering my gazillion emails, and I also appreciate that you never put pressure on me nor complain about the fact that I can only rarely be working before the very early morning (11 am). To me, it was also crucial all the enthusiasm you showed towards each of my results, and the supportive and encouraging words you always provided me with. Thanks for believing in me and for reminding me that I should do so myself. I also had the best time attending conferences with you, and after Greece and China I am so much looking forward to Switzerland in a few weeks, and hopefully in the many more yet to come. Thanks for all the interesting conversations and hilarious anecdotes during the many many afternoons with dinner and drinks we had, and for appreciating my many many questions about everything. Thanks also for the extensive lessons about wine (and for all the wine itself!). I think I have decided that Sangiovese is my favorite grape, but of course Nebiolo has an special place. I still keep the cork of the first Barolo we drank after my first paper, and I hope many more Barolo are in our way. You cared so much about my well-being that you forced me many times to eat vegetables (!), and always assumed (correctly) that I wanted more food and provided me with it. Finally, let me briefly thank you for also being supportive about more personal things, listening to me and offering wise advises. You know I will miss you a lot, but you have promised you will invite me often. Also, remember that I am still waiting for the chance to star in one of you movies. Thanks for everything, Filippo! I am very glad I can call you not only my supervisor, but also a mentor, collaborator, and friend.

Tom, I really like you both as a person and as a scientist. The very first time we met I thought you looked like a very serious person of very few words, and I hoped we would get along. Getting to know you better and learning how easy-going and actually friendly and funny you are has been one of my favorite surprises in the PhD! Having you as a supervisor and collaborator has also been great for my science (and not only for your extensive help with data reduction), and your sharp and critical view on details is something I have learned a lot from, and that I hope to acquire myself.

Betsey, I am so glad you were involved in my PhD since the beginning! Besides appreciating your always useful scientific feedback and how crucial you were for me to start working with UDGs (and my later involvement with SHIELD), I really value how caring you have been about me and my feelings. I will always remember our meeting at Starbucks in the Hoofdstation before I went to Germany to have other PhD interviews and the complete disinterestedness of your advises. I think that pretty much summarises how easy is to have an open communication with you and how selfless you are, always putting my comfort and opinion first.

Filippo, Tom, Betsey, I have learned so much from the three of you. Once again thank you very much for all the fun and support. I wish everyone could have supervisors with your same commitment. You have been awesome. I think we make a great team and I hope we keep collaborating in the future!

I would like to take this opportunity to also thank *James, Kristine*, and *Thijs*, the members of my assessment committee, for accepting to read and

evaluate the quality of my thesis. *James*, I am very happy you are coming to Groningen for my defence and I look forward to continuing the discussions we had in Oxford a few months ago. *Kristine*, we cannot meet in person this time but I hope we do it in the near future, and I foresee many interesting discussions. *Thijs*, thanks for having a detailed look at my thesis and for all the comments. Moreover, thanks for always being kind to me at Kapteyn, and for your constant interest and nice words on my work.

My thesis has greatly benefited from interactions within our research group and adjuncts. First thanks to all the 'official' members of Filippo's group during the last four years: *Ceci, Andrea, Asger, Anqi, Fernanda* (and of course Capitu), and *Barbara*. I have enjoyed quite a lot the weekly meetings and learning about all your exciting projects, it was a very stimulating, interesting, and fun environment. I should also thank the more senior 'unofficial' members of the group. In particular, I am in big debt to *Lorenzo, Antonino, Gabriele*, and *Enrico*. You guys have no idea how much I admire how smart and yet friendly and willing to help you are. *Lorenzo, Antonino*, having you at Kapteyn at the beginning of my PhD was beyond useful: you were there to help me out with my most stupid questions, and also to lead very interesting discussions that got me excited about my PhD project since day one. I have now papers with both of you, which makes me happy and proud. *Lorenzo*, I should emphasize that you have been one of my closest collaborators in the PhD and an important part of my thesis is largely a consequence of your interest and work on angular momentum. Thanks also for the vacuum cleaner! *Enrico*, thanks for all the help with Barolo and sharing lots of data with me, all of which was crucial for the success of my thesis. I remember you once said you were amazed by how smoothly the referee processes of my papers were. I think that has largely to do with the fact that my papers had already been reviewed by great collaborators like you, always providing critical and interesting comments on my work. *Gab*, you are one of the most brilliant people I have (and will ever) met. It never ceases to amaze me your deep understanding of every single astronomy subject I discuss with you. Having you at Kapteyn the last couple of years was great from a scientific point of view. Yet, it has been even greater having you as a friend, sharing many meals and even more bottles of wine. *Giuilano*, meeting you in Groningen was very nice and I am glad we have also collaborated, you and galpynamics have been crucial for a couple of chapters of my thesis. *Fra*, you are one of the nicest people I have met during the PhD. I have always been very impressed by your research skills but also your human quality. Spending time in Groningen and China was very nice (including the allergy list of course!) and I hope to meet more often in the future. *Kyle*, thanks for your very insightful and useful comments on different aspects of my work, and for all your help with simulated data cubes, and also for the kettle, which I use daily!

I would also like to thank those professors at Kapteyn that have actively interacted with me in the last years. *Marc*, I appreciate your critical view on science and your rigorously at examining data, from which I have learned. *Reynier*, in your very own you are one of the most critical and yet caring person

I know. Thanks for your support and encouragement since my MSc days. A very special thank goes to *Eline*. Eline, thanks for opening the doors of your house to me, for all the amazing meals we shared (some of the best I have had), all the interesting conversations, all the laughing, and in general all your kind words and awesome treatment to me, which made me feel as in family. As you know, you were one of my main reasons to come to Groningen for my MSc in the first place, and now you have also been crucial for me having the best time during my PhD. Thanks to other staff members like *Scotte, Inga, Rien, Amina, Raffaella, Renzo, Else, Manuela, Erwin, Mariano*, and *Bob*, for the smiles and small but yet gratifying interactions in the corridors of Kapteyn during the last years. Finally, thanks also to *Pratika*, *Reynier*, and *José Alfonso* (from the IAC), for the different lessons on galaxies during my MSc and the recommendation letters when applying for PhD positions.

Continuing with people from the institute, thanks to *Martine, Christa, Ramona*, and *María*, for all the implacable organisational work they do, making our lives at Kapteyn easy. The sames goes for *Lucia* and the super efficient management work. And a big thanks goes also to the *computer group* for the fast and efficient help always provided, with a special mention to *Leon* and *Eite*.

Office 192 has been a great environment to work, not only because of the wonderful window in front of my desk but also for the wonderful office mates I had: *Saikat, Evandro, Kevin, Kiril, Petra, Jan, Marta* and *Emma*. I must emphasize my acknowledgement to Emma and Marta, for your natural kindness and the light you always bring into the office.

And now it is time to thank the most amazing group of friends one could wish for. Ladies, gentlemen, it has been a pleasure. I have so many memories and things to say about all of you, but I will keep it very short. Here we go, in no particular order. *Smaran* (i.e. Esmaran), you are one of my closest friends and the biggest bullshiter I know. Being around you is always fun. You also helped me keeping track of NBA and brown-teaming against the pale world around us, haha. I enjoyed so much sharing your happiness the day of your register partnership (I still do not know how you managed, remember the medal I gave you) and I am sure there will be many more fun celebrations coming. *Olmo*, (a.k.a. Olmillo, a.k.a. Dr. Yushu), you are the nicest and chillest tree I know, and also one of my favorite persons in the world. I value a lot all the time we spent together, even in Torino when you tried to kill me with your driving and also with a food overdose (and also with some other of your decisions). I am very glad (unless I am not) you are coming to my defence and I hope to see you soon (not too late...) in Taiwan. *Simon*, or Diamond, thanks for your natural craziness, for all the balloons you kindly left at my place (it was a very pleasant surprise) and for the F1 conversations. And of course I will never forget the fondue and our hunting times in Geneva. *Nika*, I cannot stress enough how much I like you and how glad I am of being your friend... despite that horrible thing you did to me with the liquor chocolates. Thanks for having been there for me at any moment I needed it, and for all the nice conversations during these years. I am going to miss you a lot. *Valentina*, having a Latin American partner in

crime has been super fun, thanks for all the laughs, chill conversations, political conversations, dances, drinks, and movies we shared. Also for the crazy days in Annecy... please keep the secret, haha. Who would have guessed how close were we going to become after that morning in Heidelberg when I asked you if I could have breakfast with you and you looked at me scared! *Peter*, hermano latino, thanks for all the good moments (see above), which even include the FIFA massacres and of course the matches of the glorious Ajax. Next year European champions. *Ceci*, the famous Dr. Bacchini, mother of the volumetric star formation law, thanks for all the fun and the constant cheering. We had so many nice moments (even looking for 'the idiot' lost in the Forbidden City) that I will always remember. Of course two of them very high in the list include the fantastic food in Parma and that wonderful line in the Great Wall: 'who brought the fu*** wasabi!??'. I hope we soon get to spend more time together. Thanks a lot for coming to my defence and as always greetings to the good Fassa. *Jonas*, thanks for your characteristic kindness, and for the shared concerts, squash matches, and Dorades. Everyone will agree with me: a world with more Jonas would be a much better place. *Marinushka*, you and I share a big (although quite short really) common problem so in many ways only we understand each other. I am glad you are coming to my defence so we can celebrate as only we know. Thanks for all the fun and for being so crazy right now. I am certain the future holds great amounts of awesomeness for us. I am also looking forward to meeting my godchildren. *Katya*, my favorite TA during my MSc (do not tell Filippo M.), I am very happy the PhD gave me the chance to get closer to you. You are the sweetest person and you always make me feel appreciated and happy. I am so sorry for the pain the Russian invasion is causing on you and your beloved ones, and I hope very soon we all get to visit Ukraine in a very different context. I wish you the same enormous amount of happiness that you give to all of us:) *Enrico*, I am also happy I got to know you much better lately, thanks for the good times and your refreshing nonchalance. I am already looking forward to next year's Eurovision to continue with our tradition. Anastasia, the very first person from Kapteyn I ever contacted, we are so different and yet we have so much in common. Thanks for your constant support and motivation during these years, and for checking on me and caring about my life like a big sis. Thanks also for the wonderful invitation to Oxford and all the fun in London, I hope there is more of that in the future! *Tadeja*, I am very jealous of you: given your current circumstances and decisions it is clear you have earned paradise! In all seriousness, I am grateful for our friendship, it even survived wild Munchkin evenings, haha. *Laurent*, I am very glad we get along much better now, you have clearly become cooler. No doubts we were the best due of paranymphs in history. Thanks for the many amusing board games evenings and all the food I ate at Plutolaan 22. And obviously for Bomba. *Pranav*, saying good things about you instead of attacking you feels unnatural, so I will just say that I would be willing to help you again moving the bloody foosball because I have a good time with you and your nonsense. *Avanti*, you are a natural for making me laugh, thanks for all the smiles during these years, although I regret we did not meet as much

as we should have. We will fix that in the near future and I am very excited about December, I hope I can celebrate with you! *Kristiina* and *Karlis*, thanks for the Turkish adventures but also for your constant courtesy. I am happy you will be near me in Leiden. *Willeke*, your positivity is always uplifting, thanks for being so generous. I look forward to having a nice time in Leiden! *Emma*, thanks a lot for listening to my ranting about life when it was needed, I really appreciate our mutual trust on each other. *Marta*, thanks for all the chocolates from Torino you provided me with, and also for the fun and beers in Belgium. *Filippo M.*, my favorite TA during my MSc (do not tell Katya), I have enjoyed a lot of your craziness and your attachment to happiness (btw, the song 'Simone washes all...' will stay in my head for a long time). *Nelvy*, I am glad we have been friends during all these years, thanks for always being there with a smile, cordiality and patience. *Anne*, thanks for all the quality time during lunches and concerts. *Umit*, thanks for your sense of humor and the awesome invitation to your wedding, which remains one of the funniest experiences of my life (probably also for your family and Meltem's after seeing me dance, haha). *Andrés Felipe*, thanks for all the squash and all the conversations, and best luck with the new adventure in Utrecht. *Pier* and *Martyna*, queridos amigos. Together we scored lots of goals, got many drinks, and laughed uncountable times. I will soon visit you in Paris, be prepared. *Tegan*, I hope you know how important for me our friendship has been during these years. Thanks for all the movie nights at Pathé and at your place, for all the Harry Potter talks, for all the ribs, and for always listening to me and offering kind and useful words. *Laura*, my favorite Romanian, the walks and teas were very much appreciated, together with our very peculiar conversation style. *Angela*, it is a pity you are coming to Groningen once I am going to Leiden, but I am happy to be closer and I expect lots of visits so that we continue with our deep chats and our mistrust in humanity. *Vanda*, you have been so present and important since the last few months. Thanks for all the lovely time and for your kindness, authenticity, and that very unique spark of yours. *Vaggelis*, thanks for your refreshing attitude and the football evenings. *Teymoor*, you keep growing on me as a friend, and it has been nice having shared interests. *Alessandro*, there is a place in hell for all the tickling, but I will still visit you there because I like you that much. *Bram*, we share the best birthday, and sharing FIFA evenings and different conversations was always nice. *Tim, Wouter*, and *Patrick*, it was a pleasure sharing the basketball court with you for years. *Minke*, thanks for the gorgeous cover you designed as the presentation card of the work to whom I devoted myself during the last four years. I am very happy things worked out so well. I have also enjoyed a lot our conversations and I hope we keep contact. Thanks also to *Elaheh* and *Seyda* (who accepted me as the fifth office mate in 187), *Alka, Julia, Lorreine, Georg, Giulio, Tirna, Suma, Daniel, Akshara, Hyoyin, Javier* and *Tomás*. You all have made these years very fun and gratifying. Finally, I want to thank some people I did not have the chance to spend a lot of time with, but the little time we spent together was quite nice: *Francisco, Barbara, Eduardo, Bohdan, Amanda, Antonio, Bayron, Sabrina, Samira, Maxim*, and *Simone*. I am surely forgetting some names, but

please know that each single kind word and smile that were addressed to me have been very much appreciated and important during the PhD process.

Quiero mencionar también a mis amigos mexicanos en Groningen. Tenerlos a ustedes aquí, con el sentido de humor mexicano tan tragicómico, me ayudó a nunca sentirme lejos de nuestro México mágico. *Mariana*, desde los años de la maestría hemos sido (casi siempre) muy buenos amigos. Gracias por estar para mí en cualquier situación, por escucharme, aconsejarme, pero también echar relajo y quejarte un poco de mí. Me da gusto que ahora te alcanzaré en Leiden. *Fernando*, fue una buena decisión mover influencias para que fueras mi vecino. Gracias por todas las tardes de squash, juegos de mesa, series y cenas. Mucha suerte en Londres. *Jezabel*, eres una de las personas más desinteresadas, amables y positivas que conozco, verte y reír contigo siempre fue un gusto. *Alejandro*, definitivamente no hay otra persona en Groningen que pueda tocar el piano y fiestear tan bien como tú, gracias por toda la diversión. Y gracias también a mis amigos de México en México. En particular a *Luis*, *G/Yordi*, y *Citlalli*. Siempre hacen tiempo para verme y pasarla bien cuando voy a México (aunque la única realmente ocupada es Citla) y el hecho de que cuando voy para allá solamente le digo a mi familia y a ustedes les debe de decir algo. Luis (que como bien dijiste no eres mi amigo, eres mi hermano), gracias también por los días en Barcelona con la mismísima Patricia y a media revolución.

Andrea Afruni Strocchi, it is finally your turn, Buddy. Perhaps you noticed (probably you did not, sometimes you are a bit slow) you are in between the acknowledgements to my friends and to my family. This is because you are both, but you are also more than that (yet not boyfriends, just clarifying this for Umit and others). From the moment we met (and after my surprise realising you were a guy) we got along very well, and soon you became my best friend. Thanks for everything you have done for me, including (but not only) your support, stupid jokes, and company when I was happy, sad, annoyed, annoying, enthusiastic, frustrated, excited, or angry. Knowing that I could count on you absolutely always (except for being on time, finding the Pozzo Etrusco, or not getting lost in China) has been crucial in these years, even after you fled to Chile (I hate you and I miss you a lot). With you I always have the best time regardless of the place and situation. I started to write a list with some of my favorite moments with you. In the end, I gave up. It is just impossible to list all we have shared (ten different countries across three continents, after all), but I treasure all those countless memories and I look forward to accumulating new ones. I think you know that if I had to choose one single thing to keep from the PhD it would be a no-brainer (a bit like you): our friendship. But do not get pretentious, my dear friend. Peace and wild horses.

Y ahora finalmente toca el turno de agradecer a mi familia. No, no se me olvidaban, solamente los estaba haciendo esperar. *Mamá, papá, Ximena*, los amo, o como usualmente se los digo: ya después de tantos años se les aprecia. Las muchas o pocas cosas buenas que tengo y que he logrado son gracias a ustedes. Gracias por siempre creer en mí. *Papá*, te extraño, pero sé que estás conmigo, que estás orgulloso de mí y que éste será otro libro más que leerás. *Mamá*, no

siempre te lo digo pero valoro enormemente todo lo que tú y mi papá han hecho por mí. Poder darte un poco de vuelta es una de mis grandes alegrías, aunque mucho más te mereces. Gracias por fomentar en mí la ciencia desde pequeño. Sí te extraño ~~bueno, a veces~~. *Cuasi*, cómo me haces enojar, y aún así eres una de las alegrías más grandes de mi vida. Pasar tiempo juntos puede involucar discutir en algún momento, pero también implica risas y alegrías constantes. Siempre estaré para ti aunque seguido te mande al cuerno con tu cuerno. *Abuelitos*, no tengo palabras para decir cuánto los quiero y lo feliz que soy cuando estoy con ustedes, la mayor parte del tiempo riéndome. La magia de nuestra familia se basa en ustedes y espero que sepán que estoy muy orgulloso de ser su nieto. Gracias a todas mís tías (*tía Giselle, tía Nancy, tía Moni* y *tía Lola*), tíos (*tío Jaime, tío Noel, tío Jorge, Moon*, y hasta *Ahmed sonso*), primas (*Valeria, Anita, Giovanna, Marisol, Janeth* y *Aimée*) y primos (*Edgar, Iker, Noelito* y *Gael*). Por nuestras formas de ser, con algunos soy más cercano que con otros, pero quiero resaltar que desde la distancia, todos ustedes han sido una parte crucial no solamente de mi doctorado pero en general de cada uno de mis logros. Los quiero mucho a todos (hasta a Igar, que me traicionó y salvo a ya saben quién). El hecho de que navidad siempre haya sido mi día favorito es porque es el día que casi siempre podemos pasar todos juntos ~~lo cual significa que hay más regalos~~, y para mí es un día de magia pura. Cada palabra de aliento que me han brindado, junto con su motivación y confianza constantes son lo que siempre me empuja a dar lo mejor de mí mismo. Espero que vean esta tesis y este doctorado como un logro no exclusivamente mío, pero de toda nuestra familia.

As far as I know cities do not read, and yet I want to thank the city of *Groningen*. In the last six years, and especially during my PhD, Groningen has become my home, and is not a secret for anyone how much in love with this city I am. I will miss Groningen so badly, but I hope to come back often. Er gaat niets boven Groningen! The cover of my thesis, beautifully designed by Minke, is also my way to thank the Netherlands as a whole, for welcoming me with open arms, beautiful windmills, and lots of cheese. I am glad I will get to spend the next few years in this country that slowly I have been making my own.

'Perhaps we hurried past each other in a crowd today, and neither of us noticed, and the fibers of your coat brushed against mine for a single moment and then we were gone. I do not know who you are. But when you get home this evening, when this day is over and the night takes us, allow yourself a deep breath. Because we made it through this day as well. There will be another one along tomorrow.'

Anxious People, Fredrik Backman